High Entropy Amorphous and Crystalline Li-Garnet Films for Lithionic Applications

by

Yuntong Zhu

B.S. Materials Science and Engineering
B.S. Industrial and System Engineering

Georgia Institute of Technology, 2017

Submitted to the Department of Materials Science and Engineering
in Partial Fulfillment of the Requirements for the Degree of

Doctor of Philosophy in Materials Science and Engineering

at the

MASSACHUSETTS INSTITUTE OF TECHNOLOGY

June 2023

Authored by: Yuntong Zhu
Department of Materials Science and Engineering
Feburary 17th, 2023

Certified by: Jennifer L.M. Rupp
Visiting Associate Professor of Materials Science and Engineering
Thesis Supervisor

Accepted by: Robert J. Macfarlane
Associate Professor of Materials Science and Engineering
Chair, Department Committee on Graduate Studies

High Entropy Amorphous and Crystalline Li-Garnet Films for Lithionic Applications

by

Yuntong Zhu

Submitted to the Department of Materials Science and Engineering on Feburary 17th, 2023
in Partial Fulfillment of the requirements for the degree of
Doctor of Philosophy in Materials Science and Engineering

Abstract

Safe, reliable, and Li^+-conductive solid-state electrolytes are considered the key to unlocking the potential of solid-state and hybrid batteries, as well as lithionic devices beyond batteries, such as memristors and environmental gas sensors. The materials class of Li-garnet-type $Li_7La_3Zr_2O_{12-d}$ (LLZO) has garnered attention because of its high Li^+ conductivities, wide electrochemical stability windows, and non-flammability. However, high-temperature sintering (>1050 °C) is generally required to achieve its highly conductive cubic phase (cLLZO), which raises concerns over processing cost, sustainability, and interface stability with adjacent layers, such as cathodes. Alternative, amorphous LLZO (aLLZO) phases require lower temperatures for synthesis as compared to their crystalline counterparts, making this material an attractive option for use in solid-state batteries and beyond. However, to date, their amorphous local structure and structure-transport relationships have not been properly explored. In addition, the low-temperature synthesis routes to stabilize various aLLZO to cLLZO phases have rarely been discussed.

This thesis investigates the structure nature of a new class of high-entropy aLLZO phases and defines their low-temperature synthesis conditions towards lithionic applications. First, we explore the synthesis conditions and local structure of aLLZO and contextualize them with existing Li^+-conductive oxides. These high-entropy glass-ceramic phases consist of the highest number of local building units (LBUs) ≥ 4 being identified so far with edge- and face-shared LBUs, not conforming to the traditional Zachariasen glass formation rules. Within the aLLZO structure, we identify Zr and Li as network formers, facilitating the formation of LBU connections via bridging oxygen. A model study is next designed to confirm the role of La as a network modifier. Increasing the La concentration in aLLZO promotes local disordering. Moreover, low-temperature synthesis options for aLLZO and cLLZO are explored through crystalization enthalpy analysis and the development of the 1st Time-Temperature-Transformation (TTT) diagram for LLZO. We confirm the successful synthesis of cLLZO at a record-low temperature of 500 °C, about half of the temperature used for classic sintering. Finally, recent advancements and challenges towards the device integration of Li^+-conductive films are analyzed. This thesis sets the cornerstone for future structure optimization of high-entropy aLLZO glass-ceramics and provides low-temperature synthesis guidelines to assist the integration of aLLZO and cLLZO into lithionic devices.

Thesis Supervisor: Jennifer L.M. Rupp
Title: Associate Professor of Materials Science and Engineering

Acknowledgement

I am deeply grateful to all the individuals who have supported me throughout my PhD journey in the past five and half years at MIT. Their guidance, encouragement, and assistance have been invaluable and have greatly contributed to the success of this work. In this acknowledgement, I would like to express my sincere gratitude to the following individuals. This thesis would have not been possible without their unconditional support.

I am grateful to my advisor, Professor Jennifer Rupp, for her unwavering support, guidance, and encouragement throughout my PhD journey. From the moment I joined her lab, Professor Rupp has provided me with valuable mentorship and invaluable advice on both my research and my personal development. Her expertise in ceramic and battery research and her willingness to always make time for my questions and concerns were invaluable resources during this challenging but rewarding journey. I am also grateful to Professor Rupp for her kindness and generosity, both in and out of the lab. Her positive attitude and supportive nature have created a welcoming and inclusive atmosphere in the lab, and I have been fortunate to have her as both a mentor in research and a friend in life.

I am grateful to my committee members, Professor Carl Thompson and Professor Donald Sadoway, for their valuable feedback on my thesis research. In particular, I want to thank Professor Thompson for his guidance and numerous helpful discussions on crystallization kinetics and thin-film mechanics, which greatly enhanced the quality and depth of my work. I am also deeply thankful to Professor Sadoway for his insightful feedback on a variety of specific questions related to electrochemical systems and solid-state batteries. His enthusiasm for electrochemistry and teaching truly inspired and motivated me to pursue my own research interests and grow in the field over time. I also appreciate the support and feedback provided by Professor Krystyn Van Vliet at the beginning of my thesis research.

I am deeply grateful to have been a part of the Electrochemical Materials (ECM) Laboratory at MIT. The collaboration with my fellow lab mates has been invaluable and has made my PhD experience truly rewarding. I would like to extend my sincere thanks to Reto Pfenninger for helping me get started with my thesis project, and to Zachary Hood for his excellent mentorship and friendship. I am also grateful to Moran Balaish, Haemin Paik, Juan-Carlos Gonzalez Rosillo,

Kunjoong Kim, Lingping Kong, Katarzyna Sokol, Jesse Hinricher, Sara Sand, and Hyunwon Chu for their friendship, teamwork, and engaging discussions on science. I would also like to thank Professor Michal Struzik, Alfonso Carrillo, Alexander Bork, Andreas Nenning, Eva Sediva, Thomas Defferriere, Philipp Simons, Willis O'Leary, Drew Buzzell, and Lucie Quincke for being wonderful colleagues during my time in the group. I would like to extend a special thank you to our team's visiting scholars and students, Masaki Wadaguchi, Tibor Alec, Jun Hao Teo, and Marco Gysel, for their insights and engaging conversations on life and research. I feel honored to have had the opportunity to support and supervise Christopher Eschler and Edo Italia, two talented undergraduate and visiting master students, during my time at MIT. I have learned a lot from both of you – thank you for working with me! I would like to recognize Michael Chon from Professor Thompson's lab as a great collaborator over the years. I am grateful to Mengyi Wang, Haining Gao, Yimeng Huang, and Yiliang Li for being good friends and hiking, board game, and food companions, and Shaolou Wei and Zhe Shi for our discussions on research and career. Additional I would also like to express my appreciation to my all DMSE friends, who I will always remember fondly as we took classes and prepared for Qual and TAE together, and to my Sloan friends for the enriching classes and projects on startup entrepreneurship and energy economics. Finally, I would like to thank Mengyi Wang for being a good marathon training companion, as well as Eva Sediva and Marco Gysel for the memorable experience of running the Malden 10k together. I am also thankful to Arjun Shankar, Anvesha Sinha, Christopher Lai, John Paul Kee, and Charlene Lertlumprasert for bringing joy to my time in Seattle.

Throughout the years, I had the fortune to collaborate with some of the smartest scientists and researchers around the world. Their expertise and insights greatly enhanced the quality of this thesis, and I am deeply grateful for the opportunity to work and learn from them. Specifically, I would like to thank Prof. Clare Grey and her team members, Pedro Groszewicz, Steffen Emge, and Farheen, from the University of Cambridge for collaborations on the solid-state ^{7}Li NMR study. I would like to thank Prof. Mary Scott and her team members, Ellis Kennedy, Bengisu Yasar, and Yaqian Zhang, from the University of California Berkeley and Berkeley National Laboratory for collaborations on the fluctuation electron microscopy study. I would like to acknowledge Prof. Igor Lubomirsky and David Ehre from Weizmann Institute of Science and Prof. Anatoly Frenkel from Stony Brook University and Brookhaven National Laboratory for the fruitful discussion and data interpretation for the near order structures of amorphous Li garnets.

I would like to express my sincere gratitude to Samsung, Shell, and NGK for providing the financial support that made this thesis research possible. I also want to acknowledge the MIT Energy Initiative (MITEI) fellowship sponsored by ExxonMobil and the financial support offered by the MISTI MIT-Israel Seed Fund, which enabled me to conduct the exciting fundamental research on amorphous Li garnets. I would like to extend a special thank you to Lincoln Miara, Wonseok Chang, Andrea Maurano, Heung Chan Lee, Karen Thomas-Alyea, and Jusik Kim from Samsung for their invaluable discussions on solid electrolytes and solid-state batteries. I also greatly appreciated and enjoyed my conversations with Mohamad Kabbani from Shell on carbon-based materials and their applications in hybrid battery-supercapacitors.

Thank you to Argonne National Laboratory and Oakridge National Laboratory for providing access to their beamline and advanced electron microscopy, respectively. Their instrumental and data collection support was crucial to this study. A special thank you to Chengjun Sun for his support with XAS measurements. I also want to express my gratitude to the Materials Research Laboratory (MRL) at MIT and the Center for Nanoscale Systems (CNS) at Harvard University for their support with XPS, XRD, SEM, and EDS measurements. Thank you to Tim McClure and Charles Settens at MRL, as well as Tim Cavanaugh and Greg Lin at Harvard CNS for their training and experimental assistance. Additionally, I would like to thank Prof. Christopher Schuh's lab and Prof. Short's lab at MIT for offering access to their DSC/TGA equipment. Thank you to Edward Pang, Alan Lai, and Isabel Crystal from Prof. Schuh's lab, as well as Charles Hirst from Prof. Short's lab for providing training and support. I am extremely grateful for the support and assistance of all of these individuals and institutions.

In addition, I am deeply grateful to DMSE academic staffs, Angelita Mireles, Dominique Altarejos, and Amanda Bendzel for always being available to answer my questions and help me prepare the department letters and documents. I am also thankful to Rupp group’s administrative assistants, Priyanka Chaudhuri and Amanda Bendzel at MIT and Julia Haffendorn at TUM for their patient supports in the past years.

I am extremely fortunate to have had the opportunity to work as a research scientist intern at Meta Reality Labs in the summer of 2022. It was a thrilling and memorable summer working towards the development of future AR display technologies. I would like to give a special thank you to Alejo Lifschitz for his excellent mentorship. I also want to express my gratitude to Bo Zhao, Keren

Zhang, Igor Abramson, Anthony Phan, Sebastian Rozo, Vincent Overney, Lafe Purvis, Nidhi Shah, Scheherzad Alvi, Milind Pawar, Tony Zamora, Goeun Sim, Yu Shi, Rob Johns, Vivek Gupta, Zack Wong, Li Zheng, Josh Kaitz, Richard Farrell, Sharad Bhagat, Quandou Wang, Jonathan Onorato, Janee McNeil, Li Zhang, Joseph Yang, Jilin Yang, Austin Lane, Marvin Alim, Pasqual Rivera, Afsoon Jamali, Roy Mei, Rebecca Cheng, Le Tran, Xiaoyu Xiang, Ankit Vora, Geraud Dubois, and Matt Colburn for their contributions and support during my time at the company. I am grateful for the opportunity to be a part of this team and for the valuable experience and friendships I gained.

I would like to express my gratitude to my parents, Professor Hailei Zhao and Professor Zhiming Zhu, for their unwavering love and support. As professors themselves, they have always fostered a love of learning in me and have supported me every step of the way. Their wisdom, knowledge, and enthusiasm in research and science have shaped me into the person I am today and have played a crucial role in my academic and personal growth. Their encouragement has been a constant source of strength and motivation and helped me through some of the most challenging times. Dear mom and dad: thank you for always believing in me and for being such an important part of my life and my academic journey!

Finally, I want to thank you, my partner, Wei Zeng, for your love, patience, and support throughout this journey. Words are not enough to express my gratitude and appreciation for everything that you have done for me. Your understanding and encouragement have meant everything to me, and I could not have completed this Ph.D. without you by my side. I am excited for the wonderful prospects that await us in the future ☺

Table of Contents

List of Tables

List of Figures

1. Chapter 1: Introduction

Adapted from Yuntong Zhu, Juan Carlos Gonzalez-Rosillo, Moran Balaish, Zachary D. Hood, Kun Joong Kim, Jennifer L.M. Rupp. Lithium Film Ceramics for Solid-state Lithionic Devices. *Nature Reviews Materials* 6.4 (**2021**): 313-331.

1.1. Motivation

Over the course of history, industry has been defined by technical evolution with continual reinvention depending on the available resources, needs, and discoveries. Some industrial advancements have had such an overwhelming impact that the associated time periods and achievements have been dubbed "revolutions". For instance, "mechanization" emerged at the end of the 18th century, whereby agriculture was partially replaced by industry, providing a new foundation for the economic structure of society in what is known as the 1st industrial revolution. The extraction of coal resources and the invention of the steam engine introduced new types of energy conversion. Almost a century later, at the end of the 19th century, new sources of energy (namely, oil, gas, and electricity) gained in significance, and economic and industrial models based on "large factories" emerged in the 2nd industrial revolution. During this time, the chemical and material manufacturing industry that produced goods such as fertilizers, steel, and the first functional ceramics grew. The 3rd industrial revolution arose around the 1970s with the birth of the transistor, propelling significant advancements in electronic- and information-based technologies that drove the automation of production and computation. Notably, the new industries dedicated to the conversion of renewable energy sources and storage technologies such as batteries emerge, despite the dominance of a fuel, coal, and nuclear-based economy. The 4th industrial revolution is unfolding before our eyes; it started with the emergence of artificial intelligence (AI), driven by exponential increases in computing power and the availability of vast amounts of data in areas ranging from customer service and policymaking to drug discovery and materials design. This revolution is characterized by the fusion of technologies that cross the boundaries of the digital, physical, material, and biological spheres,[1] entering cyber-physical production systems and intertwining the real and virtual worlds **(Figure 1-1 a)**. New possibilities to power and virtually control industrial production processes using green energy technology, such as wind, solar, and

geothermal energy, will ideally be embedded in smart cities and are of immanent importance as low-waste strategies to mitigate the socio-economic risks associated with climate change. Mobile devices, such as smartphones and watches, are continuously integrated in our lives today, and these devices provide autonomous energy and data storage capabilities and access to computation, knowledge, and sensing functions, all of which greatly affect the way we live, think, feel, work, and interact with the environment. The opportunities provided by the 4th industrial revolution to further integrate these aspects into our daily life are accelerated by technical evolutions of the Internet of Things (IoT)[2] and new medical and environmental feedback loops that can save resources, reduce industry energy, minimize waste footprints, and assure high health standards.

Despite the potential for a new era driven by the development of the IoT and AI, the performance of mobile electronic devices such as phones, computers, and medical monitoring units depend on the performance and evolution of their constituent computational units such as light, pressure, chemical, and gas sensors and energy storage battery packs. The computational units still largely rely on silicon-based transistor technology from the 1970s, which formed the basis of the 3rd industrial revolution.[3] Following the trend predicted by Moore's law, transistors with 5-nm feature size have been produced and commercialized by Samsung Electronics[4] and Taiwan Semiconductor Manufacturing Company (TSMC)[5] with an exponential increase in on-chip transistor density. Nevertheless, quantum tunneling effects limit further down-scaling of the transistor's gate length and cap future transistor chip densities. In addition, one cannot ignore the exploding cost associated with down-scaling chip design and quality verification in the transistor industry over the last 20 years **(Figure 1-1 b)**,[6] which may not be economically favorable if the trend continues. Moreover, today's computers operate primarily on von Neumann architectures with all the data stored in memory and then transported to the calculation engine.[7] This physical shuttling of data requires far more energy and compute cycles than the actual computation.[7] This bottleneck inherently limits the computation speed and throughput of the transistor-based logic and results in high energy costs per computing operation.[8] In contrast, neuromorphic computing in AI with machine learning (ML) algorithms can be based on computing architectures encoding and processing data based on temporal information of spike events that mimic biological neurons. A clear definition of new materials and hardware for artificial neurons in AI and ML operations is needed to contribute to the efforts defined in the 4th industrial revolution and reduce energy consumption by orders of magnitude compared with common von Neumann computing.

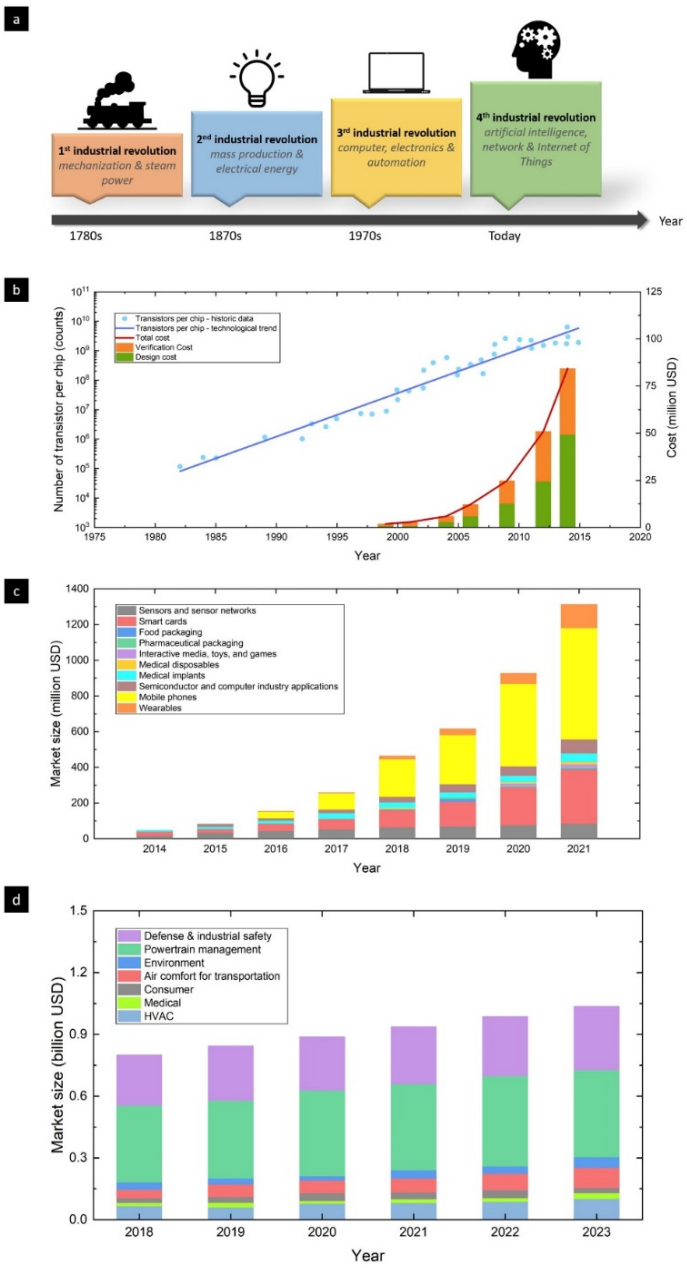

Figure 1-1. (a) Historic overview of industrial revolutions of mankind. **(b)** evolution of transistor count per chip and related design and verification costs.[1] **(c)** current and predicted market size for thin-film micro-batteries for various end-product applications.[2] **(d)** current and predicted market size for gas sensors for various end-product applications.[3]

To meet the ever-growing demand for improved energy density and cycling life for AI-chip-integrated mobile devices, further innovations in battery architectures and material components are of essence. Current battery packs and sensors remains rather bulky with >50-µm-sized

functional electrochemical cell entities; for instance, liquid-electrolyte-based Li^+ pouch-cell batteries are commonly used in current mobile phones and other portable electronics. However, today's electronics are multi-functional with increasing demand for reduction in device size and weight and even for operation in biocompatible environments. These features pose challenges for the integration of current liquid-electrolyte-based pouch cells, thereby urging the development of alternatives, such as solid-state micro-batteries and gas sensors, that would enable further miniaturization to on-chip devices. The thin-film micro-battery market size is predicted to exceed 1.3 billion U.S. dollars by 2021,[9] benefiting fields such as mobile phones, smart cards, medical implants, and food packaging **(Figure 1-1 c)**. In addition, with major global problems, including the lack of accessible medical care, disaster prediction, energy resources, and waste management as well as the prevalence of pollutants that affect the environment and agricultural food production, the gas-sensor market size is predicted to grow at a rate of ~6.25% per year and exceed 1 billion U.S. dollars in 2022 **(Figure 1-1 d)**.[10] In particular, the mobile phone, smart card, and wearables sectors are expected to see the largest growth in gas-sensor market share. These challenges motivate a quest within the 4th industrial revolution for new materials, manufacturing routes, and devices as well as improved understanding of operational chemistry and physics in the wider area of gas sensing and autonomous energy supply.

Functional ceramics offer the prominent advantage of performing multiple tasks with high efficiency, including energy storage and conversion, neuromorphic information processing, and data storage in addition to environmental gas sensing, simply based on ion transport within electrochemical cell arrangements. These materials (*e.g.,* O^{2-}, H^+, and Li^+ conductors) allow for manipulation of materials chemistry, electronic structures, and ion conduction over a wide range. Among the numerous possible functional ceramics, we focus specifically on Li-conducting oxides, their thin-film processing approaches, chemistry and opportunities and challenges for their device-level integration.

1.2. "Lithionics" Devices Operated Based on Li^+-Conducting Oxides

We introduce current initiatives and the future vision of "Lithionics" **(Figure 1-2)** by repurposing Li oxides conventionally known from large-scale battery electrochemistry for use as thin-film

electronic entities across the fields of sensing, neuromorphic computing, and on-chip energy storage to serve multiple functions in future chip architectures and electronic devices.

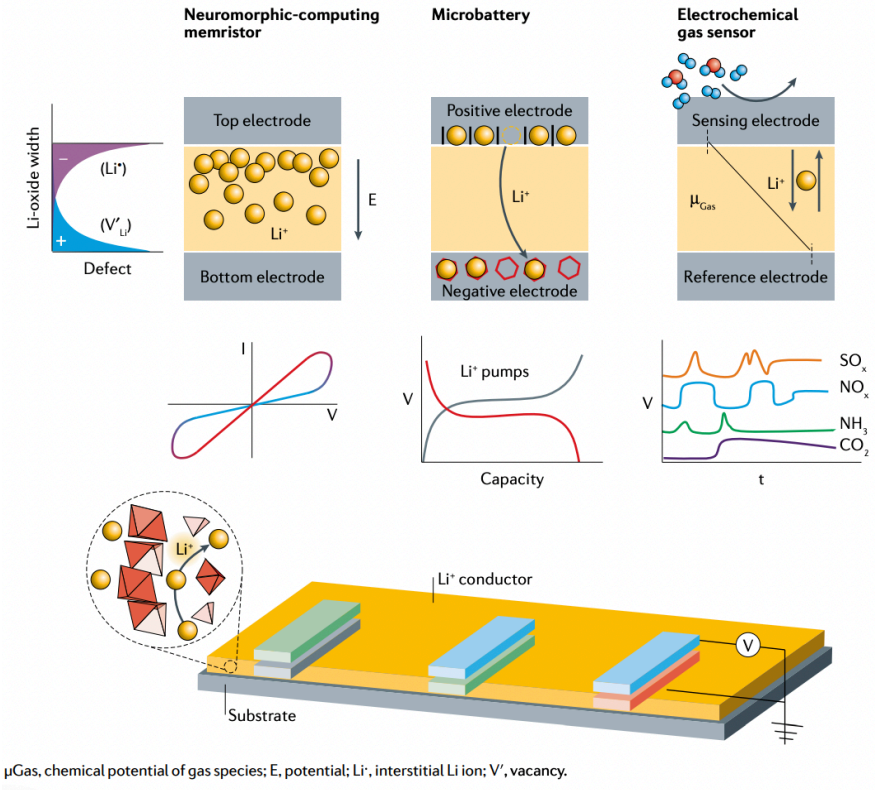

Figure 1-2. Lithionics defines a class of multifunctional, on-chip devices based on Li^+-conducting thin films. Lithionic devices include microbatteries, memristors, electrochemical gas sensors and other devices that are based on Li-oxide materials combining various functionalities. Functionalities can be achieved by varying electrode and electrolyte materials that define the electrochemistry and by varying the device design to promote Li^+ migration. in lithionics, Li ions serve as the carrier for information and energy storage, binary and neuromorphic computing, and environmental sensing and tracking.

Compared with traditional semiconducting materials for microelectronic devices, which largely operate based on the movement of electrons, Li-based materials offer an attractive opportunity to manipulate electronic states and ionic defects over a wide range depending on their Li^+ chemistry (*e.g.,* intercalation/de-intercalation, conversion, or alloying). For instance, electrochemical devices in the Lithionics vision can be operated using a few Li-oxide films but with different operation principles defined by various electrode sets. In a Li-operated neuromorphic computing memristor, Li ions are redistributed through the Li-oxide switching layer upon the application of an external electric field, resulting in different resistive states across the film. In contrast, in a micro-battery,

a Li^+-conductive electrolyte film separates the electrodes, where Li ions undergo intercalation/deintercalation upon charge and discharge. In an electrochemical gas sensor, transport of Li ions through the Li^+-conductive electrolyte layer occurs when the chemical potentials change between the sensing and reference electrodes, and gas concentrations can be determined from the voltage read-off across the Li^+-conductive electrolyte. All three devices require Li-based-oxide ceramics to be designed and processed in thin-film form with precise control of the chemistry (*e.g.,* Li stoichiometry) and microstructure to achieve high device density and functionality. However, most efforts on Li-based materials have been directed toward large-scale ceramic manufacturing of rather "bulky" and mostly microcrystalline Li-based oxides primarily targeted for solid-state batteries (SSBs). In many, if not most, instances, the characteristics and properties of a solid-state thin film can differ significantly from those of the same material scaled with larger thicknesses. The variation in materials properties is often related to size effects as thin films (with thickness < 1 μm) have a large volume ratio of grain boundaries to grains, leading to changes in space-charge potentials and local chemistry.[11] Moreover, as Li is a reactive element with light atomic weight, Li stoichiometry in films can be difficult to control, especially during deposition and post-processing at elevated temperature, which poses an additional challenge for processing Li-based thin films. Although progress has been made in controlling Li stoichiometry and film chemistry, the techniques are still far from mature and the film properties still need to be explored before integration of the films in Lithionic devices can be optimized. This process of knowledge and technology evolution may take a few decades before being fully integrated into assembly lines for the manufacture of thin-film devices. For example, within the family of solid-state Li^+ conductors, lithium phosphorous oxynitride (LiPON) was among the first Li-based materials processed as a thin film in the 1990s and had a substantial impact on the evolution of thin-film SSBs.[12] However, it took two more decades to understand the local structure and conduction path of LiPON, and to optimize performance. To reach a similar maturity level for the processing and structure control of other solid-state Li-oxide materials, such as NASICON and Li garnets in film form, an incubation period is expected with an emphasis on understanding film local structures and film property control.

Table 1-1. Li-based material requirements for lithionic devices.

Component	Thin-film microbattery	Neuromorphic-computing memristor	Electrochemical gas sensor
Electrode	Positive electrode: high voltage and capacity; good electrochemical and chemical compatibility with the solid-state electrolyte over many cycles; example materials are $LiCoO_2$, $LiMn_2O_4$, $LiNiMnCoO_2$ Negative electrode: low voltage and high capacity; uniform charge and discharge; ideally Li metal; example materials are Li metal, $Li_4Ti_5O_{12}$, Si, C	Stable against metallic electrodes at high electric fields Li intercalation at the interfaces Example materials: Pt, Au	Sensing electrode: good thermal and mechanical stability; must be in contact with electrolyte (mobile ions), metal electrode (electrical signal) and targeted gas; example materials are Li_2CO_3 (CO_2 sensor), $NaNO_2$ (NO_x sensor), Li_2SO_4 (SO_x sensor) Reference electrode: stable to avoid voltage drift in the sensor signal; high conductivity to improve response time; stable at the targeted gas concentrations; example materials are Pt, Au
Electrolyte	High ionic conductivity with low electronic conductivity (transference number, t_{ion} ~1) Low toxicity and cost Wide electrochemical-stability window Preferably compatible with Li metal Mechanically robust against Li penetration at high current density Good electrochemical and chemical compatibility with positive and negative electrode Example materials: LiPON, LLTO, LLZO	Availability of metal-to-insulator transition preferred 2D or 3D Li conductor Fast resistive switching kinetics Control over retention Long-term stability Phase evolution at high electric fields Example materials: $LiCoO_2$, $Li_4Ti_5O_{12}$	High ionic conductivity to ensure fast response Inactive (high durability at operating temperature) to the targeted gases Good chemical stability at operation temperature and atmosphere Example materials: LiPON, Li_3PO_4, LLZO

LiPON, lithium phosphorus oxynitride; LLTO, $Li_{3x}La_{2/3-x/3}TiO_3$; LLZO, $Li_7La_3Zr_2O_{12}$.

Not surprisingly, different Lithionic devices may not have the same material property requirements for each Li-oxide film component **(Table 1-1)**. For instance, Li electrolytes in micro-batteries and sensors must possess high ionic conductivity; however, although stability against Li metal is not required for electrolytes in sensors, it is preferred for those in micro-batteries to enlarge the operational voltage window and assure stable cycling and high energy density. As a result, a material class that is not ideal for one application could be ideal for another Lithionic device. For these reasons, knowledge exchange is needed among the SSB, electrochemical gas sensor, and neuromorphic computing communities to overcome manufacturing-related challenges and facilitate innovations in applications and devices.

1.3. Evolution of Thin-Film Solid-State Li^+ Conductors and Future Opportunities

1.3.1. Solid-State Li-Conducting Electrolyte Films

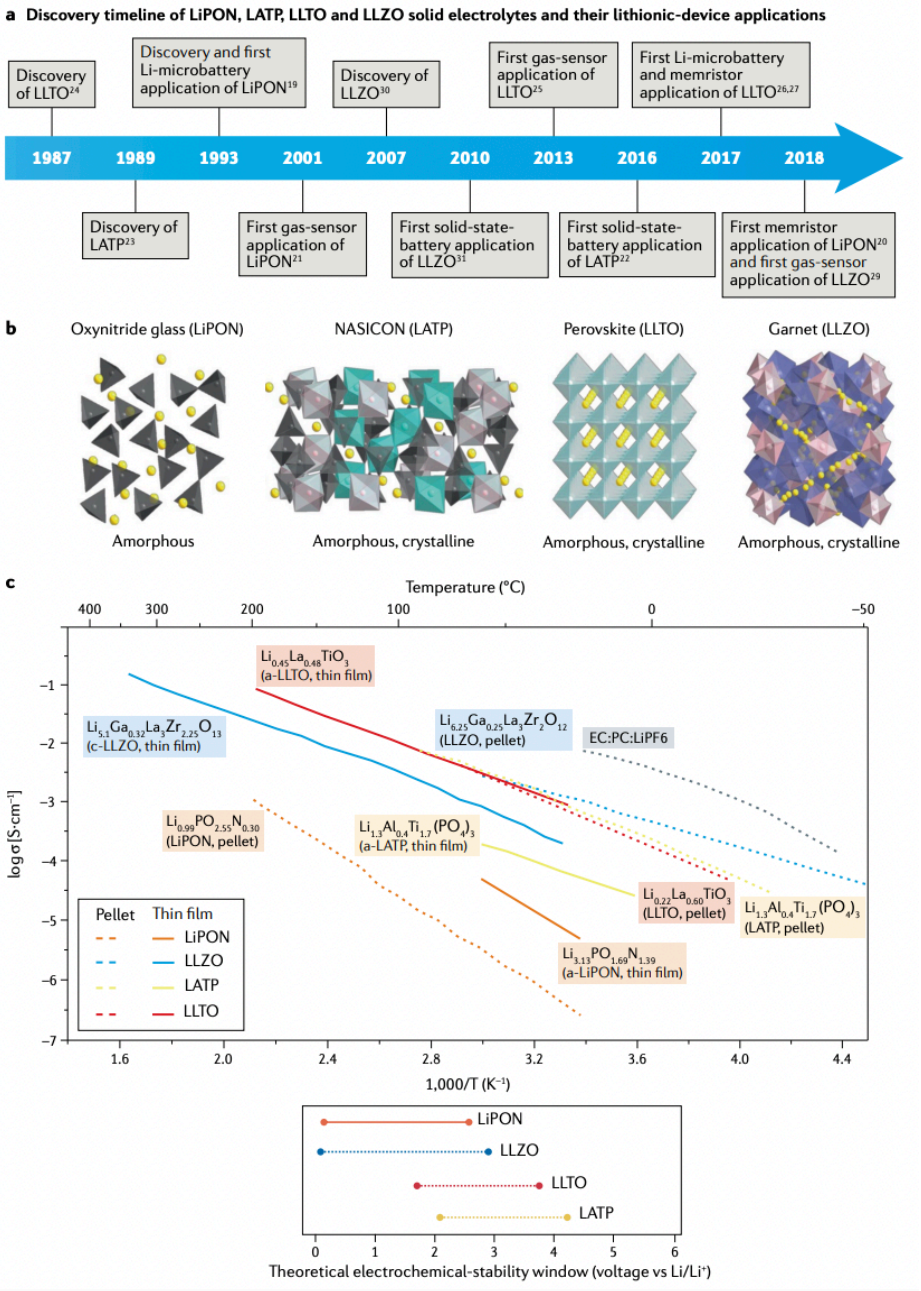

Figure 1-3. Oxide-based Li^+ conductors. **(a)** Timeline of Li-based solid electrolytes and lithionic-device applications. **(b)** Structures and Li-conduction paths of oxide-based Li^+ conductors, including amorphous lithium phosphorus oxynitride (LiPON), Na super ionic conductor (NASICON)-type $Li_{1.3}Al_{0.3}Ti_{1.7}(PO_4)_3$ (LATP), perovskite-type $Li_{3x}La_{2/3-x/3}TiO_3$ (LLTO) and garnet-type LLZO, $Li_7La_3Zr_2O_{12}$ (LLZO). **(c)** Li^+ conductivity of Li-oxide-based solid-state electrolytes in pellet and thin-film form compared with state-of-the-art liquid electrolytes, including the highest reported values of pellet-type and thin-film LLZO,[13,14] LLTO,[15,16] LATP[17,18] and LiPON,[19] and theoretical electrochemical-stability windows based on first-principles thermodynamic calculations.[201] The processing temperatures are shown for pellets and thin films. The classification as amorphous (or crystalline) thin film or pellet (or tape) are indicated by a- and c-, respectively.

The discovery of Ag^+-ion transport in crystalline silver iodide, α-AgI, in the 1830s lay the foundation for solid-state ionics, or the study of ionic motion in solid matter, and the first solid-state electrolytes.[21] However, it was only in the late 1960s that a notable change in the field occurred with the discovery of numerous new cationic and anionic solid electrolytes with high ionic conductivities, including O^{2-}-conducting doped zirconia, Na^+-conducting α-alumina, and Li^+-conducting garnets.[22–24] Since then, the study of Li-conducting solid-state electrolyte started in 1970s with a focus on Li-oxide-based[25] and Li-sulfide-based glasses,[26,27] as well as oxysalt-based electrolytes.[28] Inspired by the discovery of LiPON,[29,30] inorganic solid-state electrolytes have been intensively investigated in Li^+ battery research since the 1990s, opening up the opportunities for direct on-chip application of thin film micro-batteries. Currently, the most studied Li^+-conducting ceramics are based on oxynitride glasses (LiPON), NASICON-, perovskite-, and garnet-type structures[31] **(Figure 1-3 a and b)**. The Li^+ conductivities of most of these materials have reached on the order of 10^{-7}–10^{-3} S cm^{-1} at room temperature. Historically, the transport properties of solid-state Li^+ conductors were mostly first investigated in the rather bulky form of millimeter-sized ceramics typically processed as pellets.

As demonstrated in **Figure 1-3 a**, substantial effort is required to transform a Li^+-conducting ceramic from a classic bulky pellet to a thin film hundreds of nanometers in size: on average, more than 10 years of additional development time is needed to understand the chemistry, deposition, and characteristics of a ceramic film when starting from its pellet counterpart. For example, it is generally observed that when NASICON-type $Li(Al,Ti)_2(PO_4)_3$ (LATP), perovskite-type $Li_xLa_yTiO_3$ (LLTO), and garnet-type $Li_7La_3Zr_2O_{12}$ (LLZO) are processed as thin films, their conductivities are reduced by more than one order of magnitude at room temperature. The stellar exception is the material class of LiPON, for which the thin-film processing route was established before manufacturing routes for bulky amorphous LiPON glass pellets.[32,33] Being among the first Li-conducting solids available in thin-film form and due to their reduced thickness of less than 1 µm, LiPON films have driven the development of solid-state electrolytes for micro-batteries. Moreover, with access to more solid-state Li^+ conductor chemistries than ever before in both pellet and thin-film form and with many computational predictions for future candidates, scientist and engineers are currently in the Golden Age of solid-state "Lithionics". Opportunities in ceramic processing to define the chemistry and attain a deeper understanding of the relation between the structure and Li^+ transport in films will play a role in determining the energy and information

densities of future batteries as well as the design of new applications such as neuromorphic computing and sensing units based on Li. Most earlier reviews on these material classes focused on the materials in their ceramic pellet form, with only a few reviews focused on thin-film micro-batteries. Thus, these reviews often ignored substantial advancements in film synthesis, which poses a challenge for advancing their integration in ceramic thin-film devices other than micro-batteries. In this chapter, we wish to critically discuss the characteristics, opportunities, and challenges associated with the processing of solid-state Li-conducting ceramics and define their chemistry. Collectively, a deeper understanding of both the chemistry and ceramic manufacturing options for these films will enable their integration as functional ceramic building units for the future of "Lithionic" devices.

1.3.2. $Li_xPO_yN_z$ (LiPON)

LiPON, with the general chemical formula $Li_xPO_yN_z$, is one of the earliest developed Li-based thin-film solid electrolytes and enabled the successful commercialization of SSBs.[34] In the early 1990s, Oak Ridge National Laboratory first reported the use of LiPON as a thin-film electrolyte in micro-batteries.[33] Structurally, the basic building units of LiPON are a Li phosphate polyhedron, which either bridges over nitrogen or remains apical (meaning an apex-substituted N in a $P(O,N)_4$ tetrahedron).[35] LiPON can exist in either crystalline (γ-Li_3PO_4) or amorphous form (a-Li_3PO_4). In both forms, the PO_4 units remain isolated and are always in tetrahedral coordination, forming the sole building block unit of the structure (**Figure 1-3 b**). Through amorphization and partial N substitution for O throughout the γ-Li_3PO_4 structure and through higher structural density and increased Li–Li interactions,[36] the ionic conductivity can be enhanced by approximately 12 orders of magnitude.[30,36–38] Recently, computation and experiments on a-Li_3PO_4 have provided strong evidence of nitrogen being incorporated in the form of apex-substituted N and double-bridging N bonds within $P(O,N)_4$ tetrahedra frameworks and of the ratio between the two bonded nitrogen atoms varying with Li content, which allows Li ions to move in the amorphous network.[35]

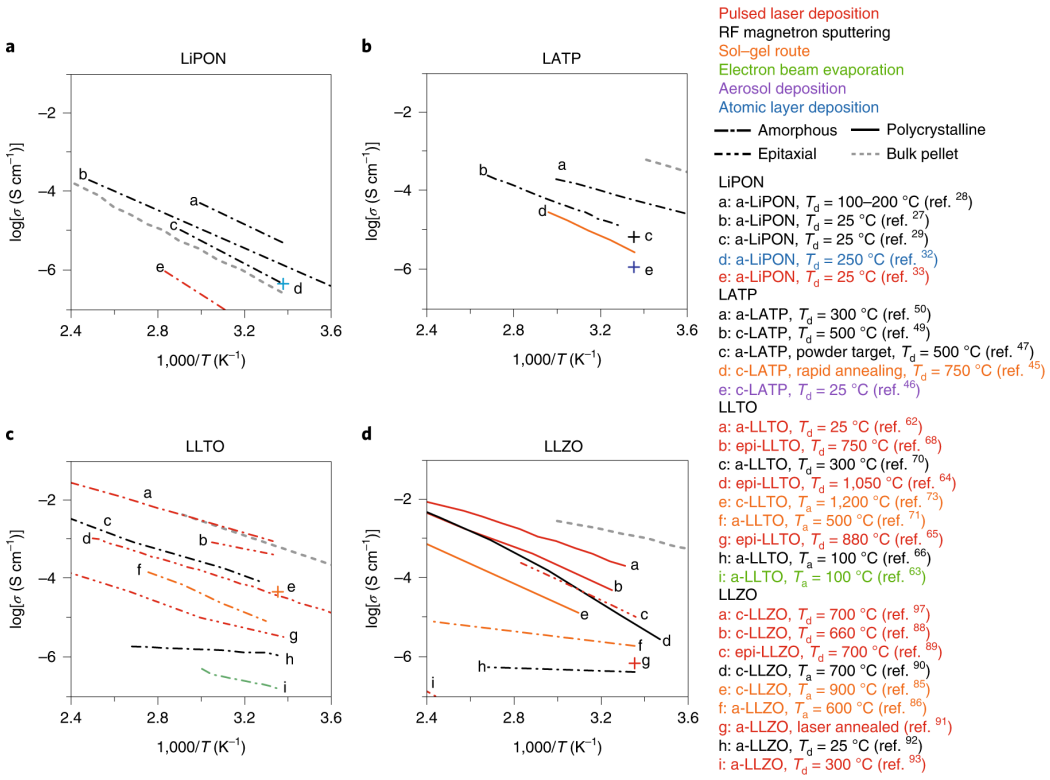

Figure 1-4. LiPON thin films (**a**), NASICON-type LATP thin films (**b**), perovskite-type LLTO thin films (**c**) and garnet-type LLZO thin films (**d**) compared with their pellet conductivity (grey dashed line). a- and c- indicate amorphous and crystalline, respectively. T_d is the deposition temperature and T_a is the annealing temperature. epi, epitaxial. Figure adapted from Ref.[39].

While bulk-pellet-type oxynitride phosphate glasses are fabricated by melting $LiPO_3$ with subsequent annealing in a nitrogen atmosphere,[32] a-LiPON thin films with one-order-of-magnitude higher ionic conductivity (on the order of ~10^{-6} S cm^{-1} at room temperature) have been successfully fabricated using the established technique of radio-frequency (RF) magnetron sputtering[40–42] with Li_3PO_4 targets under a nitrogen or ammonia atmosphere at room temperature (**Figure 1-3 c**). Normally, ~1-μm-thick films are deposited and serve as the solid electrolyte; however, because of the inherent limitations of physical deposition, to achieve sufficient N content in the deposited film, a N-enriched sputtering target is needed and highly conformal LiPON films for complex 3D micro-batteries architectures are suggested.[43,44] Alternatively, LiPON thin films (20–80 nm) have been deposited on high-aspect-ratio nanostructures by atomic layer deposition (ALD), resulting in N contents ranging from 0% to 16.3% (compared with typical contents of <10% for sputtered LiPON films)[43] and ionic conductivities on the order of ~10^{-7} S cm^{-1} at room temperature, lower than that of sputtered LiPON thin films with similar nitrogen content[40] (**Figure**

1-4 a). Similar to the sputtered LiPON film, LiPON fabricated by pulsed laser deposition (PLD) also requires N-enriched PLD targets and atmosphere control to achieve high N content in the film. In general, PLD of LiPON is challenging because of the poor surface adsorption of N_2 gas and the difficulty in transferring N and Li from the target to films[45–47] (**Figure 1-4 a**). In conclusion, considering the scalability of the major processing techniques mentioned and their resultant ionic conductivities, LiPON has mostly been deposited by RF sputtering, resulting in acceptable ionic conductivity of up to 3.3×10^{-6} S cm^{-1} at room temperature (**Figure 1-4 a**).

The acceptable ionic conductivity of LiPON and apparent wide electrochemical window (**Figure 1-3 c**) have favored its use as a thin-film electrolyte (sub-micron thickness) for micro-battery applications, allowing for a sufficiently short Li^+ transport distance and low internal resistances. According to first-principle thermodynamic calculations, LIPON has a narrow electrochemical window (0.68–2.63 V vs. Li/Li^+).[20] However, a wider electrochemical window of 0–5.5 V vs. Li/Li^+ is observed in practice,[19] mainly because of the sluggish kinetics of the decomposition products and blockage of electron conduction at the LiPON/electrode (including Li metal) interphase(*i.e.,* a thin electronically insulating but stable interphase). LiPON currently has an unmatched long-term cyclability of over 10,000 cycles operating with a pure metallic Li anode and high-voltage $LiNi_{0.5}Mn_{1.5}O_4$ cathode for micro-batteries, with remarkably low degradation in cycling performance (<10%) without any sign of Li-dendrite formation.[48] A complete $LiNi_{0.5}Mn_{1.5}O_4$/LiPON/Li battery cell exhibited an average increase in the impedance (area specific interfacial and ohmic resistances) of merely 0.003% per cycle after 4000 cycles at a rate of 5C, impressively surpassing the performance of many state-of-the-art SSB systems.[48] Another advantage of LiPON film in general over other solid-state Li electrolytes is its considerably lower processing temperature window of 25 °C–250 °C, which significantly enhances its chemical compatibility with other oxides and is preferred from a mass manufacturing viewpoint. For this reason, LiPON has also been integrated into other thin-film devices, for instance, as the Li^+ conducting layer in a 3-terminal memristive device.[49]

Alternative thin-film solid-state Li electrolytes with high ionic conductivity (>10^{-6} S cm^{-1}) have also been proposed and studied for solid-state micro-batteries in recent years. NASICON-, perovskite-, and garnet-based electrolytes possess ionic conductivities as high as 10^{-3} S cm^{-1} in ambient conditions when prepared in polycrystalline pellet form;[50,51] this value is close to the ionic

conductivity of classic liquid electrolytes such as EC:PC:$LiPF_6$ (approximately 10^{-2}–10^{-3} S cm^{-1}) (**Figure 1-3 c**), which we review in their thin-film form in the following sections.

1.3.3. NASICON-Type LATP

NASICON-based electrolytes, with the general formula $NaM_2(PO_4)_3$ where M = Ge, Ti, Zr, were discovered in 1976.[52,53] About a decade later, the first Li^+-conducting NASICON-type solid electrolyte, $LiZr_2(PO_4)_3$, was reported.[54] By replacing Zr^{4+} with Ti^{4+} and Al^{3+}, the ionic conductivity for this system is significantly increased as the conduction channels become larger and therefore more suitable for Li^+ migration.[55] For example, LATP can deliver a total conductivity of 7×10^{-4} S cm^{-1} at room temperature[55] (**Figure 1-3 c**). In LATP, PO_4 tetrahedra and $(Ti,Al)O_6$ octahedra are connected via corner-sharing O in alternating sequences to form a 3D framework. The Li migration occurs via Li ion hopping between the two Wyckoff position 6b sites, one with six-fold coordination and the other with eight-fold coordination, with both located directly between two $(Ti,Al)O_6$ octahedra. The partial occupancies of Li ions within vacancies are crucial for 3D diffusion within the structure.[56–58] Sintered polycrystalline ceramics or glass-ceramic NASICON pellets have mostly been prepared by conventional solid-state or solution-based routes. The highest total conductivity by far is 1×10^{-3} S cm^{-1} at room temperature for a LATP pellet prepared by a sol-gel route and field-assisted sintering[17] (**Figure 1-4 b**). Although the bulk ionic conductivity and oxidation potential of LATP electrolyte is quite high,[59] efforts toward battery integration have rarely been reported because of the reduction of Ti[51,60] against low-potential anodes such as Li metal or graphite. The introduction of a protective layer, for example Al_2O_3, at the interface between the LATP electrolyte and low-potential anode has been suggested to avoid the reduction and resultant electronic leakage of the electrolyte.[61–63] The fabrication and optimization of thin-film LATP electrolyte has been less frequently reported than that of other oxides such as Li perovskites and Li garnets. The maximum reported conductivity of thin-film LATP remains one order of magnitude less than that of its bulk pellet form which could be attributed to the difficulty of glass-ceramic phase control in thin films. In addition, polyanionic oxides such as LiPON and LATP are based on phosphate (*PO_4*) structural building units, which possibly limit the choice of phosphate precursors.

Thin-film LATP has been fabricated by sol-gel-driven spin coating,[64] aerosol deposition (AD),[64,65] and RF magnetron sputtering,[66,67] with 2–3 orders of magnitude reduction in the Li^+ conductivity compared with that of polycrystalline LATP pellets (**Figure 1-4 b**).[18] Among these thin-film deposition routes, AD-deposited polycrystalline LATP thin films possess ionic conductivities ranging from 1.1 to 2.7 × 10^{-6} S cm^{-1} under ambient conditions with the greatest advantage being the production of dense ceramic coatings directly from an initial polycrystalline powder without the need for a high-temperature step on a substrate.[68–71] However, the porosity, presence of amorphous residual phases, and generally low crystallinity can collectively result in a decrease in the Li^+ conductivity of AD-deposited LATP-based thin films. The highest conductivity of 2.46 × 10^{-5} S cm^{-1} was measured for purely amorphous LATP films deposited by RF magnetron sputtering[18] and was attributed to the denser and more uniform film microstructure present after deposition compared with that of thus far reported AD-deposited films **(Figure 1-4 b)**. The limited reduction potential (2.17 V vs. Li/Li^+) of LATP films makes their direct integration as an electrolyte with a Li metal anode challenging (**Figure 1-3 c**).[20] However, the higher conductivity of LATP films relative to that of LiPON films may be promising for applications such as neuromorphic-computing memristors and electrochemical gas sensors, where fast Li conduction is preferred and may be critical. Many studies on NASICON-based pellets or thick films as electrolytes for $CO_2/NO_x/SO_x$ gas sensors have been reported (see more details in the *sensor* section)**,** which will enable the reduction of device size and development of thin-film sensing units in the near future.

1.3.4. Provskite-Type LLTO

Perovskite-type LLTO is another class of materials that has been intensively studied as solid-state electrolytes in both polycrystalline pellet and thin-film form. In the LLTO structure, Li and La share the corners of a unit cell, both with cuboctahedral (12-fold) coordination; Ti sits at the center in octahedral coordination as TiO_6 units, and O sits in the face-centered positions of the cell (**Figure 1-3 b**). The specific Li-migration path varies depending on the actual crystal structure of LLTO that can be stabilized in either a simple cubic, tetragonal, or orthorhombic cell depending on the amount of lattice vacancies present and the synthesis route.[72] As depicted in **Figure 1-3 b** for an orthorhombic cell arrangement, the Li ions can be located in the structural Wyckoff 2c, 2d,

and 4f positions on the (002) La-deficient plane, enabling the transfer of Li either along 2c–4f–2c or 2c–2d–2c diffusion pathways.[73] Polycrystalline LLTO pellets are typically prepared by solid-state synthesis[72] or sol-gel processing.[74] As the Li concentration x in $Li_{3x}La_{(2/3)-x}TiO_3$ increases, the bulk (grain) Li^+ conductivity can vary from ~10^{-3} S cm^{-1} for x = 0.1 ($Li_{0.34}La_{0.56}TiO_3$) to ~10^{-4} S cm^{-1} with a further increase in the Li content due to local distortions of the lattice and an increase in the migration energy barrier, which slows down the diffusion and ion conduction.[72,75] However, the high grain-boundary resistance has been a distinct drawback thus far, leading to a total ionic conductivity of ~10^{-5} S cm^{-1}.[76–79] The origin of the high grain-boundary resistance is mostly attributed to: *i)* the presence of an ion-blocking secondary phase such as Li_2CO_3 at the grain boundary and *ii)* possible local structure deformations of the Ti–O polyhedral leading to depletion of La and Li within the grain boundary.[15,80,81] Evidence for the latter is that the highest total ionic conductivity of 4.8 × 10^{-4} S cm^{-1} was reported for LLTO ceramic pellets with excess Li at the grain boundary[15] (**Figure 1-3 c**).

LLTO thin films have been prepared using various deposition techniques including e-beam evaporation,[82] PLD,[16,83,84] RF magnetron sputtering,[85,86] and sol-gel-based spin-coating methods[87,88] **(Figure 1-4 c)**. The highest conductivity of LLTO thin films thus far, 8.7 × 10^{-4} S cm^{-1}, was achieved for grain-boundary-free amorphous LLTO (aLLTO) films prepared by PLD[16] **(Figure 1-4 c)**. In addition, total ionic conductivities of 10^{-4}–10^{-6} S cm^{-1} have been reported for films prepared by e-beam evaporation,[82] RF sputtering,[85,86] sol-gel coating,[87] and PLD[16] **(Figure 1-4 c)**. Epitaxial growth is another way to reduce the contribution of grain boundaries in the films but requires single-crystal substrates, which is thus far impractical from a manufacturing viewpoint.[83] For sol-gel-coated polycrystalline LLTO films, the grain boundary resistance sharply decreases above 1150 °C because of the decrease of the grain-boundary concentration vertical to the substrate. A total Li^+ conductivity of 4.42 × 10^{-5} S cm^{-1} can be achieved with post-annealing at 1100 °C **(Figure 1-4 c)**.

In summary, LLTO thin films can exhibit very high total Li^+ conductivity of up to 10^{-4} S cm^{-1} when appropriate deposition conditions are applied, targeting grain-boundary-free growth with either epitaxial or amorphous structures to avoid large grain-boundary resistances and increased grain-boundary volume fraction in the nanostructures. Li loss at high temperature during synthesis is another challenge. Similar to NASICON-type LATP electrolyte films, the application of LLTO

as a thin-film electrolyte for micro-batteries with a metallic Li anode could be challenging without the introduction of an artificial interfacial layer[82,89] because of the reduction of Ti at low potential. In addition, the fabrication and characterization of a-LLTO thin films should be explored for micro-battery electrolytes because of their high conductivity **(Figure 1-4 c)** and potential stability against Li metal.[90] The different set of restrictions applying to their integration as electrolytes in potentiodynamic sensors, working under open-circuit conditions, may broaden the functionality of amorphous Li-based ceramics beyond their limited use as electrolytes in energy-storage applications, correspondingly reducing fabrication costs through the use of lower-temperature processing techniques. In terms of "Lithionic" devices for neuromorphic computing, aLLTO layers may be integrated and in line with demands for low-temperature processing of the field and CMOS compatibility.[91] However, epitaxial LLTO layers would complicate processing of multi-functional layers and increase design and manufacturing costs.

1.3.5. Li-Garnet-Type LLZO

Among oxide-based Li^+ conductors, Li garnets have received attention for the last decade as a promising class of solid-electrolyte materials with high Li^+ conductivity and a wide electrochemical window (**Figure 1-3 c**), which is also the focus of this thesis study. Garnet-type materials have a general structure of $A_3B_2(XO_4)_3$, where A = La and X = Zr, Nb, Ta, and were first probed for their Li^+ conductivity[92] in 2005, with a conductivity of 10^{-6} S cm^{-1} achieved for $Li_5La_3X_2O_{12}$ with X = Nb or Ta.[93] Shortly after, cubic-phase LLZO was discovered with a higher room-temperature Li^+ conductivity (~10^{-3} S cm^{-1}) than that of its tetragonal phase polymorph present at lower sintering temperatures.[13,94] When stabilizing the cubic phase at high sintering temperatures above 1050 °C, the Li^+ conductivity was improved by over two orders of magnitude as the Li ordering was broken,[95–97] which was accomplished by creating Li vacancies by doping with cations such as Al^{3+} or Ga^{3+} at Li sites[94,96,98–100] or Ta^{5+} or Nb^{5+} at Zr sites.[101–103] The garnet-type LLZO framework structure consists of edge-sharing dodecahedral LaO_8 and octahedral ZrO_6 units (**Figure 1-3 b**). Li ions occupy and migrate three-dimensionally through two sites, the tetrahedral 24d and the distorted octahedral 96h Wyckoff sites (**Figure 1-3 b**).[31,104] Unlike LLTO,[105,106] LLZO exhibits a low grain-boundary resistance possibly because of the increased

band gap and different characteristics of the space-charge profiles,[24] which is favorable for device applications.

The synthesis and especially the stabilization of the cubic and fast-conducting LLZO phase has long posed a challenge for its thin-film form. Thin-film LLZO has been prepared using a wide variety of vacuum-based techniques, including RF sputtering,[98,107,108] PLD,[100,109–112] and wet chemical synthesis by metalorganic chemical vapor deposition (CVD) [113] and sol-gel processing.[114–116] An unusual wide spread in Li^+ conductivity over the range of 10^{-8} to 10^{-5} S cm^{-1} has been reported (**Figure 1-4 d)**, which can be explained by two reasons. First, compared with perovskite-type LLTO, LLZO has a higher configurational entropy because of the larger variety of structural polyhedra ≥4); namely, the number of local building units (LBUs) that need to be arranged during crystallization and phase formation is higher. Only the cubic phase with ordered dodecahedral LaO_8 and octahedral ZrO_6 units and disordered Li vacancies in tetrahedral LiO_4 and octahedral LiO_6 has been shown to exhibit sufficiently high Li mobility; however, the phase transition is often difficult to access in thin-film form. In contrast, a classic perovskite structure such as LLTO has less polyhedral types (=3), namely two cuboctahedra (Li and La) and one octahedron (Ti), which results in less configurational entropy when crystallizing from the amorphous oxide percolation.[117,118] Small variations in chemistry and phase change cannot be well-captured for films using averaging techniques such as X-ray diffraction (XRD) and instead require advanced techniques with the ability to characterize local structures such as extended X-ray absorption fine structure (EXAFS) spectroscopy, Raman spectroscopy, and other spectroscopy techniques.[119] Second, because LLZO has a high number of cations, vacuum-based techniques are well suited and have been explored in the majority of cases (**Figure 1-4 d**). For these techniques, prevention of Li loss during deposition and post-annealing steps was, for many years, challenging and unfortunately very easily resulted in inferior conductivities. For example, the lowered conductivities among vacuum-deposited LLZO films often results from variations in chemistry from the original desired cubic phase due to Li loss, such as the formation of the non-conducting Li-deficient pyrochlore phase $La_2Zr_2O_7$, La_2O_3, and tetragonal LLZO (tLLZO)[100,112] **(Figure 1-4 d)**. To overcome this challenge, novel strategies to control the Li stoichiometry of vacuum-deposited films such as co-deposition[98,120] and post lithiation[100,114] have been explored.[121] Thus far, the highest conductivity of 2.9×10^{-5} S cm^{-1} was reported for LLZO films deposited by PLD using a novel approach that uses two ceramic pellet targets in a so-called ‘multi-layer deposition’ with

post-annealing step[120] (**Figure 1-4 d**). The basic idea is that one target is the desired $Li_{6.25}Al_{0.25}La_3Zr_2O_{12}$ ceramic phase and the second target is a Li_3N ceramic that serves as an internal Li reservoir during the film synthesis (see details in *Processing* section). Through repetition of multilayer deposition of approximately 10–40 nm for each of the two phases, a multilayer film is built. In the later post-annealing step, the Li_3N phase layers undergo a decomposition reaction, supplying their Li to the $Li_{6.25}Al_{0.25}La_3Zr_2O_{12}$ phases of the film.[120] Importantly, Li_3N was selected because its band gap is close to that of the PLD laser, leading to fast deposition transfer without much Li loss.

The development of solution chemistry suitable for the stoichiometric composition and the desired microstructure appears to be challenging.[116] Developing solution chemistry and processing routes takes a long time, especially for structures such as LLZO that are composed of three or more cations and are condensed over their metal salts to oxides such as in pyrolysis. In addition, drying cracks and densification issues are often observed in wet-chemistry films, which undoubtedly lead to lowered overall ion conduction of the film. To date, the highest reported Li^+ conductivity for wet-chemically deposited cubic LLZO (cLLZO) films at room temperature[114] is 2.4×10^{-6} S cm^{-1} **(Figure 1-4 d)**, which is one order of magnitude lower than that achieved by 'multi-layer deposition' via PLD. However, it is promising that the Li content in the films is relatively easy to tune by simply dissolving additional Li salts into the precursor solutions,[122] which opens up the possibility of large-scale and low-cost manufacturing.

Options such as lowering the processing temperature have also been considered to further account for the needs of large-scale manufacturing and CMOS/substrate compatibility for thin-film devices. Similar to LiPON and LLTO, which can be processed as both crystalline and amorphous films and, in some cases, pellets, Li garnets can also be processed as amorphous films. In 2018, it was discovered that amorphous LLZO (aLLZO) films can be prepared via PLD followed by post-annealing at reduced temperature (as low as 300 °C) compared with that used for cLLZO films. The transport characteristics (*e.g.,* Li^+ conductivity and ion-transport activation energy) of these amorphous films vary depending on the processing temperature. Unsurprisingly, given the very recent developments in controlling Li stoichiometries for LLZO films, the fabrication of amorphous phases has been less frequently explored, and the Li^+ conductivity of their near-order amorphous structure is currently under investigation.[111] For instance, aLLZO in their doped form

contain at least four different cations in their structure, leading to near-order structures with four or more LBUs and varied connection of polyhedra, *e.g.,* [LiO_4], [LiO_6], [LaO_8], and [ZrO_6]. It remains to be investigated which of these LBUs act as network formers or network modifiers. This situation differs substantially from that of LiPON, a true Zachariasen glass[35,36] that only has one tetrahedra as LBU and no higher coordination of polyhedra, or aLLTO (similar in structure to quasi-amorphous perovskites, such as $BaTiO_3$),[117,118] which only contain 2–3 cations with corner-, edge-, or face-sharing octahedra. The local structure of aLLZO as a material class with high structural and configurational entropy requires further investigation, and attention must be paid to develop processing strategies to stabilize structures and phases.

In short, despite the potential and reported wide electrochemical stability window of sintered LLZO pellets (nearly stable against a Li metal anode) and recent advances in LLZO film processing to control Li stoichiometry, which pushed the Li^+ conductivity of films to 10^{-5} S cm^{-1}, the integration of LLZO films in Lithionic devices has not yet been explored. The major reason for this lack of exploration is that LLZO is a relatively new material discovery compared with LiPON and NASICON (**Figure 1-3 a**). Further research is required to enable device-level integration of LLZO films with high control over the phase and function. Considering the reduced thermal processing window for the cLLZO compared with that of LLTO for example, fewer compatibility issues are expected during device-level integration. Furthermore, aLLZO films are also a promising alternative with their grain-boundary-free nature and even lower processing temperatures than those for crystalline LLZO films. Although LLZO films may not be the optimal choice as switching materials for memristors because of their low electronic conductivities, they remain highly attractive for application as conductive electrolyte layers in 3-terminal Li-operated computational devices (*e.g.,* a 3-terminal LISTA device based on LiPON electrolyte).[49] In addition, environmental gas sensors such as environmental CO_2 electrochemical sensors have been designed using large-scale LLZO pellets,[123,124] building momentum for the development of miniaturized devices based on LLZO solid-electrolyte films.

1.3.6. State-of-the-Art Progress in Processing Li^+-Conducting Electrolyte into Films

In general, high-temperature processes present inherent issues of Li loss, particularly for thin films because of the aspect ratio. Amorphous thin films are processed either by vacuum- or wet-

chemical-based techniques at lower temperatures than those for their crystalline counterparts, which is a notable advantage not only in terms of the lower thermal budget, minimal material loss, and cost-effective processing but also the chemical and interfacial stability essential for their integration and stacking in energy, data, or sensing applications. Additional advantages for grain-boundary-free materials include possible lower overall resistance and the exclusion of metal dendrites for battery applications. One of the most important reasons for the successful integration of LiPON electrolytes in micro-batteries appears to be their excellent chemical compatibility with electrode materials owing to the low thermal processing cost; therefore, a higher degree of freedom and stable interfaces are expected, which have been prominent issues in the bulk battery arena. However, far more study is needed to understand the amorphous nature of Li-based films such as LLZO, LLTO, and LATP, which is currently a subject of research.

To date, the vast majority of studies on thin-film Li^+ conductors have focused on developing thin-film processing know-how to achieve high ionic conductivity similar to that in bulk pellets **(Figure 1-4 a-d).** Many different research groups have used different starting materials and deposition conditions (atmosphere, pressure, temperature, etc.) depending on the processing method, leading to differences in phases (composition, stoichiometry), microstructure, and electrochemical characterization. When deviation from the basic bulk characteristics occurs, lower conductivity is achieved; whereas thin films that have pure phase and dense microstructure will promptly exhibit reasonable conductivity. Thus far, most of the promising thin-film Li^+ conductors, including LATP, LLTO, and LLZO, have not even been properly integrated in *micro-batteries*, with the exception of LiPON[125,126] (note: LLTO has only been applied in half-cell micro-battery structures[127]). This can be explained by the fact that the electrolyte for solid-state micro-batteries must minimize Li-dendrite propagation, secure intimate contact with electrode materials, and possess low room-temperature resistance, and for many recent (non-LiPON) Li^+ conductors, the Li-dendrite resistance requires further exploration. For other Lithionics devices, such as *solid-state sensors*, there are less restrictions, which allows us to further explore the abundance of Li^+-conducting materials and recently developed vacuum-based and wet-chemistry-based processing techniques, which perhaps are still not mature enough to serve in micro-batteries. Achieving high ionic conductivity in amorphous thin-film form will remain a critical issue for promising ionic conductors; however, for LLTO thin-film solid electrolyte, the highest conductivity has been achieved for aLLTO prepared by PLD. In general, a concrete understanding of: *i)* the conduction

mechanism in amorphous thin-film Li^+ conductors and *ii)* the interfacial stability of amorphous Li^+ conductor/electrode (metal, oxide, etc. depending on the application) interfaces require more attention than for a polycrystalline Li^+ conductor. Economical processing techniques for amorphous thin-film fabrication should also be pursued, namely wet-chemical routes, opening up new paths for the development of highly conductive thin films for Lithionic devices and other micro-mechatronics applications. Compared with polyanionic oxides such as LiPON and LATP, oxide-based LLTO or LLZO solid electrolytes are far more promising when playing with wet-chemistry routes; however, one must have well-established thin-film processing methods to achieve grain-boundary-free amorphous materials with high Li^+ conductivity. Additional properties, such as electrochemical and chemical stability, require further exploration, particularly for thin-film Li^+ conductors, which may have implications for device-level integration in the next phase.

1.4. Thin-film Processing Methods for Li-based Oxide Ceramics

Ceramic processing of Li-based oxides is commonly performed via grain growth and sintering of powders into macroscopic dense solids such as pellets or tapes.[128] To reach close to theoretical densities, grain-boundary and volume diffusion must be activated during sintering, which is conventionally achieved using high temperatures (~2/3 of the melting temperature) and high pressure.[128] A survey on SSBs would reveal that more than 95% of today's solid-state Li-electrolyte conductors,[39] including garnets, perovskites, and NASICON structures reported in the literature, are processed as millimeter-sized ceramic pellets using these rather conventional ceramic processing routes. Considering the need for rapid SSB implementation to power electric vehicles (EVs) and mobile electronics beyond Li^+ (liquid) batteries, this processing route is clearly unfavorable as it results in rather bulky and heavy batteries, where precious volume that could be assigned to the active electrodes is wasted on the electrolyte. For the design of a SSB to be attractive, the size of the solid electrolyte should ideally be close to or even smaller than that of a classic polymer separator (approximately 25 μm), which is simply not realistic using classic sintering and densification of powders into pellets (which are 2–3 orders of magnitude larger) and also presents challenges for the possibility of tape processing. In addition, high processing temperatures increase the costs and are unfavorable for co-sintering strategies to assure good

mechanical bonds between the various components. Adhesion becomes even more of a challenge for the integration of cathodes in the SSB. For example, Co-free cathodes such as $LiFePO_4$ face phase-stability challenges at typical Li garnet or Li perovskite sinter temperatures.[105,129,130] It can be concluded that there is currently a slight disconnect between the major ceramic processing strategies used in academia to fabricate SSBs and the increased practical need for cost-effective (manufactured at low temperature) and high-energy-density SSB storage. To achieve these goals, ceramic processing strategies such as cold sintering,[131–133] low-temperature tape ceramic manufacturing,[134,135] and wet-chemically derived films[136–138] explored in some labs and industry need to gain more momentum and significance than studies on sintered pellets for SSBs. Moreover, considering the rising field of AI with new Li-operated hardware opportunities, significant scale down to thin-film manufacturing of the Li functional ceramic components is required. To understand the numerous methods and challenges specific to the fabrication of Li-oxide films, we provide an overview of thin-film processing methods for Li oxides, formulate a roadmap, and highlight general trends for their synthesis using *wet-chemical* and *vacuum-based processing techniques*.

Thin-film processing of Li oxides allows for direct densification from a gas, liquid, or solid state even at 1/5 to 1/3 of the melting temperature. Importantly, solid-electrolyte thicknesses can be reduced by a factor of 1000 compared with those achieved by classic sintering of pellets, and both amorphous and nanocrystalline phases can be deposited for the majority of solid-state Li^+ conductors. Ceramic solid-state Li-oxide films can be deposited either using wet-chemical methods through sol-gel routes via spin coating spray pyrolysis, dip coating, or ink-jet printing or vacuum-based techniques such as physical vapor deposition (PVD) and CVD. In general, vacuum techniques tend to result in more oriented columnar growth because of the more heterogeneous nucleation arising from the condensation of ejected high energetic particles yielding more anisotropic grain growth. In contrast, wet-chemistry techniques tend to result in thermodynamic equilibrium, leading to more isotropic and smaller grains because of the more homogeneous nucleation distributed within the film driven, in general, by grain-surface-area minimization.[139] The selected film synthesis method and conditions can tailor the density, inter-atomic bonding, phase evolution, and degree of crystallinity of the film, which can range widely from fully amorphous to nanocrystalline to coarse-grained microstructures.

1.4.1. Existing Challenges Faced by Li-Oxides Thin-Film Processing

For all Li-oxide-based ceramics, it is universal that the volatility of the rather light Li element poses difficulties in terms of controlling the phase, stoichiometry, cationic coordination, and diffusion pathways and is the main processing issue (**Figure 1-5 a**). Strategies to control the Li content require attention and fundamentally differ for sintered macro-crystalline pellets and tapes (processed at high sintering temperatures) and thinfilms (processed at low densification temperature). For example, to accommodate the Li loss during sintering, overlithiation with 5–15 mol% of extra Li source in powder synthesis and the use of O_2 gas in the sintering of the mother powder are established strategies for ceramic processing of Li-oxide pellets (*e.g.,* LLZO, LLTO, LATP). Initial lithiation strategies for the deposition of thin-film oxides differ greatly in terms of synthesis selection and require attention to achieve solid-state conductor films with high conductivity and may even govern the electronic state changes and chemistry for the operation of neuromorphic devices and sensors.

The second great challenge in film processing is the careful design of ceramic phase boundaries, their chemistries, and the associated Li^+ and electronic conductivity characteristics. The effect of grain-boundary chemistry on performance can be striking, as changes in the Li^+ transference number can, for example, alter the formation and percolation paths of Li dendrites, which are considered the highest risk for SSB failure.[140] For example, any nanocrystalline Li-oxide ceramic film possesses a high volume ratio of grain boundaries to grains and its local chemistry, grain boundary width, and transference number can vary over the nanostructure. Even within one material class of a Li oxide, the grain-boundary chemistry, transference number, and band gap can in principle vary depending on the processing conditions and method because of factors such as dopant segregation at the grain boundaries modifying Debye lengths.

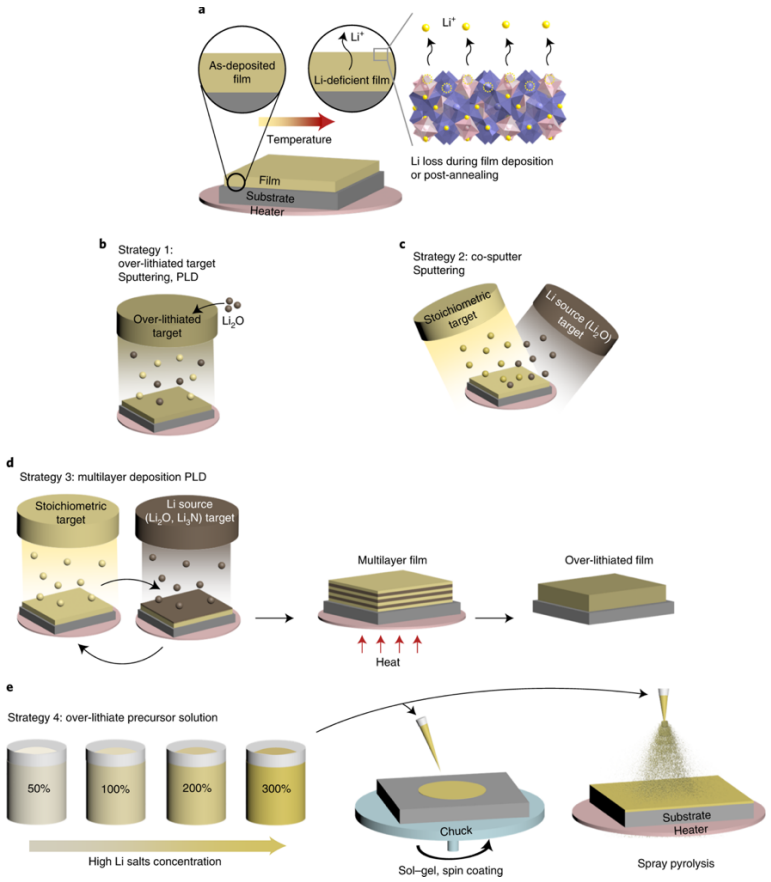

Figure 1-5. (a) Lithium loss mechanism during thin-film annealing at high temperatures. **(b)** Overlithiation of deposition target for vacuum-based films. **(c)** Co-deposition with a Li-source target for vacuum-based films. **(d)** Construction of internal lithiation sources with secondary target for vacuum-based films. **(e)** Overlithiation of precursor solution for wet-chemical films. Figure adapted from Ref.[39].

1.4.2. Wet-Chemical Synthesis of Li-Oxide Films

Among the numerous available thin-film methods, wet-chemically synthesized films are attractive in terms of cost reduction and scale up, as they do not require an expensive vacuum chamber or high-energy source. Conventionally, wet-chemical ceramic processing of films has been performed using sol-gel,[141] spray pyrolysis,[142] dip coating,[114] or spin-coating routes.[116,143] All of these sol-gel routes use a solution made by mixing the precursors of inorganic or metal–organic salts, dissolving them in suitable solvents, and reacting them either by heating or refluxing on the surface of a substrate. Alternatively, the solution can be sprayed on a heated substrate using sequential decomposition synthesis (SDS), a method derived from spray pyrolysis.[136,137] In this cost-effective, scalable technique, there is a thermal gradient of the solution from the spray nozzle

down to the heated substrate, which affects the droplet volume and composition and depends mainly on the selected precursor chemistry and substrate temperature. The challenges for most wet-chemical film deposition techniques are two-fold. First, most Li-oxide-based conductors of interest are composed of at least 2–4 cations, and specific phases are required to assure fast Li motion through the structures. For example, for doped $LiCoO_2$, such as $LiNi_{0.5-y}Al_yCo_{0.5}O_2$, coordination of the multiple and often differing metal salt decomposition points and adaption of the organic chemistry (*i.e.,* the decomposition points and chain length toward the deposition temperature) are needed for chemical decomposition, nucleation, and condensation reactions.[144] The second aspect in the art of wet-chemical film manufacturing is to gain control of drying of the Li-ceramic forming film without crack formation during deposition and post-annealing. This aspect can also technically involve a single or multi-step temperature or pH-controlled chemical reaction(s) to transfer either all of the salts to the forming oxide at once or to use different sub-reactions to control the drying during densification in a step-wise manner. For instance, for Li-oxide ceramic films, there is a large variety of possible Li salts with thermal decomposition temperatures ranging between 100 °C and 550 °C,[136,145] which is a much wider range than that for other heavier metal cations (*e.g.,* La, Ti, Zr) conventionally used in the synthesis of Li electrolyte or electrode materials. Thus, pyrolysis ceramic formation reactions during which most salts decompose at one temperature or pH event can be employed, or alternatively, the chemical reactions can be separated. For example, the reaction of the Li salt can be separated from those of other cation salts forming non-lithiated ceramics with undissolved Li salts, which would result in lithiation of the material at a higher temperature via a two-step synthesis reaction.[145]

One of the richest arguments for further exploration of wet-chemical ceramic synthesis and manufacturing for Li-based films is that in most compositions, the lithiation degree of the film can be very easily adjusted during synthesis[141] **(Figure 1-5 e)**. By simply adding more Li salt to the original precursor for as long as the component remains solvable (and therefore able to react), the Li concentration of the forming oxide can be easily steered to allow for low-temperature manufacturing below 750 ºC. For example, using spray pyrolysis, up to 250 mol.% of the Li source[136,137,146] can be dissolved into solution for Li-garnet films. Another important and new discovery in terms of ceramic processing is that the excess Li in the deposited films not only helps to stabilize the desired fast-conducting phases during post-heat treatments but also acts as a grain-boundary agent that may promote densification and improve film density.[136] This finding is

consistent with previous work on gadolinium-doped ceria ($Ce_{0.9}Gd_{0.1}O_{1.95}$), where the incorporation of Li (as little as 3 mol%) as a dopant significantly improved the density of the membrane and reduced the sintering temperature.[147] Benefiting from the excess Li source as a grain-boundary agent from the precursor solution, a recent study[136,138] reported that dense Li-garnet films with up to 10-µm film thickness could be synthesized using spray pyrolysis without cracking and with stability upon thermal annealing at 750 °C. This finding indicates the possibility of novel component synthesis targeting batteries, and sensors, of which high phase purities is not absolutely required, via inexpensive wet-chemistry routes without sintering, with thicknesses ranging from hundreds of nanometers to several micrometers, which is a range that is generally not achievable using standard vacuum-based methods. The most explored wet-chemical deposition synthesis method for Li-oxide-based thin films is the sol-gel route via spin coating. For example, layered and spinel structure materials such as Li_xCoO_2,[143,148,149] $Li_4Ti_5O_{12}$,[148,150,151] $LiNiO_2$,[141,152] $LiMn_2O_4$[141,153] and $LiFePO_4$[154] and recently more complex solid-electrolyte phases such as garnet-type cLLZO[115,116,155] and NASICON have been synthesized using this route.[156,157] The advancement of chemical synthesis routes for ceramic solid-state films of Li oxides is generally complex and time intensive, as the development of an inorganic synthesis protocol to achieve the desired phases and stoichiometry in dense thin-film form is required for each material class. However, if further improved, this route would be cost-effective and well suited for mass manufacturing to meet society's energy storage needs. In addition, the lithiation degree and distribution of Li within the grains and grain boundaries could provide a powerful tool for altering the transference numbers and structure properties of SSBs, yielding high stabilities toward pure Li metal anode and long cycle life.

1.4.3. Considerations Towards Lithionic Devices Integration

For Lithionic device manufacturing, there is vast knowledge available on Li-based thin-film deposition techniques and materials; however, thus far, they have only been optimized for battery integration and performance. Sensors or neuromorphic computing devices based on functional Li-oxide films require fine control of the microstructure, phase, and especially the lithiation degree at the local scale, presenting new challenges and requiring future synthesis optimization for Li-based thin films and their ceramic manufacturing. Considering the opportunities provided by ceramic

film processing, particularly for Li-oxide conductors and spinel, layered, and olivine materials, we highlight the following observations for ceramic manufacturing. First, novel synthesis strategies exist to tackle the challenge of Li loss associated with many film depositions. For vacuum-based techniques, innovations include working with extra internal lithiation sources (Li_2O or Li_3N) in the formation of films. For wet chemical techniques, innovations include the use of the ability of many Li salts to act as grain-boundary agents to support even rather thick film formation of up to 10 μm and more. Exploring more pathways to control Li stoichiometries coupled with an intimate understanding of the effect of synthesis parameters on film structure–transport characteristics and transference will enable the widespread realization of Li-oxide films as functional ceramic components in Lithionic devices. Second, over the last decade, for most of the fastest conducting Li-oxide ceramics and classic battery electrodes, the number of cations has been rapidly increasing to be conventionally above 3–4 (*e.g.,* LLZO, non-Co-containing battery electrodes such as $LiNiMnCoO_{2-d}$, NMC and $LiNiCoAlO_{2-d}$, NCA). With the birth of more Lithionic device functions to alter electronic states (metal–insulator transition and others or catalysis) through lithiation/deintercalation, the number of dopants is possibly increasing, resulting in more degrees to manipulate the phase structures and alter transference numbers. The use of vacuum techniques is undoubtedly the fastest route to make initial prototypes and test new device characteristics. However, rapid access to these technologies requires stronger and more active efforts to develop low-cost (low-temperature) and mass-manufacturable Li-oxide ceramics using wet chemical routes as films with multi-cation control via wet chemistry, which often makes their processing more difficult. The understanding, chemistry, and formation of phases is by far more complex during the initial development of materials using these routes, and most time–temperature–transformation (TTT) diagrams remain unpublished to date; however, gaining this type of ceramic processing know-how for Li-oxide ceramic films can result in new device manufacturing routes and reduce associated costs. Wet-chemical processing of Li-ceramic film components remains underdeveloped for most of the fastest conducting Li-electrolyte ceramics, with the exception of LiPON and LATP. We encourage ceramic science and engineering efforts to be directed toward this area to assure academic idea-to-tech product transfer for energy storage and Lithionic device applications.

1.5. Open Research Questions

Li-garnet-type LLZO, since its first discovery in 2007,[105] has been considered as a promising class of solid electrolyte Li^+ conductors for applications in batteries, as well as in other lithionic devices such as Li^+ powered electrochemical gas sensors,[123,158] owing to their high room temperature Li^+ conductivity, wide electrochemical stability window (towards both high-voltage cathode at 6 V vs. Li/Li^+ and Li metal anode at 0 V vs. Li/Li^+),[159] non-flammability, and good ambient air stability. However, high-temperature sintering (*e.g.,* >1050 °C) is generally required to accomplish phase transformation and densification and achieve their highly conductive cLLZO phases.[160] This raise concerns about interface stability with adjacent layers in lithionic devices (*e.g.,* cathode in SSBs), as well as high costs and non-sustainability in materials production. Developing low-temperature processing routes to synthesize aLLZO and crystalline cLLZO can be alternative choices for lithionic applications.[161] Moreover, the amorphous near-order structure of aLLZO requires a proper definition for future structure and transport optimization.

In this thesis, we focus on the fundamental understanding of aLLZO amorphous structures and aLLZO structure-transport relations and highlight alternative low-temperature and low-cost processing options for these phases. In addition, we discuss the future and potential for integrating LLZO and other Li-oxide materials into lithionic devices as well as their state-of-the-art challenges. Specifically, this thesis aims to address and answer the following open research questions:

- Can Li^+-conductive materials be used to operate thin-film devices beyond batteries? For instance, memristors for neuromorphic computing and solid-state electrochemical sensors for environmental gas sensing? What are their requirements?
- What classes of materials are suitable for achieving the ambitious goal of using Li^+ to power, sense, and store/compute data?
- What suitable processing routes can be designed to enable the successful low-cost and low-temperature scale-up manufacturing of the material class of Li-garnet LLZO, in both amorphous and crystalline phases and their integration into lithionic devices?
- What are the advantages of amorphous Li garnets *vs.* the classic sintered crystalline cubic Li garnets?

- How to properly describe the near-order, medium-range order (MRO), and long-range order (LRO) structure of amorphous Li garnets? What are the structural roles of each cation, *i.e.,* Li, Zr, and La, in amorphous Li garnets?
- What are some of the potential dopants that could be introduced to amorphous Li garnets?
- How to contextualize the aLLZO structures toward the existing Li^+-conductive materials? What is unique about amorphous Li garnets?
- What are the phase transformation and crystallization process and kinetics from amorphous to crystalline cLLZO?
- Can one develop a TTT diagram to quantify the phase composition of LLZO based on processing time and temperature?
- Are there alternative wet-chemical routes to process the highly conductive crystalline cLLZO in reduced temperatures below 750 ºC?
- What are the remaining questions that need to be addressed to ensure the successful integration of low-temperature-processed amorphous and crystalline cLLZO into lithionic devices?

1.6. Thesis Outline

This thesis contains four main chapters that address the open research questions outlined in Chapter 1.5. Specifically, in **Chapter 2**, we explore the structural nature of high entropy amorphous Li-conductors, namely, Li-garnet-type aLLZO, which has an unusually high number of local bonding units (LBUs) ≥ 4 and can be synthesized via low-temperature SDS. The synthesis condition and local amorphous structure vs. their Li+ transport are studied, and the roles of Zr and Li LBUs as network modifiers in determining local structure characteristics are defined. This high entropy class of aLLZO is also contextualized and compared with the existing non-Zachariasen and Zachariasen invert-glass Li^+-conductive oxides for the first time. This comparison establishes the basis for the next study on structure modifiers in aLLZO, as we detailed in **Chapter 3**. Specifically, Chapter 3 focuses on the near order, MRO, and LRO structure of aLLZO. We present a model study for aLLZO with different La concentrations that confirm the role of La as a network modifier and identify the solubility limit of La in aLLZO. This provides effective ways to tune the packing density and phase composition of aLLZO that may affect transport and mechanical

properties. Alternative network modifier dopants are also suggested based on the structure findings of the chapter. Apart from the low-temperature synthesized aLLZO phases, we also see promises of developing low-temperature synthesis routes for the highly Li^+-conductive crystalline cLLZO towards lithionics applications. To enable rational design of the low-temperature routes, in **Chapter 4**, we first gain a fundamental understanding of the phase transformation kinetics from aLLZO to crystalline cLLZO and develop a first Time-Temperature-Transformation (TTT) diagram for the multi-step phase transformations from aLLZO to crystalline cLLZO. Through the TTT diagram, we design three alternative low-temperature processing routes via SDS and confirm the successful synthesis of cLLZO at temperatures as low as 500 °C, the lowest temperature ever reported. We see both the low-temperature synthesized aLLZO and cLLZO phases to benefit the manufacturing sustainability and interface stability for battery applications and beyond. In **Chapter 5**, we analyze the state-of-the-art research progress and recent advancements in the device integration of Li^+-conductive films in memristors, micro-batteries, and gas sensors. We critically reflect on current challenges and opportunities in the research direction of lithionics. Last but not least, the thesis closes with a conclusion and outlook chapter, **Chapter 6**, highlighting the critical findings and perspectives stemming from this work and future research directions to assist the successful integration of aLLZO and cLLZO films into lithionics devices.

2. Chapter 2: High Entropy Amorphous Li-Garnet Electrolytes

Adapted from Yuntong Zhu, Zachary D. Hood, Haemin Paik, Pedro B. Groszewicz, Steffen P. Emge, Farheen N. Sayed, Chengjun Sun[d], Moran Balaish, David Ehre, Lincoln J. Miara, Anatoly I. Frenkel, Igor Lubomirsky, Clare P. Grey, Jennifer L.M. Rupp. High Entropy Amorphous Li-Battery Electrolytes . *Manuscript in-review (2022)*.

Chapter Abstract

Amorphous Li-oxides are promising solid-state electrolytes for use in hybrid or all-solid-state oxide- and sulfide-based batteries as separators or protective layers. These amorphous Li^+ conductors possess an intrinsic grain-boundary-free nature and require significantly lower temperatures for synthesis as compared to their crystalline counterparts. To date, 'low entropy' amorphous LiPON with only one type of local bonding unit (LBU) reveals the highest cycle number and battery lifetime. 'High entropy' amorphous Li^+ conductors, such as Li perovskites or Li garnets, exhibit an unusually high number of LBUs. However, their local ordering and the Li^+ dynamics remain poorly understood, in part owing to the difficulty in characterizing their disordered states. This study employed a novel synthesis protocol to stabilize amorphous Al-doped Li garnets (Al-$Li_7La_3Zr_2O_{12}$), representing so far the highest number of LBUs ($\geq$ 4) in an amorphous Li^+ conductor. Their phase evolution and local structures were resolved by a combination of spectroscopy, microscopy and calorimetry techniques. We identified a much wider (<680 °C) but processing-friendly temperature range to stabilize various amorphous phases with edge- and face-sharing Zr, La, and Li LBUs, not conforming to the formation rules for Zachariasen's glasses. These amorphous Li^+ conductors reveal an unusual setting in which Li and Zr act as the network former and La acts as network modifier, with maxima in Li-dynamics observed for smaller Li–O and Zr–O coordination among the amorphous phases. Our insight will provide fundamental guidelines for the phase, structure, and Li-transport modulation for amorphous Li garnets and pave the way for their integration in solid-state or hybrid battery designs with improved safety and lifetime.

2.1. Introduction

With the increasing demand for EVs and portable electronic devices, breakthroughs to further improve the energy density and cycle life of battery technologies are necessary.[160,162–164] Extensive research efforts have focused on reviving lithium metal as the ultimate anode for 'beyond Li^+ batteries' owing to the outstanding specific capacity of lithium metal (3860 mAh g^{-1}) and the low electrochemical potential (−3.04 V vs. standard hydrogen electrode, SHE).[165] Replacing the conventional graphite anode with lithium should in principle provide a feasible path for increasing the specific energy density by 35% to 350 Wh kg^{-1} at the pack level.[160,166] However, gas and heat evolution during lithium dendrite growth and the electrochemical instability between lithium metal and conventional liquid electrolytes remain major concerns.[167] Solid-state electrolytes, such as Li-garnet-type LLZO[96,99,105,168–170] and LiPON,[33,40] have been regarded as the key contenders for use in Li-metal batteries with increased resistance toward dendrite growth while providing high Li^+ conductivities.[163] The majority of these solid-state electrolytes, such as LLZO ceramics, exhibit their highest Li conductivity in cubic polycrystalline phase with a large grain-boundary volume, which, in turn, is more susceptible to Li dendrite growth and battery failure. Electron microscopy[140,171,172] and opto-mechanical microscopy[173] studies have revealed that Li preferentially deposits along the grain boundary for LLZO. This behavior in part stems from the variation of the transference number, which can increase the electronic conductivity at different localities of the grain boundary and thus promote Li-dendrite propagation.[140] A recent study also suggests that cubic polymorphism (*i.e.,* 220 vs. 230 space group cubic phase) could be related to dendrite nucleation and propagation in polycrystalline cLLZO due to local stress formation around 230 space group grains.[174,175] While many other theories exist implying the vulnerability of grain boundaries, the exact cause of Li-dendrite formation and propagation, however, remains to be clarified. Remarkably, amorphous Li^+ conductors such as LiPON thus far represent an exception, being inherently grain-boundary-free and offering the best cycling stability, *i.e.,* maintained for more than 10,000 cycles and at <10% degradation with a Li-metal anode.[48] It has been argued that LiPON forms a thin electronically insulating but stable interphase layer composed of Li_3PO_4, Li_3N, Li_3P, and Li_2O toward pure Li at lower voltages, contributing positively to the high cycle life.[176–178]

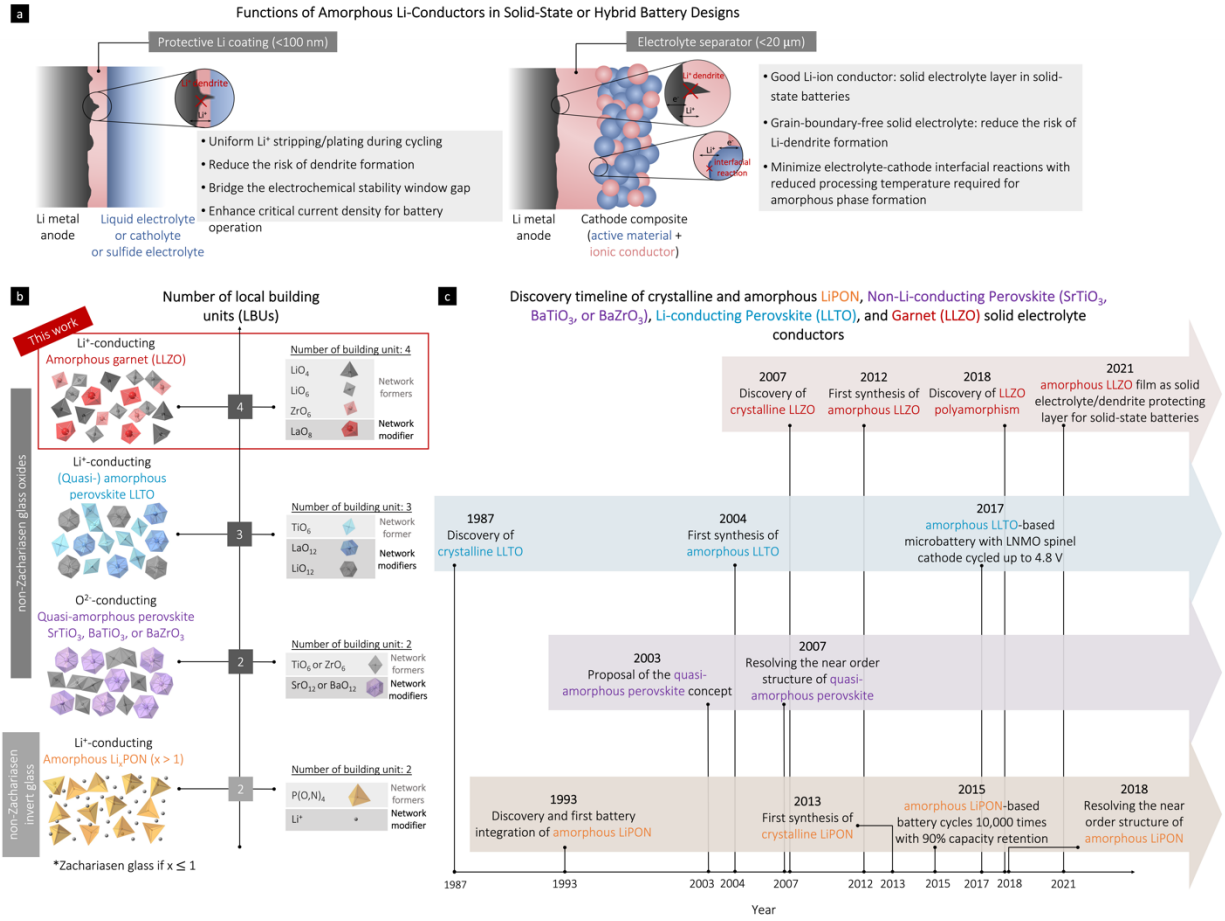

d

Materials	Li-phosphate glass LiPON	Quasi-amorphous perovskite $SrTiO_3$, $BaTiO_3$, or $BaZrO_3$	(Quasi-) amorphous perovskite LLTO	Amorphous garnet LLZO
Number of LBUs	2	2	3	4
	$[P(N,O)_4]$ and Li^+	$[TiO_6]$ or $[ZrO_6]$, and $[SrO_{12}]$ or $[BaO_{12}]$	$[TiO_6]$, $[LaO_{12}]$, and $[LiO_{12}]$	$[LiO_4]$, $[LiO_6]$, $[ZrO_6]$, and $[LaO_8]$
LBUs connection	Corners	Corners, Edges, Faces	Unknown	Unknown
Zachariasen's glass?	No	No	No	No
Known conduction mechanism	Yes	Yes	No	No
	Li hopping over interstitial sites	Under- and over-bonded O^{2-} anions enhance ion mobility		
Implement in batteries	Yes	No	Yes	Yes

Figure 2-1. (a) Functions of amorphous Li^+ conductors in solid-state or hybrid battery designs. **(b)** Newly developed classification of amorphous local structure for $Li^+(O^{2-})$-ion conductors based on the number of local bonding units (LBUs) ranging from 2 to 4. Each LBU in an amorphous structure is identified as either a network modifier or a network former based on its structural role. Among the amorphous conductors, LiPON is (in most compositions) a non-Zachariasen invert glass with $P(O,N)_4$ as a network former and interstitial Li^+ as a network modifier. Note that a special case of LiPON with ~1:1 ratio of Li^+ to $P(O,N)_4$ can be considered as a Zachariasen glass. Quasi-amorphous O^{2-}-conducting perovskites ($SrTiO_3$, $BaTiO_3$, or $BaZrO_3$), amorphous Li^+-conducting perovskite LLTO, and amorphous garnet LLZO are also classified as non-Zachariasen glasses but with more complicated CRNs. In quasi-amorphous O^{2-}-conducting perovskites ($SrTiO_3$, $BaTiO_3$, or $BaZrO_3$), TiO_6 and ZrO_6 are identified as network formers and SrO_{12} and BaO_{12} are identified as network modifiers.[117,118,179,180] In amorphous Li^+-conducting perovskite LLTO, TiO_6 is identified as a network former and LaO_{12} and LiO_{12} are identified as network modifiers. In amorphous Li^+-conducting garnet LLZO, we identified in this study that LiO_4, LiO_6, and ZrO_6 are network formers and LaO_8 is a network modifier based on the atomic radius of the La cation and the probed LBU connection. **(c)** Discovery and battery-application timeline of crystalline and amorphous LiPON,[33,35,36,48,181] O^{2-}-conducting perovskites ($SrTiO_3$, $BaTiO_3$, or $BaZrO_3$),[117,118,179,180] Li^+-conducting perovskite LLTO,[16,82,127,182] and Li^+-

conducting garnet LLZO solid-electrolyte conductors.[105,107,111,183] **(d)** Summary of structure properties, conduction mechanism, and battery applications of amorphous LiPON, quasi-amorphous O^{2-}-conducting perovskites ($SrTiO_3$, $BaTiO_3$, or $BaZrO_3$), amorphous Li^+-conducting perovskite LLTO, and amorphous Li^+-conducting garnet LLZO.

In addition to LiPON, there are many additional alternative amorphous Li-conducting materials, such as amorphous Li garnets, and opportunities for new phase definition and synthesis are manifold. These materials possess several attractive characteristics, such as their relatively low manufacturing temperature (ranging from room temperature to 600 °C), which facilitates co-synthesis with Co-substituted or even Co-free cathodes (*e.g.,* $LiNiMnCoO_2$, $LiNiCoAlO_2$, and $LiFePO_4$) that are often unstable at standard electrolyte sintering temperatures. Alternatively, they can be applied as protective coatings (electrode-electrolyte interfacial layers) toward Li anodes and other Li-free anode concepts, bridging the electrochemical stability voltage gap with liquid electrolytes or catholytes and preventing uneven interfacial reactions, which may later lead to uneven Li stripping/plating (**Figure 2-1 a**). An earlier study reported that by applying a 10 nm aLLZO protective coating on both sides of a cubic Li-garnet pellet, a 4-fold increase in critical current density (CCD) from 0.32 to 1.3 mA cm^2 can be achieved.[183] In principle, an oxide-based protective coating can also be extended to sulfide-based SSBs to bridge the large electrochemical stability voltage gap between sulfide-based electrolytes (that generally have electrochemical stability windows < 1 V)[59] and a Li anode. Their ultimate usage either as effective Li-electrolyte separators or thin protective layers remains to be explored, providing new pathways for battery designs.

In this chapter, we explore the fascinating nature of *'high entropy'* aLLZO battery conductors, which has an unusually high number of local bonding units (LBUs), generally beyond four, that affect Li transfer. Although been successfully implemented in SSBs, the nature of the aLLZO structures remains unresolved and requires a proper fundamental description. These high entropy amorphous Li garnets can exist in various phases and differ substantially from lower-entropy amorphous conductors such as Ohara glass, as the amorphous Li garnets discussed here are technically not even 'glasses' based on the Zachariasen glass theory, and the high number of LBUs (≥ 4) offer a much wider opportunity to tune the structure and transport properties. In this study, the synthesis and local amorphous structure vs. Li migration interaction are studied, and the critical

role of LBUs in determining network characteristics is explained for amorphous Li garnets. In addition, we aim to contextualize and classify these high entropy aLLZO conductors for the first time compared with existing non-Zachariasen amorphous electrolytes in the battery field. Technologically, these fundamental efforts provide blueprints on how to further modify these materials with dopants and synthesis routes for phase tailoring in follow-up studies.

2.2. Bringing Some Order into Disordered Amorphous Li Solid-Battery Electrolytes

We introduce in **Figure 2-1 b** the varied range of existing non-Zachariasen amorphous Li^+ conducting oxides as well as the concepts of LBUs, and network formers vs. network modifiers. These electrolytes constitute two or more cation polyhedra LBUs in the continuous random networks (CRNs). Depending on the arrangement and structural roles in CRNs, LBUs can be distinguished as a 'network former' or 'network modifier' [184]: *i) Network formers* facilitate the formation of a CRN by forming covalent bonds via bridging oxygen or other available atoms (*e.g.,* nitrogen in LiPON). *ii) Network modifiers* alter the CRN through the formation of ionic bonds with nonbridging oxygen atoms. The form in which the LBUs link, their distances and connection affect the ionic transport. As a second parameter, it is relevant to define whether an amorphous Li^+ conductor can be classified as a *Zachariasen glass*. Any solid amorphous oxide constitutes a majority of network-former LBUs with network-former coordination of 3 or 4 and solely corner-sharing (form covalent bonds) via bridging oxygens can be viewed as a Zachariasen glass. To provide some material examples, Li-sulfide solid electrolytes, *e.g.,* $(100-x)Li_2S$-xP_2S_5, are true Zachariasen glasses with PS_4 tetrahedra being the corner-sharing network former and Li^+ being the network modifier.[185,186]

In addition to Zachariasen glasses, there are many non-Zachariasen amorphous structures that provide far more complicated CRNs with higher structural entropy, such as metallic glasses,[187,188] high entropy disordered ceramics,[189] and invert ion-conducting glasses.[190] Specifically, invert glasses attract attention in the battery field as they can offer high Li^+ conductivity thanks to their network-modifier-dominated structures and ionic bonding characteristics.[190] For instance, the majority of LiPON can be categorized as a non-Zachariasen invert glass because it contains less

network former $P(N,O)_4$ than the network modifier Li^+ in the CRN, not conforming to the classic Zachariasen glass formation rules anymore.[190] Its glass structure and physical properties are largely determined by the network modifier cations, Li^+, and the predominate ionic bonds.

To lay the groundwork, we classify the various known non-Zachariasen amorphous Li^+- (or O^{2-})-conducting oxides according to the number of LBUs in **Figure 2-1 b**. We briefly summarize the implications of the number of LBUs on the structure coordination and transport properties and herewith propose this general classification to the field for further discussion of the definition.

2.2.1. Low Number of LBUs for Solid-State Conductors (LBUs = 2) Forming Either a Non-Zachariasen Invert Glass or a Classic Zachariasen Glass

LiPON consists of two types of LBU, *i.e.,* $P(N,O)_4$ tetrahedra as a *network former*, and Li^+ as a *network modifier*, and can be classified as either a non-Zachariasen invert glass or a classic Zachariasen glass depending on the network former to modifier ratios. In most cases, LiPON consists of more network modifier Li^+ than network former $P(N,O)_4$ and can be considered as a non-Zachariasen invert glass. The network former $P(N,O)_4$ is surrounded by a *lithia matrix* with non-bridging O or N or holding together by corner-sharing N or O atoms (**Figure 2-1 b**).[35] The ionic interactions between Li^+ and oxoanions become essential in determining the CRNs and glass properties.[190] For $P(N,O)_4$ with corner-shared N, bridging N (double bond) and apical N (single bond) prevail in the CRN when chemically satisfying $x<1$ for $Li_3PO_{(4-x)}N_{(2x/3)}$.[35] The presence of N bridges destabilizes the Li–Li interaction because of its covalent bonds with P, thus enhancing the Li^+ mobility,[36] and is the essence to modulate conductivities to nearly 10^{-5} S cm^{-1} under ambient conditions in the given CRN.[191] In a special case of LiPON, the network former to modifier ratio is ~ 1:1; by definition, this less visited LiPON structure can be classified as a true Zachariasen glass.[192,193] Techno-historically speaking, it is evident that over the last two decades, the invert glass LiPON has been the best investigated amorphous Li^+ conductor and has been integrated as a solid-state electrolyte in batteries, demonstrating the best long-term performance and compatibility with Li metal anode thus far (**Figure 2-1 c**).[48]

2.2.2. Low-to-Moderate Number of LBUs for Solid-State Conductors (LBUs = 2 or 3) Forming No True Glasses

Amorphous perovskites typically consist of 2–3 different types of LBUs, which can be either *network formers* or *network modifiers* (**Figure 2-1 b**). Some of the best-studied examples (LBU=2) include amorphous $BaTiO_3$, $SrTiO_3$, and $BaZrO_3$ perovskites.[117,118,179,180,194] In these structures, Ti or Zr octahedra have been identified as *network formers* connecting via shared corners, edges, and faces. In contrast, alkaline-earth-metal Ba or Sr cations have been observed to retard the transition from random bonding to corner-sharing polyhedral arrangements by stabilizing nonbridging oxygen for amorphous perovskites, serving as *network modifiers*. It is in fact the radii size within the amorphous network of the octahedral LBUs that determines whether they serve as a *network modifier* or *network former*. We wish to also highlight that these examples are by definition not Zachariasen glasses, as they have significantly higher coordination (≥4) octahedral LBUs. An intriguing aspect in these amorphous perovskite examples is that the LBUs (*i.e.,* octahedra) arrange into a high variety of amorphous phases and condensation states through LBU connections, disruption, and reorganization, which affect macroscopic properties such as ionic transport and mechanics.[179] Consequently, the latter characteristics of the amorphous perovskite structures differ completely from those of Zachariasen glasses such as silica or non-Zachariasen invert glass such as LiPON in terms of their ability for LBU rearrangement into quasi-stable face- and edge-sharing CRNs.

We consider the aLLTO electrolyte to be classified as similar based on LBUs >2 (**Figure 2-1 b**). Based on the structure information of previously studied amorphous $BaTiO_3$, $SrTiO_3$, and $BaZrO_3$ perovskites,[117,118,179,180] we classify the LBUs of LLTO as $[TiO_6]$ being the *network former* and $[LiO_{12}]$ and $[LaO_{12}]$ being most likely the *network modifiers*. Despite successful application in film synthesis[16,82,127], its local structure and LBU connectivity have not yet been resolved, nor has the material been optimized toward Li^+ transport. This outcome is surprising, given its successful operations in battery with 4.8 V $LiNi_{0.5}Mn_{1.5}O_4$ cathode[127] and technical success in excluding the highly resistive grain boundaries in the amorphous form, which greatly improved the power density and the CCD of LLTO-based batteries (**Figure 2-1 c**).[81,195]

2.2.3. 'High Entropy' and High Number of LBUs for Solid-State Conductors (LBUs ≥ 4) Forming No True Glasses

The local structure of aLLZO phases remains unexplored and represents a case with the highest number of LBU arrangements known for an amorphous Li^+ conductor (**Figure 2-1 b**). Applying the outlined nomenclature, we turn first to the crystalline LLZO polyhedra, which were identified earlier as containing 4 LBUs of [LaO_8] dodecahedra, [ZrO_6] and [LiO_6] octahedra, and [LiO_4] tetrahedra.[40,111] The amorphous garnet structures are believed to have a higher degree of complexity than the earlier outlined 2-LBU invert glasses (*e.g.,* LiPON) or the 2–3 LBU examples of amorphous perovskites (*e.g.,* aLLTO) because the structural entropy is increased owing to the higher polyhedra variety. Only recently in 2018, various aLLZO phases were successfully synthesized;[111] however, their local ordering as well as the structural roles and connectivity of the four LBUs in determining the Li^+ conductivity remain unexplored. Specifically, it is unclear which LBUs act as *network formers* vs. *network modifiers* for aLLZO phases. Furthermore, unlike in the crystalline garnet phase, where Li mobility is driven by structural defects and vacancies, the Li-transport mechanism in this amorphous CRN remains unknown. Even though the structure is unresolved, it holds technological relevance for the battery field. Recently, a 10-nm-thick coating layer of amorphous Li garnet on a Li-garnet pellet electrolyte was demonstrated, successfully preventing Li-dendrite formation at remarkable current densities up to 3.2 $mA \cdot cm^{-2}$ (**Figure 2-1 c**).[183] As a comparison point, the CCD reached for polycrystalline cubic Li garnet is usually approximately 0.6–1 mA cm^{-2}.[196–198] These findings suggest, even though the exact structure of the aLLZO remains unresolved, that a grain-boundary-free protective layer could help significantly enhance the CCD of batteries.

In essence, we collect evidence and descriptive factors for the structural nature of the high entropy amorphous Li^+ conductors, *i.e.,* aLLZO, with an unusually high number of LBU to alter Li motion. We define synthesis for various aLLZO phases as a model material class, representing the highest number of known LBUs, namely 4 LBUs, in an amorphous Li^+ conductor. Unlike 'low entropy' amorphous Li^+ conductors, such as LIPON, amorphous Li garnets have a much wider temperature range to stabilize and tailor LBU arrangements and therefore control the Li motion. In addition, by gaining knowledge in this work through a wide combination of techniques, such as Raman spectroscopy, high-resolution transmission electron microscopy (HR-TEM), X-ray absorption

spectroscopy (XAS), and nuclear magnetic resonance (NMR) spectroscopy, we deconvolute for the first time the types of LBU bonding and the definition of network formers and modifiers for these high entropy amorphous Li^+ conductors. Eventually, this work guides efforts towards more efficient and better performing grain-boundary-free electrolytes, or protective coatings for oxide- and sulfide-based full or hybrid SSBs.

2.3. Results and Discussion

2.3.1. Structure and Stability of the 'High Entropy' Amorphous Li-Garnet Phases

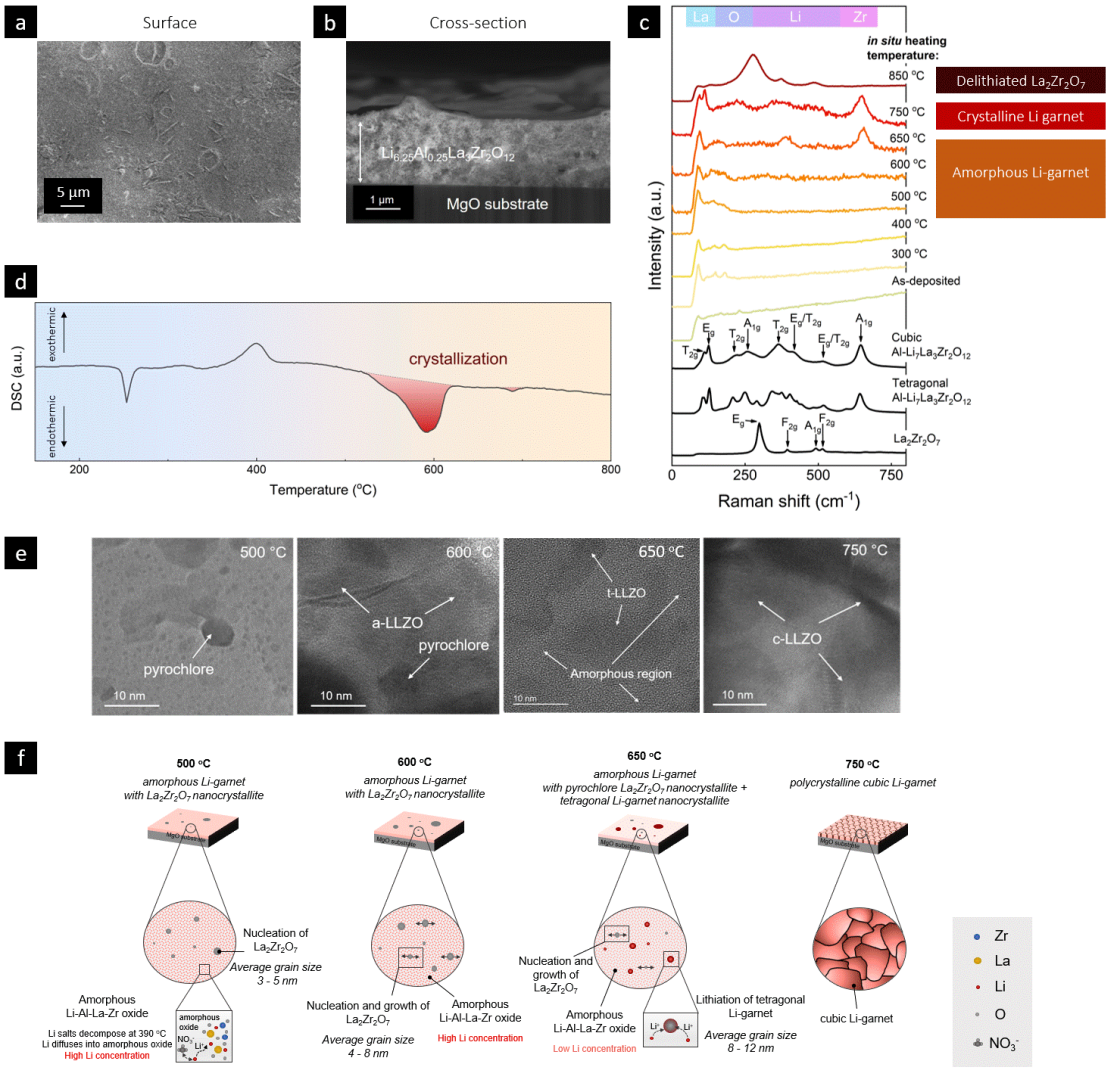

Figure 2-2. (a) SEM surface image of SDS Li garnet film annealed at 750 ºC. **(b)** SEM cross-sectional image of SDS Li garnet film annealed at 750 ºC. **(c)** *In situ* heating Raman spectra for a SDS Li garnet film

measured from room temperature to 850 ºC at a heating rate of 5 ºC min^{-1} controlled by a Linkam stage under a constant flow of O_2. Reference spectra of cLLZO and tLLZO and delithiated $La_2Zr_2O_7$ are also presented. The spectra indicate that the local structure of the film evolves with increasing temperature and that a fully crystalline film can be obtained at 750 ºC annealing. Further increasing the annealing temperature to 850 ºC will lead to significant delithiation with the formation of $La_2Zr_2O_7$. The film was prepared with 75% over-lithiation. **(d)** Non-isothermal DSC of Li garnet films prepared by SDS from 150 ºC to 800 ºC. The two peaks shaded in red correspond to amorphous local structure rearrangement and Li-garnet crystallization. **(e)** *In situ* heating HR-TEM images of a Li garnet film at 500 ºC, 600 ºC, 650 ºC, and 750 ºC. **(f)** Schematics of phase evolution at 500 ºC, 600 ºC, 650 ºC, and 750 ºC. At 500 ºC, the film is composed of a lithiated aLLZO phase with the nucleation of $La_2Zr_2O_7$ (grain size of 3–5 nm). At 600 ºC, nucleation and growth of $La_2Zr_2O_7$ continues with an average grain size of 4–8 nm. The majority of the film still remains aLLZO. At 650 ºC, while the nucleation and growth of $La_2Zr_2O_7$ continues, tLLZO nanocrystals are formed with lithiation of $La_2Zr_2O_7$. The migration of Li from the aLLZO phase to tLLZO nanocrystals results in a low Li concentration in the remaining amorphous phase. At 750 ºC, the film is fully crystallized into cubic-phase Li garnet.

Figure 2-2 a, b present top-view and cross-sectional scanning electron microscopy (SEM) images of $Li_{6.25}Al_{0.25}La_3Zr_2O_{12}$ (LLZO, or Li-garnet) films processed using the new method of SDS[136] at a deposition temperature of 300 ºC and are exemplified after post-annealing at 750 ºC for 15 min. The film presents an even coverage of the substrate with a relatively dense microstructure. The film thickness was measured to be 2.0 ± 0.3 μm. Raman spectroscopy was used to track the phase and lattice-vibrational evolution of the structure (**Figure 2-2 c**). Specifically, *in situ* heating Raman measurement was selected to attain a better understanding of the phase and local structural transition at different temperatures. The broad Raman signal for the as-deposited film indicates the amorphous nature of the film, with the minor peak at 91 cm^{-1} (T_{2g} mode) attributable to O–La–O vibration. Upon heating to 750 °C, more distinct peaks appeared, indicating phase transformation toward cubic-phase Li garnet. The peak centered at 240 cm^{-1} was assigned to the oxygen-bending band of T_{2g}/A_{1g},[199] and the uprising peaks centered at 368 and 468 cm^{-1} were assigned to the O–Li–O vibration bands (T_{2g} and E_g/T_{2g}) in LiO_6 octahedra.[200] In addition, the two intense peaks at 94 and 113 cm^{-1} are identified as T_{2g} and E_g mode of O–La–O vibration, and we also observe the O–Zr–O stretching band (A_{1g} mode) centered at 651 cm^{-1}.[199,200] To avoid thermal-induced noise and confirm the crystallization of Li garnet with better spectral resolution, we also recorded *ex situ* Raman spectra for the as-deposited film and the film after 750 °C annealing (see detailed data and analysis in **Figure 8-11**). We confirm through the appearance of the Raman vibrational bands in both the *in situ* and *ex situ* spectra the formation of cubic-phase Li garnet at 750 °C, and the amorphous nature for the as-deposited film.

Between the deposition temperature of 300 °C and the crystallization temperature of 750 °C, we observed on-going phase evolution involving several amorphous states (*i.e., polyamorphism*). Upon heating from 300 °C to 400 °C, a more significant peak appeared at 91 cm^{-1} for O–La–O T_{2g} vibration, and a few minor peaks are observed between 100 and 250 cm^{-1}, which may be attributed to the T_{2g}/A_{1g} band characteristics for the oxygen bending (210 cm^{-1}).[199] Between 500 °C and 600 °C, an additional broad peak centered at 143 cm^{-1} is observed with a higher spectra noise level, which we identified as the merged peak of the emerging T_{2g}/A_{1g} band characteristic for the oxygen bending; the noise in the spectra may indicate an ongoing local structure evolution (*i.e.,* rearrangement of LBUs). At 650 °C, two new peaks at 389 and 656 cm^{-1} emerged, which can be correlated to the T_{2g} mode of O–Li–O vibration in LiO_6 octahedra[200] and the A_{1g} mode of O–Zr–O stretching,[199,200] respectively. We also observed that the spectral noise level is higher for peaks between 150 and 550 cm^{-1} (oxygen bending and O–Li–O vibration) and comparatively lower for peaks below 150 cm^{-1} (O–La–O vibration) and above 550 cm^{-1} (O–Zr–O stretching). This difference in spectra noise suggests that Li polyhedra and the corresponding Li–O bonds are more actively rearranging in the local structure at elevated temperature. At 850 °C, however, a completely different spectrum with low noise level emerged. Three major peaks at 275, 374, and 491 cm^{-1} are observed, which can be correlated to the E_g mode, F_{2g} mode, and A_{1g}/F_{2g} modes of the (Li-loss) $La_2Zr_2O_7$ phase, respectively. The low spectral noise level observed in the spectrum also explains the complete loss of highly active Li (and the corresponding Li–O bonds).

Differential scanning calorimetry (DSC) is a well-established method used to study crystallization in glass-ceramics, and we apply it here to further probe the occurrence of the amorphous-to-crystalline transformation of Li-garnet observed in the *in situ* Raman spectra. The phase evolution was confirmed by DSC, with two endothermic peaks observed between 500 °C and 720 °C (**Figure 2-2 d**), corresponding to the local structure rearrangement and the phase transition from amorphous to crystalline Li garnet. Detailed analysis on the reactions stem from the initial SDS synthesis route can be found in **Figure 8-2** and Ref. [136].

We used *in situ* HR-TEM to further explore the phase composition and nanostructure of the film during the amorphous-to-crystalline phase transition process between 500 °C and 750 °C (**Figure 2-2 e**), which is the phase-transition temperature range suggested by the *in situ* Raman spectroscopy and DSC analyses. The three representative microstructure images collected at

500 °C, 600 °C, and 650 °C, correspond to the different amorphous phases and the one at 750 °C corresponds to the cubic phase. At 500 °C, an atomic-scale disordered structure with a few darker spots was observed in the HR-TEM image. A Fourier transform of the disordered region suggests a homogeneous amorphous film with no separate regions of a Li-rich phase (**Figure 8-3 a**), indicating the successful lithiation of the amorphous film after the decomposition of Li nitrate salt during the post-annealing process between 400 °C and 500 °C (**Figure 2-2 d**), which is also supported by the DSC (see **Figure 8-2** for details). A Fourier transform of the darker spots in the amorphous film indicates the presence of non-lithiated $La_2Zr_2O_7$ pyrochlore oxide nanocrystals with an average nuclei/grain size of 3–5 nm in (400) and $(1\bar{1}1)$ planes (**Figure 8-3 b**). Increasing the post-annealing temperature to 600 °C induces only a very minimal growth of the $La_2Zr_2O_7$ pyrochlore nanocrystals to an average grain size of 4–8 nm sitting in the predominantly amorphous and highly lithiated film (**Figure 8-3 b**). The presence of $La_2Zr_2O_7$ pyrochlore nanocrystals agrees well with the minor $La_2Zr_2O_7$ pyrochlore peaks observed from *in situ* XRD between 500 and 600 °C in our earlier work.[136] It is only at a higher temperature of 650 °C that changes in the phase nature and chemistry are observed in both the predominantly atomic-disordered amorphous structure and the isolated nanocrystalline grains. The crystalline grains grow to an average of 8–12 nm, but the Fourier transform indicates the presence of tLLZO in (101) and $(10\bar{1})$ planes (**Figure 8-3 c**), indicating an on-going phase transformation and lithiation of the originally isolated pyrochlore to tLLZO nanocrystals in the still predominantly amorphous film. This observation also corroborates with the *in situ* XRD results reported in our earlier work, where minor XRD peaks corresponding to tLLZO first appear at a temperature of 650 °C.[136] Consequently, the amorphous phase must become Li-depleted as Li diffuses to the isolated pyrochlore grains in its matrix and thereby sets off the transformation to tetragonal Li-garnet phase in the nanocrystals. This is per se an interesting finding as it suggests that the various amorphous phase states represent changes in their Li concentration, which can be tailored by the synthesis/post-annealing temperature and the isolated nuclei and nanocrystals. The differences in Li concentration and isolated nuclei types also affects Li^+ transport, which will be discussed in a later section. Finally, at 750 °C, the film surpasses the amorphous states as it exhibits a high level of crystallinity with regions of uniform lattice fringes, as confirmed by the Fourier transform as cubic phase Li-garnet in $(11\bar{2})$, $(1\bar{1}\bar{2})$, and $(2\bar{2}0)$ planes (**Figure 8-3 d**). The appearance of different plane orientations of the lattice fringes suggests the polycrystalline nature of the film with high crystallinity, which

agrees well with the cubic phase observed at 750 °C by *in situ* and *ex situ* Raman spectroscopy (**Figure 2-1 c** and **Figure 8-1**).

In conclusion, we confirmed with several independent spectroscopy, calorimetry, and microscopy methods that various and predominantly aLLZO phases can be successfully synthesized and stabilized through the SDS method within a wide temperature window below 680 °C. This result is technologically relevant as the wide stability temperature window provides a vast amount of opportunities to alter the local structure and LBU arrangement for this high entropy amorphous material with 4 different LBUs. Comparatively, amorphous LiPON films can only be stabilized from room temperature to 280 °C[39] and consist of only 2 LBUs. We found that the amorphous phases post-annealed between 500 and 650 °C must differ in their LBU arrangement and Li concentration according to the variation in Raman vibrational mode and intensity and the HR-TEM observation of different types and sizes of nanocrystals in the amorphous matrix. We also gained the first insight on the nucleation and growth steps in this high entropy amorphous material, where a temperature of 650 °C is required to induce Li depletion in the amorphous phase and trigger Li diffusion to the pyrochlore nanocrystals which then leads to the phase formation of tetragonal Li garnet and finally the crystallization of the whole film from tetragonal to cubic Li garnet. It is also important to mention that this knowledge on local phase evolution stems from a 'liquid-to-solid' processing method that starts from a liquid precursor solution to a solid oxide film, which differs in nature from the classic solid-state synthesis route that begins with calcination of solid powders and requires a rather high temperature for sintering. To better understand the local structure of each LBU type and their arrangements, we next applied XAS and NMR spectroscopy to study the variation in Zr, La, and Li local environments among a wide range of non-Zachariasen aLLZO phases.

2.3.2. Identifying the 'Network Former for a 4-LBU Li^+ Conductor: The Role of Zr

XAS is capable of detecting the local structure changes with high sensitivity and was selected to probe the local structure of the Zr LBU for the various amorphous vs. cubic crystalline Li-garnet films. Generally speaking, the X-ray absorption near edge structure (XANES) region is sensitive to a wealth of electronic structure information, which can be used to determine the oxidation state and coordination number/geometry of the absorption atom. In addition to measuring the

coordination numbers, the EXAFS region of the spectrum can also provide information about bond distances between the absorption atoms and their nearest neighbors.

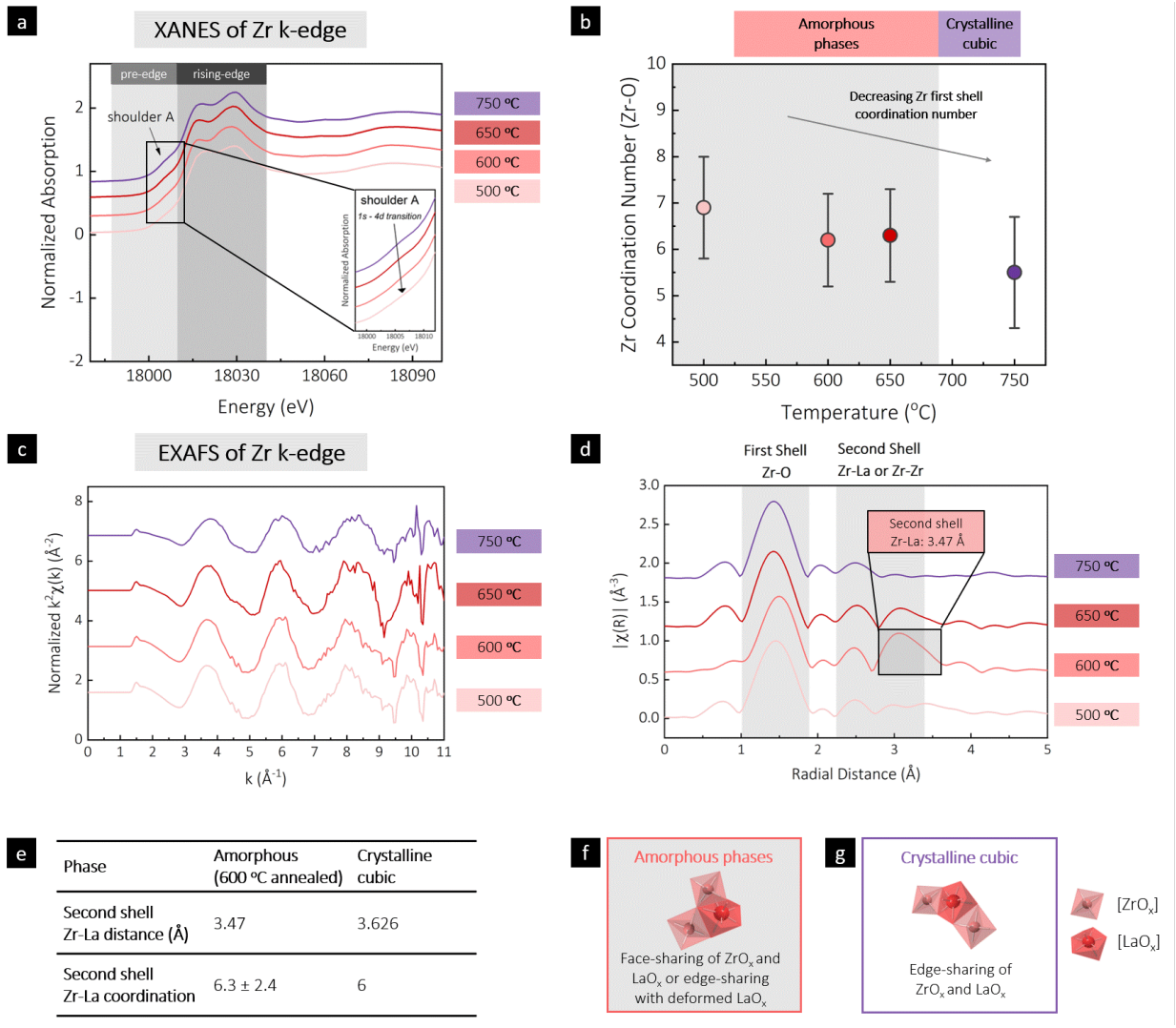

Phase	Amorphous (600 ºC annealed)	Crystalline cubic
Second shell Zr-La distance (Å)	3.47	3.626
Second shell Zr-La coordination	6.3 ± 2.4	6

Figure 2-3. (a) Zr K-edge XANES spectra of Li-garnet film processed at 500 ºC, 600 ºC, 650 ºC, and 750 ºC (shifted vertically for clarity). The spectra contain a pre-edge region for energy < 18,010 eV and a rising-edge region for energy > 18,010 eV. Inset: enlarged pre-edge region with increasing absorption in shoulder A, originating from 1*s*–4*d* transition. **(b)** Best-fitted Zr coordination number of Li-garnet films in different amorphous and crystalline phases from EXAFS spectra. A gradually decreasing Zr coordination is fitted with increasing post-annealing temperature. The large fitting errors suggest a considerable variation in Zr local structure for all the phases. **(c)** Zr K-edge EXAFS oscillation for the Li-garnet film processed at 500 ºC, 600 ºC, 650 ºC, and 750 ºC (shifted vertically for clarity). **(d)** Fourier-transform magnitudes of the k^2-weighted Zr K-edge EXAFS for the Li-garnet film processed at 500 ºC, 600 ºC, 650 ºC, and 750 ºC (shifted vertically for clarity). The peak regions corresponding to the Zr first-shell (Zr–O) and second-shell (Zr–La or Zr–Zr) bonding are highlighted. **(e)** Comparison of second-shell Zr–La distance and coordination number between amorphous (600 ºC annealed) and crystalline cubic phases. **(f-g)** Schematic representation and corresponding LBU legends of the suggested ZrO_x and LaO_x connection in **(f)** amorphous (600 ºC annealed) and **(g)** crystalline cubic Li garnets.

First, we evaluated the Zr K-edge XANES spectra in **Figure 2-3 a** in two regions, namely, the pre-edge region (18,000–18,010 eV) and the rising-edge region (18,010–18,040 eV). The pre-edge region can be used to estimate the spin state and local symmetry, and the rising-edge region contains information about the charge state and coordination environment of the absorption atom. We observed a hump in the pre-edge region at ~18,007 eV and two major peaks in the rising-edge region centered at ~18,018 and ~18,031 eV in all the amorphous phases and the cubic one (**Figure 2-3 a**). In the pre-edge region, the hump at ~18,007 eV corresponding to the 1*s*–4*d* transition energy range, is usually denoted as shoulder *A* in Zr-containing glasses.[201] This transition is dipole forbidden in the atom by the ΔL = 1 selection rule.[202] Typically, the enhanced intensity in shoulder *A* indicates distortion of the Zr site by comparison with Zr-containing alkali silicate glasses, where Zr sits in symmetric octahedral sites.[203–205] Such an intensity increase is an evidence of the *p*-*d* mixing via hybridization between O 2*p* and Zr 4*d* orbitals, a tell-tale sign of the deviation from the centrosymmetry.[206] In the 750 ºC annealed crystalline film (inset of **Figure 2-3 a**), we see an increased intensity of shoulder A as compared with the lower-temperature amorphous films, which indicates an increasing Zr site distortion from the centrosymmetric octahedral sites (**Figure 2-3 a**). In the rising-edge region, the two peaks centered at ~18,018 and ~18,031 eV are typically observed in Zr K-edge XANES spectra of Zr(IV)-containing glass-ceramic oxides, *e.g.,* ZrO_2–SiO_2 glasses[203] and nanocrystalline ZrO_2,[207] indicating that Zr in all the samples is close to octahedral-coordinated. Typically, higher coordination numbers cause absorption edge maxima to be shifted to a lower energy and suggest a Zr coordination number larger than 6.[203,208] We fit the Zr K-edge EXAFS spectra and obtained a Zr coordination number of 6.9 ± 1.1, 6.2 ± 1.0, and 6.3 ± 1.0, for the aLLZO films post-annealed at 500 ºC, 600 ºC, and 650 ºC, respectively, and 5.5 ± 1.2 for the 750 ºC annealed cubic one. We conclude that the Zr LBU exhibits a general decreasing trend on its coordination number with increasing post-annealing temperature (**Figure 2-3 b** and **Table 8-1**). Compared to the coordination numbers for the three lower temperatures amorphous films, the aforementioned cubic phase has a smaller coordination number of < 6. Both the distortion from centrosymmetric octahedral sites observed from the pre-edge XANES region and the under-coordination varied from the ideal octahedral LBU fitted from the EXAFS region suggest that the films possess a high local-structure disorder with non-centrosymmetry, as opposed to the classic solid-state-processed ceramic pellets or tapes after sintering (see Ref.[209] for comparison).

Next, we turned to the EXAFS analysis of the next nearest neighbors to Zr. The EXAFS spectrum is shown as a function of the photoelectron wave number, *k* (**Figure 2-3 c)**. Fourier transform (FT) was performed for each k^2-weighted Zr K-edge EXAFS spectrum, and the normalized intensity of the FT, χ, was plotted as a function of the radial distance, *R* (**Figure 2-3 d**). In a Fourier-transformed spectrum, the radial distances of the prominent peaks generally correspond to the bond distances between the near neighbors and the absorbing atoms, albeit the peak positions are shifted to the lower distances compared to the real space distances due to the photoelectron phase shift in EXAFS equation. Specifically, we observed two major peak regions in **Figure 2-3 d**, with the first one sitting between 1.0 and 1.8 Å, and the second one sitting between 2.2 and 3.4 Å, corresponding to the first- and second-shell neighbors to Zr, respectively. Next, to best determine the first-shell Zr–O distance in the complex amorphous system with 5 different elements, we performed linear combination fitting for the first-shell region of each Fourier-transformed spectrum in **Figure 8-6** to **Figure 8-9**. The fittings indicated a decreasing trend of Zr–O radial distances of 2.12 ± 0.01 Å, 2.11 ± 0.01 Å, 2.10 ± 0.01 Å, and 2.10 ± 0.01 Å for amorphous films post-annealed at 500 ºC, 600 ºC, and 650 ºC, and the cubic one post-annealed at 750 ºC, respectively (**Table 8-1**).

The second shell of the Zr spectrum fitting suggested that Zr–La fits exclusively to the second shell, and the best fit results are illustrated and summarized in **Figure 2-3 d, e**. Notably, the Zr–La distance in the exemplified 600 ºC amorphous film (3.47 Å) is significantly shorter than that corresponding to the edge-sharing units in the previously reported cubic phase LLZO (3.626 Å).[210] The Zr–La coordination of the 600 ºC amorphous sample is 6.3 ± 2.4, presenting a larger variation than the number of second-shell La neighbors (6) in crystalline cLLZO.[210] We conclude from the fitting data of the second-shell Zr–La interaction that in aLLZO, either LaO_x and ZrO_x are not edge sharing but possibly face-shared (or that the LaO_x units are undercoordinated and deformed) (**Figure 2-3 f, g**). This differs clearly from the edge-sharing ZrO_x and LaO_x in cubic Li garnet.

Collectively, we obtained several pieces of information about the Zr and La local structure from the XAS measurement. For the first-shell neighbor of Zr, we observed a deceasing trend for both the Zr–O distance and Zr–O coordination as crystallization progressed from 500 ºC to 750 ºC. For the second shell, we identified a higher second-shell Zr–La coordination and shorter second-neighbor La–Zr distances than that of the crystalline cubic Li garnet, indicating a possibly face-shared (or undercoordinated and deformed) LBU connection among LaO_x and ZrO_x (**Figure 2-3**

f, g). Here, we identify Zr as a network former as the Zr LBU shares edges and faces with neighboring LBUs in different amorphous and crystalline phases, promoting the formation of CRN. On the contrary, La may be a network modifier that alters the CRN and retards the crystallization, as La has a large atomic radius and is 8-fold coordinated, which prevents thermodynamically stable connection with 6- or 4-fold coordinated LBUs. Doping at the La site with low-coordination dopants can be a potential strategy to alter and stabilize the CRN in amorphous Li garnets. To better understand the role of Li in local structure evolution, we next applied ^{7}Li NMR to probe the Li coordination and short-range ordering in amorphous and crystalline Li garnets.

2.3.3. Understanding Local Li-Disorder and Li-Dynamics

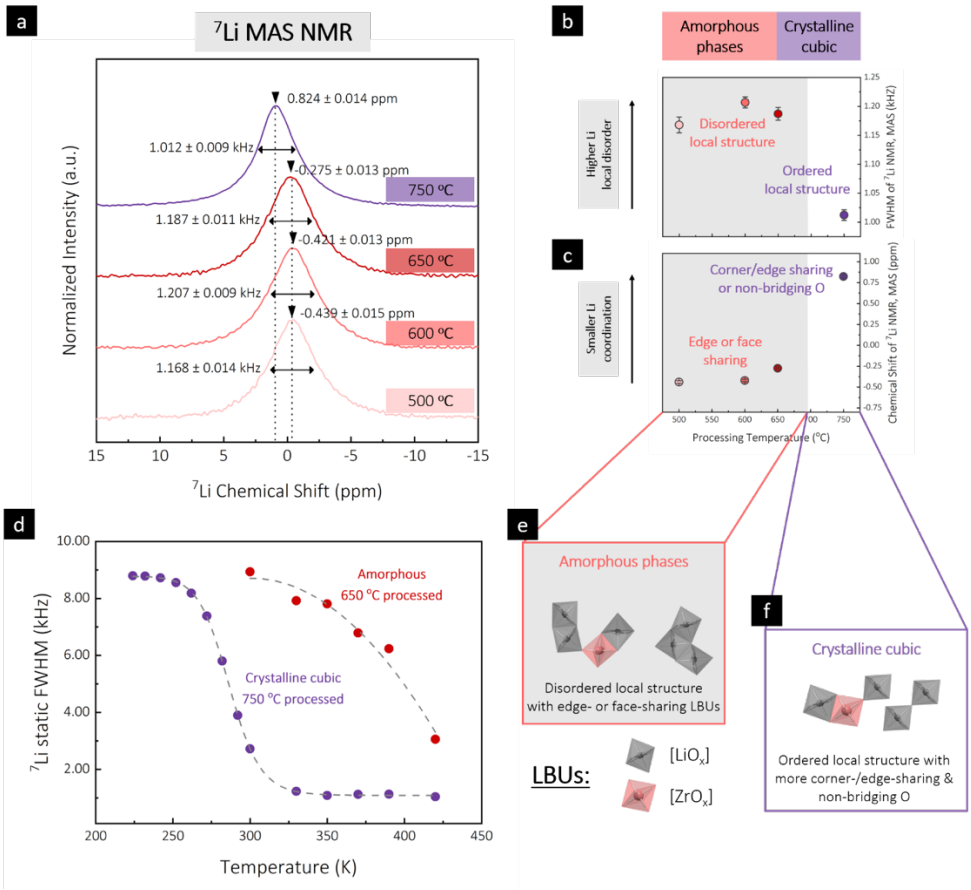

Figure 2-4. (a) ^{7}Li MAS NMR spectra for Li-garnet film annealed at 500 ºC, 600 ºC, 650 ºC, and 750 ºC. **(b)** FWHM of ^{7}Li chemical shifts from MAS NMR spectra. With increasing annealing temperature, a Lorentzian lineshape is observed with the largest FWHM for the 600 ºC annealed film and smallest FWHM for the 750 ºC annealed film (crystalline cubic). The small fitting errors indicate that the changes are significant. **(c)** Changes of ^{7}Li chemical shift of MAS NMR spectra. With increasing annealing temperature,

a monotonic increase in chemical shift is observed. The small fitting errors indicate that the changes in the chemical shifts are significant. **(d)** FWHM of ^{7}Li VT NMR for 650 ºC annealed amorphous Li garnet and 750 ºC annealed crystalline cubic Li garnet. **(e-f)** Schematic representation and corresponding LBU legends of the suggested Li local structure in **(e)** amorphous and **(f)** crystalline cubic Li garnets.

^{7}Li NMR measurements are highly sensitive to the Li coordination and short-range ordering. Here, ^{7}Li NMR was used to characterize both the various amorphous states (*i.e.,* post-annealing at 500 ºC, 600 ºC, and 650 ºC) and cubic one (post-annealed at 750 ºC) of Li garnets. Magic angle spinning (MAS) ^{7}Li NMR spectra were collected to study the chemical shift (δ) behavior in terms of the mean value and distribution width, the latter being a possible indicator of the degree of local structure disorder (**Figure 2-4 a**). Narrower peaks in MAS spectra suggest a higher degree of local structural ordering; in contrast, a broader peak could be the result of slight differences in local Li environments leading to a wider distribution of chemical shifts and thus indicating higher disorder around Li. The position of ^{7}Li resonances is indicative of the Li coordination number and previous studies on *e.g.,* Li-containing phosphate glasses also indicate a possible correlation between lower chemical shift and higher Li–O coordination numbers.[211]

From ^{7}Li MAS NMR measurement, we observed a significantly narrower peak for the cubic Li garnet than for the various aLLZO phases (**Figure 2-4 a**). Specifically, a full width at half maximum (FWHM) of 1.012 ± 0.009 kHz was obtained from the cubic film, compared with a FWHM of 1.168 ± 0.014 kHz, 1.207 ± 0.009 kHz, and 1.187 ± 0.011 kHz obtained from the aLLZO phases annealed at 500 ºC, 600 ºC, and 650 ºC, respectively (**Figure 2-4 a, b** and **Table 8-2**). Within the amorphous phases, the FWHM showed an initial increase and peaked for the 600 ºC post-annealed Li garnet, followed by a sharp decrease for the cubic sample (750 ºC post-annealed), exhibiting a narrower peak with a more Lorentzian than Gaussian line shape (**Figure 2-4 b**). Because contributions from dipolar coupling are averaged out under MAS, and a significant contribution from broadening due to 2nd-order quadrupolar coupling can be dismissed, we attribute the line width in these ^{7}Li MAS spectra to a distribution of chemical shift values. This interpretation is corroborated by the Gaussian contribution to line shape of ^{7}Li lines for samples annealed below 650 ºC. The width of this distribution, and hence the FWHM of the ^{7}Li MAS NMR signal, should reflect the disorder in Li local environments. We conclude that all aLLZO phases exhibit larger disorder than the crystalline cubic Li garnet, with the maximum degree of structural disorder observed for the 600 ºC annealed film.

In addition, we noted an increase of the chemical shift (δ) from the 500 ºC post-annealed aLLZO to the cubic Li-garnet sample (**Figure 2-4 a**). Specifically, δ of -0.439 ± 0.015 ppm, -0.421 ± 0.013 ppm, -0.275 ± 0.013 ppm, and 0.824 ± 0.014 ppm were measured for the amorphous Li garnet annealed at 500 ºC, 600 ºC and 650 ºC, and the cubic one annealed at 750 ºC, respectively (**Figure 2-4 a, c** and **Table 8-3**). Previous studies of Li-containing phosphate and silicate glasses [211,212] have indicated that lower δ generally suggests a larger Li coordination. For Li garnets, the increase in δ could indicate a decreasing Li coordination from amorphous to crystalline phases. In this study, Li coordination can be regarded as Li–O bonding coordination because of the oxide nature of the material, which precludes direct cation interactions. Among the amorphous samples, negative δ ranged from -0.44 ppm (for 500 ºC Li garnet) to -0.27 ppm (for 650 ºC Li garnet), suggesting larger Li–O coordination. Conversely, the cubic sample exhibited a positive δ of 0.82 ppm, which implies a significantly different and overall smaller Li–O coordination environment than the amorphous ones. This suggests that possibly more Li LBUs in amorphous phases are 6-fold coordinated (exist as LiO_6) as compared to the 1:2 ratio of the 4- and 6-fold coordinated Li LBUs (exist as LiO_4 and LiO_6, respectively) in cubic Li garnet. Similar to the Zr coordination and LBU connection changes suggested by the XAS analysis, we rationalize that the comparatively larger Li–O coordination in amorphous phases based on the interpretation of the NMR spectra may suggest either deformed LiO_x polyhedra or edge- and face- oxygen sharing of LiO_x polyhedra with other LBUs (**Figure 2-4 e, f**).

To further explore the Li-transport dynamics and deconvolute peak-narrowing causes (chemical shift distributions and motional narrowing), we also performed ^{7}Li variable temperature (VT) NMR for the cubic and 650 ºC annealed aLLZO phases (**Figure 2-4 d**) without MAS. For the cubic Li-garnet example, a typical motional line narrowing is observed from 224 K to 420 K **(Figure 2-4 d** and **Figure 8-10)**, similar to the dynamics observed in the previously reported cubic Al-doped Li garnet.[213] Also, this coincides with a steep decrease in linewidth between 250 K and 300 K **(Figure 8-10)**. In contrast, the exemplary aLLZO film presents a less steep transition from the rigid to mobile lattice regime, which starts at 300 K and is not yet fully narrowed at 420 K (**Figure 2-4 d** and **Figure 8-11**). The different line-narrowing behavior observed in static VT NMR can be interpreted as a broader distribution of local Li environments with varying Li mobilities for the amorphous sample and corroborates the observation of line width from MAS spectra. Although VT-NMR spectra were not recorded for all amorphous samples, it is likely that they are also within

the rigid lattice regime at room temperature. Similar peak widths were observed in the ^{7}Li static NMR spectra for the amorphous films (**Figure 8-12**), with the FWHM varying in the range of approximately 7.3–7.5 kHz (**Table 8-4** and **Figure 8-13**). This contrasts sharply with the line width of 3.074 kHz for the 750 ºC annealed cubic Li garnet recorded under the same conditions, for which the onset of motional narrowing lies below room temperature (**Figure 2-4 d**).

In essence, we conclude that amorphous Li garnets possess the following characteristics from the ^{7}Li NMR analysis. First, all the studied aLLZO phases present greater structure disorder than the cubic phase, based on the FWHM of ^{7}Li MAS NMR spectra. Second, among the various amorphous phases studied here, we observe variation in Li local structure disorder with the highest degree of Li local disorder for the 600 ºC post-annealed film, suggesting a generally looser LBUs arrangement with higher structural entropy. Third, various aLLZO phases potentially possess increased Li–O coordination, as inferred from the ^{7}Li chemical shift values, suggesting either deformed LiO_x polyhedra or edge- and face-sharing LiO_x polyhedra with other LBUs as a part of the CRN. Importantly, this finding differs substantially from the classic Zachariasen glass formation rules where Li, with small atom radius, are generally considered as a network modifier or an interstitial ion in the CRN, but not as a network former. Nevertheless, this result aligns with the LBU connections as suggested by the independent EXAFS analysis, where ZrO_x and LaO_x are either face-shared or undercoordinated and deformed. Fourth, amorphous and crystalline Li garnets exhibit clearly different Li-transport dynamics. The earlier motional narrowing onset temperature for the cubic sample in VT NMR suggests a generally faster local Li^+ motion. This trend is in line with the later and less steep onset for motional narrowing of ^{7}Li NMR lines upon heating for the amorphous sample, which implies a broader distribution of Li^+ dynamics as a consequence of the higher structural disorder of Li, Zr, and La LBUs.

2.3.4. Li^+ Transport in 'High Entropy' Li Garnets and Battery Integration Perspectives

Electrochemical impedance spectroscopy (EIS) was selected to study the Li-transport behavior in the amorphous and crystalline Li-garnet films. All the EIS spectra were collected with an in-plane geometry (inset of **Figure 2-5 a**), and a resistor–constant phase element equivalent circuit model (inset of **Figure 2-5 a**) was used for fitting (see **Figure 8-14** and **Figure 8-15** for more details).

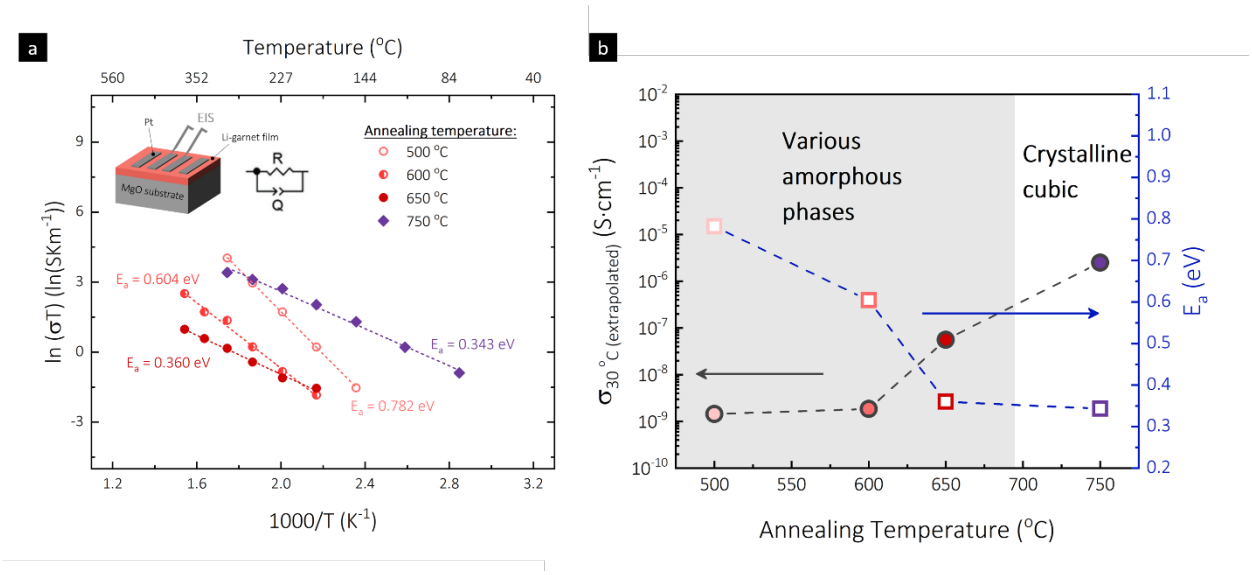

Figure 2-5. (a) Arrhenius representation of Li^+ conductivity measured for Li-garnet films annealed at 500 ºC, 600 ºC, 650 ºC, and 750 ºC. Inset: schematic representation of in-plane EIS measurement on a Li-garnet film. Inset: resistor–constant phase element equivalent circuit model used for fitting. **(b)** Calculated activation energy and extrapolated room-temperature conductivity (30 ºC) as a function of the annealing temperature for the Li-garnet films.

We display in **Figure 2-5 a** an Arrhenius representation for the Li^+ conductivities measured among the various aLLZO and cLLZO films. The films exhibited room-temperature Li^+ conductivities of 1.44×10^{-9}, 1.85×10^{-9}, and 5.59×10^{-8} S cm^{-1} for the various amorphous phases post-annealed at 500 °C, 600 °C, and 650 °C, respectively, and 2.51×10^{-6} S cm^{-1} for the cubic one. The minimum of activation energy is found from the amorphous phase post-annealed at 650 °C and the cubic phase at 0.360 and 0.343 eV, respectively (**Figure 2-5 a, b**, and **Table 8-5**). The other lower temperature annealed amorphous phases reveal rather high activation energies up to 0.78 eV. The variation in activation energy agrees with the line-narrowing behavior observed in VT NMR, where we observed a broader distribution of local Li environments with varying Li mobilities in amorphous films. For the cubic Li-garnet film, the improved ion transport corresponds to the formation of a LRO structure, which lowers the activation-energy barrier for Li^+ hopping (see **Figure 8-16** for more detailed analysis). It is also worth noting that the ionic conductivity of the cubic Li-garnet film obtained in this study agrees well with the previously reported conductivity values from the SDS-processed Li-garnet films[136] and films deposited using other wet-chemical methods,[114–116] which are generally lower in Li^+ conductivity compared with bulk Li-garnet pellets or tapes.[39,161] The reduced conductivity can be related to the Li loss at elevated temperature during

the deposition or the post-processing steps or the high grain boundary to grain bulk volume ratio (generally, grain boundaries have lower Li^+ conductivities), which is commonly observed for almost all solid-state Li-oxide conductors.[160,161] Importantly, we believe this structure–property understanding of the 4-LBU amorphous Li garnets can not only benefit the fundamental materials science for high entropy amorphous oxides but also brings new opportunities for next-generation battery electrolyte advancement (**Figure 2-6**).

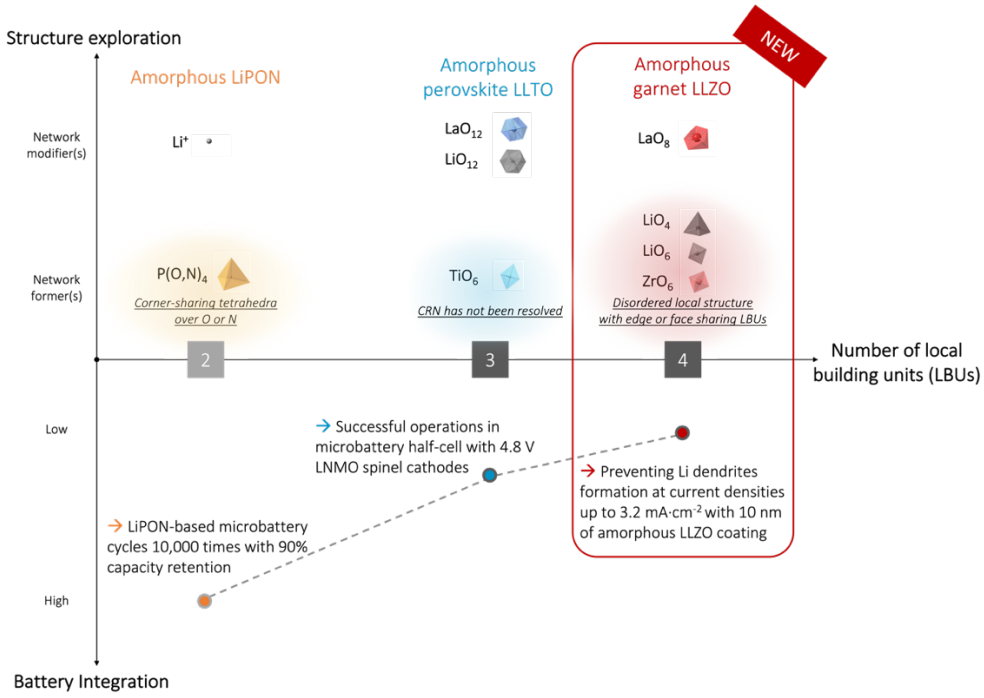

Figure 2-6. Roadmap for the recent advancement of amorphous Li solid-battery electrolytes. The summary includes progress of the local structure exploration and battery integration for amorphous LiPON, amorphous perovskite LLTO, and amorphous garnet LLZO.

Compared with LiPON, which has only 2 LBUs of $P(O,N)_4$ and Li^+, and the amorphous perovskite LLTO, which has 3 LBUs of TiO_6, LaO_{12}, and LiO_{12}, amorphous Li garnet sits in a unique position with high structural entropy of 4 different LBUs. This structure offers vast opportunities to tune the chemistry and CRN of the material, *e.g.,* by doping on the network modifier site, to further improve the transport properties. In terms of battery applications of amorphous oxide-based electrolytes, LiPON thus far represents the highest level of battery performance with the best-performing microbattery cycled over 10,000 times with less than 10% capacity loss.[48] Comparatively, aLLTO shows less progress in terms of battery integration. It was only in 2016

that a microbattery half-cell with an aLLTO solid-state electrolyte and a high-voltage (4.8 V) LNMO spinel cathode was demonstrated.[127] Even later, in 2021, the first aLLZO-based microbattery was demonstrated with amorphous Li garnet acting as a solid electrolyte separator layer, successfully cycled at 10 C for over 500 cycles; the same study also reported the use of a 10-nm amorphous Li garnet as a coating layer on cubic Li-garnet pellet, preventing Li dendrite formation up to 3.2 mA cm^{-1}.[183] This outstanding battery performance already achieved in this early stage of the field justifies the potential of such high entropy aLLZO conductors with new opportunities awaiting to be discovered. With both experimental and simulation efforts, we see a vast space ahead for further optimizing the structure, conduction, and battery integration of high entropy amorphous Li garnets.

2.4. Conclusion and Outlook

Next-generation hybrid and SSBs rely on electrolyte materials to guarantee good chemical and electrochemical stability at interfaces to avoid the formation of high-resistance interfacial layers and the growth of Li-dendrites. This chapter illustrates a class of high entropy amorphous Li^+ conductors, namely amorphous Li garnets with the highest number of LBUs (≥ 4) been identified so far, that can be stabilized over a wide thermal processing window at low temperatures. We propose a sorting metric to the battery field by contextualizing this material class towards other 'low entropy' amorphous Li electrolytes based on the numbers and types of network formers and network modifiers and their LBUs hierarchy. A multi-faceted investigation has been carried out to resolve the structure of these high entropy aLLZO phases, to identify major roles of the LBUs, and to understand their implications on Li-dynamics. Specifically, we observed edge- and face-shared LiO_x, LaO_x, and ZrO_x LBUs in aLLZO phases presenting a much higher structural entropy than the solely corner-shared LiPON conductor with only 2 types of LBU. In addition, the high-entropy edge- and face-sharing CRNs in amorphous Li garnets offers wider opportunities to tune the ion transport as compared to the quasi-stable amorphous perovskites with 3 LBUs. Within these aLLZO phases, Li and Zr have been identified as network former and La as network modifiers with the highest Li^+ conductivity observed for films with smaller Li–O and Zr–O coordination. These findings set the cornerstone for developing novel structure modulation strategies, *e.g.,*

doping the network modifier La site or tunning Li concentration, to further influence the Li^+ dynamics.

With a low but wide temperature window to stabilize the various amorphous states and the ability to access multiple CRNs via structure modulation, we see opportunities for high entropy Li^+ conductors to play different roles in both hybrid (*i.e.,* liquid-electrolyte) and solid-state (*i.e.,* oxide- or sulfide-based electrolyte) batteries. In hybrid and sulfide-based SSBs, the amorphous Li garnets can be applied as a thin protective layer on a Li-metal anode to bridge the stability voltage gap and reduce the risk of uneven Li deposition and local strain formation in polycrystalline cubic Li garnets and minimizing the subsequential growth of Li dendrite. Whereas in oxide-based SSBs, the amorphous Li garnets can be used as the active electrolyte layer with the advantage of reduced thermal processing budget (<680 ºC) and therefore eliminates the need for a high-temperature co-sintering step with cathodes. This is significant as it improves the accessibility to a wider selection of Co-reduced or even Co-free cathodes (*e.g.,* $LiNiMnCoO_2$, $LiNiCoAlO_2$, and $LiFePO_4$), which often show limited chemical compatibility with oxide-based electrolytes at a temperature above 700 ºC.

Finally, this work demonstrates a successful protocol for describing the CRN of these high entropy amorphous Li^+ conductors with 4 unique LBUs, investigating some of the many phases present, and describing the local bond, coordination, Li environments, and LBU connections. While this work is primarily focusing on the role of major LBUs in amorphous Li garnets, we anticipate further attention on the role of various network modifiers (*i.e.,* new dopant series) and Li concentration and their implications on transport properties. Considering the two decades LiPON took to successfully resolve the CRN and tune the Li dynamics to the best, research on high entropy amorphous Li garnets is still in an early stage. We anticipate additional experimental and computational efforts on amorphous Li garnets in the next 5−10 years to achieve their best performance. Especially, the high number of LBUs (≥ 4) within amorphous Li garnets offers a much wider room to tune the structure and transport properties than the 2-LBU amorphous LiPON. Given the good cell performance recently reported with amorphous Li garnets employed both as electrolyte separators and protective layers without much structure optimization, we see promise and significance of our contribution here serving as a blueprint for structure and phase modulation to enable hybrid or SSB designs with further enhanced safety, energy density, and lifetime.

2.5. Experimental

2.5.1. Preparation of Amorphous to Crystalline Solid-State Li-Garnet Films by SDS

The SDS precursor solution was prepared in the $Li_{6.25}Al_{0.25}La_3Zr_2O_{12}$ stoichiometric ratio with 75 mol.% extra Li by dissolving $LiNO_3$, $Al(NO_3)_3 \cdot 9H_2O$, $La(NO_3)_3 \cdot 6H_2O$, zirconium(IV) acetylacetonate into methanol:1-methoxy-2-propanol:bis(2-ethylhexyl) phthalate (1:1:1 vol.%) solvent. Our previous study[136] suggested including a 75 mol% excess of Li in the SDS precursor solution can lead to the successful synthesis of cubic Li-garnet phase with the highest Li^+ conductivity and relatively high film density. Thus, 75 mol% of excess Li was used for the SDS solution preparation in this work as a model case. There is room to further optimize the Li concentration to achieve improved transport properties for amorphous Li garnets. The concentration of the solution was 0.015 M. All the SDS solutions were stirred overnight for at least 12 h before use for SDS. $LiNO_3$ (≥ 99%), zirconium(IV) acetylacetonate (97%), and 1-methoxy-2-propanol (≥ 99.5%) were purchased from Sigma-Aldrich; $Al(NO_3)_3 \cdot 9H_2O$, $La(NO_3)_3 \cdot 6H_2O$ (99.99%), and bis(2-ethylhexyl) phthalate were purchased from Alfa Aesar; and methanol was purchased from VWR. Because Li garnet does not react with MgO, single-side-polished MgO (001) substrates (10 × 10 × 0.5 mm) were purchased from MTI Corporation and used as the substrate for the SDS process.

To deposit the Li-garnet electrolyte film, the MgO substrates were placed on a heated stainless-steel hot plate at 300 ºC with the polished side facing up. A K-type thermocouple was placed on the side of the MgO substrate to monitor the temperature of the substrate surface. During deposition, the SDS solution was transferred from a polypropylene syringe and pumped at a rate of 10 mL h^{-1} into a spray atomizer (DeVILBLISS, AG361). Compressed gas with a pressure of 0.3 bar at the atomizer was used as the carrier gas for the deposition. The distance between the spray atomizer and MgO substrate was maintained at 25 cm throughout the deposition. For all the films studied in this work, a thickness of 2 μm was achieved with 1-h deposition. After deposition, the films were post-annealed in an alumina crucible in a temperature-calibrated tube furnace between 500 °C and 750 °C under a flow of pure O_2 (Airgas) with a ramp rate of 5 ºC min^{-1}. The post-annealed films were stored inside an Ar-filled glovebox before measurements to prevent potential exposure to ambient air and moisture and to minimize chemical degradation.

2.5.2. Phase, Thin-Film Chemistry, and Microstructure Characterization

The local phase structure of the Li-garnet films was characterized using Raman spectroscopy (WITec alpha 300 M+). A laser wavelength of 532 nm was applied with a power of 10 mW, a grating of 300 g mm^{-1}, and a spectral resolution of 0.1 cm^{-1} to obtain all the Raman data presented in the chapter. A 50x long-distance objective (Zeiss, Germany) with a numerical aperture (NA) of 0.7 was used for the laser focusing, giving an approximate laser spot size of 1 μm. A Linkam TS1500 stage was used as the temperature- and atmosphere (synthetic air)-controlled stage for *in situ* heating measurements from room temperature to 850 ºC (calibrated actual temperature) with a heating rate of 5 ºC min^{-1}.

Surface and cross-sectional SEM images of the deposited Li-garnet films were collected with a Zeiss Supra55VP field emission scanning electron microscope using an accelerating voltage of 3.0–10.0 kV. An In-lens SE detector and Everhart-Thornley SE detector were used for SEM image collection for all the samples in this study. For the cross-sectional samples, a diamond blade was used to cut the sample before imaging. Conductive carbon tape was used to tape the sides of the samples to ensure sufficient electronic conductivity during imaging.

2.5.3. Thermal Properties Characterization and Crystallization Kinetics Analysis

The sample for the DSC experiments was collected in powder form by scratching off the as-deposited films from MgO substrates. MgO crucibles (Ozark Technical Ceramics) were selected for the DSC experiments to avoid high-temperature reaction and diffusion between the Li garnet and crucibles. Since the as-deposited amorphous Li garnets were processed via a wet-chemical SDS method without the presence of Mg precursors during deposition, the tendency of Mg diffusion from MgO crucibles/substrates to Li garnet films is low. Furthermore, we have confirmed in our previous work[136] through the XPS depth profile of an SDS processed Li-garnet film that there was no measurable Mg in the post-annealed film. The experiments were performed using a Mettler Toledo Thermal Analysis System TGA/DSC 3+ under a constant flow of synthetic air from room temperature to 1000 ºC with a ramp rate of 10 °C min^{-1}. A constant flow of Ar (Airgas) was used as protective gas during the experiments.

2.5.4. *in situ* TEM

HR-TEM was performed on an aberration-corrected FEI Titan S 8-300 TEM/STEM equipped with a Gatan Image Filter Quantum-865 operated at 300 kV. The specimens were prepared by depositing films via SDS (thicknesses of 50–80 nm) onto a MEMS-based heating chip (Protochips). A Protochips Aduro heating holder was used for all the *in situ* heating experiments. The specimens were heated at a rate of 20 °C min^{-1} with isothermal dwells of 0.5–60 min to evaluate the atomistic evolutions during the post-processing of the films. The electron beam was carefully tuned to minimize any electron-beam-induced damage to the films. All TEM images and data were post-processed using DigitalMicrograph (Gatan Microscopy Suite) software.

2.5.5. Local Ordering Structure Characterization

EXAFS/XANES fluorescence Zr K-edge XAS was performed for the post-annealed Li-garnet films at beamline 20-BM of the Advanced Photon Sources. The samples were deposited on MgO substrates and sealed in a vacuum bag before conducting the experiments to minimize surface contamination due to air exposure. The fluorescence mode was selected as it can penetrate through the entire layer of the Li-garnet film, which minimizes the effect of possible surface contamination caused by air exposure (*i.e.,* Li_2CO_3 formation). The measurement on each sample was repeated for 5 times and the averaged spectrum was used for data analysis.

Athena software, a part of Demeter software suite,[214] is used for data analysis and linear combination fitting. The collected XAS spectra were normalized in intensity for better comparison. The model for data analysis had the amplitude factor fixed to 0.79, obtained from the Zr foil analysis. The Zr–O coordination number and the distance and disorder parameters were varied in the fit, along with the energy origin correction. In the first-shell region, the data were analyzed concurrently with the same energy correction.

Room-temperature ^{7}Li MAS-NMR spectra were obtained on a Bruker 700 MHz (16.4 T) magnet with an Avance III console using a Bruker 1.3 mm HXY MAS probe. A MAS rate of 10 kHz was applied to avoid sample heating due to friction. A single-pulse sequence with a total of four scans was used, with a recycle delay of 100 s, using the appropriate Ernst angle as a compromise for

long spin-lattice relaxation times (on the order of 100 s). The spectra were externally referenced against Li_2CO_3 powder (0 ppm).[215]

Static VT ^7Li NMR spectra were acquired on a Bruker 500 MHz (11.8 T) magnet with an Avance III console using a Bruker 4 mm HFXY MAS probe in static mode. The spectra were externally referenced against LiCl saturated aqueous solution (0 ppm).[215] High-temperature NMR spectra were measured between 300 K and 420 K after an equilibration time of at least 20 min after each temperature was reached where heated nitrogen gas was used as heating source. Low-temperature NMR spectra were measured between 224 and 292 K using nitrogen gas and a Bruker cooling unit (BCU-II). Powder $Pb(NO_3)_2$ was used for temperature calibration.[216]

A regular zg/one-pulse pulse program was used to obtain the spectra using flip angles of $\leq\pi/2$ (2 μs). All the samples were packed in 1.3 mm (MAS-NMR) or 4 mm (static VT NMR) ZrO_2 rotors under an Ar atmosphere inside a glovebox (M. Braun; $p(O_2)/p0 < 1$ ppm, $p(H_2O)/p^0 < 1$ ppm). Bruker Topspin 3.5 pl7,[217] Mestrenova 11.0.0, and Origin 2019 were used for raw data handling and processing. The uncertainty for the FWHM and chemical shift were based on noise contribution and were estimated by determining their variation across 100 samples of random points from the spectra.

2.5.6. Electrochemical Characterization

The Li^+ conductivity of the SDS Li-garnet thin films was measured with an in-plane geometry by electrochemical impedance spectroscopy (Zahner IM6). Platinum (Pt)-blocking electrodes (3 mm in length with a separation distance of 0.25 mm) were deposited on the Li-garnet films using a Cressington 108 Auto sputter coater with a stainless-steel shadow mask. The measurement was conducted with Au-coated W tips. A temperature- and atmosphere-controlled Linkam HFS-600E stage was used for the measurements, with a thermocouple placed directly on the membrane surface to rectify the temperature profile. An AC amplitude of 50 mV was applied with frequencies between 1 MHz and 0.1 Hz. For each film, an impedance spectrum was obtained every 50 ºC from 100 ºC to 500 ºC (set temperature) with 2-min stabilization time for two consecutive heating and cooling cycles to ensure measurement accuracy. All the impedance measurements were performed under a constant flow of dry synthetic air. The collected data were analyzed using ZView 3.4F.

3. CHAPTER 3. Uncovering the Network Modifier for High Entropy Amorphous Li Garnets

Adapted from Yuntong Zhu, Ellis R. Kennedy, Bengisu Yasar, Haemin Paik, Yaqian Zhang, Zachary D. Hood, Mary Scott, Jennifer L.M. Rupp. Uncovering the Network Modifier for High Entropy Amoprhous Li-Garnet Glass-Ceramics, *Manuscript in revision (2023)*

Chapter Abstract

High-entropy aLLZO, which possesses an unusually high number of LBUs of ≥4, is a promising class of electrolyte separators and protective layers for hybrid or all-SSBs. Particularly attractive features of these materials include their grain-boundary-free nature and wide electrochemical stability window along with the possibility of using low-energy functional glass-ceramic processing routes, thereby supporting sustainability goals for future battery designs. Unlike low-entropy Zachariasen and non-Zachariasen ionic invert glasses such as LiPON, these high-entropy aLLZO phases offer a higher number of stable structure arrangements over a wide tunable synthesis temperature range, as they are not confined by the traditional Zachariasen's glass rules to tune the LBU-Li^+ transport relation. We reveal that lanthanum (La) is the active "network modifier" for this new class of high-entropy Li^+ conductors, whereas zirconium and lithium serve as "network formers". Specifically, we demonstrate that within the solubility limit of La in aLLZO, increasing the La concentration can result in longer bond distances between the 1^{st} nearest neighbors of Zr–O and La–O within the same LBU and the 2^{nd} nearest neighbors of Zr–La across two adjacent network-former and network-modifier LBUs, suggesting a more disordered medium- and long-range local structure in LLZO. The discovery of the network-modifier role of La and the deeper understanding of these highly disordered structures open new avenues for the future design of high-entropy amorphous Li^+ electrolytes and the selection of network-modifier dopants. Moreover, the wide yet relatively low synthesis temperatures of these compounds make these glass-ceramics attractive candidates for low-cost and more sustainable hybrid- or all-SSBs for energy storage.

3.1. Introduction

Unraveling the potential of Li^+ batteries requires innovations in materials and cell design to meet the safety, manufacturing cost, and performance requirements for electric vehicles and emerging decarbonized technologies.[160,162,164,197] One of the most promising approaches is to replace the traditional organic liquid electrolytes with solid Li^+-ion-conducting electrolytes in an all- or semi-solid-state hybrid battery configuration and to pair these electrolytes with a Si/C or Li-metal anode for enhanced energy density, **Figure 3-1 a**.

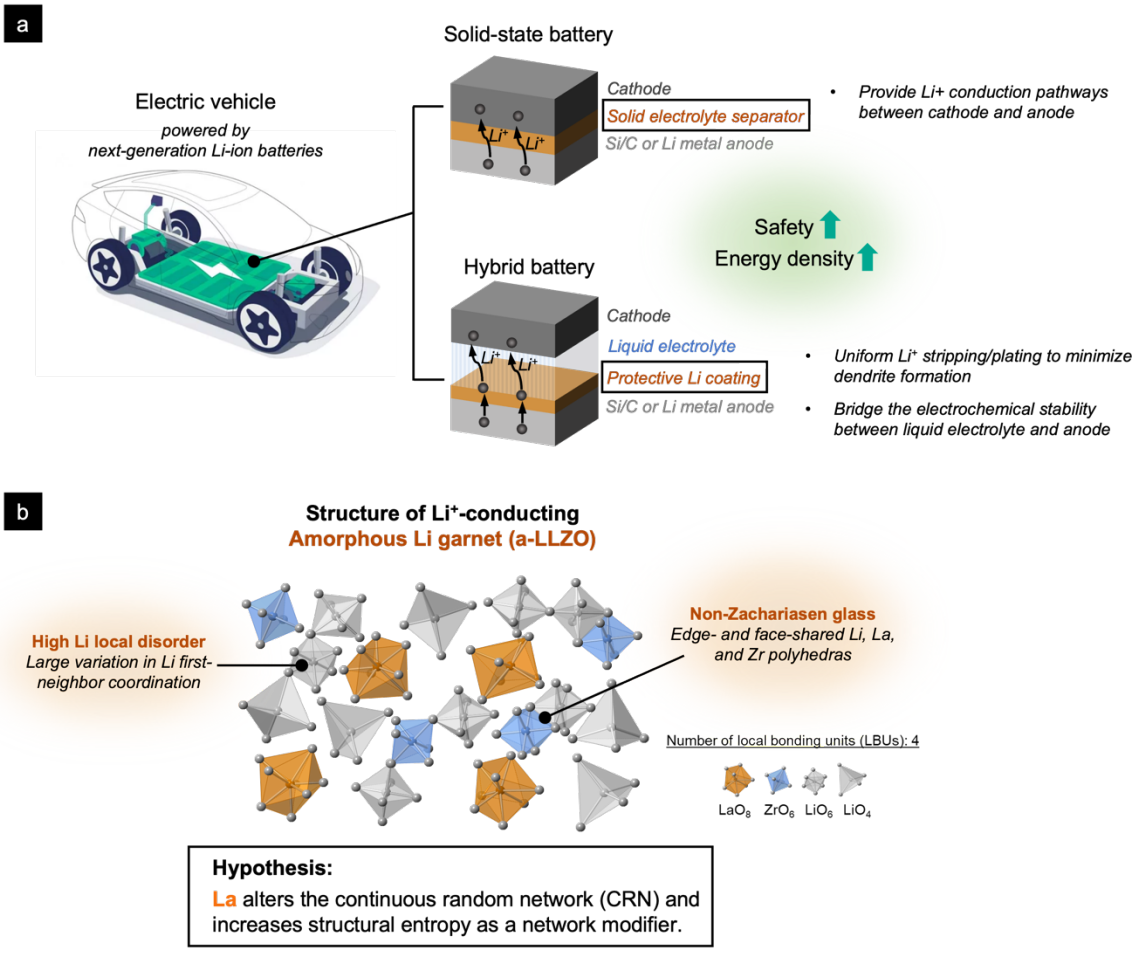

Figure 3-1. (a) Schematic illustration of EVs powered by next-generation Li^+ batteries, including a SSB with a solid-electrolyte separator and a hybrid battery with a protective Li coating on the anode side. Both designs have the advantages of improved safety and energy density compared with state-of-the-art Li^+ batteries using organic liquid electrolytes. **(b)** Structure of aLLZO based on four LBUs, *i.e.,* LiO_4, LiO_6, ZrO_6, and LaO_8.

In an all-SSB design, the liquid electrolyte is fully substituted with a solid-state-electrolyte separator, requiring the electrolyte material to possess high Li^+ conductivity and excellent chemical and electrochemical stability with both the anode and cathode sides of the battery.[197] Alternatively, a hybrid battery design includes a thin Li^+-conducting protective coating layer toward the anode side, bridging the electrochemical-stability voltage gap between the liquid electrolyte or sulfide-based electrolyte towards the Li anode and thus preventing interfacial reactions and Li-dendrite formation.[134,197] Solid-state electrolyte materials include oxide- and sulfide-based ceramics and glasses, which are attractive because of their enhanced resistance to Li-dendrite growth at high Li^+ conductivity[173] as well as the Li^+ transference number of nearly unity for certain oxide-based ones.[197] The sulfide-based electrolytes, such as argyrodite-type Li_6PS_5X (X=Cl, Br, I)[218,219], $Li_2S–P_2S_5$,[40,220] and $Li_{10}GeP_2S_{12}$ glasses,[221] have limited electrochemical stability windows (<1 V)[59,197,222] and are not suitable for direct pairing with either a high-voltage cathode or Li anode. Thus, Li^+-conducting protective coatings are generally required for their applications in Li^+ batteries to widen the electrochemical stability window. In addition, sulfide-based electrolytes exhibit poor air stability, as they undergo a rapid hydrolysis reaction with moisture in the air and generate toxic H_2S gas,[223] which sets limits for their scalable production. The alternatives are oxide-based solid-state electrolytes such as garnet-type LLZO,[99,105,170] which offer wider electrochemical stability windows[59] that can even enable direct pairing with Li anodes. Although oxide-based LiPON[33,126] has by itself a limited electrochemical stability window that is unstable against Li, its formation of a thin and stable interphase layer composed of Li_3PO_4, Li_3N, Li_3P, and Li_2O at the anode–electrolyte interface[176–178] results in remarkable stability, *i.e.,* cells can operate for >10,000 stable cycles with the Li anode.[48]

Nonetheless, three major challenges remain in the battery integration of oxide-based solid-state electrolytes to achieve higher energy and power density and longer cycle life at reduced processing cost.

The first challenge concerns the "*co-sintering of solid electrolytes and oxide-based cathodes"*. Oxide-based electrolytes often exhibit their best transport properties in crystalline phases, requiring high-temperature sintering (*e.g.,* >1050 °C for cLLZO) to stabilize the desired highly conductive phase and achieve densification; see Refs. [99,160,197] for a more in-depth discussion. This high-temperature processing is not favorable for integration with the majority of Co-reduced and Co-free cathodes such as $LiNiMnCoO_2$ and $LiFePO_4$. The high temperatures required to solidify

and stabilize the cathode–electrolyte solid interfaces lead to irreversible phase changes or decomposition of the cathode materials into low-capacity variants.[129,224] To ensure that the oxide-based cathode materials remain in their high-capacity phases with conventional solid electrolytes such as LLZO, unconventional manufacturing strategies are required to maintain the co-processing temperature below 600 °C, which is approximately 400 °C lower than the classic co-sintering temperature, see Ref.[129,224] for details.

The second challenge is linked with the goal of *"increasing CCDs"* for SSBs to enhance their rate performance. It has been commonly observed that Li preferentially deposits along the grain boundary of a ceramic polycrystalline electrolyte.[140,171–173] One of the reasons is that the grain boundary is a sink of defects that often exhibits a lowered local Li^+ transference number (see evidence from electron microscopy[140,171,172] and opto-mechanical microscopy[173] experiments). The resulting local reduction and uneven deposition of Li can accelerate Li-dendrite growth and lead to battery failure at low CCDs. Alternative "grain-boundary-free" electrolyte concepts have been proposed as attractive options to mitigate dendrite growth at high current density.[174,175]

The third challenge is associated with *"the high cost and energy consumption of SSB manufacturing"*. An earlier cost analysis[39] indicates that the high-temperature annealing and sintering step is a major driver for the high processing costs in solid-state-battery manufacturing. In addition, the same- or higher-temperature processes are generally required for the end-of-life treatment for batteries, *i.e.,* pyrometallurgy recycling,[225] which add additional energy inputs and costs to the lifecycle of a battery and are unfavorable for environmental sustainability goals. This issue is exacerbated when energy costs rise, triggering a severe increase in production costs, as clearly exemplified in 2022, when the high cost of energy even led to the temporary closure of some glass and ceramic production lines in the United States. Hence, any opportunity for lowering the synthesis temperature of the Li^+-conducting electrolyte material (which is responsible for ~75% of its cost) is significant for the market entry of SSBs with further enhanced production sustainability.[39]

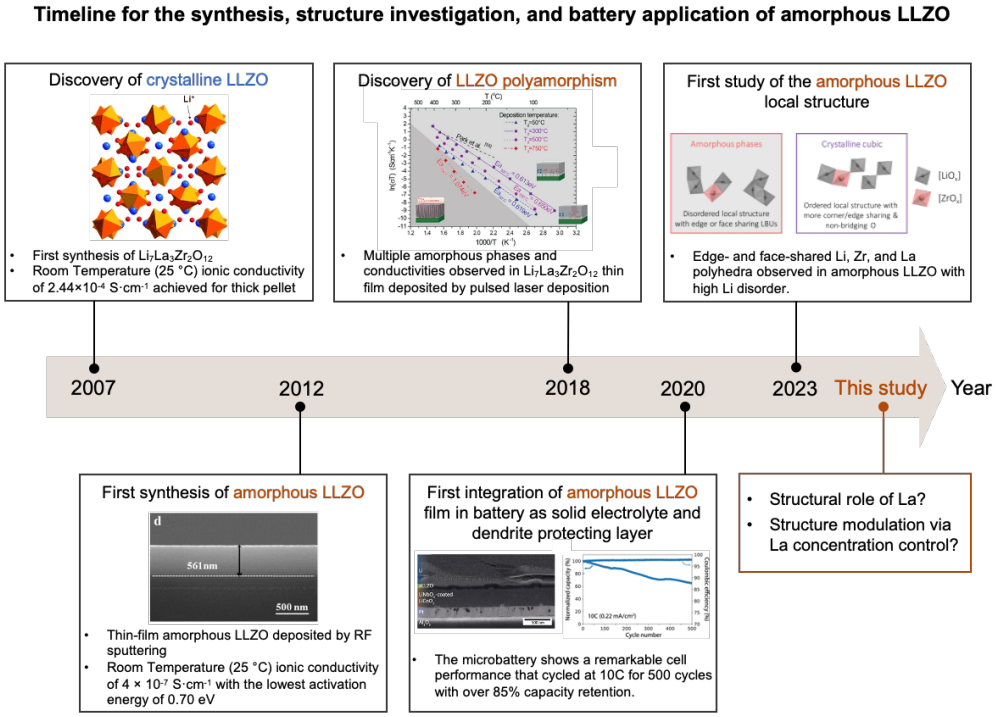

Figure 3-2. Timeline for the discovery of crystalline cubic LLZO (cLLZO) and the synthesis, structure investigation, and battery-cell application of aLLZO.[105,107,111,138,183]

Low-temperature-processed Li^+ electrolyte films have been developed in the past years and applied in various solid-state and hybrid battery concepts. Amorphous oxide-based solid-electrolyte films offer good chemical and electrochemical stabilities against Li and do not require high-temperature sintering steps, attracting particular attention from the field. For instance, LiPON represents the most studied Li^+ electrolytes that are generally deposited using energy-intensive radio frequency sputtering. Its structure consists of only two types of LBUs connected solely via corners (*i.e.,* $P(O,N)_4$ and Li), and it can be classified as a non-Zachariasen ionic conducting invert glass.[36,138,190] Unlike the low-entropy LiPON electrolyte, aLLZO structures contain at least four unique LBUs, *i.e.,* LiO_4, LiO_6, ZrO_4, and LaO_8, and can be arranged in a greater variety of CRNs through a widened and processing-friendly temperature range (room temperature to 680 °C). These aLLZO phases contain edge- and face-shared LBUs, with Zr and Li being identified as "network formers" (which facilitate the formation of LBU connections via bridging oxygen) and the 8-fold coordinated La considered a "network modifier" (which modulates the local disordering and therefore the Li^+ motion), **Figure 3-1 b**.[138] Similar to the techno-historic evolution of the low-entropy glassy conductor LiPON, the promising cell performance of high-entropy aLLZO was first

reported in all-solid-state thin-film batteries ahead of understanding of its structure,[183] as summarized in **Figure 3-2** (see Supporting Information for more details). Without any structure optimization, the first aLLZO-based cell already exhibited excellent resistance against Li-dendrite formation up to 3.2 mA·cm^{-2} (in contrast to the CCD of 0.6–1 mA·cm^{-2} generally observed for polycrystalline cLLZO).[183] To further improve the Li-transport dynamics and therefore the aLLZO-based cell performance, we consider modulating the near-order structure of aLLZO to be an attractive option. Specifically, the 8-coordinated La, among the 4 LBUs in aLLZO, does not form thermodynamically stable bonds with surrounding neighbors, and a small variation in its concentration and coordination can strongly affect the local order in aLLZO. However, studies on the effect of La on the aLLZO local structure and packing density remain lacking.

In the present study, we examine the hypothesis of whether La, as a network modifier in aLLZO, can be used to modulate the local structure of aLLZO. A combination of multiple spectroscopy, electron microscopy, and diffraction techniques are used to resolve the structural variation in MRO and LRO upon changes in the La concentration. We confirm the role of La as a network modifier, identify its solubility limit, and discuss its effect on the packing density and local chemistry. We consider this work relevant for the development of alternative network-modifier doping strategies in the high-entropy aLLZO material class for further performance optimization as battery electrolytes or Li^+ protective coatings.

3.2. Results and Discussion

3.2.1. Role of La Concentration on the Phase Composition of aLLZO

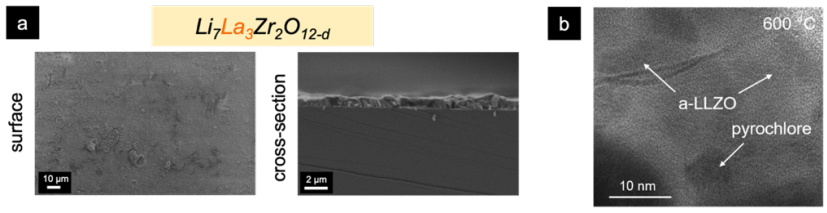

Figure 3-3. (a) Surface and cross-sectional SEM images and **(b)** HR-TEM image of 600 ºC post-annealed aLLZO film with medium La concentration. The film is composed of a predominately amorphous phase and isolated pyrochlore $La_2Zr_2O_7$ nuclei.

In amorphous materials, the concentration of the network-modifier elements can generally affect the CRNs due to their thermodynamically metastable or unstable connections with the surrounding network-former LBUs. In this study, we test the hypothesis of whether the phase composition and local structure of aLLZO can be controlled by tuning the concentration of the network modifier, that is, the 8-fold-coordinated La. As such, we define as model structures three La concentrations for the aLLZO ranging from 50 mol.% to 150 mol.%, *i.e.,* $Li_7La_{1.5}Zr_2O_{12-d}$ (low-La-concentration aLLZO), $Li_7La_3Zr_2O_{12-d}$ (medium-La-concentration aLLZO), and $Li_7La_{4.5}Zr_2O_{12-d}$ (high-La-concentration aLLZO). These model structures were synthesized via SDS[136,137] at 300 ºC, followed by post-annealing at 600 ºC to fully decompose the precursor salts and attain aLLZO (see **Figure 8-17** for more details). The surface and cross-sectional SEM images of the post-annealed aLLZO films reveal a continuous and dense microstructure with film thicknesses of approximately 1.1 ± 0.3 μm, **Figure 3-3 a**. Increasing the La concentration in aLLZO leads to a higher film density and improved aLLZO surface smoothness, which can be attractive for application in solid-state or hybrid batteries to minimize interfacial resistance; detailed analysis of the role of La in aLLZO microstructure control can be found in Supporting Information, **Figure 8-18**. The HR-TEM image in **Figure 3-3 b** reveals the glass-ceramic nature of a medium-La-concentration aLLZO film, composed of a predominately amorphous Li-containing oxide phase and a minor phase of 4–8-nm isolated pyrochlore $La_2Zr_2O_7$ nuclei (see Ref.[138] for more details).

Raman spectroscopy can be used to detect vibrational changes based on the local inelastic scattering of light and was therefore used to identify the local structure and phase composition of aLLZO films with La concentrations of 50 mol.%, 100 mol.%, and 150 mol.% (as compared to LLZO stoichiometry of $Li_7La_3Zr_2O_{12-d}$); the spectra are displayed in **Figure 3-4 a**. We assigned vibrational modes to the observed Raman active peaks and performed a careful analysis on the O–Li–O and O–Zr–O peak shifts for the three aLLZO films with different La concentrations. As Li and Zr act as network formers in aLLZO (see analyses on Zr K-edge XAS and ^{7}Li NMR in Ref.[138] for details), understanding their corresponding Raman shifts provides information on the effect of the La concentration on the CRN connection and packing density of aLLZO.

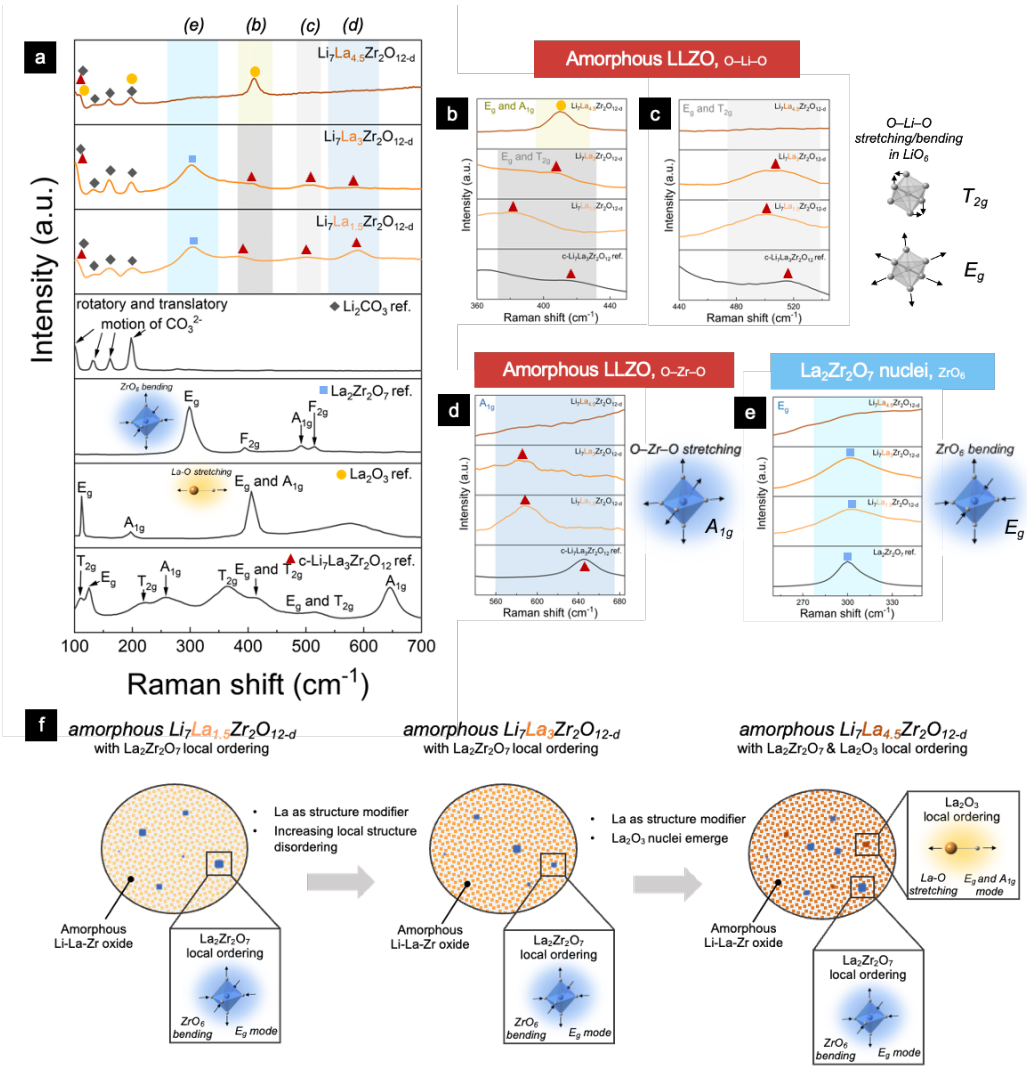

Figure 3-4. Effect of La concentration on the phase composition and near-order structure of aLLZO films. **(a)** Raman spectra of aLLZO with low, medium, and high La concentrations. Additional reference spectra of Li_2CO_3, $La_2Zr_2O_7$, La_2O_3, and cubic $Li_7La_3Zr_2O_{12}$ are displayed in black. Insets: Graphic illustrations of E_g mode (300 cm^{-1}) of ZrO_6 bending in $La_2Zr_2O_7$ and of E_g and A_{1g} modes (406 cm^{-1}) of La–O stretching in La_2O_3. **(b–c)** Zoom-in of Raman spectra in **(a)**, emphasizing the O–Li–O vibration bands (E_g and T_{2g} modes) at **(b)** ~410 cm^{-1} and **(c)** ~514 cm^{-1} in LiO_6 octahedra. **(d–e)** Zoom-in of Raman spectra in **(a)**, emphasizing **(d)** the O–Zr–O stretching band (A_{1g} mode) of aLLZO and **(e)** the ZrO_6 bending (E_g mode) of pyrochlore $La_2Zr_2O_7$ nuclei. **(f)** Schematic illustration of the phase and local structure of aLLZO with low, medium, and high La concentrations based on the interpretation of the Raman spectra.

We first focus on the Raman spectra of the aLLZO films with low-to-medium La concentration, *i.e.,* 50 mol.% and 100 mol.% La. These spectra suggest a glass-ceramic nature of the films with peaks and uprising bands developing from aLLZO and minor crystalline phases of $La_2Zr_2O_7$ nuclei.

Specifically, in aLLZO phases with low-to-medium concentrations of La, we detected broad peaks centered at 410 and 514 cm^{-1}, **Figure 3-4 b, c,** and assigned them to the O–Li–O vibration bands (E_g and T_{2g}) in LiO_6 octahedra according to Ref. [200]. Blueshifts of these E_g and T_{2g} peaks from 381 to 407 cm^{-1} and from 499 to 506 cm^{-1} occurred as the La concentration increased from low to medium concentration, suggesting, on average, a shorter Li–O bond distance in LiO_6 octahedra, **Figure 3-4 b, c**. Furthermore, a broad uprising peak center at 651 cm^{-1} is attributed to the O–Zr–O stretching band (A_{1g} mode) in aLLZO;[199,200] **Figure 3-4 d** provides a zoomed-in view of this A_{1g} Raman mode. In moving from low to medium La concentration, a pronounced redshift is observed for O–Zr–O bond stretching from 588 to 578 cm^{-1}, signifying a longer Zr–O bond in ZrO_6 octahedra. Moreover, an intense peak at 100 cm (T_{2g} mode) is attributable to O–La–O vibration in aLLZO.[199,200]

In addition to the Raman modes that correspond to the near-order vibrations from the amorphous phase, a prominent peak at ~300 cm^{-1} was observed (attributed to the E_g mode of ZrO_6 bending) [226,227], suggesting the presence of minor $La_2Zr_2O_7$ nuclei in the glass-ceramic aLLZO. The Raman peak of the minor $La_2Zr_2O_7$ phase agrees with our previous study on aLLZO phase evolution during annealing**,** where $La_2Zr_2O_7$ nanocrystals formed as an intermediate phase during the crystallization of LLZO while the majority of the film remained amorphous (see Ref.[138] for further details). As displayed in **Figure 3-4 e**, the E_g peak experienced a redshift from 292 to 302 cm^{-1} when increasing the La concentration from a low to medium level, suggesting, on average, a longer Zr–O bond in $La_2Zr_2O_7$ nuclei. We note that other lower-intensity Raman modes (*i.e.,* F_{2g} and A_{1g} modes) of $La_2Zr_2O_7$ are not separable from the spectra, which may be merged or overshadowed by Raman modes of aLLZO and other minor phases.

Next, we turn to the Raman spectrum collected from the aLLZO film with high La concentration, *i.e.,* 150 mol.% La. The spectrum suggests the phase composition of aLLZO with a high concentration of La differs significantly from that with a low-to-medium La concentration, as additional Raman modes appear in the high-La-concentration aLLZO spectrum and are assigned to the exsolution of La_2O_3 nuclei. Specifically, we observed prominent peaks at 110, 197, and 410 cm^{-1} in the spectrum of the high-La-concentration aLLZO film, corresponding to the E_g, A_{1g}, and E_g and A_{1g} modes of La–O stretching in and out of the (0 1 0) plane[228,229] in the hexagonal La_2O_3 structure, inset of **Figure 3-4 a**. Similar phenomena were observed with La-site dopants, Ce^{4+}, and

Li site dopants, Fe^{3+}, in cLLZO, where nanocrystalline CeO_2 or $FeLaO_3$ precipitated out along the grain boundaries when Ce or Fe surpassed their solubility limit.[230,231] The rest of the Raman spectrum of the high-La-concentration aLLZO, however, does not allow separation of vibrational modes that originate from the aLLZO phase. This observation may be explained by the highly disordered structure nature of aLLZO in high-La-concentration aLLZO that significantly increases the variation in Zr–O and Li–O bond distances, thus broadening the peaks; the broad and weak Raman modes may be overshadowed by the more pronounced Raman peaks from minor crystalline phases, such as La_2O_3 nuclei. In addition to the aforementioned glass-ceramic structures in the three different La-concentration aLLZO films, minor peaks were also detected at 101, 132, 160, and 198 cm^{-1} in all three aLLZO spectra. These peaks are attributable to the rotatory and translator motion of CO_3^{2-} from the surface chemistry variation of Li_2CO_3,[232,233] which may originate from the direct contact of the films with moisture in the air during sample transfer and spectroscopy measurements (see further details on the as-deposited aLLZO films in **Figure 8-19)**.

Collectively, based on the Raman spectra, we interpreted the role of the La concentration in the phase formation and composition of the aLLZO films, as presented in **Figure 3-4 f**. We first confirmed the glass-ceramic nature of the aLLZO films, composed in all cases of an aLLZO phase with minor crystalline $La_2Zr_2O_7$ nuclei (and additional La_2O_3 nuclei in the high-La-concentration aLLZO). The aLLZO films with low-to-medium La concentrations, *i.e.,* $Li_7La_{1.5}Zr_2O_{12-d}$ to $Li_7La_3Zr_2O_{12-d}$, revealed that La acts as a network modifier in aLLZO; this is based on the observation that smaller Li–O bond distances and longer Zr–O bond distances prevail with increasing La concentration. These results serve as the first evidence that the bond lengths of the network modifiers Li and Zr with their 1st neighbor, O, can be successfully altered in these aLLZO structures via the network modifier, La. A prior study based on XAS suggests that longer Zr–O bond in aLLZO are associated with more disordered and "jammed" local structures, where the network former, Zr LBU, exhibits a face-sharing tendency [138] with the network modifier, La LBU. Therefore, the medium-La-concentration aLLZO, *i.e.,* $Li_7La_3Zr_2O_{12-d}$, is suggested to consist of a more disordered amorphous local structure than the low-La-concentration one, *i.e.,* $Li_7La_{1.5}Zr_2O_{12-d}$. In addition, we detected a solubility limit of the La modifier that can be incorporated in an aLLZO structure with the threshold falling between 100 mol.% and 150 mol.% La in $Li_7La_3Zr_2O_{12-d}$.

It is challenging to probe the structure of amorphous metal oxides. One may conclude from this study that Raman spectroscopy provides useful insights for analyzing the near-order structure of aLLZO glass-ceramics; however, it is limited in its ability to describe atomic interactions beyond the 1st nearest neighbors. Thus, we turn to study the MRO structure of aLLZO through fluctuation electron microscopy (FEM) to gain further understanding of the effect of La-network-modifier modulations on the local packing density of aLLZO structures.

3.2.2. Medium-Range-Order (MRO) Structure in Disordered Amorphous Regions of High-Entropy aLLZO

FEM is a scanning transmission electron microscopy (STEM) technique that measures the statistical fluctuations in the scattering of electrons arising from nanometer-scale ordered regions (generally in a length range of 0.5–2.0 nm)[234] and was therefore employed to characterize the effect of the La concentration on the MRO structure variations in the predominantly amorphous region of the aLLZO films (see Supporting Information for more details about FEM data collection and interpretation).

Figure 3-5 a–c presents the normalized variance of the image intensity as a function of the scattering vector for the as-deposited and 600 ºC *in situ* annealed aLLZO films with three different La concentrations, *i.e.,* 50 mol.% La, 100 mol.% La, and 150 mol.% La. The corresponding nanodiffraction images of the annealed aLLZO films are displayed as insets of **Figure 3-5 a–c**. Our aim here is to investigate *i)* the local structure variation between as-deposited films and 600 ºC annealed films, *ii)* the effect of the La concentration, varying from 50 mol.% to 150 mol.% La, on MRO formation. For aLLZO with all three La concentrations, two MRO peaks centered at scattering factors of 3.2 and 5.3 nm^{-1} (*i.e.,* ~3.1 and ~1.9 Å, respectively) are identified and highlighted in gray and light orange in **Figure 3-5 a–c**; these peaks correspond to the 2nd and 1st nearest neighbor distances in aLLZO, respectively. The following characteristics are summarized from the FEM plots. First, the peak centered at 3.2 nm^{-1} appears in both the as-deposited and 600 ºC annealed aLLZO, as opposed to the peak centered at 5.3 nm^{-1}, which was not observed in the as-deposited aLLZO with medium-to-high La concentrations. This observation suggests that the MRO at 5.3 nm^{-1} (1.9 Å) is not readily formed during SDS deposition but only upon annealing at 600 ºC. Second, for each of these film compositions, the full width at half maximum (FWHM) of

the peak centered at 3.2 nm^{-1} in the 600 ºC annealed aLLZO film was smaller than that of the as-deposited film, suggesting the formation of more uniform 2nd nearest neighbor distance with less disorder after the 600 ºC annealing. This interpretation is corroborated by the Raman spectra collected from the as-deposited and annealed aLLZO, see **Figure 8-19** and **Figure 3-4 a**, where more prominent Raman bands and less local disorder were observed after 600 ºC annealing for all three aLLZO compositions. Third, by comparing the intensity of the two peaks for each aLLZO composition, we identified that the relative intensity of the peak centered at 3.2 nm^{-1} to that of the peak centered at 5.3 nm^{-1} increases as the La concentration in aLLZO increases, suggesting that higher La concentration promotes the local order in aLLZO with a bond length of 3.1 Å.

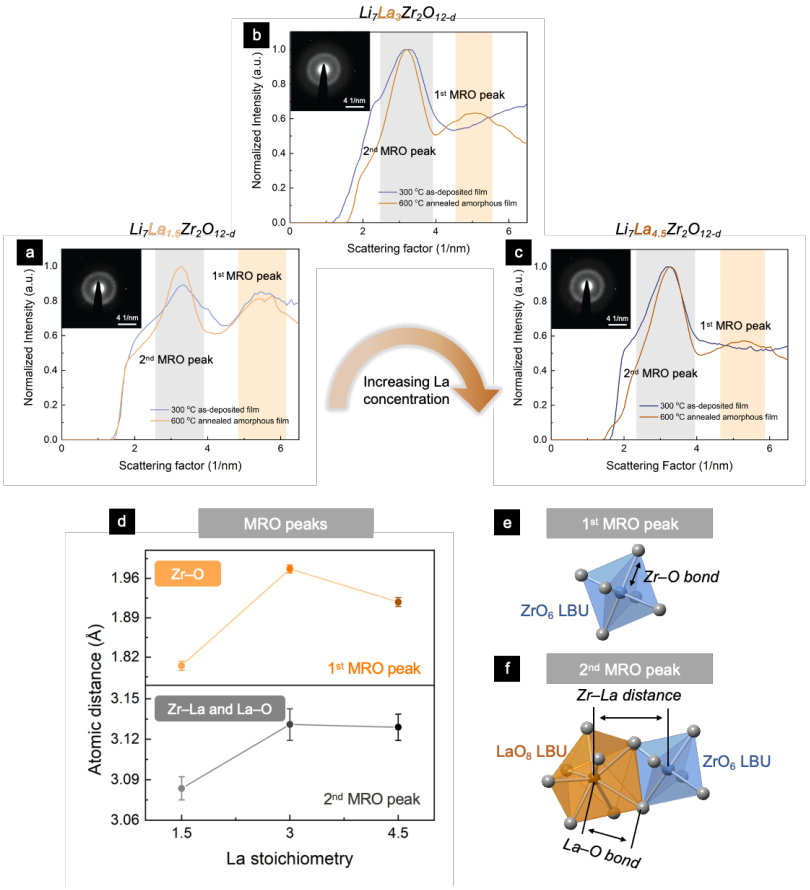

Figure 3-5. MRO measured by FEM applied to aLLZO with **(a)** low, **(b)** medium, and **(c)** high La concentration. The peaks corresponding to the 2nd and 1st MRO peaks are highlighted in light gray and light orange, respectively. **(d)** 1st and 2nd MRO peak positions as a function of the La content in aLLZO films. The 1st MRO peak is predominately attributable to the Zr–O bond. The 2nd MRO peak is predominately attributable to Zr–La and La–O bonds. **(e)** Structure of the ZrO_6 LBU in aLLZO. The Zr–O bond length matches most closely with the 1st MRO peak measured from FEM. **(f)** Structure of the edge- or face-shared LaO_8 and ZrO_6 LBUs. The La–O and Zr–La distances match most closely with the 2nd MRO peak measured from FEM. The ZrO_6 is presented as blue octahedra, and the LaO_8 is presented as yellow dodecahedra.

We next performed Gaussian fitting for the two MRO peaks centered at 5.3 and 3.2 nm^{-1} to evaluate the effect of the La concentration on the MRO distances and their uniformity in the 600 ºC annealed aLLZO. The fitted 1st nearest neighbor distance (peaks centered at 5.3 nm^{-1}) and 2nd nearest neighbor distance (peaks centered at 3.2 nm^{-1}) are presented in **Figure 3-5 d**, and their corresponding FWHM are summarized in **Figure 8-20**. First, as depicted in **Figure 3-5 d**, both the 1st and 2nd nearest neighbor distances show an initial increase for aLLZO with low to medium concentrations of La from 1.81 ± 0.01 to 1.98 ± 0.01 Å and from 3.08 ± 0.01 to 3.13 ± 0.01 Å, respectively. A moderate drop in the 1st and the 2nd nearest neighbor distances to 1.92 ± 0.01 Å and 3.13 ± 0.01 Å follows for aLLZO with high La concentration, respectively. Second, the FWHM of the 1st MRO peak, **Figure 8-20**, exhibited a monotonic decreasing trend from 1.89 ± 0.08 nm^{-1} to 1.77 ± 0.08 nm^{-1} for aLLZO with increasing La concentration from 50 mol.% to 150 mol.%, indicating more uniform bond lengths of approximately 1.9 Å for higher-La-concentration aLLZO. Conversely, the FWHM of the 2nd MRO peak, **Figure 8-20**, exhibited a monotonic increasing trend from 0.99 ± 0.03 to 1.17 ± 0.03 nm^{-1} for aLLZO films with higher La concentration, suggesting a wider distribution of the 2nd nearest neighbor distance and the corresponding bond lengths around 3.1 Å when increasing the La concentration in aLLZO.

To understand the effect of the MRO distances toward bonding, we compared the fitted peaks with literature data to identify the chemical bonds (and their bond distances) that correspond to the 1st and 2nd nearest neighbor distances in aLLZO. We note that each MRO distance obtained from FEM measurements generally represents a group of bonds, and the Li-containing bonds are generally not detectable by FEM. To set the groundwork, we first summarized the local bonding distances of aLLZO[138] and crystalline cLLZO,[210] $Li_2Zr_2O_7$,[235] and La_2O_3[228] in **Table 8-6** as these phases may exist in the 600 ºC annealed aLLZO based on the Raman spectra in **Figure 3-4 a**. Particularly, the nearest Zr–O bond was reported to have a bond length of 2.12 Å in aLLZO and cLLZO and 2.11 Å in $La_2Zr_2O_7$, suggesting that the 1st MRO peak observed in FEM (with a distance of ~1.9 Å) could be correlated to the Zr–O bonds. In addition, the nearest La–O bond lengths and nearest Zr–La distances are also presented in **Table 8-6**, implying that the 2nd MRO peak observed in FEM (with a distance of ~3.1 Å) may be associated with both La–O and Zr–La distances. From a structure perspective, the Zr–O and La–O interactions indeed exist in aLLZO as the 1st nearest neighbors to each other, forming direct bonds within the Zr and La LBUs, as displayed in **Figure 3-5 e**, and the Zr–La interaction exists as the 2nd nearest neighbors to each

other, forming no direct bond, but rather as edge- or face-sharing LBUs,[138] as illustrated in **Figure 3-5 f**.

Collectively, the role of the network modifier La and its effect on the MRO of aLLZO can be interpreted as consisting of two steps of structural evolution. First, for films with a low-to-medium La concentration, *i.e.,* $Li_7La_{1.5}Zr_2O_{12-d}$ to $Li_7La_3Zr_2O_{12-d}$, increasing the La concentration leads to further separation between both the 1st nearest neighboring Zr–O and La–O bonds within the LBUs and the 2nd nearest neighboring Zr–La bond between the adjacent network-former and network-modifier LBUs. This finding corroborates the previous Raman spectra analysis, where we found that increasing La network-modifier concentrations promoted local structure disordering, as indicated by the red shifts of the O–Zr–O stretching band (A_{1g} mode) in **Figure 3-4 d**. We note that the 2nd MRO peaks are close to the Zr–La distances in edge- or face-shared LaO_8 and ZrO_6 LBUs for the probed aLLZO, not as edge-shared in a classic crystalline cLLZO. This finding agrees well with an independent XAS measurement, which previously indicated the face-sharing nature of La and Zr LBUs in aLLZO (see more information in Ref.[138]). Second, smaller MRO distances are detected for both the 1st and the 2nd nearest neighbors upon further increasing the La concentration to 150 mol.% in aLLZO, which is possibly due to the presence of the exsolved La_2O_3 nuclei that promotes local-structure reordering, as detailed in the Raman section.

To obtain a full picture of the aLLZO phases and local structure upon variation of the La concentration, we next used grazing incident X-ray diffraction (GIXRD) to study the LRO in the nanocrystalline regions (*i.e.,* $Li_2Zr_2O_7$ and La_2O_3).

3.2.3. Long-Range-Order (LRO) Structure in Nanocrystalline $La_2Zr_2O_7$ Nuclei

We consider it important to investigate these structure variations in the nanocrystalline regions of the films as different nuclei sizes and types could potentially alter the structure-reordering kinetics and, as a result, affect the packing density of aLLZO and potentially their Li^+ transport. Herein, we collected GIXRD patterns for the three aLLZO with different La concentrations to identify the crystalline phases within the nanocrystalline regions and their structure and grain-size variation, as displayed in **Figure 3-6 a**. For all three aLLZO, crystalline peaks emerged at approximately 2θ = 28.5°, 32.5°, 47.2°, and 56.8°, attributed to the (222), (400), (440), and (622) planes of the

$La_2Zr_2O_7$ pyrochlore phase (*Fd-3m* space group), as illustrated in **Figure 3-6 c**. The formation of crystalline LLZO can be excluded as no cLLZO or tLLZO peaks were detected in the collected GIXRD patterns. In addition, peaks corresponding to Li_2CO_3 were also observed in the three aLLZO films, suggesting the variation in surface chemistry arising from the contact with moisture in the air, possibly during sample transfer and measurements. Interestingly, although the Raman spectra in **Figure 3-4 a** imply the local ordering of La_2O_3 in the high-La-concentration aLLZO, La_2O_3 crystalline peaks were not detected in the corresponding XRD pattern. This observation presumably stems from the limited La_2O_3 nuclei sizes with less confined LRO structures, which, as a result, are not detectable by GIXRD. A peak at $2\theta = 42.5°$ appeared in all three aLLZO films, corresponding to the (200) plane of the single-crystal MgO substrates, depicted in **Figure 8-21**. Moreover, upon comparison to the GIXRD patterns of the as-deposited films in **Figure 8-22**, we noted that no crystalline phase was formed in the as-deposited films. Only a general amorphous background was observed with a broad hump centered at $2\theta = 28.5°$ for the three films, possibly corresponding to the nano-sized local ordering of $La_2Zr_2O_7$ with less confined bond distances. This result is consistent with previous studies on the LLZO phase evolution,[138] where the clear presence of $La_2Zr_2O_7$ nanocrystals only emerged and evolved upon post-annealing beyond 500 °C.

Significant shifts of the $La_2Zr_2O_7$ crystalline peaks are observed in the XRD patterns of the three aLLZO films in **Figure 3-6 a**, generally indicating variation in the d-spacing within the crystalline nuclei. To better understand the effect of the La concentration on the structure and nuclei sizes of $La_2Zr_2O_7$, we performed peak fitting for the most prominent $La_2Zr_2O_7$ peak at $2\theta = 28.5°$ (the peak highlighted in red in **Figure 3-6 a**), and the results are presented in **Figure 3-6 b**. Specifically, the peak positions of $28.81 \pm 0.01°$, $28.32 \pm 0.01°$, and $28.82 \pm 0.01°$ in **Figure 3-6 b** (more information can be found in **Figure 8-23 a**) and FWHMs of $1.07 \pm 0.01°$, $1.16 \pm 0.02°$, and $1.04 \pm 0.01°$ in **Figure 8-23 b** were obtained from the XRD peak fitting for low-, medium-, and high-La-concentration aLLZO, respectively. From a structure perspective, the peak at $\sim 2\theta = 28.5°$ corresponds to the (222) plane in the $La_2Zr_2O_7$ pyrochlore structure, as presented in **Figure 3-6 c**. The d-spacing between two (222) planes (denoted as the d_{222}-spacing in later discussion) can be interpreted as the distance between two planes consisting of ordered La and Zr atoms, as illustrated in **Figure 3-6 d**.

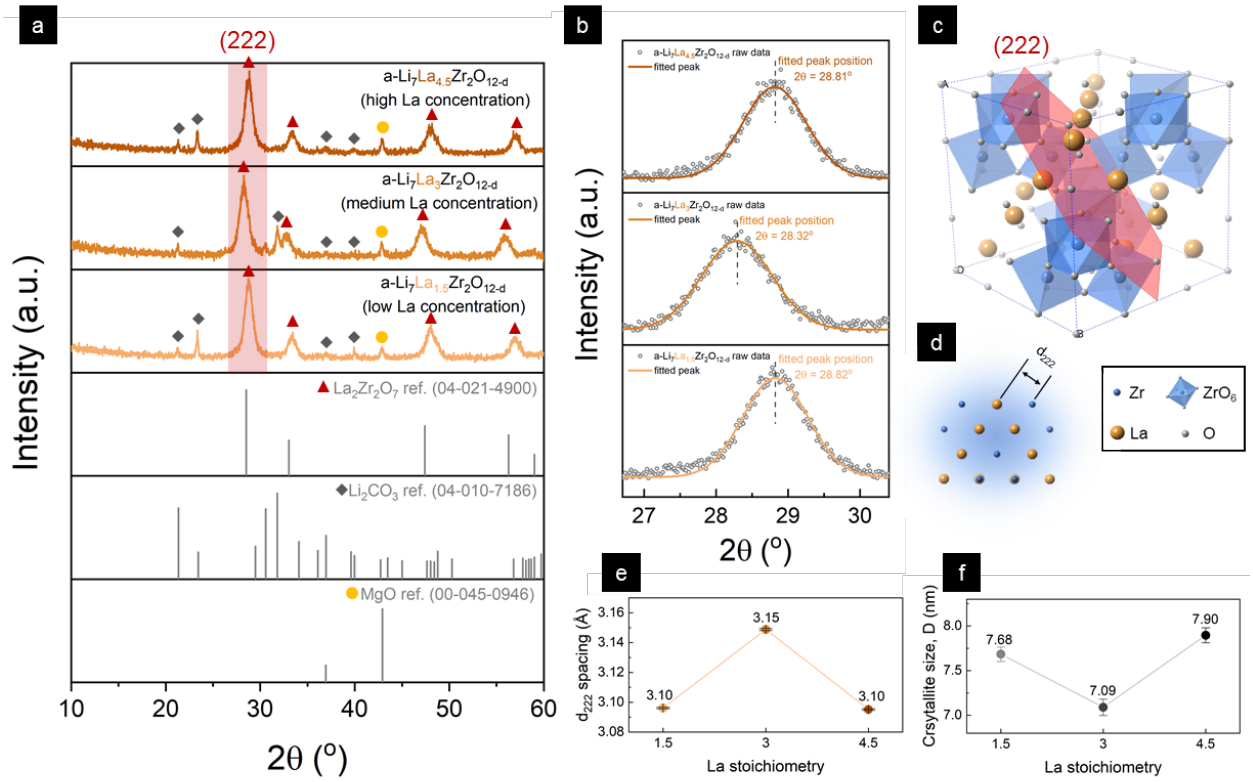

Figure 3-6. LRO structure for the crystalline regions in aLLZO. **(a)** GIXRD patterns for aLLZO with low, medium, and high La concentrations. Broad peaks of $La_2Zr_2O_7$ and Li_2CO_3 were detected in all three aLLZO compositions. MgO peaks were detected from the substrates. References: $La_2Zr_2O_7$ [04-021-4900], Li_2CO_3 [04-010-7186], MgO [00-045-0946]. **(b)** Fitting of GIXRD peak in a 2θ range of 26.5–30.5º corresponding to the (222) plane of the pyrochlore $La_2Zr_2O_7$. The peak positions were fitted at 28.82º, 28.32º, and 28.81º for aLLZO with low, medium, and high La concentrations, respectively. **(c)** Structure of pyrochlore $La_2Zr_2O_7$ (cubic, Fd-3m). The Zr, La, and O atoms are presented in blue, yellow, and dark gray, respectively, and the ZrO_6 is presented as blue octahedra. The (222) plane is highlighted in red. **(d)** View of the d_{222} spacing of $La_2Zr_2O_7$ along the [110] direction. **(e)** Calculated d_{222} spacing of $La_2Zr_2O_7$ as a function of La concentration in aLLZO. **(f)** Calculated $La_2Zr_2O_7$ crystallite size (D) as a function of La concentration in aLLZO.

Hence, we next applied Bragg's equation[236] and the Scherrer equation[237] to calculate the d_{222}-spacing and the average crystallite size of $La_2Zr_2O_7$ based on the peak position and FWHM data obtained from peak fitting. **Figure 3-6 e** shows a volcano-shaped trend for the d_{222}-spacing, which increases from 3.10 ± 0.00 Å to 3.15 ± 0.00 Å in moving from the low- to medium-La-concentration aLLZO films and then decreasing to 3.10 ± 0.00 Å for the high-La-concentration aLLZO film. Conversely, the crystallite size (D) summarized in **Figure 3-6 f** shows an initial drop from 7.68 ± 0.08 nm to 7.09 ± 0.09 nm in moving from the low- to medium-La-concentration aLLZO films, followed by an increase to 7.90 ± 0.08 nm for the high-La-concentration aLLZO

film. The small errors in both the d_{222}-spacing and crystallite-size calculations indicate that the trends are significant.

Several important conclusions can be made from the GIXRD peak analysis. First, the calculated grain sizes of the $La_2Zr_2O_7$ nanocrystals in the three amorphous films fall within the range of <8 nm, similar to the previously reported $La_2Zr_2O_7$ grain size of 4–8 nm for the 600 °C aLLZO film in Ref.[138], also displayed in **Figure 3-3 b**. We hence confirmed that the films were predominately amorphous but exhibited a glass-ceramic nature with scattered $La_2Zr_2O_7$ nuclei. Second, for aLLZO with a low-to-medium La concentration, a larger d_{222}-spacing was observed for aLLZO with higher La concentration; this result is in good agreement with the observed redshift of the E_g mode (ZrO_6 bending) in the Raman spectra, presented in **Figure 3-4 d,** and is similar to the increased 1st and 2nd MRO distances detected by FEM in **Figure 3-5 d**. We relate this trend to the fact that La acts as a network modifier in aLLZO, promoting structure disorder and reducing the packing density in both amorphous and crystalline regions. Third, for films with a medium-to-high La concentration, increasing the La concentration leads to a larger $La_2Zr_2O_7$ nuclei size with reduced d_{222}-spacing. This feature can be attributed to the exsolution of heterogenous La_2O_3 nuclei, as suggested by Raman spectroscopy, which lowers the energy barrier for nucleation and growth within aLLZO glass-ceramics. Fourth, we observed that the calculated d_{222}-spacings (3.09–3.15 Å, the distances between two planes consisting of ordered La and Zr atoms in $La_2Zr_2O_7$ nuclei) are close to the 2nd MRO distances (3.07–3.15 Å, mostly associated with La–O and Zr–O distances in aLLZO) obtained from FEM, as depicted in **Figure 3-5 d**. We understand this observed concurrence in bond distances as the following. Part of the La and Zr LBUs in aLLZO that sit close to the already formed $La_2Zr_2O_7$ nuclei may arrange in an MRO with similar bond distances as in the $La_2Zr_2O_7$ nuclei, although the phase transition from aLLZO to $La_2Zr_2O_7$ is far from being completed and high local disorder in the LBU arrangement is still present and prevails. We present in the next section a summary of the role of La in the aLLZO structure and phase evolution with the MRO and LRO structure data collected from FEM and GIXRD and discuss their implications toward battery integration.

3.2.4. Modulating La Concentration in aLLZO towards Battery Applications

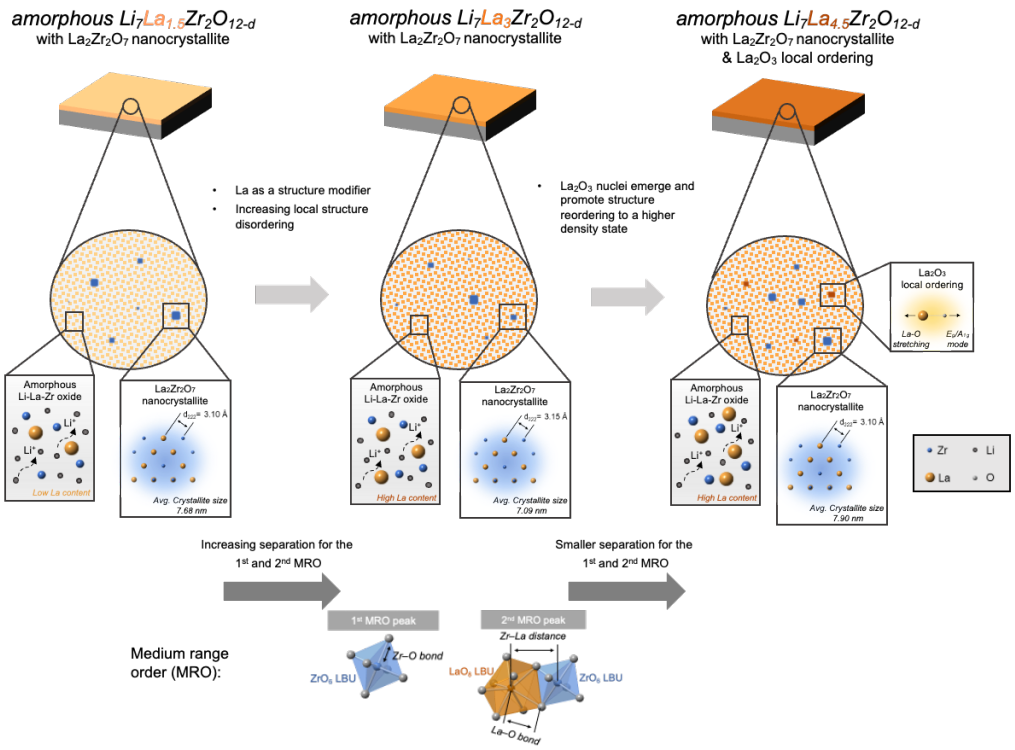

Figure 3-7. Schematic illustration of the phase and local structure of aLLZO with low, medium, and high La concentration, based on the interpretation of the collected Raman spectra, GIXRD patterns, and FEM diffraction data.

Figure 3-7 displays schematic illustrations of the phase and local structure of aLLZO with low-to-high La concentrations, *i.e.,* $Li_7La_{1.5}Zr_2O_{12-d}$, $Li_7La_3Zr_2O_{12-d}$, and $Li_7La_{4.5}Zr_2O_{12-d}$, based on the MRO and LRO structure analysis. First, we confirmed that aLLZO are generally composed of a predominate disordered amorphous phase with a minor presence of crystalline nuclei. On a microscopic level, we identify the role of La as a network modifier in aLLZO. When the La concentration is below its solubility limit in aLLZO (low-to-medium concentration of La), La fully dissolves in the amorphous structure matrix and promotes local structure disordering. Here, we observed looser LBU connections and larger MRO distances from Raman spectra and FEM analysis, as shown in **Figure 3-4 a** and **Figure 3-5 d**, as well as a larger d_{222}-spacing in crystalline $La_2Zr_2O_7$ regions with increasing La concentration up to 100 mol.% La, as displayed in **Figure 3-6 e**. These observations suggest a lower packing density of aLLZO upon increasing the La concentration from a low to medium level. Once the La concentration exceeds its solubility limit

in aLLZO, *i.e.,* 150 mol.% La, the local ordering of La_2O_3 appears as secondary nanosized nuclei (detectable by Raman, but non-detectable by GIXRD) and promotes heterogenous nucleation with a lowered energy barrier for structure reordering. This leads to a more ordered and higher-packing-density local structure for aLLZO with high La concentration. Specifically, larger nuclei sizes with a smaller d_{222}-spacing nuclei are detected for crystalline $La_2Zr_2O_7$ nuclei and tighter LBU connections, and smaller 1st nearest neighbor distances are observed in the amorphous region of aLLZO. These findings showcase the role of the La network modifier in aLLZO and the solubility limit of La into various aLLZO phases, providing guidelines for future structure modulation.

Based on these findings, we see opportunities to modulate the local structure of aLLZO by doping various alternative network-modifier ions at the La sites. It was well known in the glass-ceramics field that not only the concentration of network-modifier elements but also the field strength (*i.e.,* valence-to-radius ratio) can affect the coordination of the surrounding network-former LBUs, therefore altering the packing density and glass properties.[190,238] For instance, we are convinced that various to-be-explored La-site dopants can affect the coordination and packing density of the aLLZO glass-ceramics and significantly alter the Li^+ transport through the modulation of the Li^+ hopping pathway and distances. Future efforts can be focused on doping at La modifier sites with elements in the lanthanide series, *e.g.,* Ce and Er,[239] which have the same valence number and the same outermost-shell electronic structure but different atomic radii. Alternatively, one may consider group II elements, *e.g.,* Ca and Sr, as network-modifier dopants, which offer a "1+" difference in the valence state. Both strategies can alter the field strength surrounding the network-modifier elements and help achieve precise control over the coordination and connection of LBUs within aLLZO.

In terms of battery applications, the phase composition and glass packing density of aLLZO films are considered to be critical properties in determining their suitability for use as electrolyte separators or protective coating layers in cell designs, as they may affect the ion-transport and mechanical properties of the aLLZO films. Indeed, earlier studies on many other Zachariasen and non-Zachariasen invert glasses such as LIPON indicate that the local bonding and electronic structure can be tuned by varying the type and concentration of network modifiers, and therefore, is a way to alter the transport properties of the glass.[190,240,241] We present here a model study that confirms the role of La in aLLZO as a network modifier, identifies the solubility limit of La in aLLZO, and provides effective ways to tune the packing density and phase composition of aLLZO

films that may later affect the transport and mechanical properties. Technologically, we see multiple opportunities for integrating the aLLZO films in solid-state or hybrid batteries, as illustrated in **Figure 3-1 a**. They could be introduced as a Li protective coating layer between the Li-metal anode and liquid or sulfide electrolytes, reducing the tendency of Li-dendrite formation during Li plating and preventing the formation of a low-conduction SEI layer due to electrochemical instability at the interfaces. Alternatively, aLLZO films could be applied as a solid-electrolyte separator, providing Li^+ conduction while bridging the stability windows between the anode and cathode. Together with these efforts, we foresee the importance and applicability of our findings in guiding the design and optimization of aLLZO-based all-solid-state and hybrid batteries.

3.3. Conclusion

Amorphous Li^+ electrolyte films have been identified as promising candidates for use in all-solid-state or hybrid batteries as solid-electrolyte or protective-coating layers to further enhance the energy density and battery safety. High-entropy Li-garnet-type aLLZO has attracted attention as an alternative to amorphous LiPON electrolytes owing to its wide electrochemical stability window, low vulnerability towards Li-dendrite growth (due to the elimination of highly dendrite-susceptible grain-boundary areas), and reduced yet wider thermal processing window (room temperature to 680 ºC) to stabilize various amorphous phases.[39,138,161] In addition, aLLZO phases offer the opportunity to bypass the classic high-cost sintering processes typically required for crystalline Li^+-electrolyte synthesis, which becomes especially relevant with the recent spike in world energy prices. In 2023, high-entropy aLLZO phases, composed of four different LBUs (namely, LiO_4, LiO_6, ZrO_6, and LaO_8) were described for the first time in terms of their LBU connections with their structure–Li^+ transport relations established, see Ref. [138] for details. Based on XAS and ^7Li NMR analyses, Li and Zr were clearly identified as network formers. However, it remained to be seen whether La was the effective network modifier in aLLZO and whether it could be used to modulate the MRO and LRO in aLLZO. Furthermore, the solubility limit of La in aLLZO solid solution remained unclear.

Through this study, we designed model cases of aLLZO structures, namely, $Li_7La_{1.5}Zr_2O_{12-d}$, $Li_7La_3Zr_2O_{12-d}$, and $Li_7La_{4.5}Zr_2O_{12-d}$, to probe the structural role of La and define its solubility

limit in aLLZO. This study is crucial in determining potential dopant sites for network modifiers beyond La in aLLZO. Through near-order, MRO, and LRO structure probing techniques, we confirmed the glass-ceramic nature of the aLLZO films composed of a predominate amorphous phase and minor $La_2Zr_2O_7$ nuclei when La remains within its solubility limit in aLLZO. The MRO analysis via FEM confirmed, within the solubility of La, its role as a network modifier in aLLZO; increasing the La concentration leads to larger distances between the 1st nearest neighbors of Zr–O and La–O within the same LBU and the 2nd nearest neighbors of Zr–La across two adjacent network-former and network-modifier LBUs. We also defined the solubility threshold between 100 mol.% and 150 mol.% for La in aLLZO via Raman spectroscopy. Through the definition of the role of La in aLLZO as a network modifier, we see perspective to explore in future work doping or co-doping strategies at La sites, including elements in the lanthanide series and alkaline-earth metals in group II, for these high-entropy aLLZO structures to further modulate the Li^+-transport properties and identify the optimum Li concentration on the tetragonal LiO_4 site and octahedral LiO_6 site. We encourage both computational and experimental efforts to investigate the role of these network-modifier dopants in structure density modulation. Additional attention should be paid to the electrochemical stability between various aLLZO phases *vs.* the Li-metal anode; it is also suggested that critical current densities be measured for various aLLZO phases designed based on careful selection of network-modulating dopants. Collectively, we are confident that with low-temperature and low-energy synthesis options to achieve manufacturing sustainability, amorphous Li garnets will be a material class of interest for future battery cell designs.

3.4. Experimental

3.4.1. Preparation of aLLZO Films by SDS

Three SDS precursor solutions were prepared in $Li_7La_{4.5}Zr_2O_{12-d}$, $Li_7La_3Zr_2O_{12-d}$, and $Li_7La_{1.5}Zr_2O_{12-d}$ stoichiometric ratio with 75% extra Li by dissolving $LiNO_3$, $La(NO_3)_3 \cdot 6H_2O$, and zirconium(IV) acetylacetonate into a solvent mixture of methanol:1-methoxy-2-propanol:bis(2-ethylhexyl) phthalate (1:1:1 vol.%). The concentration of the SDS solution was 0.015 M, and the solution was stirred overnight for 12 h before deposition. $LiNO_3$ (≥ 99%), zirconium(IV) acetylacetonate (97%), and 1-methoxy-2-propanol (≥ 99.5%) were purchased from Sigma-Aldrich; $Al(NO_3)_3 \cdot 9H_2O$, $La(NO_3)_3 \cdot 6H_2O$ (99.99%), and bis(2-ethylhexyl) phthalate were purchased from

Alfa Aesar; methanol was purchased from VWR. Single-side-polished MgO (001) substrates (10 × 10 × 0.5 mm) were purchased from MTI Corporation and used as the substrate for SDS to prevent interfacial reactions.

The SDS of aLLZO starts with placing a MgO substrate on a heated stainless-steel hot plate at 300 ºC with the polished side facing up. A K-type thermocouple was used to monitor the deposition temperature by placing it aside the MgO substrate. To deposit a film, the SDS solution was pumped through a polypropylene syringe at a rate of 10mL h^{-1} into a spray atomizer (DeVILBLISS, AG361). Throughout the deposition, compressed gas with a pressure of 0.3 bar at the atomizer was selected as the carrier gas, and the distance between the spray atomizer and the MgO substrate was maintained at 25 cm. For each film stoichiometry, the as-deposited films were obtained after a 30-min deposition. To prepare the post-annealed aLLZO film, the as-deposited films were post-annealed in an alumina crucible in a temperature-calibrated tube furnace at 600 ºC under a flow of pure O_2 (Airgas). A heating and cooling rate of 5 min $ºC^{-1}$ was used to minimize surface strain on the films. The post-annealed aLLZO films were stored inside an Ar-filled glovebox before measurements to prevent exposure to moisture and to minimize chemical degradation.

3.4.2. Microstructure Characterization

Surface and cross-sectional SEM images of the aLLZO films were collected using a Zeiss Ultra Plus field-emission scanning electron microscope with an accelerating voltage of 3.0–5.0 kV and a working distance of 3–8 mm. An in-lens secondary electron (SE) detector was used for SEM image collection in this study. A diamond blade was used to cut the sample before imaging the cross-section of the films. Conductive carbon tape was used to tape the side of the samples to ensure sufficient electronic conductivity during imaging.

3.4.3. Local Structure and Phase Composition Characterization

The near-order structure of aLLZO was characterized using Raman spectroscopy (WITec alpha 300 M+). A laser wavelength of 532 nm with a power of 10 mW, a grating of 300 g mm^{-1}, and a spectral resolution of 0.1 cm^{-1} were applied to obtain all the Raman data. A 50× long distance

objective (Zeiss, Germany) with a numerical aperture (NA) of 0.7 was used for the laser focusing, giving an approximate laser spot size of 1 μm.

3.4.4. MRO Structure Characterization

To prepare samples for *in situ* FEM measurements, the precursor solutions (0.015 M) were diluted to a concentration of 0.0003 M with methanol (VWR). The diluted solution was cast onto a silicon TEM grid (Norcada, TA301Z). Each grid contained a 3 × 3 array of 0.1×0.1 mm windows covered by 10-nm-thick silicon nitride membranes.

A FEI heating holder was used for the *in situ* experiments. The samples were heated at 300 ºC and 600 ºC, respectively, on the TitanX, operated at 200 keV. At each temperature, FEM patterns were collected with a convergence angle of 0.51 mrad, a probe diameter of 2.2 nm, and a camera length of 245 mm. For each sample, over 400 scanning nanodiffraction images were collected in one scan. As FEM is a statistical approach, to reduce the error in FEM analysis, we collected four scans for each sample. For FEM data analysis, we used a custom MATLAB script to calibrate the data by removing the ellipticity and to determine the differences in variance as a function of the spatial frequency as a function of the scattering angle. Data processing and analysis were performed, following the procedure outlined in Ref.[242]. Two decimal places and a 95% confidence interval were reported for the atomic distances and FWHM obtained from the fitted MRO peaks.

3.4.5. LRO Structure Characterization

GIXRD patterns of both the as-deposited and post-annealed aLLZO films were collected using a Rigaku SmartLab diffractometer with Cu Kα irradiation (λ = 1.5406 Å). An omega angle of 1°, a scan step size of 0.02° at a speed of 5° per minute, and an X-ray voltage of 45 kV and current of 200 mA over the 2θ angular range of 15°–60° were used for all the measurements. Automatic z-axis height adjustment was applied based on the intensity of the XRD signal. The XRD patterns were used for peak fitting to obtain the changes in the peak position and FWHM for the annealed samples. Note that the peak positions of the annealed samples were not corrected by the refractive index as the films were mostly amorphous with undefined refractive index. This could potentially lead to a maximum of 0.1° of error in the peak position due to minor differences in the sample

alignment during the XRD measurements, which would not change the trend depicted from the current peak fitting. Bragg's equation, $n\lambda = 2d \sin\theta$, was used to calculate the d-spacing of the $La_2Zr_2O_7$ nanocrystals, where n is an integer (n = 1 is used for this study), λ is the X-ray wavelength (1.5406 Å), d is the spacing of the diffracting planes, and θ is the Bragg angle. The crystallite domain sizes (D) were obtained using Scherrer's equation, $D = K\lambda/(\beta \cos\theta)$, where K is the dimensionless shape factor (K = 0.9 used for this study), λ is the X-ray wavelength (1.5406 Å), β is the FWHM in radians, and θ is the Bragg angle.

4. CHAPTER 4. Time-Temperature-Transformation (TTT) Analysis of Phases for Low-Temperature Sustainable Synthesized Crystalline Cubic Li Garnets

Adapted from Yuntong Zhu, Michael Chon, Carl V. Thompson, Jennifer L.M. Rupp. Time-Temperature-Transformation (TTT) Analysis of Phases for Low-Temperature Sustainable Synthesized Battery-Grade Li-Garnet Electrolyte Films, *Manuscript in revision (2023)*

Abstract

Developing more energy-efficient and cost-effective methods for synthesizing Li^+-conductive functional ceramics is crucial for the scalable production and sustainable use of Li^+ solid electrolytes in all-solid-state and hybrid batteries. Among the plethora of solid electrolytes, Li-garnet LLZO has garnered attention because of its high Li^+ conductivity and wide electrochemical stability window. Nevertheless, the high sintering temperatures (>1050 °C) required to achieve the highly conductive cLLZO phase raise concerns about the LLZO–cathode interface stability. Additionally, the high costs of ceramic powder processing and high-temperature sintering pose a challenge, especially when energy prices rise, as in 2022. A comprehensive redefinition of the synthesis routes for cLLZO is thus desired to ensure sustainable production and cell integration. In this study, we employed an alternative route involving SDS (a direct "liquid-to-solid" route without sintering) to synthesize cLLZO films at half the temperature used in conventional sintering. A 1st TTT diagram for amorphous-to-crystalline LLZO transformation was constructed and analysis of the crystallization enthalpy was performed for guidance. The successful synthesis of cLLZO at a record-low synthesis temperature of 500 °C was confirmed by Raman spectroscopy and further compared toward existing synthesis processes. Our findings demonstrate the use of TTT diagrams for the design of sustainable ceramic film processing and provide guidelines for the low-temperature synthesis of cLLZO toward high-energy SSBs.

4.1. Introduction

Battery performance and costs are the two most important factors when evaluating specific cell design and cell chemistry for use in EVs.[39,243–245] The former largely determines the driving distance and lifetime of EVs, whereas the latter dictates the cost-competitiveness of EVs relative to internal combustion vehicles (ICVs).[243,244] To date, Li^+ batteries have shown promise as the most reliable energy-storage solution for EVs owing to their improved energy density and cycle life compared with that of earlier developed battery systems (*e.g.,* lead-acid batteries, nickel-cadmium batteries). State-of-the-art Li^+ batteries with graphite (or graphite/Si composite) anodes, NMC or NCA cathodes, and organic liquid electrolytes are able to achieve gravimetric energy densities of 250–300 Wh kg^{-1} at the cell level,[243] associated with a cost of approximately US$100 kWh^{-1}.[246] To accelerate the transition from ICVs to EVs, the US Department of Energy (DOE) set long-term objectives of reaching a production cost of <US$60 kWh^{-1} at the cell level and a specific energy density of >500 Wh kg^{-1} at the battery level by 2030.[247] One promising approach to achieve this ambitious goal is to revive the use of a Li-metal anode in an all-solid-state or hybrid battery configuration with partial or full substitution of the state-of-the-art organic liquid electrolytes and polymer separators by thin ceramic solid-electrolyte separators to achieve high energy density while minimizing the risk of Li dendrite growth and thermal runaway.[39,248] The ideal solid-electrolyte separators should possess high Li^+ conductivity over a wide temperature range and good electrochemical and chemical stability against both the Li-metal anode and the high-voltage oxide cathode.[39,136,248] In addition, the electrolyte materials should be mechanically robust (*i.e.,* exhibit high fracture toughness) against Li-dendrite propagation.[39,173–175,249] State-of-the-art ceramic solid electrolytes can be classified into two types based on their chemical composition, namely, oxides and sulfides.[248] Sulfide-based electrolytes, including argyrodite-type Li_6PS_5X (X=Cl, Br, I)[218,219] and Li_2S–P_2S_5 glasses,[40,220] possess limited electrochemical stability windows (<1 V)[59,197,222] and poor air stability, restricting their energy density, scale-up processibility, and safety toward application in battery cells.[248] Comparatively, oxide-based electrolytes offer wider electrochemical stability windows and higher fracture toughness and require a less constrained atmosphere for processing.[39,48,59,161,248]

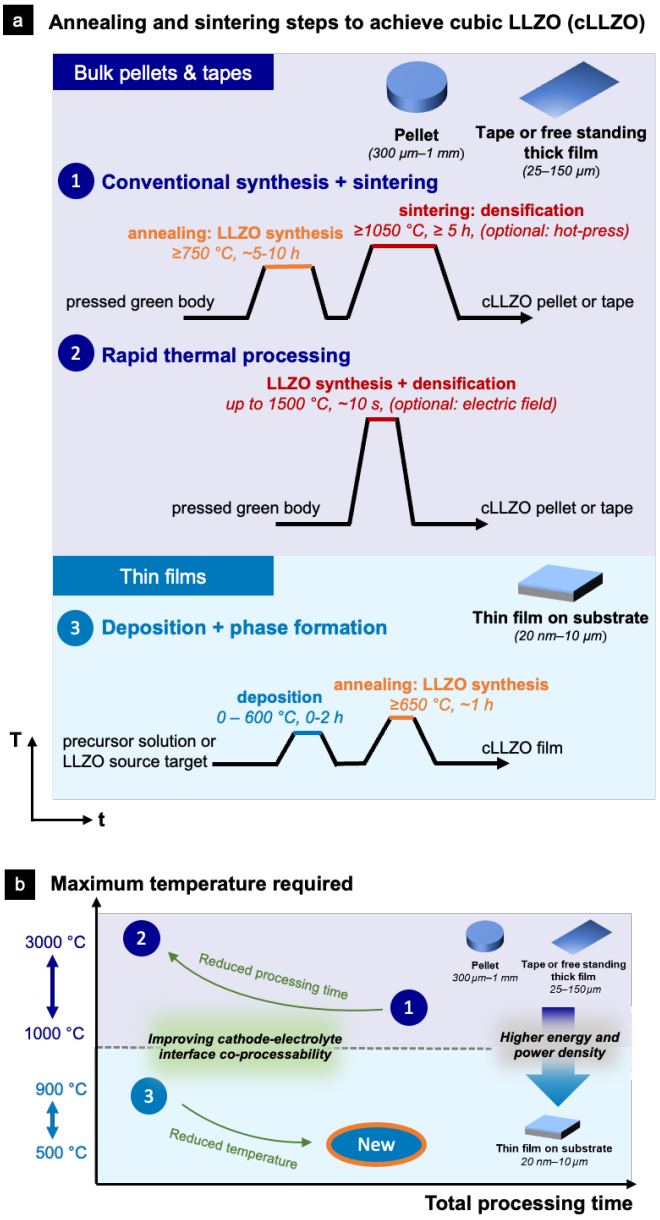

Figure 4-1. (a) Annealing and sintering steps to achieve cubic-phase LLZO under three different processing routes, including conventional synthesis + sintering and rapid thermal processing for bulk pellet and tape processing, and deposition + phase formation for thin-film processing. **(b)** Schematic illustration of the state-of-the-art maximum processing temperature vs. processing time. Reducing the processing temperature or time are both viable and preferred routes to improve the cathode–electrolyte interface co-processability and reduce interfacial ion diffusion and chemical reaction. The energy and power density of a SSB can be improved by reducing the solid-electrolyte thickness (shifting from ceramic pellets or tapes to thin films).

Among the widely studied oxide electrolytes, garnet-type LLZO has demonstrated electrochemical stability between 0 and 6 V,[39,105] enabling direct and stable pairing with high-voltage cathodes and

a Li-metal anode, making this material an attractive option for use in high-energy-density all-solid-state or hybrid batteries. To date, LLZO electrolytes can be processed either as bulk pellets or tapes with thicknesses generally >25 μm (tapes <100 μm can be brittle and difficult to handle)[250,251] or as thin films with thicknesses between 0.2 and 10 μm (**Figure 4-1 a**).[39,120,136] Depending on the form and desired thickness of LLZO, either sintering (>1050 °C for pellets or tapes)[99,105,129,168,169,252–256] or annealing (>650 °C for films)[98,100,113,114,116,120,136] are required to synthesize LLZO in its highly conductive cubic phase (**Figure 4-1 b)**, see Ref. [257] for high-statistics data mining on sintering. An additional summary of the bulk and thin-film LLZO synthesis is presented in **Table 8-7**.

From a cell-integration perspective, these LLZO pellets, tapes, or films need to be co-processed with high-voltage oxide-based cathodes (*e.g.,* NMC and NCA) to achieve good mechanical bonding and low interfacial resistance at the LLZO–cathode interface.[129] However, prior studies have shown that oxide-based cathodes can be irreversibly reduced or decomposed into low-capacity phases at a co-processing temperature above 600 °C,[129,224] which is clearly lower than the classic sintering temperatures for pellet and tape-type LLZO and therefore lead to a reduced total capacity for the cathodes. Thus, the commercialization of oxide-electrolyte-based SSBs necessitates a complete rethinking and redesign of electrolyte separator processing as well as the cell-integration routes, preferably at lowered co-sintering or co-annealing temperatures. Importantly, newly defined processing routes should ensure chemical stability at cathode–electrolyte interfaces and show promise toward achieving the DOE cost projection of <US$60 kWh^{-1}.[247]

From a second perspective, low-temperature processing is favorable for next-generation Li^+ ceramic electrolytes as it can significantly reduce manufacturing costs by lowering the energy input. An earlier cost analysis suggested that the high-temperature annealing and sintering steps account for approximately 75% of the total production cost for Li^+ solid electrolytes.[39] This cost can make up an even higher fraction of the production cost when there is a spike in energy prices. For instance, the 2022 rise in energy costs led to temporary challenges for the energy-intensive ceramic and glass industries. It is now critical for the industry to re-examine the state-of-the-art processing routes and point toward a future where achieving greater energy efficiencies in production is a top priority. Specifically, any option to achieve similar structure and functionality

for a Li^+ ceramic (or glass) electrolyte at lowered processing temperatures without sintering steps is of utmost importance for future sustainable and low-cost electrolyte and SSB production. Alternative sinter-free processing routes stemming from the direct "liquid-to-solid" densification of Li^+ electrolytes at low temperatures are promising options to be explored. Additionally, these direct densification routes do not require ceramic powder processing, which is beneficial in reducing the cost and energy consumption associated with the production of ceramic Li^+ electrolytes. However, to date, only a few academic works have explored the direct "liquid-to-solid" densification routes for battery-grade Li^+ ceramic electrolyte processing, see Ref. [136] and [138] for studies on the SDS of LLZO. Despite being a timely and relevant process, an annealing temperature of 750 °C is still required to achieve the highly conductive cLLZO via SDS, which can still be too high for LLZO–cathode co-processing. Low-temperature processing options have yet to be explored.

In this work, we explore alternative synthesis conditions to crystallize the directly "liquid-to-solid" SDS-processed LLZO electrolytes at reduced temperatures through the establishment of the first TTT diagram. To enable rational design of the low-temperature routes, we first obtain a fundamental understanding of the kinetics of the phase transformation from aLLZO to crystalline cLLZO through Raman spectroscopy and DSC.[258] A common approach to understand and modulate the phase-transformation kinetics of a glass-ceramic or metallic glass is through the construction of a TTT diagram,[259–262] a 2D representation plot of the temperature and time at which a material undergoes a phase transformation.[261,263] Specifically, we deconvoluted the crystallization process of SDS-processed LLZO into three unique steps and constructed the very first TTT diagram for LLZO based on the analysis of crystallization enthalpies. From there, we designed three alternative low-temperature processing routes and confirmed the successful synthesis of cLLZO at temperatures as low as 500 °C.[264] Fundamentally, we demonstrate the establishment and use of a TTT diagram in analyzing the phase-transition and crystallization kinetics of LLZO and designing alternative ceramic film processing routes. Technologically, we see the promise of the newly proposed low-temperature processing routes to benefit the materials integration and manufacturing scale-up at a reduced cost for LLZO-based SSBs and beyond.

4.2. Results and Discussion

4.2.1. Synthesis and Phase Evolution from aLLZO to Crystalline cLLZO

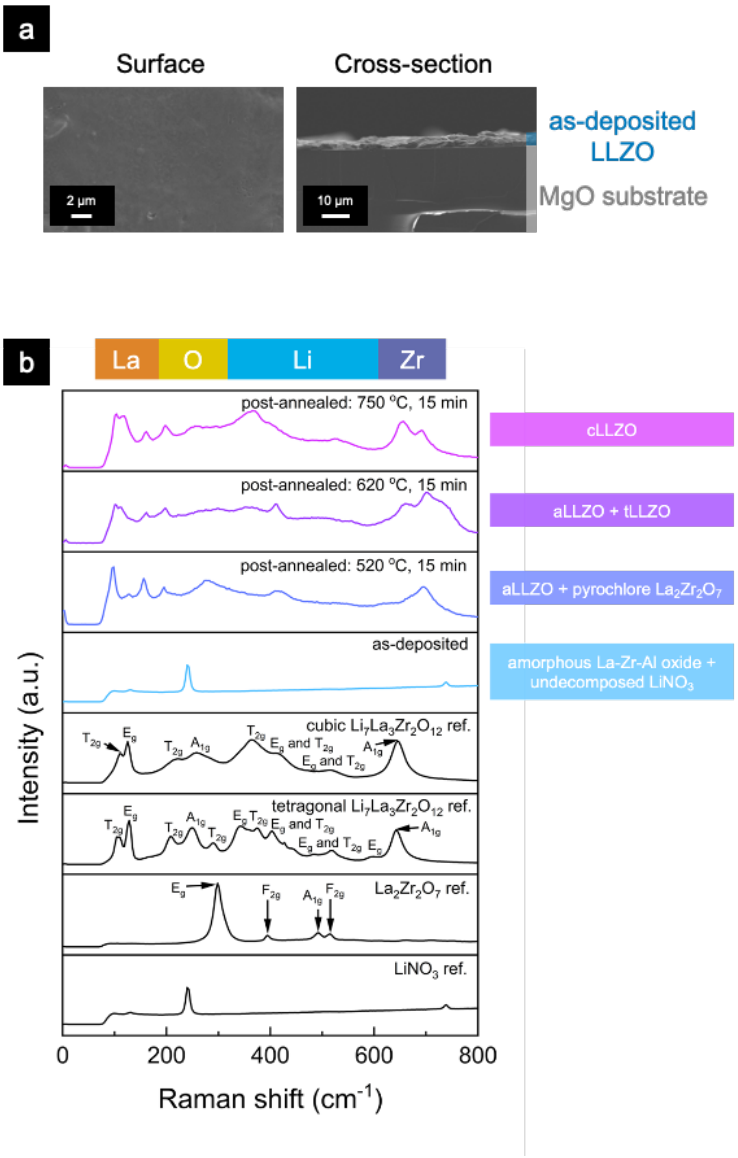

Figure 4-2. (a) Surface and cross-sectional SEM images of a 300 ºC as-deposited LLZO film. The film exhibits full surface coverage with a thickness of 3.0 ± 0.8 µm. **(b)** Raman spectra of the as-deposited LLZO film, and the 520 ºC, 620 ºC, and 750 ºC post-annealed LLZO films. Additional reference spectra of $LiNO_3$, $La_2Zr_2O_7$, tetragonal $Li_7La_3Zr_2O_{12}$, cubic $Li_7La_3Zr_2O_{12}$ are displayed in black.

Figure 4-2 a displays surface and cross-sectional SEM images of the as-deposited Al-doped LLZO film prepared by the SDS method (see Ref. [136] for more details about this low-cost "liquid-to-solid" direct densification method that allows the direct formation of ceramic films without powder

processing). The film exhibits an even and full surface coverage on the MgO substrate with a thickness of 3.0 ± 0.8 μm. Raman spectroscopy provides insights into the LLZO phase evolution and crystallization. **Figure 4-2 b** displays the Raman spectra of the 300 °C as-deposited film and the 520 °C, 620 °C, and 750 °C post-annealed films (isothermal time = 15 min), along with reference spectra of cubic $Li_7La_3Zr_2O_{12}$, tetragonal $Li_7La_3Zr_2O_{12}$, pyrochlore $La_2Zr_2O_7$, and $LiNO_3$, the original Li salt used in SDS processing.

For the *as-deposited film*, we observed a general amorphous nature of the film with bands developed from the undecomposed $LiNO_3$ precursor salt. Specifically, a broad Raman signal was detected for wavenumbers between 300 and 700 cm^{-1} with no appearance of the O–Li–O vibrational band (E_g and T_{2g}) or O–Zr–O stretching band (A_{1g}), suggesting a highly disordered amorphous structure with only short-range order. Outside of the 300–700 cm^{-1} wavenumber range, the two predominant peaks at 240 and 738 cm^{-1} and two minor peaks at 100 and 131 cm^{-1} indicate the presence of undecomposed $LiNO_3$ precursor salt. At 750 °C, we observed a fully crystallized cLLZO film, in agreement with the previously reported crystallization temperature from *in situ* TEM and *in situ* Raman spectroscopy.[138] Specifically, the two intense peaks at 105 and 116 cm^{-1} were identified as the T_{2g} and E_g mode of O–La–O vibration, and the two peaks centered at 655 and 691 cm^{-1} were assigned to the O–Zr–O stretching band (A_{1g} mode).[199,200] The peak divergence of the O–Zr–O stretching band may be defect-related, which causes deviation of the local symmetry and introduces anisotropic strains to the lattice (similar effects have been reported in metal-oxide thin films, including doped CeO_2 films in Ref.[119,265]). Alternatively, the peak divergence may be correlated to the co-existence of more than one LLZO cubic phase, *i.e.,* 220 (*I-43d*) and 230 (*Ia-3d*) space-group cubic phases. These phases have different Li coordination sites and symmetries[174], which may lead to the local structure deviation in ZrO_6 LBU. Other cLLZO phase characteristics include the peak centered at 255 cm^{-1}, corresponding to the oxygen-bending band of T_{2g} and A_{1g},[199] and the peaks centered at 368 and 527 cm^{-1}, assigned to the O–Li–O vibration bands (T_{2g} and E_g/T_{2g} mode) in LiO_6 octahedra.[200]

We next analyzed the local structure evolution between 300 °C and 750 °C based on the Raman spectra displayed in **Figure 4-2 b**. Upon heating to 520 °C, the film was composed of aLLZO with the additional presence of pyrochlore $La_2Zr_2O_7$ nuclei. Specifically, the prominent peaks observed at 96 and 127 cm^{-1} (T_{2g} mode) signify the O–La–O vibration in aLLZO, and the broad peaks at 415 and 697 cm^{-1} can be correlated to the E_g and T_{2g} modes of O–Li–O vibration[200] and the A_{1g}

mode of O–Zr–O stretching in aLLZO,[199,200] respectively. In addition, the peak centered at 279 cm^{-1} is attributed to the E_g mode of ZrO_6 bending in pyrochlore $La_2Zr_2O_7$.[226,227] This result is consistent with the earlier reported *in situ* TEM and *in situ* XRD results in Ref.[136,138], where $La_2Zr_2O_7$ nuclei appear as an intermediate phase during LLZO crystallization. Crystallization progressed with diminishing of the pyrochlore $La_2Zr_2O_7$ local ordering and the ongoing formation of tLLZO local ordering as we further increased the film annealing temperature to 620 °C. The peak at 279 cm^{-1} (E_g mode of ZrO_6 bending from pyrochlore $La_2Zr_2O_7$) disappeared, and three broad peaks emerged at 296, 361, and 410 cm^{-1}, corresponding to the A_{1g} mode of oxygen bending, E_g mode of O–Li–O vibration, and T_{2g} mode of O–Li–O vibration in tLLZO,[200] respectively. These results also agree with earlier reported *in situ* TEM results (see Ref.[138] for more evidence), where tLLZO nuclei emerged through Li diffusion from aLLZO to the prior formed $La_2Zr_2O_7$ nuclei.[138] We also observed minor peaks at 155 and 196 cm^{-1} in all the spectra, attributable to the rotatory and translator motion of CO_3^{2-} from the surface chemistry variation of Li_2CO_3,[232,233] which may be formed from the direct contact of films with moisture in the air during sample transfer and spectrum collection.

We hereby confirm by Raman spectroscopy the formation of cLLZO at 750 °C for a heating rate of 5 °C min^{-1} through multi-step nucleation and phase evolutions from the original aLLZO phase. Specifically, the 1st step involves the formation of pyrochlore $La_2Zr_2O_7$ nuclei in the predominate aLLZO structure, as evidenced by the 520 °C post-annealed aLLZO spectra. Upon further increasing the temperature to 620 °C, the formation of tLLZO through lithiation of $La_2Zr_2O_7$ nuclei was confirmed, which we denoted as the 2nd crystallization step. The 3rd crystallization step starts off at a temperature above 620 °C with the transformation from aLLZO and tLLZO to cLLZO. As suggested by earlier LLZO structure studies, see Ref. [266], this step involves Li local reordering in the occupied sites within the crystalline tLLZO structure, which transforms tLLZO (with regular and fully occupied Li sites) into cLLZO (with disordered Li site occupation). We next employed DSC to further investigate the kinetics of the phase transformation from aLLZO to crystalline cLLZO.

4.2.2. Deconvolution of Crystallization Kinetics from aLLZO to Crystalline cLLZO

DSC measurements were performed at different heating rates (*i.e.,* 5 to 20 °C min^{-1}) to characterize the kinetics and enthalpy changes during the crystallization from aLLZO to cLLZO. This analysis forms the basis for constructing the first TTT diagram to enable precise phase definitions and to guide future LLZO low-temperature processing. Four major peaks were observed for each of the DSC measurements, as displayed in **Figure 4-3**, including an exothermic peak at ~341–450 °C and three endothermic peaks at ~243–277 °C, ~490–663 °C, and ~667–710 °C. The two endothermic DSC peaks at ~490–663 °C and ~667–710 °C in **Figure 4-3** can be correlated to the crystallization of LLZO according to the phase evolution depicted in the Raman spectra in **Figure 4-2 b**, where fully crystallized cLLZO is detected at 750 °C annealing. In addition, our previous study on aLLZO suggested that the crystallization of LLZO occurs between 490 and 720 °C (see TEM and *in situ* Raman analyses in Ref. [138] for more details), corroborating the DSC observation in this work. Prior to the crystallization, the endothermic peak at ~243–277 °C can be assigned to the melting of $LiNO_3$, the Li precursor salt typically used in SDS processing, during which the deposited LLZO sample intakes heat and leads to a solid-to-liquid phase transformation for $LiNO_3$.[267] Furthermore, the exothermic peaks at ~341–450 °C can be related to the decomposition of $LiNO_3$ (see detailed analysis in Fig. 2g of Ref.[136]).

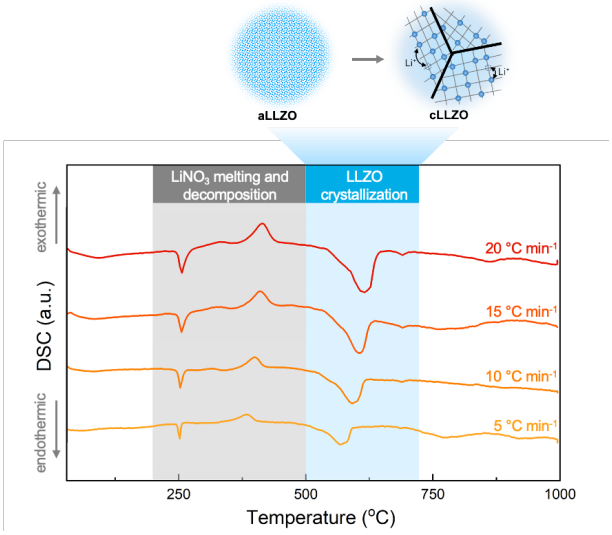

Figure 4-3. Non-isothermal DSC of the LLZO films measured from 25 ºC to 1000 ºC at four different heating rates of 5, 15, 20, and 25 ºC min^{-1}. The two peaks at lower temperatures (shaded in light gray) correspond to melting and decomposition of the $LiNO_3$ precursor. The two later peaks (shaded in light blue) are considered to be the crystallization peaks for LLZO for further analysis. A schematic illustration of the phase transformation from aLLZO to cLLZO is presented.

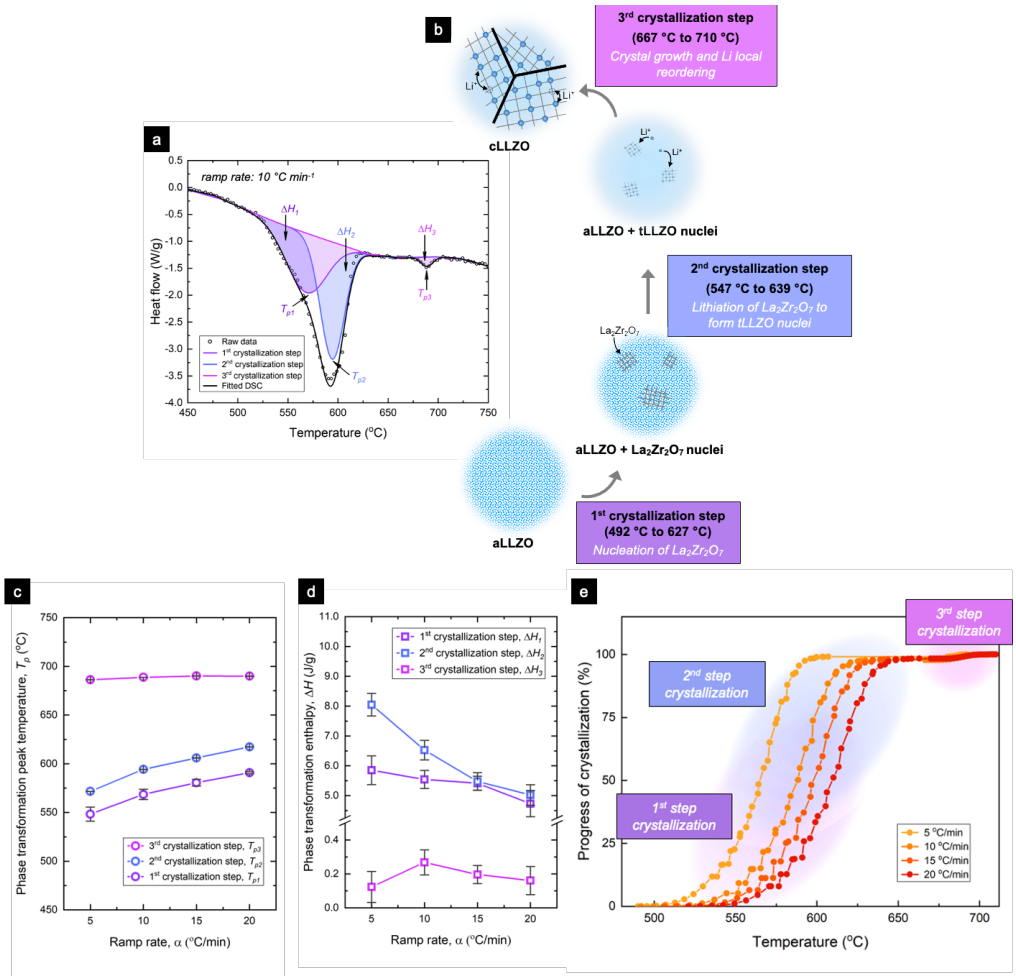

Figure 4-4. (a) Fitting and deconvolution of the LLZO crystallization peaks for the DSC measured at a heating rate of 10 ºC min^{-1}. Two peaks, denoted as the 1st and the 2nd crystallization steps, were deconvolved from the endothermic peak ranges between 492 ºC and 639 ºC. The minor endothermic peak between 667 ºC and 710 ºC was identified as the 3rd crystallization step. The peak temperature and peak area (enthalpy) for each of the three crystallization steps are indicated in the figure as T_{p1}, T_{p2}, and T_{p3}, and ΔH_1, ΔH_2, and ΔH_3, repsectively. (b) Schematic illustration of the 1st, 2nd, and 3rd crystallization steps. The 1st crystallization step corresponds to the nucleation of $La_2Zr_2O_7$ within the aLLZO matrix. The 2nd crystallization step corresponds to the lithiation and phase transformation from $La_2Zr_2O_7$ to tLLZO. The 3rd crystallization step corresponds to the transformation from tLLZO to cLLZO with local Li reordering. **(c)** Phase-transformation peak temperatures (T_p) for the 1st, 2nd, and 3rd crystallization steps as a function of the DSC heating rate. For all three crystallization steps, the peak temperature increases as the heating rate increases. **(d)** Calculated phase-transformation enthalpy changes (ΔH) for the 1st, 2nd, and 3rd crystallization steps as a function of the DSC heating rate. For the 1st and 2nd crystallization steps, the phase-transformation enthalpy decreases as the heating rate increases. No direct correlation between the phase-transformation enthalpy change and the DSC heating rate are observed for the 3rd crystallization step, possibly due to the small energy variation during the Li reordering step that lies within the error bars of the fitted enthalpy. **(e)** Calculated non-isothermal crystallized fraction of LLZO measured at heating rates of 5, 10, 15, and 20 ºC min^{-1}. The temperature and transformation fraction ranges corresponding to the 1st, 2nd, and 3rd crystallization steps are highlighted in violet, lavender blue, and lilac, respectively, corresponding to the events of nucleation of $La_2Zr_2O_7$, lithiation of $La_2Zr_2O_7$ to form tLLZO, and Li local reordering, respectively.

To better understand the kinetics of the observed crystallization peaks (*i.e.,* the peaks at 490–663 °C and 667–710 °C), we next performed peak deconvolution and fitting and obtained phase-transformation peak temperatures (T_p) and phase-transformation enthalpy changes (ΔH). We present a DSC curve measured at a heating rate of 10 °C min^{-1} in **Figure 4-4 a**, where the first and second endothermic peaks sit between 492–639 °C and 667–710 °C, respectively, representing the crystallization of SDS-processed LLZO. The asymmetric shape of the first crystallization peak with a left-skewed tail (evidenced by different slopes) suggested a sequence of two chemical and structural transformation processes and was fitted into two sub-peaks, including the lower-temperature sub-peak fitted in violet at 492–627 °C and the higher-temperature one fitted in lavender blue at 547–639 °C in **Figure 4-4 a**. The lower-temperature sub-peak is associated with the 1st crystallization step of pyrochlore $La_2Zr_2O_7$ nuclei formation illustrated in **Figure 4-4 b,** as evidenced by the analysis of the Raman spectra in **Figure 4-2 b** and the *in situ* TEM results in Ref. [138]. Furthermore, the Raman spectra indicate the emergence of tLLZO when the annealing temperature increases above 620 °C, suggesting that the higher-temperature sub-peak may be related to the 2nd crystallization step of lithiation and transformation from pyrochlore $La_2Zr_2O_7$ to tLLZO nuclei, depicted in **Figure 4-4 b**. Unlike the first DSC peak, the second DSC peak (T_{p2}: 667–710 °C) in **Figure 4-4 a** has a symmetric shape and can be fitted into a single peak centered at 689 °C. The fitted peak overlaps with the temperatures at which the formation of cLLZO was observed in the Raman spectra, see **Figure 4-2 b**, and is therefore assigned as the 3rd crystallization step. We present further details on the DSC peak fittings in **Figure 8-24 a–c**.

Figure 4-4 c and d denote the crystallization peak temperatures, *i.e.,* T_{p1}, T_{p2}, and T_{p3}, and their corresponding crystallization enthalpies, *i.e.,* ΔH_1, ΔH_2, and ΔH_3, with respect to the heating rates for the three fitted crystallization peaks (also see data in **Table 8-8**). By increasing the heating rate from 5 ºC min^{-1} to 20 ºC min^{-1}, T_{p1} and T_{p2} significantly shift from 546 °C to 591 °C and from 571 °C to 617 °C, respectively. The delayed T_p at a higher heating rate is commonly observed in calorimetric studies of ceramics and metals due to the kinetic limit of heat transfer.[268] However, only a small variation in T_{p3} was observed from 686 °C to 690 °C, possibly related to the insensitivity of the Li^+ reordering step toward changes in the heating rate. The crystallization enthalpies, *i.e.,* ΔH_1, ΔH_2, and ΔH_3, varied as the heating rate increased. Upon increasing the heating rate from 5 ºC min^{-1} to 20 ºC min^{-1}, the phase-transformation enthalpies for the 1st and 2nd crystallization steps exhibited monotonic decreasing trends from 5.85 ± 0.48 to 4.73 ± 0.44 J g^{-1}

and from 8.05 ± 0.38 to 5.02 ± 0.34 J g^{-1}, respectively. Conversely, no direct correlation was detected for the 3rd crystallization step between ΔH_3 (ranging between 0.12 and 0.27 J g^{-1}) and the heating rates, which may also be related to the heating-rate insensitivity of the Li^+ reordering step.

We next developed the progress of the crystallization plot in **Figure 4-4 e** based on the three crystallization steps deconvoluted in **Figure 4-4 a.** Different from classical glass-ceramic or metallic glass TTT diagrams, where the cooling curves are recorded for the transformation from the undercooled liquid to the crystalline state, the LLZO films crystallize upon heating to temperatures higher than the SDS deposition temperatures.[261] The progress of phase transformation from aLLZO to biphasic aLLZO + $La_2Zr_2O_7$ nuclei and tLLZO nuclei and finally to fully crystallized cLLZO at different temperatures was calculated by dividing the enthalpy consumed at a specific temperature by the sum of the measured enthalpies of the 1st, 2nd, and 3rd crystallization steps. Specifically, the 1st and 2nd crystallization steps account for over 95% of the enthalpy consumed during transformation from aLLZO to crystallized cLLZO, and the 3rd crystallization step only accounts for <5% of the total crystallization enthalpy. Importantly, we note that the progress of crystallization only indicates the amount of heat consumed at a specific temperature compared to the total enthalpy required to complete the crystallization and should not be directly correlated to the percentage of cubic phase LLZO in the film. We also note that shifts in the crystallization temperature and the progress of crystallization may be detected when compared with the phase evolution detected via *in situ* techniques, such as *in situ* TEM[138], primarily due to the difference in the sample forms used for the measurements (DSC was performed with scratched-off LLZO films *vs.* the ultra-thin as-deposited LLZO films, *i.e.,* less than 100 nm, used for the *in situ* TEM study).

We have now deconvoluted the three crystallization steps from DSC and revealed the progress of the crystallization plot based on crystallization enthalpy analysis. In the next section, we apply this information and construct the first TTT diagram for the transformation from aLLZO to crystalline cLLZO films.

4.2.3. Developing the Time-Temperature-Transformation (TTT) Diagram for LLZO

The TTT diagram provides guidelines on the phase evolution over temperature and time and can be used to perform quantitative analysis on the status of the transformation from aLLZO to crystalline cLLZO. By convention, a TTT diagram plots the temperature along the x-axis and the percentage along the y-axis and contains iso-phase lines that represent 1%, 50%, and 99% of transformation at different annealing times and temperatures.[260–262,269,270] We obtained this information for the transformation of aLLZO to crystalline cLLZO from the progress of the transformation plot displayed in **Figure 4-4 e** and constructed the first TTT diagram for LLZO crystallization in **Figure 4-5**.

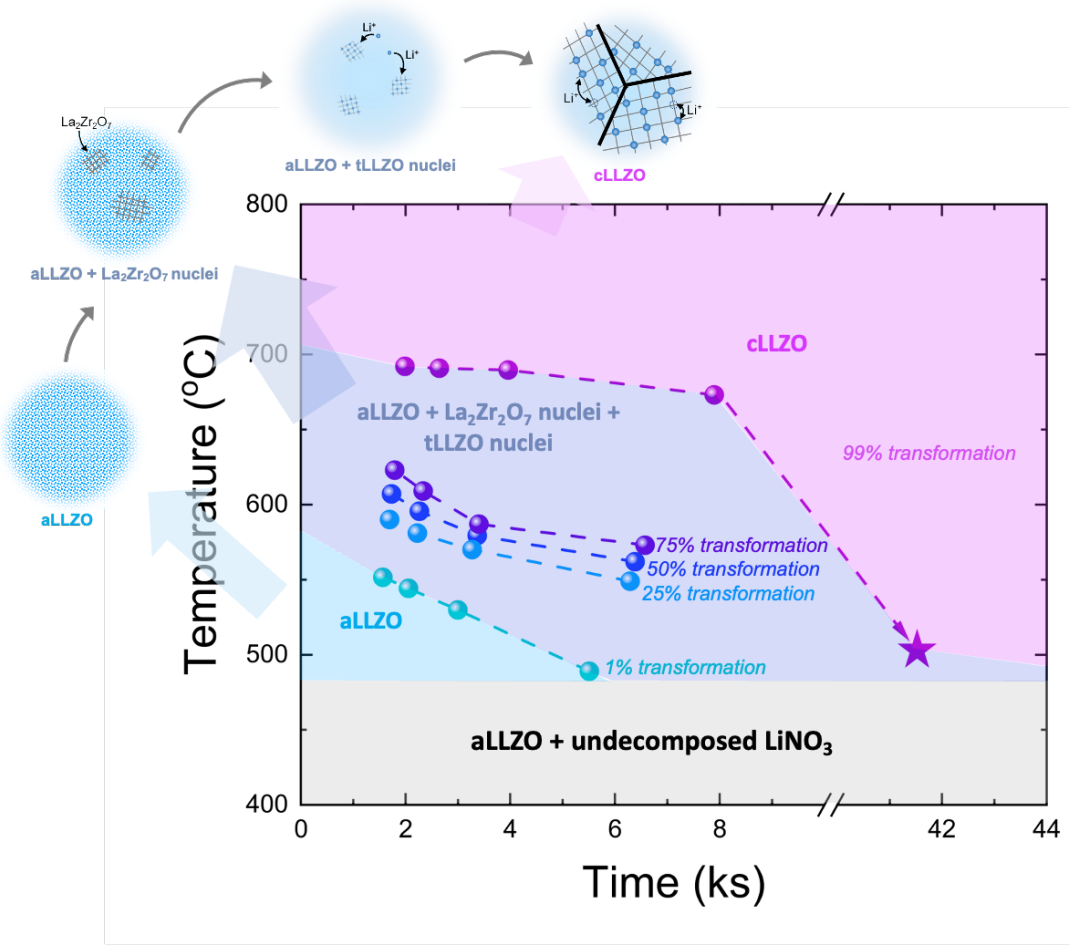

Figure 4-5. TTT diagram for LLZO from amorphous to crystalline cubic phase. The 1%, 25%, 50%, 75%, and 99% iso-phase lines are presented. Specifically, the 1%, 50%, and 99% iso-phase lines are indicated as the beginning, mid-point, and final stage of the phase transformation from amorphous to crystalline cLLZO. The annealing condition of 500 ºC, 10 h is highlighted. Schematic illustrations of the phase compositions at each crystallization stages are provided.

Specifically, we divide the TTT diagram in two sections: below 480 ºC, the film remains amorphous with undecomposed $LiNO_3$ salt precursor (Ref.[136,138] indicates that $LiNO_3$ decomposes at 400–480 ºC), and above 480 ºC, the film undergoes a three-step phase transformation, as detailed in an earlier section, see **Figure 4-4 b**, from aLLZO to fully crystallized cLLZO. The percentage of transformation data points presented in **Figure 4-5** correspond to specific temperatures and times (calculated based on the heating rates) required to achieve 1%, 25%, 50%, 75%, and 99% of the transformation from aLLZO to cLLZO. The 1%, 50%, and 99% iso-phase lines represent the beginning, mid-point, and final stage of the transformation, respectively. Specifically, for temperatures above 480 ºC and below the 1% iso-phase line, the film is in an amorphous state, *i.e.,* aLLZO, highlighted in light blue. Between the 1% and 99% iso-phase lines, the region in lavender blue represents phase compositions of aLLZO + $La_2Zr_2O_7$ nuclei + tLLZO nuclei, indicating ongoing phase transformations through the 1st and 2nd crystallization steps, see schematic illustration in **Figure 4-5**. Finally, we highlight in violet the annealing temperature and time needed to achieve fully crystallized cLLZO for temperatures and times above the 99% transformation iso-phase line. Importantly, we note that the percentage of transformation in the TTT diagram only indicates the ratio of enthalpy consumed at a specific temperature and time to the total enthalpy required to complete the crystallization. This should not be interpreted as the percentage of film that has been transformed into crystalline LLZO phases, as the transformation from aLLZO to cLLZO involves three unique steps, as illustrated in **Figure 4-4 b**, and requires different enthalpies to complete each step. With extended annealing time, the TTT diagram exhibits a downward trend of annealing temperatures to achieve the same state of phase transformation from aLLZO to crystalline cLLZO. The observed trend suggests that lowering the annealing temperature with extended annealing time may be a route to crystallize LLZO in its cubic phase, as highlighted in **Figure 4-5**.

In the next section, we discuss alternative low-temperature processing routes to stabilize cLLZO, as inspired by the TTT diagram, and track their phase and local structure variation via Raman spectroscopy.

4.2.4. Achieving Cubic-Phase LLZO Films at Reduced Temperatures Based on the TTT Diagram Phase Evolution Roadmap

In the previous section, we demonstrated the successful synthesis of cLLZO at 750 ºC for 15-min isothermal annealing (denoted as route I) and constructed the TTT diagram for the transformation of aLLZO into crystalline cLLZO. Based on the as-developed TTT diagram, we proposed three alternative post-annealing routes to synthesize cLLZO at lower temperatures and extended isothermal annealing times (**Figure 4-6 a**). Specifically, these newly defined routes include annealing at 650 ºC for 5 h (route II), 525 ºC for 10 h (route III), and 500 ºC for 10 h (route IV) at an initial heating rate of 5 ºC min^{-1}.

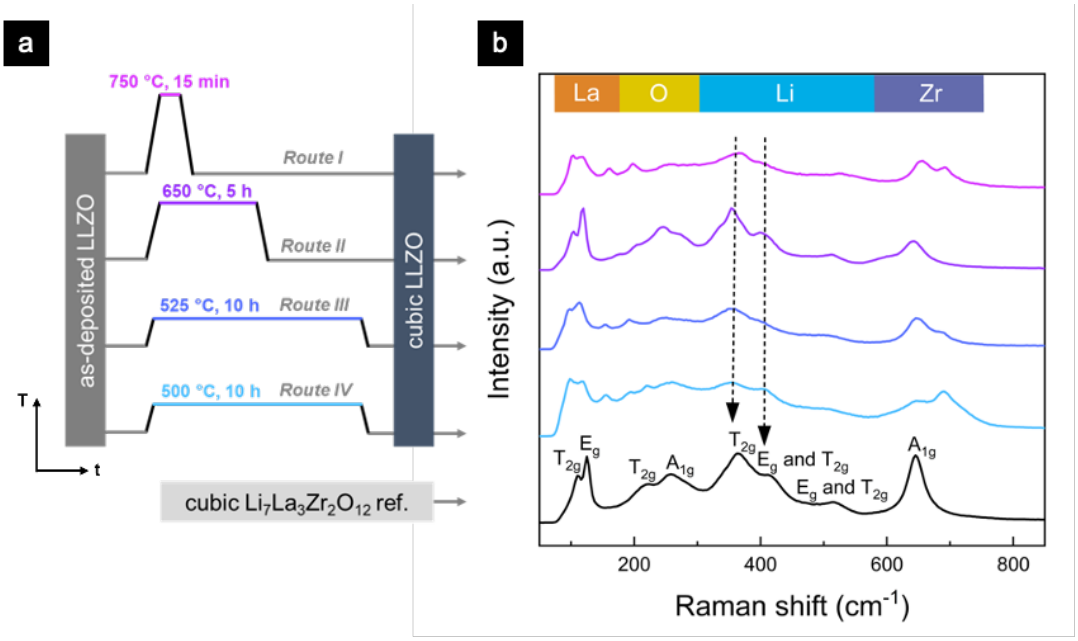

Figure 4-6. (a) Illustration of the four post-annealing routes (isothermal annealing temperature + isothermal holding time) applied to synthesize cLLZO, including route I of 750 ºC for 15 min, route II of 650 ºC for 5 h, route III of 525 ºC for 10 h, and route IV of 500 ºC for 10 h. All four post-annealing routes were performed at a heating rate of 5 ºC min^{-1} for both heating and cooling. **(b)** Raman spectra of the four LLZO films synthesized via post-annealing routes I–IV. Additional reference spectra of cubic $Li_7La_3Zr_2O_{12}$ are displayed in black. All four LLZO films reveal a cubic structure with peak shifts observed for the O–Li–O vibration (352–412 cm^{-1}), suggesting variations in structure compaction and local strain among the four cLLZO films.

Raman spectroscopy was performed to identify the phase composition and local structure vibration for the LLZO films obtained from the three alternative post-annealing routes, *i.e.,* route II–IV. The three Raman spectra were also compared with the spectrum of cLLZO synthesized via route I, *i.e.,*

750 ºC for 15-min isothermal annealing, as displayed in **Figure 4-6 b**. Overall, the spectra of the four LLZO films all reveal cubic-phase structures but with noticeable shifts of the O–Li–O vibration bands and peak divergence of the O–Zr–O stretching band.

We first summarize the Raman peaks observed in the four LLZO spectra. The two intense peaks at 94 and 113 cm^{-1} were identified as the T_{2g} and E_g modes of O–La–O vibration, and the peaks centered at 220 and 265 cm^{-1} were assigned to the oxygen-bending band of T_{2g} and A_{1g}, respectively.[199] The pronounced peaks centered at 360 and 404 cm^{-1} and the minor peak centered at 514 cm^{-1} were attributed to the O–Li–O vibration bands (E_g and T_{2g}) in LiO_6 octahedra,[200] and the two peaks at 651 and 686 cm^{-1} correspond to the O–Zr–O stretching band (A_{1g} mode). In addition to the major Raman peaks in the four spectra corresponding to cubic phase LLZO, we also observed minor peaks at 160 and 198 cm^{-1} in all the spectra, attributable to the rotatory and translator motion of CO_3^{2-} from the surface chemistry variation of Li_2CO_3.[232,233]

We next performed detailed analysis on the O–Li–O and O–Zr–O bands, as Li and Zr are the two network formers that define the local structure and transformation from aLLZO to crystalline cLLZO. Additionally, the Li–O bond distance can affect the activation energy needed for Li to hop from one site to another, which is a critical property in determining its use in SSBs. To understand how different annealing routes affect the local structures and bonding around Li, we fitted the two major O–Li–O vibrational bands (E_g and T_{2g}) and reported their fitted positions in **Figure 8-25**. Upon lowering the annealing temperature from 750 ºC to 650 ºC (and therefore prolonging the annealing time), the E_g and T_{2g} peaks first exhibited redshifts from 368 to 354 cm^{-1} and from 407 to 401 cm^{-1}, respectively. Further lowering the annealing temperature to 500 ºC led to a blueshift of the E_g and T_{2g} peak to 410 cm^{-1} with no change of the T_{2g} peak position near 354 cm^{-1}. In general, a redshift of the Raman peaks suggests longer bond distances (and vice versa for a blueshift). The observed trend indicates a longer Li–O bond in LiO_6 octahedra when annealed at 650 ºC for 5 h as compared to those annealed at 500 ºC, 525 ºC, and 750 ºC. In general, a longer Li–O bond suggests a lower bond strength and therefore reduced energy required for Li^+ to migrate to its neighboring sites, which is preferred for application as a solid electrolyte or protective coating layer in batteries.[271–273]

We also observed peak divergence of the O–Zr–O stretching band (A_{1g} mode) with two peaks emerging at various ratios at 651 and 686 cm^{-1} for films annealed at different temperatures and

times.[199,200] The appearance of the two peaks may be defect-related or may be correlated to the co-existence of two LLZO cubic phases (*i.e.,* 220 and 230 space-group cLLZO), introducing anisotropic strains to the lattice (as detailed in the earlier Raman section).[119,265]

In summary, all four annealing routes with isothermal temperatures ranging between 500 and 750 ºC resulted in successful synthesis of cLLZO films. We observed two interesting phenomena from the collected Raman spectra, including*: i.* significant O–Li–O vibrational bands shifts and *ii.* O–Zr–O stretching band divergence for LLZO films crystallized at different temperatures. Similar O–Li–O vibrational band shifts have been reported in previous studies on PLD-processed aLLZO and cLLZO films, with the shifts attributed to variations in the Li^+ concentration (lithiation) and the small LLZO nanocrystallite sizes.[111,120] Indeed, these may also be the reasons leading to the O–Li–O vibrational band shifts in the current study, as different isothermal times can result in different nucleation rates, affecting the size of the LLZO nanocrystallite and local strains. Furthermore, variation in the annealing time and temperature may also lead to different amounts of Li losses (that is, different Li concentrations remain in the LLZO films), therefore affecting the ratio of the 220 and 230 space-group cubic grains and generating anisotropic local strains in polycrystalline cLLZO films. Further investigation using experimental and computational methods (*e.g.,* DFT and high-energy X-ray spectroscopies) is needed to understand the origin of the A_{1g} peak divergence of the O–Zr–O stretching band and to clarify the role of the annealing temperature and time on the grain distribution and cubic-phase compositions (*i.e.,* 220 vs. 230 space groups), as they may have substantial implications on the Li^+ dynamics for SSB applications.[174,175]

4.3. Advantages of Low-Temperature Annealed LLZO Films

We compared, from cost and battery integration perspectives, the processing temperatures and times required to achieve cLLZO, as proposed in this study, *i.e.,* route I–IV, to those reported in the literature for bulk-type pellets/tapes and thin-film LLZO in **Figure 4-7**. Here, we only note the maximum annealing/sintering temperatures and the corresponding isothermal time, as these factors play a key role in determining the stability at LLZO–cathode interfaces during co-processing and defining the thermal budget and associated processing costs. Importantly, we highlight the newly proposed processing routes with annealing temperatures of 500 ºC and 525 ºC, representing the lowest annealing temperatures reported to crystallize LLZO films. These

temperatures are particularly attractive for reducing interfacial degradation during LLZO–cathode co-processing.

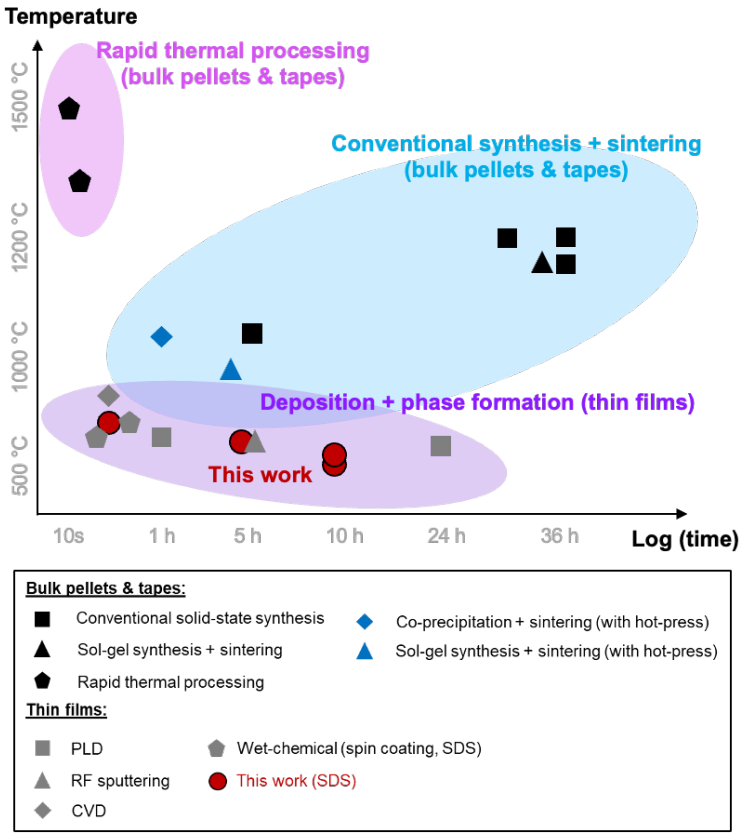

Figure 4-7. Comparison of the maximum processing temperature and processing time of bulk[105,129,168,169,252–256] (pellets and tapes) and thin-film[98,100,113,116,120,136] LLZO via different synthesis routes.

Specifically, we outline in **Figure 4-7** the three major routes to process cLLZO, namely, conventional synthesis + sintering for bulk pellets and tapes (highlighted in light blue), rapid thermal processing for bulk pellets and tapes (highlighted in lilac), and deposition + phase formation for thin films (highlighted in violet) and provide a brief discussion on their maximum sintering or annealing temperature and time as follows. The bulk pellet and tapes processed via conventional synthesis + sintering generally require a high-temperature sintering process at 1050–1230 ºC for 1–36 h (generally >5 h) to eliminate pores and achieve complete densification.[105,129,168,252] There are a few variations of the conventional synthesis + sintering routes for which the LLZO powder (starting material for LLZO pellet sintering) may be synthesized via different routes, including sol-gel synthesis + sintering[255,256] and co-precipitation + sintering[169];

hot pressing may also be used to facilitate densification during the process.[169,256] However, this method is not cost-effective for LLZO–cathode co-processing because of the high sintering temperature and long sintering time. Alternatively, we consider rapid thermal processing as a more cost-effective route for sintering bulk pellets and tapes, which generally requires a sintering temperature of >1300 ºC for 10–15 s.[253,254] However, the thicknesses that can be achieved via bulk pellet/tape sintering (*i.e.,* <25 μm) are not of particular interest toward battery integration as they will unavoidably increase the internal resistance and lower the energy density of the cell.

To further enhance the energy density, thin-film LLZO with a thickness <10 μm is preferred.[39] Thin-film LLZO can be deposited using vacuum-based or wet-chemical methods and then annealed at a much lower temperature to transform the film from the amorphous to crystalline cubic phase without the need for sintering to achieve densification. The annealing temperature for thin-film LLZO typically ranges between 600 and 950 ºC with an isothermal time of 15 min to 24 h.[98,100,113,114,116,120,136] More excitingly, our newly designed annealing method enables the synthesis of cLLZO films using a direct liquid-to-solid method at temperatures as low as 500 ºC (for 10-h isothermal annealing), which is a significantly lower temperature than that used in previously reported methods. Admittedly, there is still room to further shorten the isothermal time for the 500 ºC annealing route to promote its direct integration with the state-of-the-art roll-to-roll processes for battery cells. Future work is recommended to focus on exploring the crystallization kinetics for LLZO with various dopants and optimized Li^+ concentrations to further reduce the processing time needed to crystallize cLLZO.

In summary, solid-state electrolyte films are essential components in future high-energy SSBs to enable direct pairing with a Li-metal anode and high-voltage cathodes. The newly developed low-temperature annealing routes for cLLZO synthesis shed light on LLZO–cathode co-processing strategies without the need for sintering, providing room to further boost the energy and power densities of the cell at a reduced cost.

4.4. Conclusion

Novel lower-energy- and cost-intensive functional ceramic synthesis routes are essential to define socio-economically tolerable solid Li^+-conductive electrolytes for all-solid-state and hybrid

batteries. The Li-garnet-type solid-state Li-metal batteries offer a promising option for achieving these goals owing to its high room-temperature Li^+ conductivity up to 10^{-4} S cm^{-1} and wide electrochemical stability window (*i.e.,* 0–6 V) that enables stable pairing with Li metal and high-voltage cathodes. Despite the promise, the scale-up fabrication for these functional Li-containing ceramics has been hindered by their limited chemical stability toward co-processing and integration with Co-reduced cathodes, such as NMC and NCA, at a temperature above 600 °C. The high processing costs associated with ceramic powder processing and high-temperature sintering is another obstacle limiting their scale-up, especially during energy price spikes, as experienced in 2022. Therefore, there is a need for the SSB and glass-ceramic industries to redefine the ceramic processing routes, such as for cLLZO solid electrolytes, toward lower temperatures with a possible reduction of sintering steps.

In this work, we provide evidence and alternative routes to synthesize cLLZO films via SDS, a "liquid-to-solid" direct densification method, to aid the integration of LLZO electrolyte separators in SSBs at approximately half of the classic sintering temperatures typically used to densify cLLZO pellets and tapes. We developed the first TTT diagram for the glass-ceramic LLZO based on crystallization enthalpy analysis as well as local structure and phase evolution studies. This is an important step, as we demonstrated in prior work, see Refs. [136,138], that LLZO can be synthesized and fully densified through an amorphous-to-crystalline cubic multi-step phase transformation at 750 ºC. Nevertheless, the optimal heating rate and minimum crystallization temperature to reach the fast-conducting cubic phase remain unclear. The TTT diagram established for the Li^+ solid-electrolyte cLLZO provides insights on optimizing the synthesis conditions to achieve the lowest crystallization temperature ever reported to stabilize cLLZO as a dense solid film at 500 ºC with 10-h isothermal annealing, as proven through Raman spectroscopy in this work. Looking ahead, we see a bright future for the use of liquid-to-solid densifications such as SDS synthesis in a combination of TTT diagrams to define new processing routes for the functional Li-garnet ceramic, cLLZO, and to design strategies to optimize not only the costs and sustainability for battery production but also the chemical stability and processing compatibility with Co-reduced high-voltage cathodes, such as NMC or NCA, to achieve long-life and high-energy batteries.

4.5. Experimental

4.5.1. Preparation of Al-LLZO Films by SDS

The precursor solution for SDS was prepared in $Li_{6.25}Al_{0.25}La_3Zr_2O_{12}$ (Al-LLZO) stoichiometric ratio with 75% extra Li by dissolving $LiNO_3$, $Al(NO_3)_3 \cdot 9H_2O$, $La(NO_3)_3 \cdot 6H_2O$, zirconium(IV) acetylacetonate into solvent mixed by methanol:1-methoxy-2-propanol:bis(2-ethylhexyl) phthalate (1:1:1 vol.%) with a Al-LLZO concentration of 0.015 M. The as-prepared SDS solution was stirred overnight for 12 h before deposition. $LiNO_3$ (≥ 99%), zirconium(IV) acetylacetonate (97%), and 1-methoxy-2-propanol (≥99.5%) were purchased from Sigma-Aldrich; $Al(NO_3)_3 \cdot 9H_2O$, $La(NO_3)_3 \cdot 6H_2O$ (99.99%), and bis(2-ethylhexyl) phthalate were purchased from Alfa Aesar; methanol was purchased from VWR. Single-side polished MgO (001) substrates (10 × 10 × 0.5 mm), purchased from MTI Corporation, were used as the substrate for SDS deposition.

Four MgO substrates were placed on a heated stainless-steel hot plate at 300 ºC with the polished side facing up. A K-type thermocouple placed aside of the MgO substrate was used to monitor the deposition temperature. To deposit a film, the SDS solution was pumped through a polypropylene syringe at a rate of 10mL h^{-1} into a spray atomizer (DeVILBLISS, AG361). Compressed gas with a pressure of 0.3 bar at the atomizer was selected as the carrier gas, and the distance between the atomizer and the MgO substrate was kept at 25 cm. The as-deposited Al-LLZO films were obtained after a 30-min deposition.

4.5.2. Microstructure Characterization of the SDS-Processed Al-LLZO Films

Surface and cross-sectional SEM images of the as-deposited Al-LLZO films were collected with a Zeiss Ultra Plus field-emission scanning electron microscope using an accelerating voltage of 3.0–5.0 kV and a working distance of 3–8 mm. An in-lens SE detector was used for all the SEM images presented in this paper. To prepare the cross-sectional sample, a diamond blade was used to cut the sample into two pieces directly before the imaging to prevent surface contamination. During imaging, conductive carbon tape was used to tape the side of the samples to provide electronic conduction and improve the image quality.

4.5.3. Thermoanalytical Characterization and Crystallization Kinetics Analysis

DSC was applied as a thermoanalytical tool to study the thermal properties and the crystallization kinetics of the Al-LLZO films prepared by SDS. The samples for the DSC experiments were collected in powder form by scratching off the as-deposited Al-LLZO films from the MgO substrates. MgO crucibles (Ozark Technical Ceramics) were used for the DSC experiments to avoid high-temperature reaction and diffusion between Al-LLZO and the ceramic crucibles. The experiments were performed using a Mettler Toledo Thermal Analysis System TGA/DSC 3+ under a constant flow of synthetic air. Before each DSC measurement, the weight of the collected Al-LLZO powder was recorded and used to normalize the DSC data. Four measurements were performed from 50 ºC to 1000 ºC with heating rates of 5, 10, 15, and 20 ºC min^{-1}. A constant flow of Ar (Airgas) was used as a protective gas during all the measurements. The collected DSC curves were rectified by the background curve measured with empty MgO crucibles ahead of each experiment. The obtained DSC curves were fitted and deconvoluted to peaks corresponding to different crystallization steps. For each DSC curve, the peak temperature (T_p) and the enthalpy change (ΔH) for each of the three crystallization steps were calculated.

4.5.4. Phase Evolution Characterization

The phase structure of the as-deposited and 520 ºC, 620 ºC, and 750 ºC post-annealed (with a heating rate of 5 ºC min^{-1} and an isothermal holding at the annealing temperature for 15 min) Al-LLZO films was characterized by Raman spectroscopy (WITec alpha 300 M+). A laser wavelength of 532 nm with a power of 10 mW, a grating of 300 g mm^{-1}, and a spectral resolution of 0.1 cm^{-1} were applied to obtain all the Raman data. A 50× long-distance objective (Zeiss, Germany) with a numerical aperture (NA) of 0.7 was used for the laser focusing, giving an approximate laser spot size of 1 μm.

Raman spectroscopy was also used to analyze the phase structure of the Al-LLZO films after post-annealing routes suggested by the TTT diagram. The four Al-LLZO films were annealed at 500 ºC for 10 h, 525 ºC for 10 h, 650 ºC for 5 h, and 750 ºC for 15 min, respectively. The same laser and objective length conditions described above were used for characterizing these four Al-LLZO films.

5. Chapter 5: Lithium Flim Ceramics for Solid-State Lithionic Devices

Adapted from Yuntong Zhu, Juan Carlos Gonzalez-Rosillo, Moran Balaish, Zachary D. Hood, Kun Joong Kim, Jennifer L.M. Rupp. Lithium Film Ceramics for Solid-state Lithionic Devices. *Nature Reviews Materials* 6.4 (**2021**): 313-331.

Abstract

The search for alternatives to traditional Li^+ batteries has sparked interest in the chemistry and manufacturing of solid-state Li^+ conductors. Li^+ conductors are traditionally processed as millimetre-sized pellets using conventional ceramic processing routes. However, in thin-film form, Li^+ conductors offer applications beyond energy storage, such as smart sensing. In this chapter, we present the state-of-the-art progress and discuss challenges and opportunities for the integration of Li-oxide films in microbatteries for energy storage and sensors for toxins and greenhouse gases. Li oxides in thin-film form provide fast Li^+ movement, which increases cycle speed and endurance of Li-conductor-based devices. We provide a future vision of lithionic devices integrating Li-based ceramics for the design of microdevices beyond batteries.

5.1. Solid-State Thin-Film Batteries

The increasing complexity of portable electronics and personal tracking devices has led to a growing demand for energy storage solutions with improved gravimetric and volumetric energy density.[274–276] Current technologies mainly rely on Li^+ batteries with liquid organic electrolytes, limiting the volumetric energy density of the battery. From an industry perspective, the targeted energy density of next-generation batteries is >500 Wh kg^{-1},[277] which is significantly higher than that of state-of-the-art automotive Li^+ batteries (~210 Wh kg^{-1}),[278] with a target power output density of 2000–4000 W L^{-1} and a pack cost below 125 US$ kW h^{-1}.[277] The replacement of liquid organics with solid-state electrolytes is expected to not only reduce the volume and weight of batteries, but to also enable the use of high-capacity anodes (for example, Li metal) and high-voltage cathodes (for example, $LiNi_{0.5}Mn_{1.5}O_4$ or $LiNi_{1/3}Co_{1/3}Mn_{1/3}O_2$).[126,279,280] Furthermore, solid-state electrolyte films can be used as barriers for Li filament formation. To meet these energy and cost targets, and to compete with liquid organic electrolytes, mass-manufacturable ceramic processing techniques need to be developed that are suitable for thin films.

5.1.1. Thin-Film Battery Architectures

The fabrication of Li oxide solid-state electrolytes by ceramic thin-film processing technologies gave rise to thin-film microbatteries, which are a promising solution for on-chip integrated energy storage with 3D stacking potential and improved safety compared to liquid-electrolyte-based battery packs.[281,282] Solid-state microbatteries consist of two current collectors and an electrolyte sandwiched between two active electrodes (**Figure 5-1 a**). Compared to classic Li^+ batteries, the main difference is that microbatteries use a solid-state ceramic Li^+ conductor instead of an organic liquid and a porous polymer separator. The rate performance of planar microbatteries is generally lower than that of state-of-the-art Li^+ batteries. However, 3D microbatteries with a large interfacial contact area can address this limitation, because they show better charge-transfer efficiency and higher energy and power density owing to higher volumetric mass loading of the active electrode materials.[282,283]

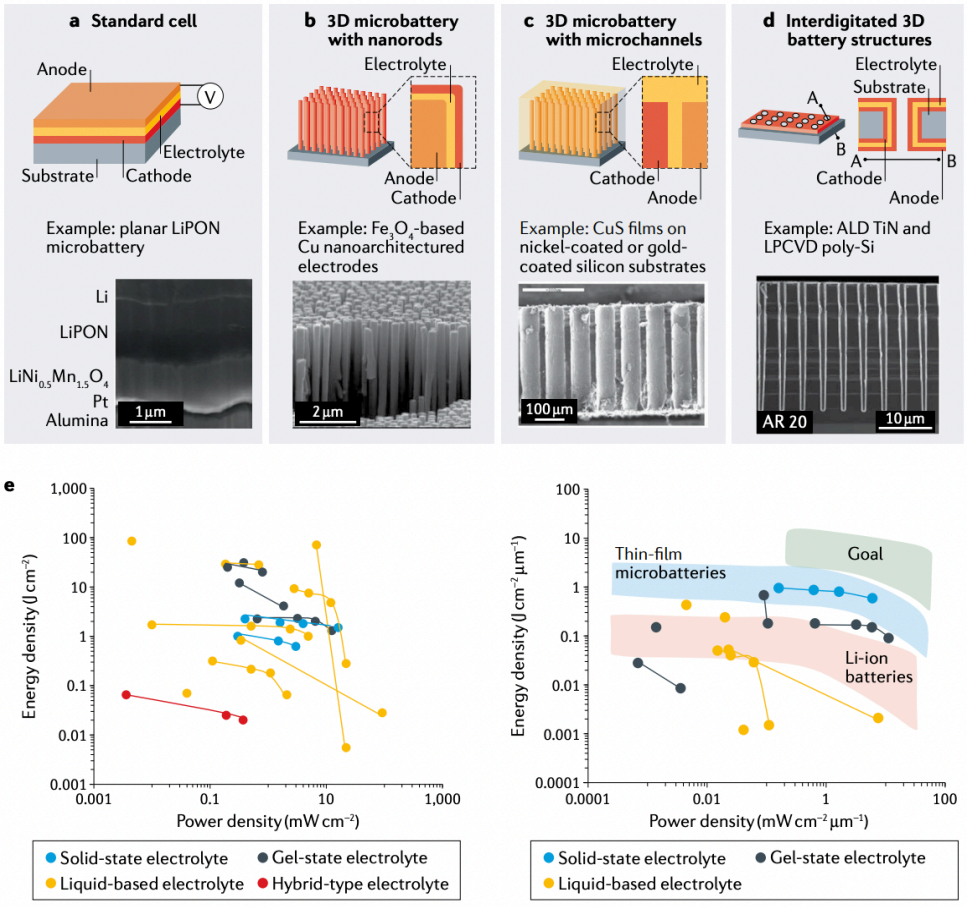

Figure 5-1. Thin-film solid-state battery designs. **(a)** Standard design of a thin-film solid-state microbattery.[48] **(b)** 3D microbattery based on nanorods.[284] **(c)** 3D microbattery based on microchannels.[285] **(d)** Interdigitated 3D battery.[286] **(e)** Energy density versus power density for various state-of-the-art battery systems[126,287–300] Panel **(a)** reprinted from Ref.[48]. Panel **(b)** reprinted from Ref.[284]. Panel **(c)** reprinted from Ref.[285]. Panel **(d)** adapted from Ref.[286].

3D microbattery architectures can be fabricated by additive manufacturing using templates to directly grow shapes, such as pillars or rods, for one of the electrodes, followed by film deposition to add the electrolyte and second electrode. Alternatively, subtractive manufacturing can be applied; for example, etching of channels in the substrate using shadow masking or photolithography, followed by filling of the channels with the microbattery materials. Various 3D microbattery architectures have been fabricated, including 3D microbatteries with nanorods, 3D microbatteries with microchannels and interdigitated 3D battery structures (**Figure 5-1 b-d**). Compared to planar batteries, the volumetric loading of the active anode and/or cathode is higher in 3D architectures, leading to improved cycling performance.

3D Microbatteries with Nanorods

Cu-nanorod current collectors grown by electrolysis can serve as template for the deposition of conversion-type Fe_3O_4 (**Figure 5-1 b**).[284,287,301] The main advantages of this approach are the simple fabrication of 3D electrodes and that the size of the nanorods can be tuned by using template membrane or substrates. However, template-assisted deposition produces substrates with open structures, which can affect the subsequent deposition of the battery layers.

3D Microbatteries with Microchannels

3D architectures of thin CuS films on gold- or nickel-coated silicon substrates can be fabricated by forming microchannels using electrodeposition (**Figure 5-1 c**).[285] Electrodeposition allows the control of the amount of deposited material, the formation of conformal layers onto 3D porous structures and scalable depositions on large areas.

Interdigitated 3D Structures

Interdigitated 3D battery structures rely on the formation of 3D trenches (**Figure 5-1 d**). The trenches are etched into polycrystalline Si, followed by low-pressure chemical vapour deposition of TiN, which serves as current collector and Li-barrier layer. Compared to planar battery geometries, the capacity of microbatteries with trench structures is at least 5 times higher.[286,302] The main advantage of 3D trenches is the good processing compatibility with Si-based CMOS manufacturing.

These 3D architectures permit solid-state diffusion of Li into the electrodes, which improves the kinetics during charging and discharging of microbatteries. Furthermore, macroscopic film techniques, such as bio-templating[303,304] and 3D printing,[305,306] could be used in combination with thin-film deposition techniques (vacuum-based or solution-based) to improve the electrochemical performance of thin-film batteries with a better control of the charge-transfer kinetics at higher charge and discharge rates. However, 3D printing is typically not used for thin films because it requires post-sintering. In addition, details of the structure–performance relationships of 3D microbatteries remain elusive thus far.

5.1.2. Thin-Film Battery Materials

A variety of materials and electrode−electrolyte combinations are theoretically suitable for microbatteries; however only two solid-state electrolytes have been used for the design of microbatteries thus far (**Table 5-1**).[48,126,127] For example, LiPON-based microbatteries show impressive cyclability of up to 10,000 cycles at a rate of C/10 with a Li metal anode, a $LiNi_{0.5}Mn_{1.5}O_4$ cathode and a LiPON electrolyte film (thickness of 1–2 μm).[48] In this microbattery, a planar cell is deposited on an alumina substrate, and the cathode and electrolyte films are fabricated by radio frequency magnetron sputtering.[48] The good rate performance demonstrates the potential of LiPON as a solid-state electrolyte, which has already been commercialized.

Table 5-1. Li-oxide-based all-solid-state thin-film batteries.[48,126,127]

Material			Deposition method			Capacity ($mAh\,g^{-1}$)	Cycling number
Electrolyte	Cathode	Anode	Electrolyte	Cathode	Anode		
LiPON	$LiCoO_2$	Li metal	RF sputtering	RF sputtering	Thermal evaporation	137	4,000
	$LiNi_{0.5}Mn_{1.5}O_4$	Li metal	RF sputtering	RF sputtering	Thermal evaporation	122	10,000
Perovskite (amorphous LLTO)	$LiNi_{0.5}Mn_{1.5}O_4$	$LiNi_{0.5}Mn_{1.5}O_4$	PLD	PLD	PLD	–	50

LiPON, lithium phosphorus oxynitride; LLTO, $Li_{3x}La_{2/3-x/3}TiO_3$; PLD, pulsed laser deposition; RF, radio frequency.

Microbatteries based on perovskite-structured LLTO solid electrolytes have not yet reached the maturity of LiPON-based microbatteries (**Table 5-1**). For example, aLLTO films can be deposited by PLD onto $LiNi_{0.5}Mn_{1.5}O_4$ to form a half cell, which maintains 98% capacity retention for 50 cycles up to 4.8 V.[127] Only very recently, the first aLLZO-based microbattery was demonstrated with aLLZO acting as a solid electrolyte separator layer and cycled at 10 C for over 500 cycles.[183] Nevertheless, to the best of our knowledge, thin-film microbatteries with NASICON-based electrolytes have not yet been developed, possibly owing to the fact that the high conductivity of these materials in film form has only recently been reported.

The interplay between high current density (> 1 mA cm^{-2}) and safety is an important consideration for microbatteries. Cycling at high current densities would enable faster charge and discharge,

facilitating new applications of microbatteries in lithionic devices, for example, three-terminal memristive devices. However, nucleation and growth of Li dendrites can occur in solid electrolytes, including in poly- and single-crystal garnet-type LLZO and amorphous sulfide.[140] Grain boundaries are susceptible to Li dendrites and facilitate their intergranular propagation through the solid electrolyte (demonstrated in bulky pellet tests) at low current densities.[173,307] By contrast, in amorphous LiPON, Li deposition is confined to an artificial LiPON–LiPON interface (prepared by radio frequency magnetron sputtering), which is located parallel to a $LiCoO_2$ cathode.[308] The confinement of Li dendrites to the LiPON–LiPON interface suggests that the homogeneous, grain-boundary-free morphology of amorphous LiPON is crucial for the blocking of Li dendrite growth, even at high current density (that is, 10 mA cm^{-2}).[126,309] Other amorphous Li-oxide films, for example aLLTO,[82,90] could also be integrated into microbatteries, which will require a thorough investigation of the electrode−electrolyte interface to establish the electro-chemo-mechanics and to develop microbatteries with high volumetric energy density. To overcome dendrite growth in microbatteries, grain-boundary chemistry and interparticle structures could be modified to improve the mechanical strength, toughness and elastic modulus of the solid-state electrolyte. In addition, the strains at the interfaces in microbatteries, which can be induced by lattice mismatch or by the substrate, need to be analysed in detail. Finally, fully amorphous and defect-free Li oxide electrolytes with high Li^+ conductivities could be developed to minimize non-uniform current densities and to prevent dendrite propagation; the bandgap, surface chemistry and transference number of the electrolyte need to be considered to engineer barriers for Li dendrites.

5.1.3. Power and Energy Density

Cyclability of up to 10,000 cycles has been demonstrated for state-of-the-art microbatteries with a Li-metal anode; however, cyclability at high current densities (>1 mA cm^{-2}) needs to be achieved to enable their application in lithionic devices. The energy and power densities of microbatteries can vary by nearly 5 orders or magnitude per unit area (**Figure 5-1 e**). The highest power density (30 mW·cm^{-2}) has been reported for LiPON-based microbatteries.[309] Therefore, a common research goal is to increase the power and energy densities of Li-metal batteries to > 1 mW cm^{-2} μm^{-1} and > 1 J cm^{-2} μm^{-1}, respectively (**Figure 5-1 e**), which requires the transformation of conductors from pellet or tape form to thin-film form to produce thin-film solid-state electrolytes

with high Li^+ conductivity (>10^{-5} S cm^{-1} at room temperature) coupled with 3D architecture electrodes. Indeed, integrating amorphous solid electrolytes directly into 3D microbatteries would increase the power and/or energy densities of the entire cell; however, the electrode−electrolyte interfacial compatibility needs to be thoroughly investigated and the interfacial resistance reduced. The interfacial reaction, which can extend up to 100 nm and adversely affect battery performance,[310] can be prevented by applying an interfacial barrier layer between the electrode and the electrolyte (as thin as 5 nm).[311]

Thin-film processing enables the integration of different thin-film Li-conductors into microbatteries and more precise tuning of grain-boundary chemistry and structure as compared to sintered ceramics; however, the chemistry at grain boundaries needs to be resolved at the atomic scale. Faster charging and discharging rates as well as higher volumetric and gravimetric energy densities will be achieved in solid-state microbatteries by capitalising on the advances in Li-thin-film conductor fabrication as solid-state electrolytes with higher Li ion conductivities (for example, thin-film Li-garnets), as well as by designing batteries with porous electrodes enabling high loadings of high-voltage cathodes.[129,248]

5.2. Solid-State Electrochemical Sensors

Severe air pollution and emission of greenhouse gases in major cities around the globe caused by human and industrial activities[312,313] has accelerated the irreversible melting of Antarctic glaciers, triggering a rapid rise in sea levels.[314–316] Therefore, there is an increasing interest and need for monitoring gas-phase chemicals, such as carbon oxides (CO_x), sulfur oxides (SO_x), nitrogen oxides (NO_x), ozone and volatile organic compounds. The commercial small gas sensor market for monitoring ambient gas is segmented by technology, that is, resistive (semiconductor metal oxide) sensors, electrochemical sensors, and dispersive infrared radiation absorption and photo ionization detection sensors. Solid-state electrochemical gas sensors are not as sensitive as resistive sensors, but offer higher selectivity and stability, making them suitable for sensing of multiple gas species.[317] Furthermore, solid-state electrochemical gas sensors do not require as high maintenance as photo ionization sensors, which need periodic calibration and lamp replacement.[317,318] In addition, they are available for a wide range of gas chemicals, as compared to infrared radiation

absorption sensors, which show water−vapour and multi-gas interference.[317–319] Moreover, electrochemical sensors have the potential for miniaturisation from ceramic pellet and thick-film components to on-chip devices using functional thin films as sensor components.[319–322] Solid-state electrochemical gas sensors can be divided into three classes based on their operating principle and their specific input and output sensing signals: potentiometric, impedancemetric and amperometric gas sensors. As opposed to amperometric sensors, potentiometric gas sensors operate under thermodynamic principles and are independent of device geometry, obviating the need for complicated electronics and making them cost-effective and suited for a variety of applications.

5.2.1. Potentiometric Gas Sensors

Potentiometric gas sensors are composed of an electrochemical cell with a sensing electrode (SE), a solid electrolyte and a reference electrode (RE). Derived from the Nernst equation,[323] the difference in the chemical potential and different partial pressures at the two electrodes define the electromotive force (EMF) of the gas sensor, characterising the voltage of the cell. Depending on the ionic species of the gas, potentiometric gas sensors can be classified into type I (mobile ions), type II (immobile ions) or type III (neither mobile nor immobile ions).[123]

In type I sensors, the detected gas species reacts with the solid electrolyte at the gas–SE–electrolyte triple phase boundary, and is then converted into a mobile ion in the solid electrolyte (**Figure 5-2 a**). Type I sensors are typically used as O_2 sensors,[324] for example, in automobile exhausts with a zirconium dioxide electrolyte and porous platinum electrodes. However, these sensors are not commonly used for complex gases composed of multiple elements owing to a lack of solid-state electrolytes that can conduct complex and often immobile gas species in the solid state.[321] By contrast, type II sensors (**Figure 5-2 b**) enable the detection of more complex gas species, such as CO_2, NO_x and SO_x, because the gas species is identical to the immobile ions in the electrolyte. Unlike in type I sensors, in type II sensors, ions different from the gas phase species have sufficient mobility to conduct in the solid electrolyte.[325,326] From an electrochemical cell design perspective, both type I and type II sensors require separate gas environments for the SE and RE, which makes their integration into commercial applications more complex.[322] In type III sensors (**Figure 5-2 c**), an auxiliary phase is used for the SE, which contains both the gaseous ions and the mobile ions

from the solid electrolyte.[105,321,322] Type III sensors offer high sensitivity independent of size, but they rely on the number of triple-phase-boundary reactive sites in the auxiliary electrode. Compared with type I sensors, type III sensors also allow the detection of complex gas species, such as CO_2, NO_x and SO_x.[123,327] Moreover, owing to the presence of an auxiliary phase, the selection of mobile and immobile ions for the solid electrolyte is not restricted as in type II sensors, which opens the door for fast ions, such as Na^+ or Li^+, and for as of yet unexplored material combinations for sensing devices operating at low temperatures.

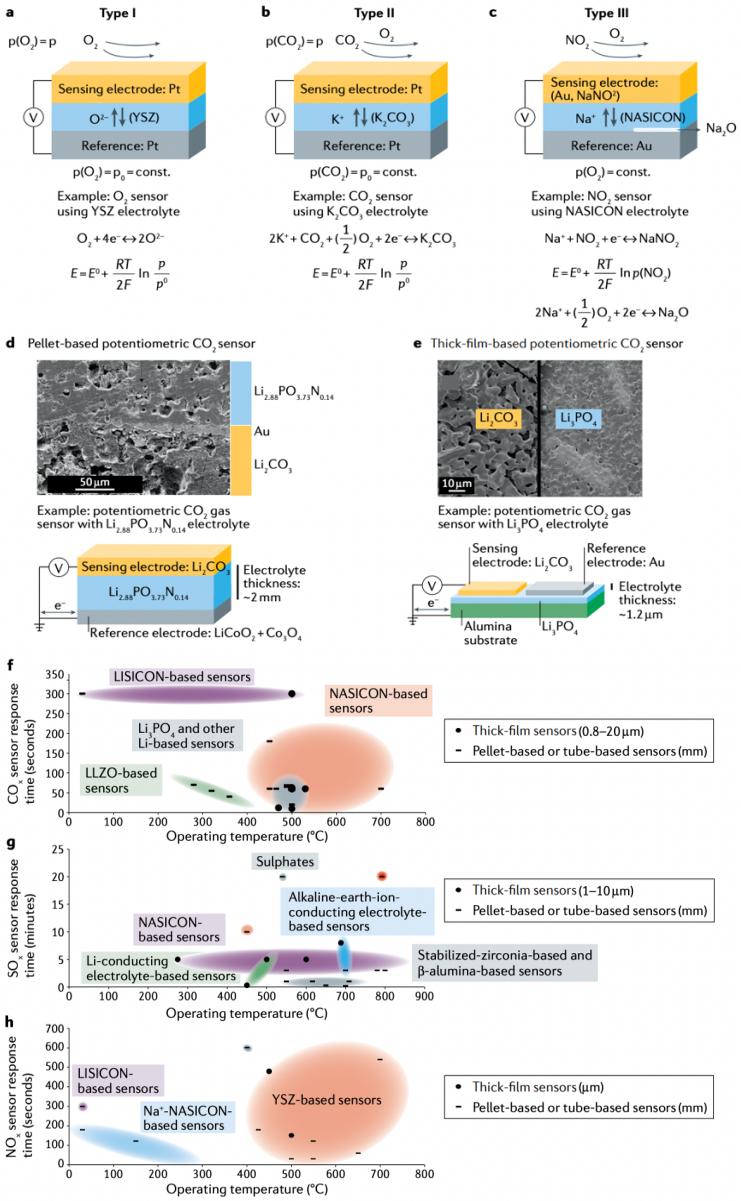

Figure 5-2. Solid-state electrochemical gas sensors. Electrochemical gas sensors based on Weppner's classification.[323] **(a)** Type I solid-state electrochemical gas sensors operate by direct measurement of mobile

ions in the solid electrolyte. **(b)** Type II solid-state electrochemical gas sensors operate by indirect measurement of immobile ions in the solid electrolyte. **(c)** Type III solid-state electrochemical gas sensors operate by analysis of other ion species through auxiliary solid phases. **(d)** Type III pellet-based CO_2 potentiodynamic sensor with a lithium phosphorus oxynitride (LiPON) electrolyte and Li_2CO_3 as the sensing electrode.[328] **(e)** Type III CO_2 potentiodynamic sensor with a Li_3PO_4 thick-film electrolyte and Li_2CO_3 as the sensing electrode.[329] **(f)** Comparison of sensor response time and operating temperature of Li-conductor-based solid-state CO_2 sensors, including Na super ionic conductor (NASICON)-based sensors,[156,330–336] Li super ionic conductor (LISICON)-based sensors,[337,338] $Li_7La_3Zr_2O_{12}$ (LLZO)-based sensors,[123,158] Li_3PO_4-based sensors,[329,339–343] garnet-type $Li_6BaLa_2Ta_2O_{12}$-based sensors,[344] $Li_{3x}La_{2/3-x/3}TiO_3$ (LLTO)-based sensor[345] and LiPON-based sensors.[328] **(g)** Comparison of sensor response time and operating temperature of state-of-the-art solid-state potentiometric SO_x sensors, including sensors based on stabilized zirconia,[346,347] NASICON,[327,348–351] β″-alumina,[352–356] sulfates,[357] alkaline-ion-conducting electrolytes[358,359] and Li-conducting electrolyte-based sensors.[360] **(h)** Comparison of sensor response time and operating temperature of state-of-the-art solid-state potentiometric NO_x sensors, including LISICON-based sensors,[337] zirconia-based sensors[361–367] and NASICON-based sensors.[368–370] Panel **(d)** reprinted from Ref.[328]. Panel **(e)** reprinted from Ref.[329].

5.2.2. Type III Gas Sensors

Solid electrolytes for type III sensors must provide high ionic conductance to ensure a fast sensing response with high thermal and chemical stability for the detection of a specific gas. Type I solid-state gas sensors require a high operating temperature (> 600-1000°C) with zirconia-based electrolytes to account for insufficient oxygen ion conductance (~10^{-8} S cm^{-1} at 300 °C). By contrast, type III sensors with a LiPON pellet-based electrolyte (**Figure 5-2 d**)[328] or a Li_3PO_4 thick-film electrolyte (**Figure 5-2 e**)[329] require a medium-to-low temperature range (<500 °C) for Li ion conductivity (~10^{-8}–10^{-6} S cm^{-1} at ambient temperatures).[19,38,41] However, lower operating temperatures and response times (<60 s) are needed for applications of these sensors on chips and noses. The sensing speed of solid-state type III gas sensors is mainly limited by the low mobility of Li^+ and Na^+ ions in the solid ceramic thin-film electrolyte, in addition to slow gas oxidation kinetics at interfaces and poor long-term chemical and structural stability under a reactive atmosphere (such as, humidity and SO_x). Solid-state Li-conductors with high conductivities could address these limitations.

The development of type III sensors has historically been related to progress in ceramic manufacturing and to the phase determination of fast Li- and Na-ion conductors primarily applied in batteries. Type III electrochemical solid-state potentiometric gas sensors using Li^+ or Na^+ have been explored for the detection of CO_x (**Figure 5-2 f**), SO_x (**Figure 5-2 g**) and NO_x (**Figure 5-2 h**) gas. Oxide-based Li-conductors, such as Li super ionic conductor (LISICON),[337,338]

Li_3PO_4,[329,339,341–343] garnet-type $Li_6BaLa_2Ta_2O_{12}$,[344] perovskite-type LLTO,[345] and garnet-type LLZO have good structural and chemical stability and sufficiently high ionic conductivities ($\geq 10^{-6}$ S cm^{-1} at room temperature)[50,371] for fast sensing at low temperatures. Oxide-based Li-conductors are usually processed as millimetre-sized pellets and have mainly been used for environmental CO_2 sensing thus far (**Figure 5-2 f**). Fast conductors, such as Ta-doped LLZO pellets, have also been integrated in potentiometric type III gas sensors, showing high Li^+ conductivity and good electrolyte stability, and thus, a fast CO_2 sensing response time of <60 s at an operating temperature of ~320 °C.[123]

In general, Li-electrolyte materials in sensors are thick (0.8–20 μm) and pellet- or tube-based, and they require high operation temperatures and show slow response times (>60 s). For example, Na^+-conducting NASICON electrolytes, which can be used for the detection of CO_2,[330–335,372] suffer from poor structural stability in humid environments,[373–375] cross-sensitivity with other gaseous species,[376] and, most importantly, the need for high operation temperatures (> 400 °C)[330,333,377] owing to sluggish electrolyte conduction, electrode kinetics and long response times (>60 s) (**Figure 5-2 f**).[330,377,378] SO_x sensors using stabilized zirconia,[346,347] Na-conducting NASICON,[327,348,349] β''-alumina[353–356] or other alkaline-ion-conducting materials[358,359] (**Figure 5-2 g**) have similar problems (that is, high operating temperature, long response time and poor electrolyte stability in an SO_x environment). By contrast, state-of-the-art solid-state NO_x sensors (**Figure 5-2 h**) with perovskite-based,[379] zirconia-based[361,380,381] or NASICON-based[369,370,382] electrolytes require lower operation temperatures (~200 °C).These type III sensors are further limited by poor selectivity, stability and sensitivity in corrosive environments (**Table 8-9**).

Li-based thin-film sensors could enable the design of cost-effective, low-power multi-sensing arrays with a fast response, new sensing electrode chemistries and an expanded scope of gases (for example, CO_x, SO_x and NO_x). However, this will require a reduction of the operating temperature and response time, which may be achieved by thin-film processing of Li-oxide films by wet-chemistry[136] and vacuum-based techniques,[120] which allow sufficient control of the lithiation stoichiometry during manufacturing and conductivities of $>10^{-5}$ S cm^{-1} at ambient conditions. In addition, films processed at low temperature, in particular, amorphous Li-phases, could reduce fabrication costs and enable integration with on-chip applications. Fabricating stable Li-based thin films for sensors may be challenging; however, clever material selection considering electrode,

electrolyte and gas chemical compatibility and adequate encapsulation solutions may resolve the stability issue, which will require multidisciplinary contributions.

5.3. Conclusions and Outlook

The development of new chemistry and processing methods for solid-state Li ceramics has enabled a new generation of Li^+ batteries. The downscaling of solid-state chemistries to film form will further increase the variety of Li^+ conductors, whose variability in terms of Li intercalation and de-intercalation and fast solid-state ionic motion make them interesting for applications beyond batteries; for example, Li^+ conductors for environmental, health and chemistry sensors. Indeed, the functionalities can be further expanded by changing the electrode electrochemistry.

We envision that lithionic chip units could be made of one type of Li^+ conductor film. The electrochemistry could then be defined simply by varying the electrode material. For example, by reducing the size of Li ceramics from millimetres to micrometres or nanometres, a variety of new functionalities can be achieved using one type of material. From environmental and economic viewpoints, using less materials and reducing the effective ceramic mass per device volume also decreases the amount of waste and costs; for instance, commercialized LiPON-based microbatteries for small-scale energy storage could also become an integral part of electrochemical sensing units or neuromorphic computing units. Similarly, multifunctional devices, such as three-terminal computation units coupled with microbatteries (for example, Li reservoir), could combine two or more functionalities in one on-chip device unit.[49]

Solid-state lithionics offer vast application opportunities based on Li ceramics in film form, whose chemistry and thermal processing can be modified to design a range of microdevices beyond batteries. Collaborations between material scientists, chemists and device engineers will lead to new material chemistries and device structures, to achieve the ambitious goal of using Li ions to power, compute and sense the world.

6. CHAPTER 6: Conclusions and Future Directions

6.1. Conclusions

In this thesis, we explore the local structure of a new class of high entropy Li^+ conductors, namely, amorphous to crystalline LLZO, and their low-temperature processing options for future applications in lithionic devices.

First, in **Chapters 2 and 3**, we explore the near order structure of high entropy aLLZO, with the highest number of LBUs (≥ 4) being identified so far, that can be stabilized over an unusual wide thermal processing window at low temperatures (up to 650 ºC). A multi-faceted investigation has been carried out to resolve the structure of these high entropy aLLZO phases, to identify the major roles of the LBUs, and to understand their implications on Li-dynamics. Specifically, we observed via XAS and ^{7}Li NMR edge- and face-shared LiO_x, LaO_x, and ZrO_x LBUs in aLLZO phases; these edge- and face-sharing CRNs in amorphous Li garnets offer wider opportunities to tune the ion transport. Within these aLLZO phases, Li and Zr have been identified as network former and La as network modifiers, with the highest Li^+ conductivity observed for films with smaller Li–O, and Zr–O coordination. Moreover, we design a model study to probe the effect of network modifier La concentration on the near order, MRO, and LRO structure of aLLZO, and define its solubility limit in aLLZO. The MRO analysis via FEM confirmed La role as a network modifier in aLLZO when La stays in its solubility limit in aLLZO; increasing the La concentration leads to greater separations between the 1st nearest neighbors of Zr–O and La–O within the same LBU and the 2nd nearest neighbors of Zr–La across two adjacent network former and modifier LBUs. We also define the solubility threshold between 100 mol.% and 150 mol.% for La in aLLZO via Raman spectroscopy. Further, we propose a sorting metric by contextualizing this material class towards other 'low entropy' amorphous Li electrolytes based on the numbers and types of network formers and network modifiers and their LBUs hierarchy. Collectively, we see these efforts set the cornerstone for designing aLLZO local structures to achieve the optimal Li+ transport and mechanical properties for use as solid electrolytes in batteries and other lithionic devices.

Second, in **Chapter 4**, novel annealing routes to synthesize cLLZO films via SDS that bypass sintering is designed and validated, which only require half of the temperature used to densify cLLZO pellets and tapes. To achieve this goal, we develop the 1st TTT diagram for the glass-

ceramic LLZO based on the crystallization enthalpy analysis as well as the local structure and phase evolution studies. The TTT diagram provides insights on optimizing the synthesis conditions to achieve the lowest crystallization temperature ever reported to stabilize cLLZO as a dense solid film at 500 ºC as proven by Raman spectroscopy. This work provides guidelines for the use of liquid-to-solid densifications such as SDS synthesis in a combination of TTT diagrams to define new annealing routes to stabilize cLLZO and Li-containing ceramics beyond cLLZO, that assist the low-cost sustainable Li^+ ceramic film production towards batteries and lithionic applications.

Finally, we present in **Chapter 5** an overview of the state-of-the-art progress in applying Li^+ ceramic film towards lithionic applications for energy storage and sensors for toxins and greenhouse gases. We specifically discussed the existing challenges especially associated with Li^+ thin-film processing, and the future opportunities we foresee from today. We anticipate the effort of this thesis to aid the integration of low-temperature-synthesized aLLZO and cLLZO for microdevice applications beyond batteries.

6.2. Future Directions

6.2.1. Alternative Network-Modifier Dopant for aLLZO to Optimize Li^+ Transport and Thin-Film Mechanical Properties

Through the definition of the La role in aLLZO as a network modifier in this thesis, we see perspective to explore dopants at La sites to further modulate the amorphous near-order structure and optimize Li^+ transport as well as thin-film mechanical properties towards device integration. Future work can focus on elements in the Lanthanide series, *e.g.,* Ce and Er, which have the same valance number and the same outmost shell electronic structure but different atomic radii, and alkaline-earth metal elements in group II, *e.g.,* Ca and Sr, which offer a "1+" difference in valance state. Both groups of dopants can alter the field strength surrounding the network modifier elements and therefore modulate the coordination and connection of LBUs within aLLZO, which directly influences the Li^+ transport and mechanical properties of the aLLZO thin films. These transport and mechanical properties can be crucial in determining their usefulness in lithionic devices such as batteries and electrochemical gas sensors. We encourage both computational and experimental efforts to investigate the role of these network-modifier dopants in aLLZO structure.

6.2.2. Integrating Low-Temperature-Processed aLLZO and cLLZO Films into Lithionic Devices

Another direction to be explored is towards device-level integration of these low-temperature and low-cost processed aLLZO and cLLZO films. Specifically, these Li^+ electrolyte films can be integrated as Li^+ electrolyte layers in SSBs, memristors, and electrochemical gas sensors or as protective coating layers in hybrid batteries. No matter which lithionic devices they are functioning in, special attention should be paid to the chemical and electrochemical stability at interfaces. For instance, electrochemical stability between various aLLZO phases vs. Li metal anode should be clarified for battery applications. Furthermore, CCDs, being critical in determining the battery power performance, are also encouraged to be measured for various highly Li^+-conductive aLLZO phases designed based on careful selection of network modulating dopants. Furthermore, low-temperature processing routes developed by this thesis can be explored for scaleable production of batteries and other lithionic devices to lower processing costs and energy consumption and achieve environmental sustainability goals.

7. Biographical Notes and Publications

Yuntong Zhu was born in Beijing, China. She attended Georgia Institute of Technology from 2013 to 2017 and obtained two Bachelor of Science degrees, one in Materials Science and Engineering and one in Industrial and System Engineering. During her undergraduate studies, she was a part of Prof. C.P. Wong's lab, where she conducted research on graphene-based supercapacitors and flexible electronics. Yuntong was also a part of Prof. Seung Soon Jang's lab, where she focused on DFT studies of high-voltage organic materials for Li^+ battery cathodes. In Summer 2016, she received ThinkSwiss scholarship sponsored by the Embassy of Switzerland in the U.S. and conducted summer research on machine-learning-based high-throughput materials structure prediction at École polytechnique fédérale de Lausanne (EPFL), Switzerland. In Fall 2017, she began her doctoral studies in the Department of Materials Science and Engineering (DMSE) at Massachusetts Institute of Technology, under the supervision of Prof. Jennifer L.M. Rupp. During her doctoral study, Yuntong investigated the high entropy structure and alternative low-temperature synthesis routes for aLLZO and cLLZO solid electrolytes. She has been a part of the collaboration project with Samsung and co-invented two low-cost wet-chemical routes to achieve LLZO thin films in thickness of 1–10 um, namely, SDS and freeze-drying-assisted drop casting. Yuntong led the study on high-entropy aLLZO near order structure and was the first one to fundamentally clarify the role of LBUs in aLLZO. She formed multiple academia, industry, and national laboratory collaborations in the U.S., U.K., Israel, and Germany. She also proposed ultra-low-temperature cLLZO synthesis routes based on the development of TTT diagram and successfully stabilized cLLZO at unprecedently low temperatures of 500–650 ºC. Beyond studies on LLZO electrolytes, she proposed the novel concept of Lithionics, defining a class of multifunctional on-chip devices based on Li^+ -conducting thin films. Yuntong was also involved in Shell and NGK collaboration projects, focusing on CNT-based battery-supercapacitor hybrids and LLZO-cathode interfaces, respectively. In Summer 2022, Yuntong joined Meta Reality Labs in Redmond, WA, as a Research Scientist Intern and conducted research on inorganic thin-film coating materials for AR waveguides. Yuntong became an MIT Energy Initiative (MITEI) fellow in 2020, and her research was sponsored by the MITEI-ExxonMobil fellowship in the 2020–2021 academic year. She was also a student delegate for the President's Council of Student Advisors (PCSA) within the American Ceramic Society (ACerS) in the 2020–2021 academic year.

Yuntong Zhu is a co-author of the following publications and a co-inventor of the following patents during her doctoral study at MIT:

Publications:

1. Uncovered phase polymorphism steers chemo-mechanics of garnet electrolytes
   Yuntong Zhu, Moran Balaish, Jennifer L.M. Rupp

   Joule 6.12 (**2022**): 2680-2682.

2. A sinter-free future for solid-state battery designs
   Zachary D. Hood, **Yuntong Zhu**, Lincoln J. Miara, Won Seok Chang, Philipp Simons, Jennifer L.M. Rupp
   Energy & Environmental Science 15.7 (**2022**): 2927-2936.

3. Lithium film ceramics for solid-state lithionic devices
   Yuntong Zhu, Juan Carlos Gonzalez-Rosillo, Moran Balaish, Zachary D. Hood, Kun Joong Kim, Jennifer L.M. Rupp
   Nature Reviews Materials 6.4 (**2021**): 313-331.

4. Processing thin but robust electrolytes for solid-state batteries
   Moran Balaish, Juan Carlos Gonzalez-Rosillo, Kun Joong Kim, **Yuntong Zhu**, Zachary D. Hood, Jennifer L.M. Rupp
   Nature Energy (**2021**): 1-13.

5. High entropy amorphous Li-battery electrolytes
   Yuntong Zhu, Zachary D. Hood, Haemin Paik, Pedro B. Groszewicz, Steffen P. Emge, Farheen N. Sayed, Chengjun Sun, Moran Balaish, David Ehre, Lincoln J. Miara, Anatoly I. Frenkel, Igor Lubomirsky, Clare P. Grey, Jennifer L.M. Rupp
   (in review)

6. Uncovering the network modifier for high entropy amorphous Li-garnet glass-ceramics
   Yuntong Zhu, Ellis R. Kennedy, Bengisu Yasar, Haemin Paik, Yaqian Zhang, Zachary D. Hood, Mary Scott, Jennifer L.M. Rupp
   (in revision)

7. Time-Temperature-Transformation (TTT) Analysis of Phases for Low-Temperature Sustainable Synthesized Battery-Grade Li-Garnet Electrolyte Films
   Yuntong Zhu, Michael Chon, Carl V. Thompson, Jennifer L.M. Rupp
   (in revision)

8. Dual-phase salt-oxide composite battery electrolyte films with enhanced Li-ion conduction
   Yuntong Zhu, Zachary D. Hood, Sara Sand, Haemin Paik, Moran Balaish, Lincoln J. Miara, Jennifer L.M. Rupp
   (in revision)

9. Insights into Li^+ storage mechanisms, kinetics, and reversibility of multi-walled carbon nanotubes
   Lingping Kong, **Yuntong Zhu**, Jason P. Williams, Mohamad Kabbani, Fikile Brushett, Jennifer L. M. Rupp
   (in revision)

10. Rational Design of Fast-charging Lithium-ion Battery-Supercapacitor Hybrid Devices
    Lingping Kong, Katarzyna P. Sokol, **Yuntong Zhu**, Hyunwon Chu, Jesse J. Hinricher, Jason Williams, Mohamad Kabbani, Jennifer L.M. Rupp
    (in revision)

11. Emerging processing guidelines for solid electrolyte in the era of oxide-based solid-state batteries
    Moran Balaish, Kun Joong Kim, Hyunwon Chu, **Yuntong Zhu**, Juan Carlos Gonzalez-Rosillo, Lingping Kong, Haemin Paik, Lincoln J. Miara, Jennifer L.M. Rupp
    (in revision)

Patents:

1. Solid-State Electrolyte and Method of Manufacture Thereof
   Yuntong Zhu, Zachary D. Hood, Lincoln J. Miara, Jennifer L.M. Rupp
   US 16/224,968 (*granted*)

2. Solution-Processed Solid-State Electrolyte and Method of Manufacture Thereof
   Yuntong Zhu, Zachary D. Hood, Lincoln J. Miara, Jennifer L.M. Rupp
   US 16/225,068 (*granted*)

3. Multi-Phase Electrolyte Film and Method of Making the Same
   Yuntong Zhu, Jesse J. Hinricher, Zachary D. Hood, Lincoln J. Miara, Heung Chan Lee, Won Seok Chang, Jennifer L.M. Rupp
   US 17/365,441 *(pending)*

4. Lithium Solid Electrolyte and Method of Manufacture Thereof
   Yuntong Zhu, Won Seok Chang, Lincoln J. Miara, Jennifer L.M. Rupp
   US 16/860,326 (*pending*)

5. Spray Pyrolysis of Lithium Salt Films
   Yuntong Zhu, Moran Balaish, Lingping Kong, Jennifer L.M. Rupp
   PCT/US21/59339 (*pending*)

6. Solid-State Battery and Method of Manufacturing Solid-State Battery Utilizing Spray Pyrolysis
   Andrea Maurano, Jesse J. Hinricher, So Yeon Kim, Jennifer L.M. Rupp, Ju Li, **Yuntong Zhu**, Hyunwon Chu, Zachary D. Hood, Won Seok Chang, Kai Pei, Yimeng Huang, Srinath Chakravarthy, Ziqiang Wang
   US 17/745,776 (*pending*)

Yuntong Zhu is a co-author of the following publications prior to her doctoral study at MIT:

1. Boron-doped coronenes with high redox potential for organic positive electrodes in lithium-ion batteries: a first-principles density functional theory modeling study
   Yuntong Zhu, Ki Chul Kim, Seung Soon Jang
   Journal of Materials Chemistry A 6.21 (**2018**): 10111-10120.

2. Effect of polymer binders on graphene-based free-standing electrodes for supercapacitors
   Bo Song, Fan Wu, **Yuntong Zhu**, Zhaoxia Hou, Kyoung-sik Moon, Ching-Ping Wong
   Electrochimica Acta 267 (**2018**): 213-221.

3. Sub-stoichiometry-facilitated oxidation kinetics in a δ-TixC-doped Ti-based alloy
   Shaolou Wei, Lujun Huang, **Yuntong Zhu**, Zhe Shi, Xinting Li, Lin Geng
   npj Materials Degradation 3.1 (**2019**): 1-5.

4. Systematic study on structural and electronic properties of diamine/triamine functionalized graphene networks for supercapacitor application
   Bo Song, Jingxiang Zhao, Mingjun Wang, Jeffrey Mullavey, **Yuntong Zhu**, Zhishuai Geng, Dongchang Chen, Yong Ding, Kyoung-sik Moon, Meilin Liu, Ching-Ping Wong
   Nano Energy 31 (**2017**): 183-193.

5. Molecular level study of graphene networks functionalized with phenylenediamine monomers for supercapacitor electrodes
   Bo Song, Ji Il Choi, **Yuntong Zhu**, Zhishuai Geng, Le Zhang, Ziyin Lin, Chia-chi Tuan, Kyoung-sik Moon, Ching-ping Wong
   Chemistry of Materials 28.24 (**2016**): 9110-9121.

6. Miniaturized Integrated Micro-Supercapacitors as Efficient Power Sources for Wearable and Biocompatible Electronic Devices
   Bo Song, Liyi Li, **Yuntong Zhu**, Kyoung-Sik Moon, CP Wong
   IEEE 66th Electronic Components and Technology Conference (ECTC) (**2016**): 2046-2050.

7. Highly conductive polyurethane/polyaniline-based composites for wearable electronic applications
   Bo Song, Chia-Chi Tuan, Liyi Li, **Yuntong Zhu**, Kyoung-Sik Moon, CP Wong
   IEEE 66th Electronic Components and Technology Conference (ECTC) (**2016**): 2424-2429.

8. Three-dimensional graphene-based composite for flexible electronic applications
   Bo Song, Zhenkun Wu, **Yuntong Zhu**, Kyoung-sik Moon, CP Wong
   IEEE 65th Electronic Components and Technology Conference (ECTC) (**2015**): 1803-1807.

9. Synthesis and electrochemical characterization of InSn4 and InSn4/C as new anode materials for lithium-ion batteries
   Yuntong Zhu, Xin Liu, Hailei Zhao, Jie Wang
   Ionics 19.5 (**2013**): 709-715.

10. Thermodynamic and kinetic analysis for carbothermal reduction process of CoSb alloy powders used as anode for lithium ion batteries
Jianying Yang, Mengwei Wang, **Yuntong Zhu**, Hailei Zhao, Ronglin Wang, Jingbo Chen*Journal of Alloys and Compounds* 509.28 (**2011**): 7657-7661.

8. Appendices

8.1. Appendix A: Supplementary Information to Chapter 2

Discovery timeline of amorphous solid-state Li^+ electrolytes (bulk vs. thin films)

In the quest for alternative amorphous solid-state Li^+ electrolyte materials, we wish to briefly review the discovery timeline (**Figure 2-1 c**), which is often connected to prior crystalline phase discoveries and more complicated structure types. In the 1980s, a promising perovskite-type LLTO electrolyte was first discovered to have high Li ion conductivity and was synthesized in crystalline pellet form. However, it was only until 2004, about 30 years later, the first aLLTO was synthesized in thin-film form through high-energy PLD deposition. Since then, aLLTO gained increasing amount of attentions because of its improved Li^+ conductivity (than crystalline LLTO) and reduced processing temperature requirement. However, the local structure of the aLLTO film, till now, has not been resolved, although device level implementation has been successfully demonstrated. Around the same time in the late 2000s, a few other amorphous perovskites oxygen film conductors (i.e., $BaTiO_3$, $SrTiO_3$, and $BaZrO_3$) also raised attention and the near order structure and O^{2-} conduction mechanism has been resolved in detail, which also offer structural insights for aLLTO. In the year of 2008, a new structure of garnet-structure LLZO synthesized in its crystalline cubic phase has been discovered with high Li^+ conductivity of 10^{-3} S cm^{-1},[13,50,94,105] wide electrochemical stability window (nearly stable at 0 V vs. Li/Li^+),[20,383] good chemical stability,[170,371] and non-flammability,[371] which was considered as a promising solid electrolyte candidate for solid state batteries.

It is only rather recent, in 2012, that the first amorphous phases of LLZO were reported to be existent by RF sputtering, providing ionic conductivity up to 4×10^{-7} S cm^{-1}. In 2018, Rupp et al. demonstrated that for several aLLZO phases existed for films synthesized by PLD at different temperatures for which the conductivity and activation energy varied accordingly. However, it remains unclear in these findings what are the structural roles of different metal cations and how they affect Li ion conductions in the film. In addition, the so far reported aLLZO films were all prepared by high energy vacuum-based deposition techniques (RF sputtering and PLD), which is hard to achieve film thickness > 500 nm and limit its potential for scale-up manufacturing in industry.

Additional analysis of Raman spectra:

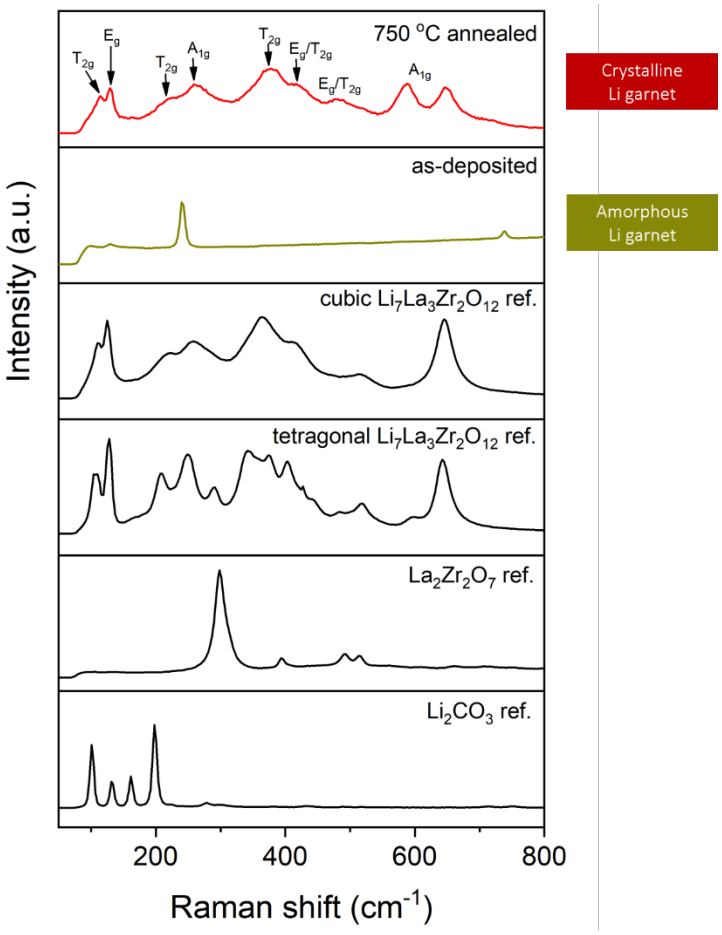

Figure 8-1. *ex situ* Raman spectra collected for as-deposited film and crystalline cLLZO film after 750 ºC annealing. Reference spectra of cLLZO and t LLZO, delithiated $La_2Zr_2O_7$ and Li_2CO_3 are also presented.

For the spectrum of the as-deposited film (**Figure 8-1**), peaks at 241 cm^{-1} and 738 cm^{-1} were observed, indicating the presence of undecomposed $LiNO_3$ precursor salt. The $LiNO_3$ precursor decomposes at 400 – 500 ºC (detailed discussion about precursor decomposition and chemistry changes can be found in Ref. [136]).

We identified cubic phase Li-garnet from the spectrum of 750 °C annealed sample. The two intense peaks at 113 and 130 cm^{-1} are identified as T_{2g} and E_g mode of O–La–O vibration. The peak centered at 218 and 261 cm^{-1} were assigned to the oxygen-bending band of T_{2g} and A_{1g},[199] and the uprising peaks centered at 377, 418, and 482 cm^{-1} were assigned to the O–Li–O vibration bands

(T_{2g} and E_g/T_{2g}) in LiO_6 octahedra.[200] The two broad peak centered at 587 and 648 cm^{-1} are assigned to A_{1g} mode of O–Zr–O stretching.[199,200]

It is also important to stress that the peaks in the *in situ* heating spectra (**Figure 2-2 c**) exhibit a left-side shift toward lower wavenumbers compared with those in the reference spectra and the *ex situ* Raman spectra. This phenomenon is commonly observed in *in situ* heating experiments because of the more significant thermal vibration at elevated temperatures, which leads to increased average bonding distances and weaker bond strength.

DSC analysis:

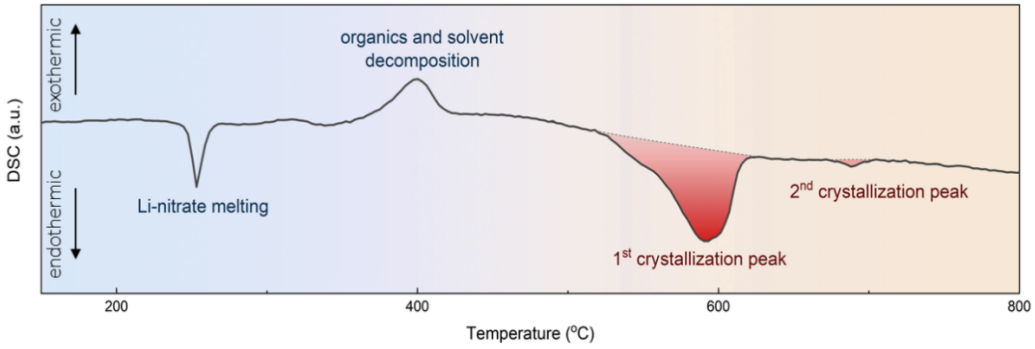

Figure 8-2. Non-isothermal DSC of LLZO films by SDS from 150 ºC to 800 ºC. The four peaks from lower to higher temperature represent endothermic Li-nitrate melting, exothermic Li-nitrate decomposition, 1st-step crystallization and 2nd-step crystallization, respectively.

Fourier transform of TEM:

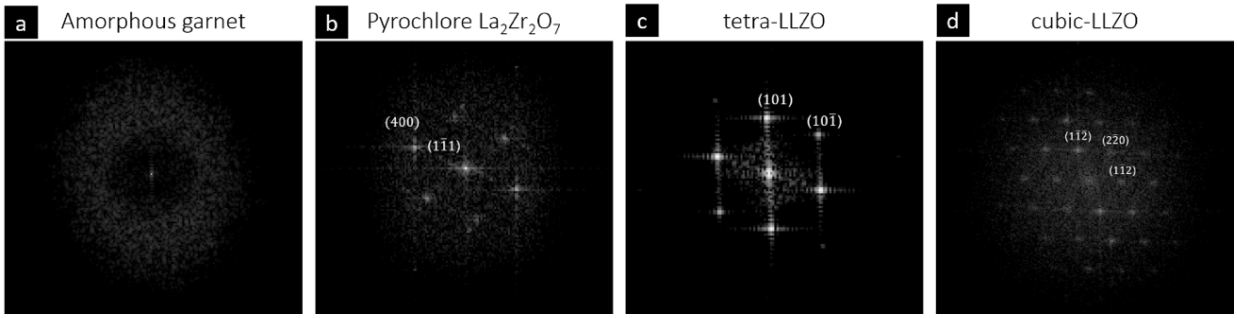

Figure 8-3. Fourier transform of HR-TEM images in the region of **(a)** aLLZO, **(b)** Pyrochlore $La_2Zr_2O_7$, **(c)** tLLZO, and **(d)** cLLZO.

XAS analysis:

Table 8-1. Summary of the estimated Zr coordination and associated error from linear combination analysis of XANES and summary of the estimated nearest neighbor distance (Zr–O) and associated error of Zr from EXAFS of Li-garnet films post-annealed at 500 ºC, 600 ºC, 650 ºC, and 750 ºC. Fitting errors of Zr coordination is shown in the parentheses. Uncertainties in the last significant digit of first nearest neighbor distance are shown in parentheses.

Post-annealed Temperature (ºC)	500	600	650	750
N(Zr–O)	6.9(1.1)	6.2(1.0)	6.3(1.0)	5.5(1.2)
R(Zr–O), Å	2.12(1)	2.11(1)	2.10(1)	2.10(1)
σ^2 (Zr–O), Å^2	0.0076(25)	0.0042(20)	0.0054(25)	0.0047(28)

The *in situ* TEM data from **Figure 2-2 e** suggests that the nucleation of $La_2Zr_2O_7$ already occurs at 500 ºC. However, the effect of $La_2Zr_2O_7$ nucleation on Zr local structure arrangement remains undefined. Thus, we specifically performed linear-combination fitting for the 500 ºC Zr K-edge XANES spectrum with the 750 ºC crystalline garnet spectrum measured from this work and the nanocrystalline-ZrO_2 (nc-ZrO_2) spectrum from the literature[207] as standards. First, by comparing the Zr K-edge XANES region of the 500 ºC spectrum and the two standard spectra, we observed the presence of six isosbestic points in the 500 ºC XANES spectrum at 18,017, 18,027, 18,045, 18,065,18,086, and 18,110 eV (**Figure 8-4**), whereas at these energy levels, the X-ray absorbance does not change among the 500 ºC amorphous, 750 ºC crystalline garnet, and nanocrystalline ZrO_2 spectra. The isosbestic points indicate that the local structure around Zr is heterogeneous, consistent with the phase mixture (aLLZO + nucleation of $La_2Zr_2O_7$) observed in *in situ* TEM (**Figure 2-2 e**). Quantitatively, the linear combination analysis suggests that the 60.9 mol.% Zr local structure at 500 ºC is close to that of the 750 ºC annealed sample and the 39.1 mol.% of the Zr local structure is close to that of the nc-ZrO_2 structure (**Figure 8-5**).[207] We may conclude that those 39.1 mol.% of Zr in the 500 ºC film, which has a similar local structure as nc-ZrO_2, participated in the nucleation of $La_2Zr_2O_7$ while the rest remained as ZrO_x LBUs in the amorphous Li garnet.

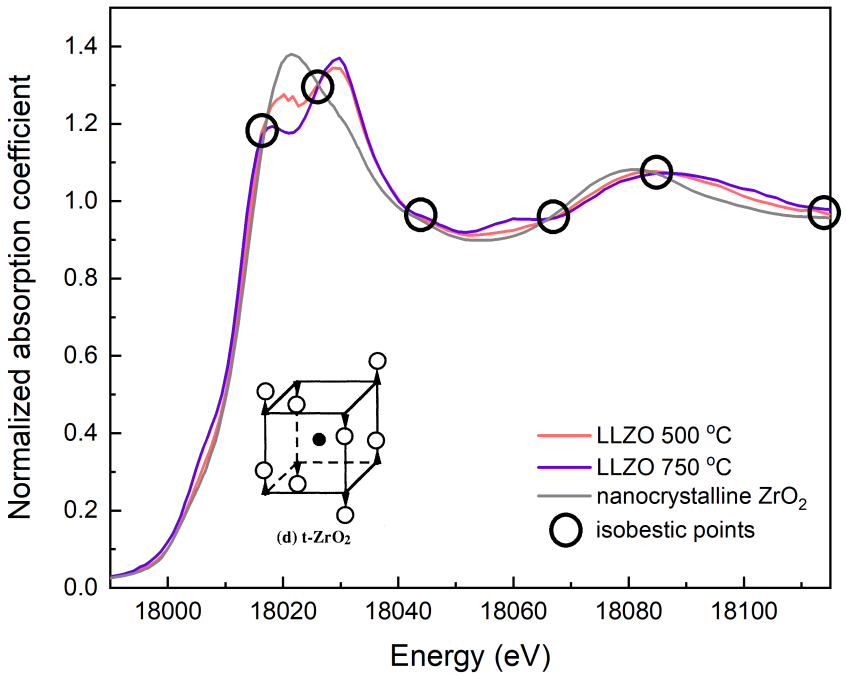

Figure 8-4. Comparison of the Zr K-edge XANES spectra of the 500 ºC and 750 ºC samples with the reference of ZrO_2 (nc). Multiple isosbestic points indicate heterogeneous environment of Zr in the 500 ºC sample. Inset: The local structure in monoclinic ZrO_2 and tetragonal ZrO_2 from Ref. [207].

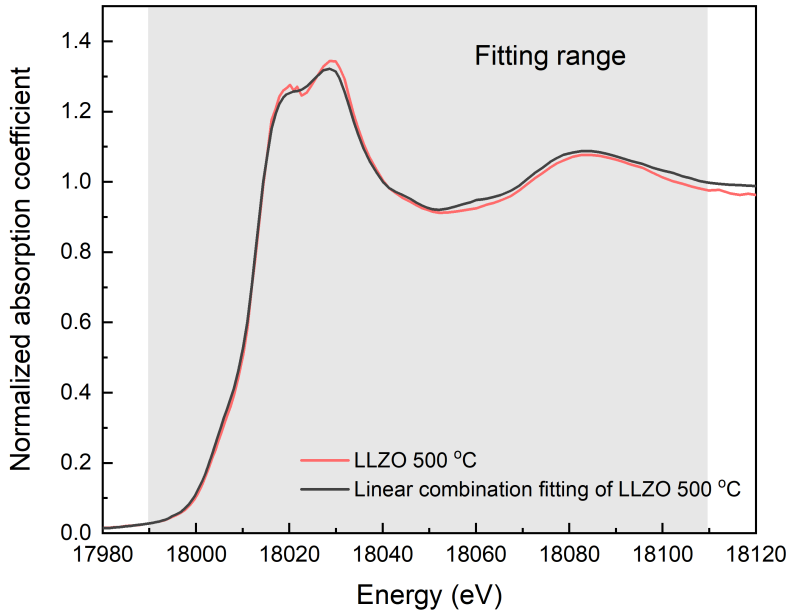

Figure 8-5. Fitting of XANES spectrum of 500 ºC annealed Li-garnet film (LLZO 500 ºC) after linear combination analysis with spectra of 750 ºC annealed sample (cubic phase) and nanocrystalline ZrO_2 selected as standards.

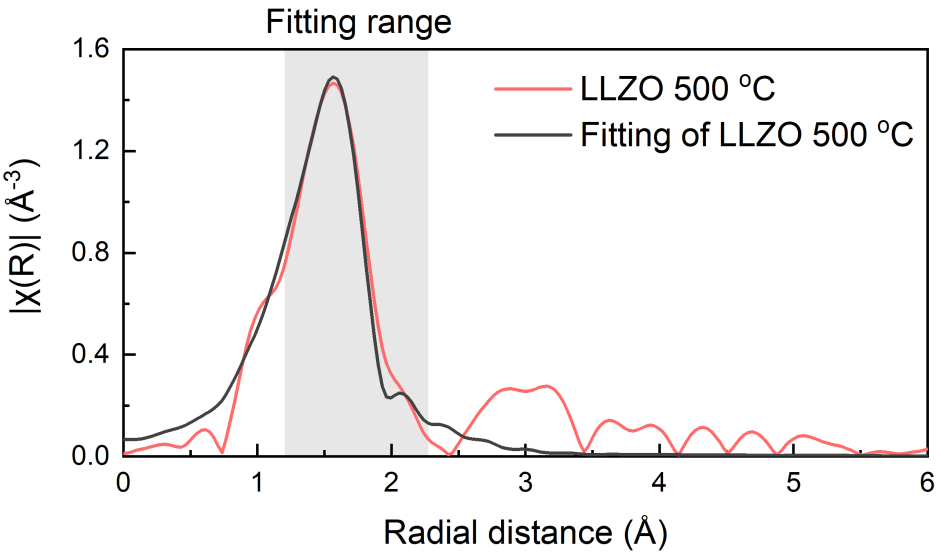

Figure 8-6 Fitting of the nearest neighbor (1st shell) of Zr k-edge EXAFS spectrum of 500 ºC annealed Li-garnet film (LLZO 500 ºC).

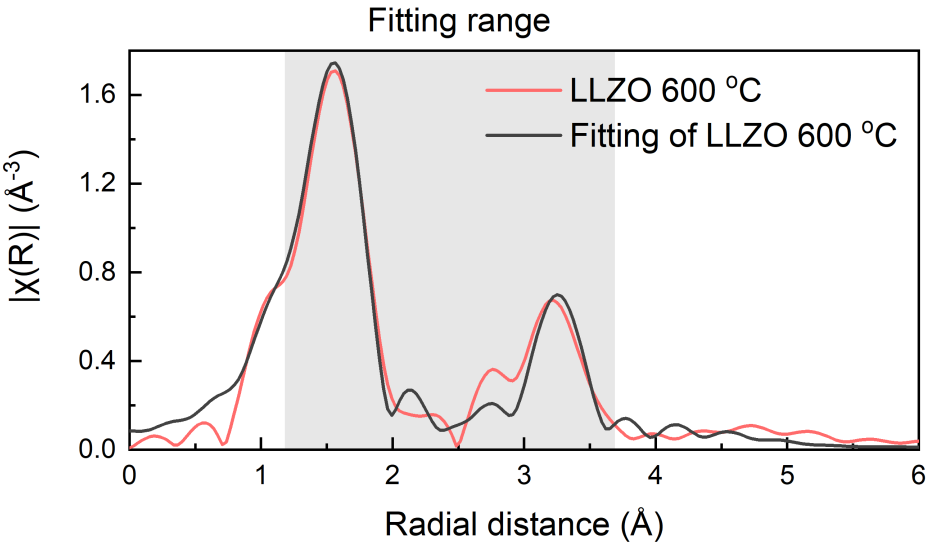

Figure 8-7. Fitting of the nearest neighbor (1st shell and 2nd shell) of Zr k-edge EXAFS spectrum of 600 ºC annealed Li-garnet film (LLZO 600 ºC).

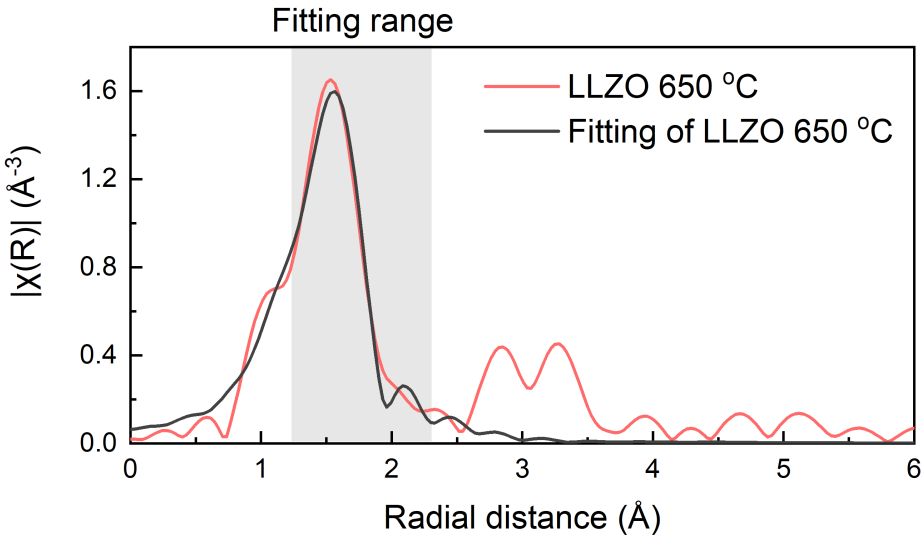

Figure 8-8. Fitting of the nearest neighbor (1st shell) of Zr k-edge EXAFS spectrum of 650 ºC annealed Li-garnet film (LLZO 650 ºC).

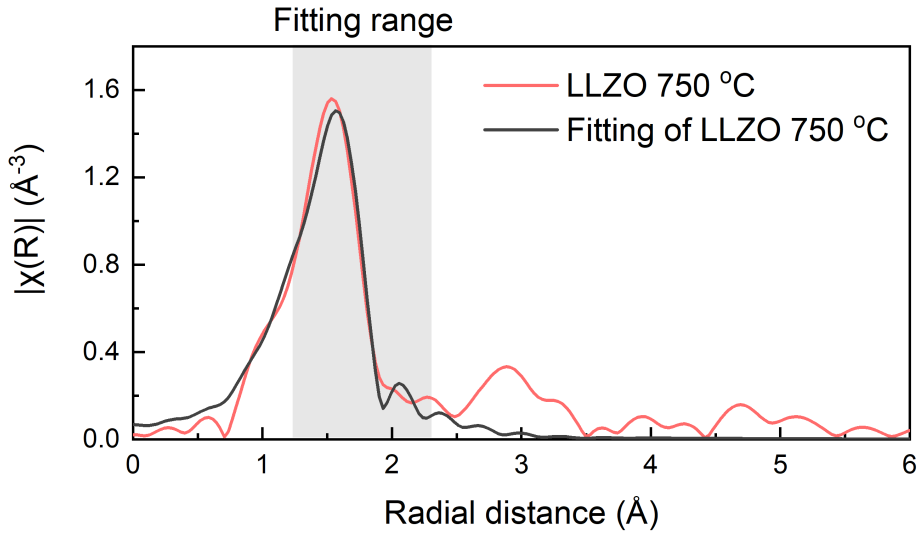

Figure 8-9. Fitting of the nearest neighbor (1st shell) of Zr k-edge EXAFS spectrum of 750 ºC annealed Li-garnet film (LLZO 750 ºC).

NMR analysis:

Table 8-2. Summary of the FWHM and associated error after Gaussian fitting of ^{7}Li MAS NMR peak of post-annealed Li-garnet films at 500 ºC, 600 ºC, 650 ºC, and 750 ºC (room temperature, 16.5 T).

Post-annealing Temperature (°C)	500	600	650	750
FWHM (kHz)	1.168	1.207	1.187	1.012
Error (kHz)	±0.014	±0.009	±0.011	±0.009

Table 8-3. Summary of the change of chemical shift, δ, and associated error after Gaussian fitting of ^{7}Li MAS NMR peak of post-annealed Li-garnet films at 500 ºC, 600 ºC, 650 ºC, and 750 ºC (room temperature, 16.5 T).

Post-annealing Temperature (°C)	500	600	650	750
δ (ppm)	-0.439	-0.421	-0.275	0.824
Error (ppm)	±0.015	±0.013	±0.013	±0.014

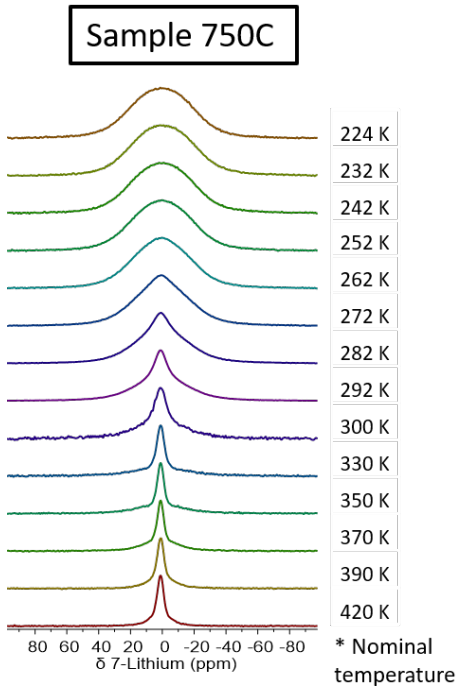

Figure 8-10. ^{7}Li Variable Temperature (VT)-NMR spectra measured from 224K to 420 K for 750 ºC annealed crystalline cubic Li-garnet (11.8 T).

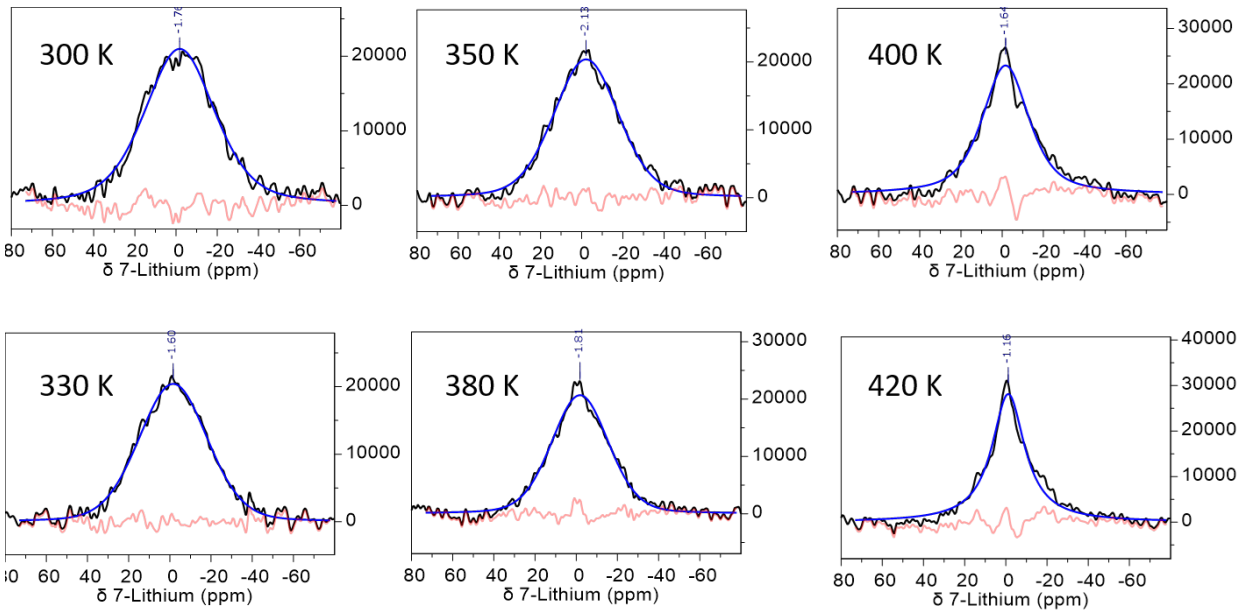

Figure 8-11. ^{7}Li VT-NMR spectra measured from 300K to 420 K for 650 ºC annealed aLLZO (11.8 T).

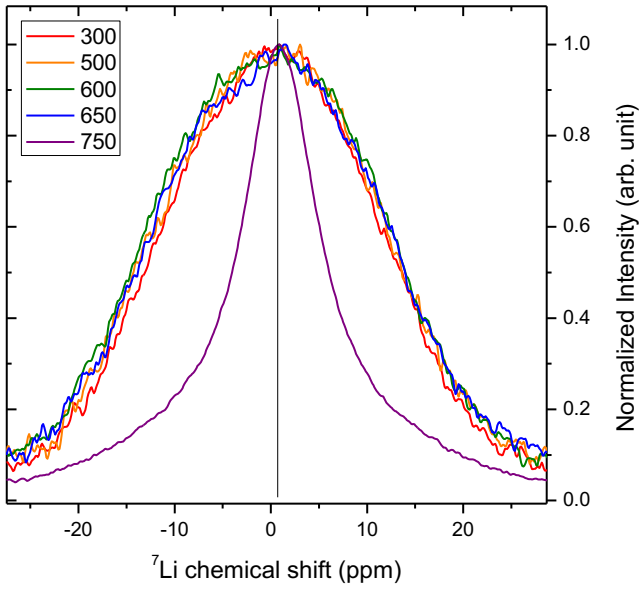

Figure 8-12. Static ^{7}Li NMR spectra of Li-garnet films post-annealed at 500 ºC, 600 ºC, 650 ºC, and 750 ºC measured at room temperature on a 16.5 T magnet.

Table 8-4. Summary of the FWHM and associated error after Gaussian fitting of ^{7}Li static NMR peak of post-annealed Li-garnet films at 500 ºC, 600 ºC, 650 ºC, and 750 ºC (room temperature, 16.5 T).

Post-annealing Temperature (°C)	**500**	**600**	**650**	**750**
FWHM (kHz)	7.325	7.521	7.452	3.074
Error (kHz)	±0.056	±0.069	±0.063	±0.079

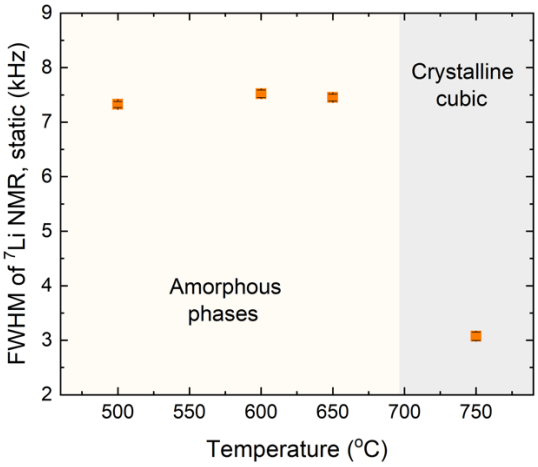

Figure 8-13. FWHM of ^{7}Li chemical peaks from static NMR spectra (room temperature, 16.5 T). With increasing annealing temperature, a peak sharpening and a more Lorentzian than Gaussian lineshape is observed. The largest FWHM is found for the 650 ºC annealed film and smallest FWHM for the 750 ºC annealed film (crystalline cubic). Small fitting errors indicate the changes are significant.

Analysis on the Li^+ transport

Nyquist plots measured at 78 °C and 150 °C are shown in **Figure 8-14** and **Figure 8-15** where only one semicircle at high-to-medium frequencies and a straight-line tail toward high impedance values at low frequency are observed. The semicircle can be reflected as the bulk and grain boundary contribution of Li^+ transport. Meanwhile, the low-frequency part of the straight-line tail matches well with the typical behavior of a blocking electrode and was thus assigned to the top Pt electrodes.

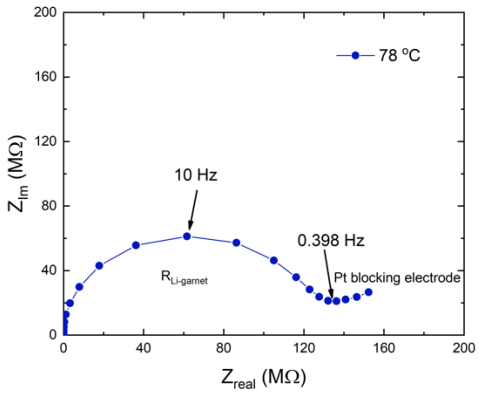

Figure 8-14. Representative Nyquist plot for 750 ºC annealed film measured at 78 ºC.

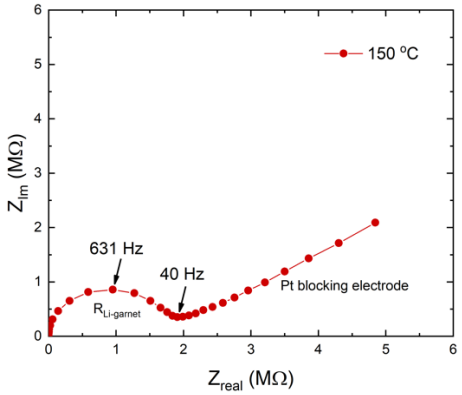

Figure 8-15. Representative Nyquist plot for 750 ºC annealed film measured at 150 ºC.

Table 8-5. Summary of Li^+ conductivity at 30 ºC and 188 ºC and activation energy for amorphous and crystalline Li-garnet films annealed at different temperatures.

Annealed temperature / ºC	Conductivity at 30 ºC (extrapolated), σ_{30} / S·cm^{-1}	Conductivity at 188 ºC, σ_{188} / S·cm^{-1}	Activation energy, E_a / eV
500	1.44×10^{-9}	2.77×10^{-5}	0.782
600	1.85×10^{-9}	3.44×10^{-6}	0.604
650	5.59×10^{-8}	4.58×10^{-6}	0.360
750	2.51×10^{-6}	1.66×10^{-4}	0.343

Building a phase–local ordering– Li^+ transport relationship:

Based on the insightful data collected from various spectroscopy and microscopy techniques, we reflect on the effect of phase evolution and local ordering on Li^+ conductivity for amorphous and crystalline Li-garnet films. First, we compared the structure and transport properties among amorphous films (**Figure 8-16**). In terms of phase evolution, the Raman spectra and *in situ* HR-TEM images (**Figure 2-2 c, e**) suggest a two-step crystallization event, with the first step being the nucleation and growth of $La_2Zr_2O_7$ nanocrystals in an amorphous film starting from 500 ºC and the second step being the lithiation of $La_2Zr_2O_7$ nanocrystals and the formation of tLLZO starting from 650 ºC. Importantly, the second-step lithiation process consumes Li in the amorphous phase, resulting in a lowered Li concentration in the aLLZO film at 650 ºC relative to that in the amorphous phase at 500 ºC–600 ºC. In terms of the LBU evolution among the amorphous phases, the maximum local structure disorder was observed near the crystallization peak temperature measured from DSC (**Figure 2-2 d**) at approximately 600 ºC, with the highest Li disordering and

largest Li coordination compared with those of the 500 °C and 650 °C phases (**Figure 8-16**). This, in turn, suggests the formation of a vast amount of face- and edge-shared LiO_x LBUs. The high Li local disordering hinders the Li^+ transport and thus results in low ionic conductivity and high ion-transport activation energy. Further increasing the annealing temperature to 650 ºC, a reduced Li disordering and smaller Li coordination numbers are observed (**Figure 8-16**). This implies that more corner- and edge-shared LBUs are formed with improved short-range ordering during the lithiation of $La_2Zr_2O_7$, which leads to the increase in ionic conductivity.

Next, we compare the structure and Li^+ transport properties between aLLZO and the 750 °C-annealed crystalline cLLZO. Unlike the amorphous structure, the HR-TEM images of the 750 °C sample suggest a polycrystalline film with cubic-phase lattice structure. In terms of the Li^+ transport, we see in **Figure 8-16** a sharp increase in the room-temperature Li^+ conductivity to 1.66 $\times 10^{-4}$ S cm^{-1}. The improved Li^+ transport is due to the formation of a LRO structure in the cLLZO film, which is connected by corner- and edge-shared Li, La, and Zr LBUs but not the face-shared ones. In addition, the Li local ordering significantly improved with a smaller Li coordination than the values obtained for the amorphous phases, resulting in a reduced activation energy barrier for Li^+ transport.

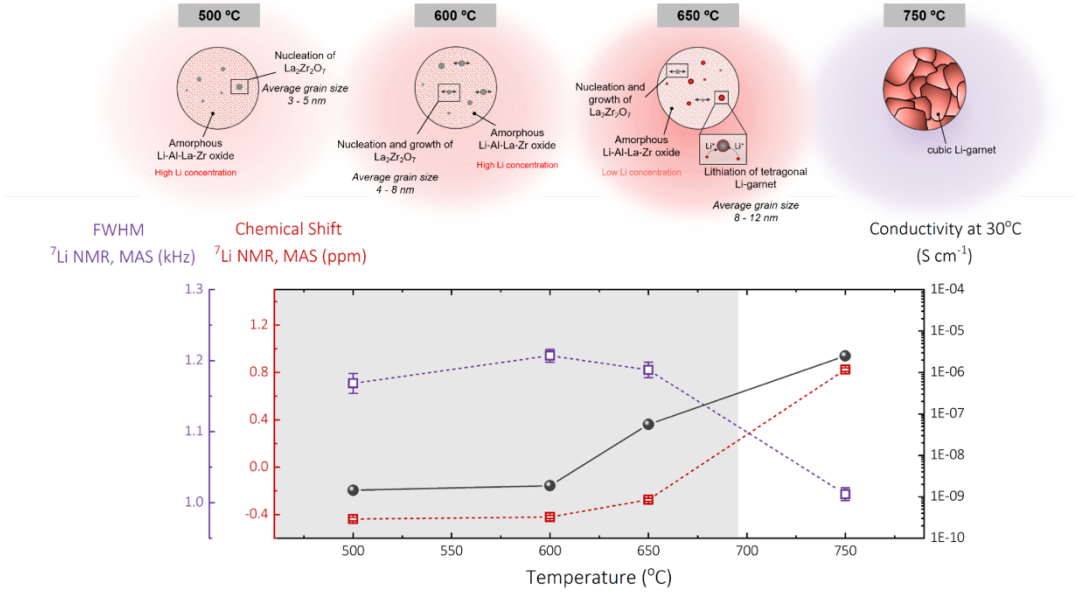

Figure 8-16. Comparison of Li local structure (chemical shift and FWHM of ^{7}Li MAS NMR spectra) and Li^+ conductivity as a function of annealing temperature (500 ºC, 600 ºC, 650 ºC, and 750 ºC). A more positive chemical shift of ^{7}Li MAS NMR represents smaller averaged coordination of Li, and vice versa. A larger FWHM indicates a higher degree of Li local structure disorder, and vice versa.

8.2. Appendix B: Supplementary Information to Chapter 3

Discovery and development history of aLLZO

We provide a summary of the discovery and development history of aLLZO in chronological order (**Figure 3-1 c**). This summary aims to provide background information for the field to better identify the achievements made thus far in aLLZO electrolyte development in the past 10 years and the challenges we are still facing. The first aLLZO film was synthesized by RF sputtering in 2012,[107] about 5 years after the first discovery and synthesis of crystalline cLLZO.[105] In this thesis, it was reported that the first aLLZO film provides a room-temperature (25 °C) conductivity of 4×10^{-7} S cm^{-1} with the lowest activation energy measured at 0.70 eV.[107] However, it was only until the year 2018, the polyamorphism nature of aLLZO was discovered with multiple amorphous phases and conductivities observed in aLLZO films prepared by PLD.[111] Not long after the discovery of polyamorphism in aLLZO, in 2020, the first aLLZO-based microbatteries were assembled with a Li metal anode, a $LiNbO_3$-coated $LiCoO_2$ cathode, and a 70-nm aLLZO thin film as the solid electrolyte layer.[183] The microbattery shows a remarkable cell performance that cycled at 10C for 500 cycles with over 85% capacity retention.[183] It was only until 2023 the high entropy nature of the aLLZO structures has been discussed, containing at least 4 unique LBUs, *i.e.,* LiO_4, LiO_6, ZrO_4, and LaO_8, that can be arranged in a greater variety of CRNs.

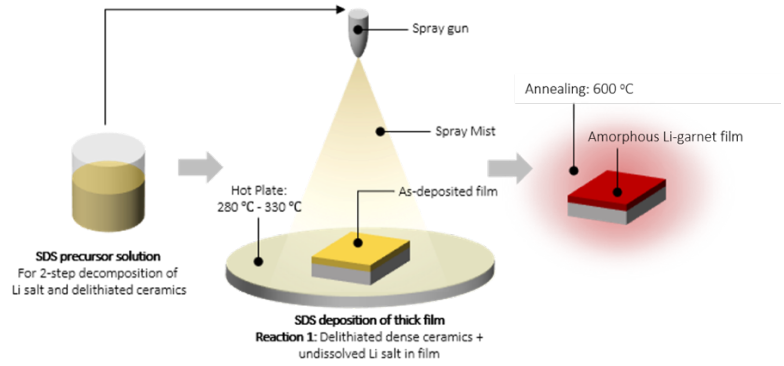

Chemical composition	Change of La stoichiometry compared to $Li_7La_3Zr_2O_{12}$
$Li_7La_{1.5}Zr_2O_{12-d}$	-50% La
$Li_7La_3Zr_2O_{12-d}$	Same
$Li_7La_{4.5}Zr_2O_{12-d}$	+50% La

Figure 8-17. Schematic illustration of the SDS setup used to deposit aLLZO films. SDS precursor solutions with three different La concentrations were prepared to synthesis aLLZO films with stoichiometry of $Li_7La_{1.5}Zr_2O_{12-d}$, $Li_7La_3Zr_2O_{12-d}$, and $Li_7La_{4.5}Zr_2O_{12-d}$. SDS schematic illustration adapted from Hood et al.[136]

Role of La on the microstructure and surface morphology of aLLZO films

To probe the effect of La concentration on the microstructure and morphology evolution, we collected surface SEM images for the 300 ºC as-deposited aLLZO films, and the surface and cross-sectional SEM images of 600 ºC annealed aLLZO films (**Figure 8-18 a**). Several interesting trends and features are observed. First, all films exhibit full surface coverage on MgO substrates. Second, the surface SEM images suggest that both the as-deposited films and the annealed aLLZO films exhibit a reduced surface roughness with increasing La concentration. Specifically, unlike the aLLZO films with low and medium La concentrations, we noticed some needle-like crystalline features with a length of 5-20 μm on the surface of the aLLZO film with high La concentration, which can be ascribed to the local nucleation during the crystallization process. Third, from the cross-sectional images of the aLLZO films, we observed an overall increased film density with reduced porosity and film thickness for aLLZO with a higher concentration of La (the schematic representation displayed in **Figure 8-18 b**). Specifically, the aLLZO with low La concentration has an average film thickness of 1.5 ± 0.5 μm, exhibiting a rough film surface with a high structure porosity. On the contrary, the aLLZO films with medium and high La concentrations reveal a generally dense microstructure with an average film thickness of 1.1 ± 0.3 and 1.0 ± 0.2 μm, respectively.

In short, we conclude that a higher La concentration in aLLZO can positively influence the film density and surface smoothness, which are generally more attractive for the application as solid electrolyte layers or protective coatings in solid-state or hybrid batteries. Nevertheless, aLLZO with low concentration of La may be of interest for the design of the electrolyte-cathode interface, for which a composite cathode-electrolyte gradient layer with finely tuned porous microstructure and high surface area has been proposed to reduce the interfacial resistance and improve the Li^+ transport dynamics.[129]

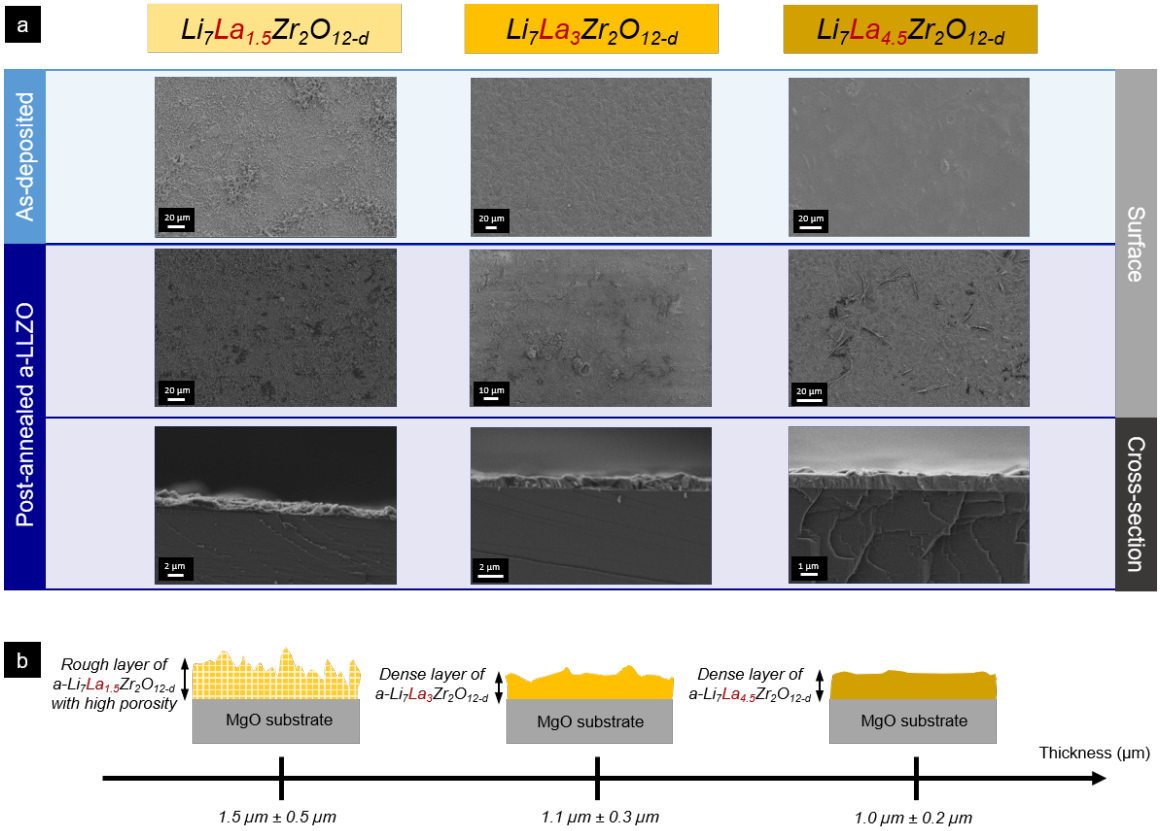

Figure 8-18. Effect of La concentration on the microstructure and surface morphology for the aLLZO films. **(a)** Surface SEM images of 300 ºC as-deposited aLLZO films in three compositions, *i.e.,* $Li_7La_{1.5}Zr_2O_{12-d}$, $Li_7La_3Zr_2O_{12-d}$, and $Li_7La_{4.5}Zr_2O_{12-d}$. Surface and cross-sectional SEM images of 600 ºC annealed aLLZO films in three compositions, *i.e.,* $Li_7La_{1.5}Zr_2O_{12-d}$, $Li_7La_3Zr_2O_{12-d}$, and $Li_7La_{4.5}Zr_2O_{12-d}$. All films exhibit full surface coverage of MgO substrates. **(b)** Schematic illustration of the density, surface morphology, and cross-sectional film thickness of the 600 ºC annealed aLLZO films in three compositions, *i.e.,* $Li_7La_{1.5}Zr_2O_{12-d}$, $Li_7La_3Zr_2O_{12-d}$, and $Li_7La_{4.5}Zr_2O_{12-d}$. The $Li_7La_{1.5}Zr_2O_{12-d}$ film presents a rough surface with high porosity. The $Li_7La_3Zr_2O_{12-d}$ film and $Li_7La_{4.5}Zr_2O_{12-d}$ film exhibit a dense microstructure with less surface roughness. The film thicknesses were measured at 1.5 ± 0.5 µm, 1 ± 0.3 µm, and 1.2 ± 0.2 µm, for the $Li_7La_{1.5}Zr_2O_{12-d}$, $Li_7La_3Zr_2O_{12-d}$, and $Li_7La_{4.5}Zr_2O_{12-d}$. Overall, higher La concentration improves the surface morphology and increases the film density, which leads to reduced cross-sectional film thickness.

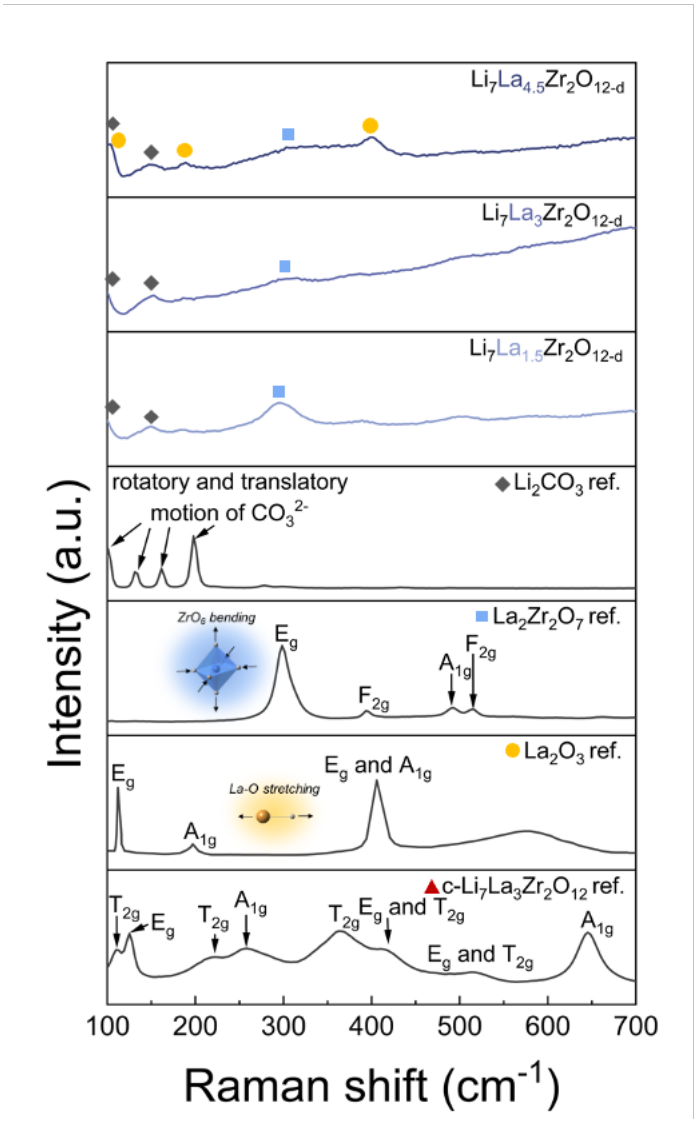

Figure 8-19. Raman spectra of 300 ºC as-deposited aLLZO films in three compositions, *i.e.,* $Li_7La_{1.5}Zr_2O_{12-d}$, $Li_7La_3Zr_2O_{12-d}$, and $Li_7La_{4.5}Zr_2O_{12-d}$. In all films, $La_2Zr_2O_7$ and Li_2CO_3 local ordering emerged in the surface layer. The formation of Li_2CO_3 on film surface is due to the film exposure to moisture air during the measurement. Additional reference spectra of Li_2CO_3, $La_2Zr_2O_7$, La_2O_3, and cubic $Li_7La_3Zr_2O_{12}$ are displayed in black. Inset: Graphic illustration of E_g mode (298 cm^{-1}) of ZrO_6 bending in $La_2Zr_2O_7$. Inset: Graphic illustration of E_g and A_{1g} modes (406 cm^{-1}) of La–O stretching in La_2O_3.

Interpreting data collected from fluctuation electron microscopy (FEM)

In the FEM method, nanobeam diffraction patterns are collected across nano-volumes of a sample. The variations in scattering intensity are attributed to the fluctuation incoherence that originated from random atom alignments (*i.e.,* statistical randomness, which can be eliminated by stacking and averaging the image intensity) or local structural ordering (*i.e.,* presence of medium range

order, MRO). If MRO presents in the film, the normalized variance of the image intensity will increase at specific scattering vectors (*i.e.,* peaks at certain scattering vectors), corresponding to the structural length scale of the MRO or average nearest neighbor distances.[384] In addition, the height (*i.e.,* intensity) and the full width at half maximum (*i.e.,* FWHM) of the normalized variance peak generally indicate the relative degree of MRO and the uniformity of the MRO distances (or the corresponding bond lengths), respectively. A more prominent peak suggests a greater degree of MRO. Conversely, a narrower peak indicates a more uniform distribution of MRO and higher consistency of the corresponding nearest neighbor bond lengths.[385]

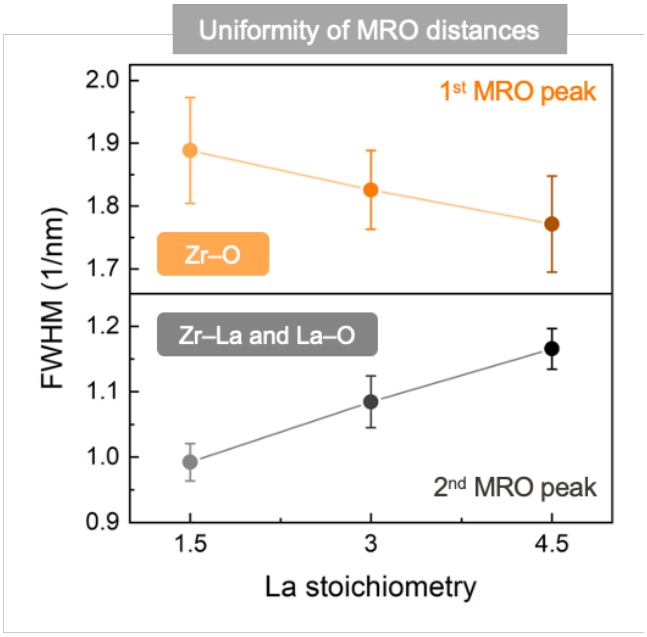

Figure 8-20. FWHM of the 1st and 2nd V(k) peaks corresponding to MRO as a function of the La concentration in aLLZO films. The 1st MRO peak is predominately attributable to Zr–O bonds and the 2nd MRO peak is predominately attributable to Zr–La and La–O bonds. The FWHM value suggests the uniformity of the MRO distance, *i.e.,* the corresponding bond lengths. The larger the FWHM, the less uniform the corresponding bond length is, and vice versa.

Table 8-6. Summary of nearest neighbor distances in aLLZO[138], cLLZO,[210] crystalline $La_2Zr_2O_7$,[235] and crystalline La_2O_3[228] from literature.

Material (structure, space group)	Nearest neighbor pairs	Bond length (Å)
Al-$Li_7La_3Zr_2O_{12}$ (aLLZO)	Zr-O	2.12
	Zr-La	3.47
Al-$Li_7La_3Zr_2O_{12}$ (cLLZO, *Ia-3d*)	Zr-O	2.12
	La-O	2.54 or 2.66 for different site of La
	Zr-La	3.68
$La_2Zr_2O_7$ (pyrochlore, *Fd-3m*)	Zr-O	2.11
	La-O	2.33 or 2.61 for different site of La
	Zr-La	3.81
La_2O_3 (trigonal, *P-3m1*)	La-O	2.37 or 2.73 for different site of La

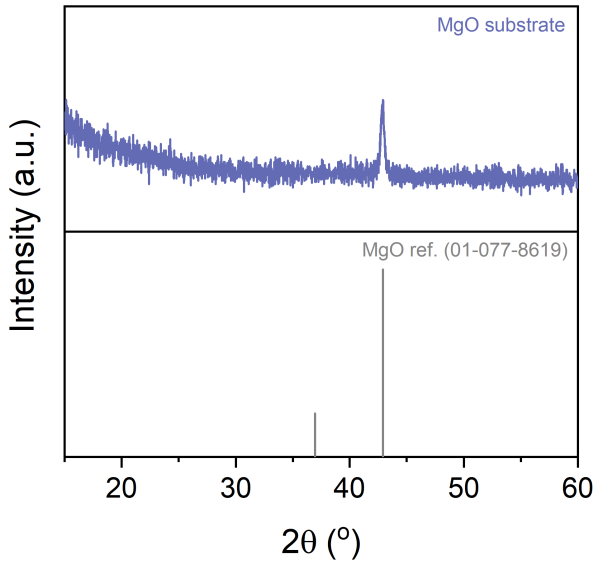

Figure 8-21. GIXRD patterns of the MgO substrate. References: MgO [00-045-0946].

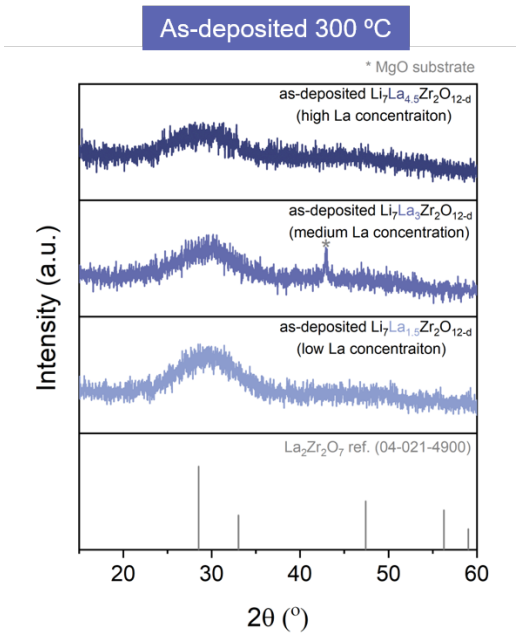

Figure 8-22. GIXRD patterns of 300 ºC as-deposited aLLZO films in three compositions, *i.e.,* $Li_7La_{1.5}Zr_2O_{12-d}$, $Li_7La_3Zr_2O_{12-d}$, and $Li_7La_{4.5}Zr_2O_{12-d}$. A broad peak centered at ~29º was detected in all three compositions, corresponding to the (222) plane of the pyrochlore $La_2Zr_2O_7$. A sharp peak at ~43º was detected, corresponding to the MgO substrate. References: $La_2Zr_2O_7$ [04-021-4900].

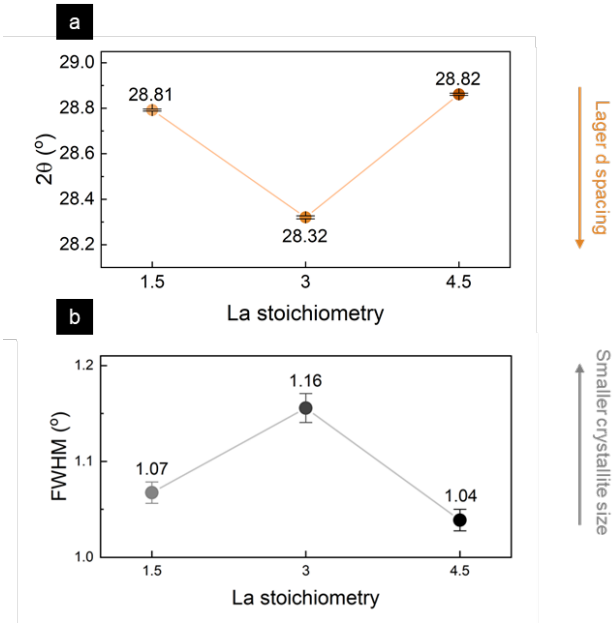

Figure 8-23. (a) The fitted 2θ value of the GIXRD peak that corresponding to the (222) plane in $La_2Zr_2O_7$ as a function of the La content in 600 ºC annealed aLLZO films. A smaller 2θ value indicates a larger d_{222} spacing, and vice versa. **(b)** The fitted FWHM of the GIXRD peak that corresponding to the (222) plane in $La_2Zr_2O_7$ as a function of the La concentration in 600 ºC annealed aLLZO films. A larger FWHM value indicates a smaller crystallite size, and vice versa.

8.3. Appendix C: Supplementary Information to Chapter 4

Table 8-7. Summary of processing routes and their corresponding maximum processing temperatures and processing time reported for bulk[105,129,168,169,252–256] and thin-film[98,100,113,114,116,120,136] cLLZO synthesis.

Forms of cLLZO	Processing routes			Chemical composition	Maximum processing temperature (time) used to achieve cLLZO
Bulk pellets or tapes	Conventional solid-state synthesis			$Li_7La_3Zr_2O_{12}$	1230 °C (36 h)
				$Li_{7-x}La_3Zr_{2-x}Nb_xO_{12}$ (x=0–2)	1200 °C (36 h)
				$Li_{6.5}La_3Zr_{1.5}Ta_{0.5}O_{12}$	1100 °C (5 h)
				Al-stabilized $Li_7La_3Zr_2O_{12}$	1230 °C (30 h)
	Sol-gel + sintering			$Li_{6.4}Al_{0.19}La_3Zr_2O_{11.8}$	1200 °C (36 h)
				$Li_{6.28}Al_{0.24}La_3Zr_2O_{12}$	1000 °C (4 h, with hot pressing)
	Co-precipitation + sintering			$Li_{6.75}La_3Zr_{1.75}Ta_{0.25}O_{12}$	1050 °C (1 h, with hot pressing)
				$Li_{6.15}La_3Zr_{1.75}Ta_{0.25}Al_{0.2}O_{12}$	
				$Li_{6.15}La_3Zr_{1.75}Ta_{0.25}Ga_{0.2}O_{12}$	
	Rapid thermal processing			$Li_{6.5}La_3Zr_{1.5}Ta_{0.5}O_{12}$	1500 °C (10 s)
				Al-stabilized $Li_7La_3Zr_2O_{12}$	1300 °C (15 s, with electric field)
Thin films	Deposition + phase formation	Vacuum-based deposition	PLD	$Li_{6.25}Al_{0.25}La_3Zr_2O_{12}$	660 °C (~1 h)
				Al-stabilized $Li_7La_3Zr_2O_{12}$	600 °C (24 h)
			RF sputtering	$Li_{7-3x}Ga_xLa_3Zr_2O_{12}$, (x=0.14–0.20)	650 °C (5 h)
			CVD	$Li_7La_3Zr_2O_{12}$	900-950 °C (15 min)
		Wet-chemical deposition	Spin coating	Al-stabilized $Li_7La_3Zr_2O_{12}$	600-800 °C (10 min)
			Dip coating	Al-stabilized $Li_7La_3Zr_2O_{12}$	900 °C
			SDS	$Li_{6.25}Al_{0.25}La_3Zr_2O_{12}$	750 °C (30 min)

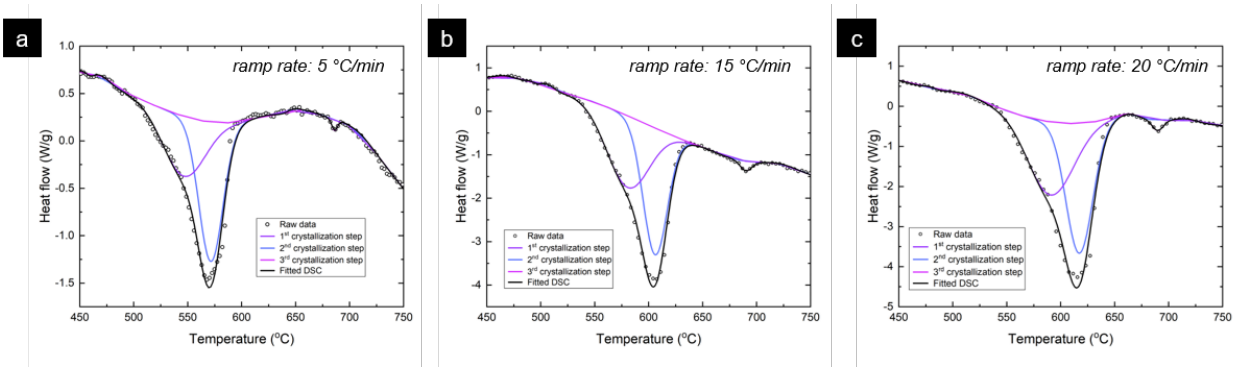

Figure 8-24. Fitting and deconvolution of the LLZO crystallization peaks for the DSC scans measured at a ramp rate of **(a)** 5, **(b)** 15, and **(c)** 20 ºC min^{-1}. For each presented DSC, two peaks denoted as the 1st and the 2nd crystallization steps, were deconvolved from the endothermic peak ranging between 490 ºC and 670 ºC, corresponding to the nucleation and growth of $La_2Zr_2O_7$ nanocrystals and the lithiation and phase transformation from $La_2Zr_2O_7$ to tLLZO, respectively. The minor endothermic peak centered at ~680 ºC was identified as the 3rd crystallization step, corresponding to the transformation from tLLZO to cLLZO with local Li reordering.

Table 8-8. Summary of the phase transformation peak temperatures (T_p) and the phase transformation enthalpy changes (ΔH) for the 1st, 2nd, and 3rd crystallization steps obtained from different DSC ramp rates.

Ramp rate	5 °C min^{-1}	10 °C min^{-1}	15 °C min^{-1}	20 °C min^{-1}
T_{p1}	546	569	581	591
T_{p2}	571	594	606	617
T_{p3}	686	689	690	690
ΔH_1	5.85	5.54	5.41	4.73
ΔH_2	8.05	6.53	5.48	5.02
ΔH_3	0.12	0.27	0.20	0.16

Developing TTT Diagram based on DSC data

TTT diagrams typically have C-shaped curves because they show the progression of a phase transformation as a function of temperature and time.[263,269,386] The shape of the curve reflects the rate at which the transformation occurs at different temperatures and times, which is influenced by the nucleation and growth process of the new phase.[261,263,269,386] During the nucleation process, small clusters or "seeds" of the new phase form within the material. These seeds then grow and merge to form the new phase, a process known as growth. The rate of nucleation and growth is influenced by the temperature, time, and other processing conditions, and determines the overall rate of transformation. At the start of the transformation, the rate of nucleation is low, and the rate of growth is also low, resulting in a relatively slow rate of transformation. As the temperature increases, the rate of nucleation increases and the rate of growth also increases, leading to a faster rate of transformation. This is reflected in the steep slope of the curve in the initial stages of the transformation. As the temperature continues to increase, the rate of transformation begins to level off, and the slope of the curve becomes less steep. This is because the material has reached the point where the rate of nucleation and growth are balanced, and the transformation is occurring at its maximum rate. As the temperature approaches the maximum temperature at which the transformation can occur, the rate of transformation begins to slow down again. This is reflected in the downward slope of the curve as it approaches the end of the transformation. Overall, the C-shaped curve of a TTT diagram reflects the changing rate of transformation as a function of temperature and time, and can be used to understand the relationships between these variables and the evolution of the microstructure.[386,387]

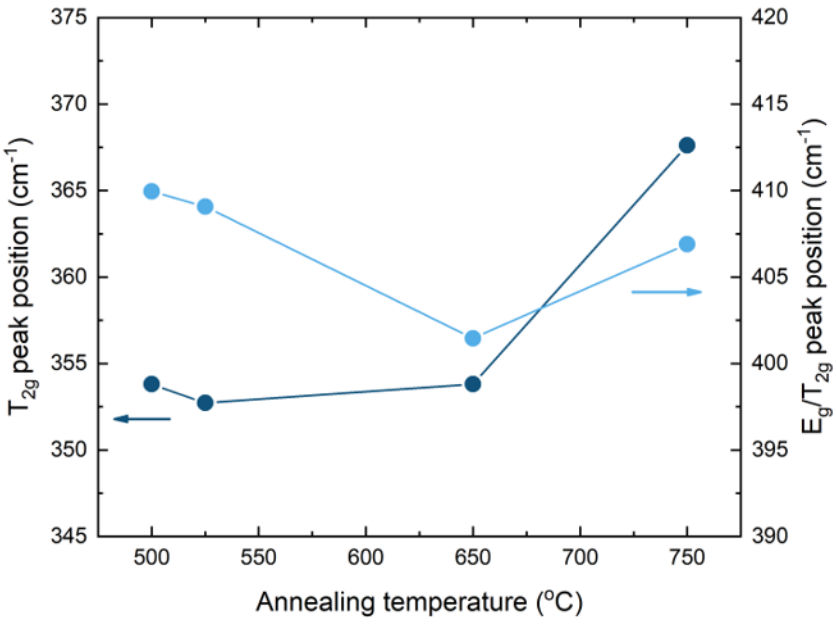

Figure 8-25. Summary of the T_{2g} and E_g/T_{2g} peak positions (O–Li–O vibration) for cLLZO synthesized via different post-annealing routes, including route I of 500 ºC for 10 h, route II of 525 ºC for 10 h, route III of 650 ºC for 5 h, and route IV of 750 ºC for 15 min. Variation in peak positions suggests changes in the Li–O bond distance, structure compaction, and local strain among cLLZO films processed via different routes.

8.4. Appendix D: Supplementary Information to Chapter 5

Table 8-9. Summary of Type III CO_x, NO_x, and SO_x gas sensors using different types of solid electrolytes and sensing electrolytes from the literature.[123,328,329,333,334,337–340,342–347,349–352,356,360,362,364–366,368–370,372,388–390]

Ion-conductor	Gas sensed	Potentiometric Type III Sensors: Reference electrolde|Electrolyte|Sensing Electrode	Operating Temperature [°C]	Concentration range [ppm]	Approx. response time [s]	Sensitivity [mV/dec]	Electrolyte processing technique	Electrolyte dimentions [mm]
O2- Conductors	NOx	Pt, NOx+O2+N2|YSZ| Au-YSZ, NOx+O2+N2	450	20-100	480	52	Screen-printed on alumina substrate followed by sintering	Thick film
			500		150	-		
		Pt, air|YSZ| CdCr2O4, NOx+air, Pt	550	20-200	30	40 @500C	Commercial	Tube: OD-8, ID-5.
		Pt-Y, NO+O2+N2|YSZ|WO3, NO+O2+N2, Pt	425	NO: 5-80 ppb using 30 sensor array	180	-	Commercial	Pellet: D-10; Thickness-1
		Pt,NOx+air|YSZ| La2CuO4, NOx+air, Pt	500	NO: 50-650	30	9.72	Commercial	Substrate: 20X10X0.1
	SO2	Pt, air|MgO-PSZ|Li2SO4-Ca2SO4-SiO2|SO2+air, Pt	650	2-200	15	91.6	Commercial	Tube: OD-8; ID-5
		Ag|Ag-β''-alumina|SO2+ SO3+O2, Pt	550	10-50000	60		Commercial	Tube: OD-10; ID-8; Length-40
		Ag|Ag-β''-alumina|SO2+ SO3+O2, Pt	700	20-200	12	96.5	Commercial	Tube
		Pt, SO3, O2|Sr-β-Al2O3(+PSZ)|NASICON(+glass)|Na2SO4|O2, SO3, Pt	709	1-1000	60		Commercial tube Conventional NASICON synthesis	Tube+pellet; Length-14; D-6
NASICON	CO2	Pt|NASICON|Li2CO3–BaCO3|CO2, air, Pt	500	300-750	50	-	Screen-printed on alumina substrate followed by sintering	Thick film
		Pt|NASICON|Li2CO3–BaCO3|CO2, air, Au	500	400-2000	60	77.0	Conventional high temperature solid-state synthesis	Pellet: D-8; Thickness-0.5
		C/Pt|NASICON|Na2CO3|CO2, air, Pt	465	100-10000	60	73.0	Conventional high temperature solid-state synthesis	Pellet
		Pt|NASICON|Li2CO3–BaCO3|CO2, air, Pt	470	1000-10000	12	73.0	Screen-printed on alumina substrate followed by sintering	Thick film
	NO2	air, Pt|NASICON|NaNO2, Au, NO2+air	150	0.1-200	120	84	Conventional high temperature solid-state synthesis	Pellet; D-8; Thickness-0.5
		air, Pt|NASICON|Pb2[Ru1.5Pb0.5]O7-y, Au, NO+air	400	20-200	600	40	Conventional high temperature solid-state synthesis	Pellet; D-11; Thickness-0.8
		air,Au|NASICON|NaNO2-Li2CO3, ITO, Au, NO2+air	30	2-7	180	-	Conventional high temperature solid-state synthesis	Pellet; D-9; Thickness-1.2
	SO2	Pt, SO2, O2|Na2SO4-BaSO4|NASICON|Na2SiO3|Pt	550	5-95	180	164	Conventional high temperature solid-state synthesis	Pellet
		Au, O2+SO2, LaxSm1-xFeO3|NASICON|O2+SO2, Au	275	0.005-5	300	0.2-5 ppm (86 mV/dec @275C) 0.005-0.2 ppm (8 mV/dec @275C)	Conventional high temperature solid-state synthesis	Thick film
		Au, O2+SO2,(V2O5-WO3-TiO2)|NASICON|O2+SO2, Au	600	20-200	300	85@700C	Screen-printed on alumina substrate followed by sintering	Thick film
Li3PO4	CO2	Au|Li2TiO3–TiO2|Li3PO4 |Li2CO3–BaCO3|CO2, air, Au	500	500-1000	20	77.19	Conventional high temperature solid-state synthesis	Pellet; D-12; Thickness-1.0
		Au, Li2TiO3|Li3PO4|Li2CO3|CO2, air, Au	500	500-5000	60	75.0	Thermal evaporation on alumina substrate followed by sintering	Thick film: Thickness-1 um
		Au|Li2TiO3–TiO2|Li3PO4|CO2, air, Au	530	250-5000	60	41.2	Thermal evaporation on alumina substrate followed by sintering	Thick film: Thickness-0.8 um
		Au, Li2TiO3–TiO2|Li3PO4|Li2CO3, air, Au	500	250-5000	300	For 1.2um: 61	Thermal evaporation on alumina substrate followed by sintering	Thick film: Thickness-0.3, 0.65, 1.2 um
		Au|Li3PO4|Li2CO3, air, Au	500	250-2500	10	76.7	Thermal evaporation on alumina substrate followed by sintering	Thick film: Thickness-1.2 um
	SO2	Au, SO2, O2|Li3PO4-Li2SiO3|Li2SO4-V2O5|SO2+O2,Au	450	10-100	18	57.19	RF sputtering	Thick film: Thickness-1 um
		Au, SO2+O2|Li3PO4|Li2SO4-V2O5|SO2+O2,Au	500	0-100	300	32.47	Resistance heating evaporation followed by sintering	Thick film: Thickness-1 um
Other Li-conducting electrolyets	CO2	Au|LiCoO2 + 5 mol% Co3O4|Li2.88PO3.73N0.14|Li2CO3|CO2, air, Au	500	250-3000	20	68.8	Conventional high temperature solid-state synthesis	Pellet: D-12; Thickness- 2.5
		Pt, CO2(po), air|LISICON|Li2CO3|CO2, air, Pt	500	1000-100000	300	70-80	Screen-printed on alumina substrate followed by sintering	Thick film: Thickness-20 um
		ITO, air|LISICON|ITO–Li2CO3–BaCO3|CO2, air	30	250-2500	300	20.0	Conventional high temperature solid-state synthesis	Pellet: D-10; Thickness- 1.0
		Li2TiO3–TiO2|Li0.35La0.55TiO3|Li2CO3|CO2, air, Au	450	500-4000	60	70.3	Conventional high temperature solid-state synthesis	Pellet: D-5.4; Thickness- 0.9
		Au|Li0.36WO3|Li6BaLa2Ta2O12|Li2CO3|CO2, air, Au	500	100-100000	60	75	Conventional high temperature solid-state synthesis	Pellet: D-8; Thickness- 1.0
		Au|Li6.75La3Zr1.75Ta0.25O12-d|Li2CO3|CO2, air, Au	280	400-4000	70	-	Conventional high temperature solid-state synthesis	Pellet: D-12; Thickness- 1.5
			321		55	58.2		
			360		40	-		
	NOx	air,Au|LISICON|NaNO2-ITO, Au, NO2+air	30	2-7	300	41.4	Conventional high temperature solid-state synthesis	Pellet: D-10; Thickness- 1.0
	SO2	Au, O2+SO2, 0.7La2O2SO4-0.3(0.8Li2SO4+0.2K2SO4)|Zr39/40TaP2.9W0.1O12|Zr, Pt	400	500-3000	240	66.7	Conventional high temperature solid-state synthesis	Pellet

9. References

1. Becerra, J. The digital revolution is not about technology – it's about people. *World Economic Forum* (2017).
2. Atzori, L., Iera, A. & Morabito, G. The Internet of Things: A survey. *Computer Networks* **54**, 2787–2805 (2010).
3. Gerrish, H. H. *Transistor Electronics*. (Goodheart-Willcox, 1969).
4. Anton Shilov. Samsung completes development of 5nm EUV process technology. (2019).
5. Anton Shilov. TSMC announces performance-enhanced 7nm & 5nm process technologies. *AnandTech* (2019).
6. Olofsson, A. *Silicon Compilers - Version 2.0*. http://www.ispd.cc/slides/2018/k2.pdf (2018).
7. von Neumann, J. & Godfrey, M. D. First Draft of a Report on the EDVAC. *IEEE Annals of the History of Computing* **15**, (1993).
8. Hruska, J. Microfluidics: DARPA is betting embedded water droplets could cool next-gen chips. *ExtremeTech* (2016).
9. NanoMarkets. Opportunities for Thin-film Batteries. https://www.slideshare.net/NanoMarkets/thin-batteries (2014).
10. Frank, R. What's happening in air quality sensing? *Sensor Tips* (2019).
11. Maier, J. Space charge regions in solid two-phase systems and their conduction contribution-I. Conductance enhancement in the system ionic conductor-'inert' phase and application on AgC1:Al2O3 and AgC1:SiO2. *Journal of Physics and Chemistry of Solids* **46**, 309–320 (1985).
12. Bates, J. B. *et al.* Thin-Film Rechargeable Lithium Batteries. *J Power Sources* **54**, 58–62 (1995).
13. Wu, J. F. *et al.* Gallium-doped Li7La3Zr2O12 garnet-type electrolytes with high lithium-ion conductivity. *ACS Appl Mater Interfaces* **9**, 1542–1552 (2017).
14. Sastre, J. *et al.* Lithium Garnet Li7La3Zr2O12 Electrolyte for All-Solid-State Batteries: Closing the Gap between Bulk and Thin Film Li-Ion Conductivities. *Adv Mater Interfaces* **7**, 2000425 (2020).
15. Kwon, W. J. *et al.* Enhanced Li+ conduction in perovskite Li3XLa2/3-x□1/3-2xTiO3 solid-electrolytes via microstructural engineering. *J Mater Chem A Mater* **5**, 6257–6262 (2017).
16. Furusawa, S. I., Tabuchi, H., Sugiyama, T., Tao, S. & Irvine, J. T. S. Ionic conductivity of amorphous lithium lanthanum titanate thin film. *Solid State Ion* **176**, 553–558 (2005).
17. Bucharsky, E. C., Schell, K. G., Hintennach, A. & Hoffmann, M. J. Preparation and characterization of sol-gel derived high lithium ion conductive NZP-type ceramics Li1 + x AlxTi2 - X(PO4)3. *Solid State Ion* **274**, 77–82 (2015).

18. Chen, H., Tao, H., Zhao, X. & Wu, Q. Fabrication and ionic conductivity of amorphous Li-Al-Ti-P-O thin film. *J Non Cryst Solids* **357**, 3267–3271 (2011).

19. Yu, X., Bates, J. B., Jellison, G. E. & Hart, F. X. A Stable Thin-Film Lithium Electrolyte: Lithium Phosphorus Oxynitride. *J Electrochem Soc* **144**, 524–532 (1997).

20. Zhu, Y., He, X. & Mo, Y. Origin of Outstanding Stability in the Lithium Solid Electrolyte Materials: Insights from Thermodynamic Analyses Based on First-Principles Calculations. *ACS Appl Mater Interfaces* **7**, 23685–23693 (2015).

21. Faraday, M. *Experimental researches in electricity*. *Experimental Researches in Electricity* vol. 1 (Read Books Ltd, 2016).

22. Knödler, R. Thermal properties of sodium-sulphur cells. *J Appl Electrochem* **14**, 39–46 (1984).

23. Yung-Fang Yu Yao & Kummer, J. T. Ion exchange properties of and rates of ionic diffusion in beta-alumina. *Journal of Inorganic and Nuclear Chemistry* **29**, 2453–2475 (1967).

24. Knauth, P. & Tuller, H. L. Solid-state ionics: Roots, status, and future prospects. *Journal of the American Ceramic Society* **85**, 1654–1680 (2002).

25. Johnson, R. T. Ionic Conductivity in Solid Electrolytes Based on Lithium Aluminosilicate Glass and Glass-Ceramic. *J Electrochem Soc* **123**, 680 (1976).

26. Kennedy, J. H. & Yang, Y. A Highly Conductive Li+-Glass System: (1 − x) (0.4SiS2 - 0.6Li2 S) - xLiI. *J Electrochem Soc* **133**, 2437–2438 (1986).

27. Mercier, R., Malugani, J. P., Fahys, B. & Robert, G. Superionic conduction in Li2S - P2S5 - LiI - glasses. *Solid State Ion* **5**, 663–666 (1981).

28. Pizzini, S. Ionic conductivity in lithium compounds. *J Appl Electrochem* **1**, 153–161 (1971).

29. Dudney, N. J., Bates, J. B., Zuhr, R. A., Luck, C. F. & Robertson, J. D. Sputtering of lithium compounds for preparation of electrolyte thin films. *Solid State Ion* **53**, 655–661 (1992).

30. Bates, J. B. *et al.* Electrical properties of amorphous lithium electrolyte thin films. *Solid State Ion* **53**, 647–654 (1992).

31. Meesala, Y., Jena, A., Chang, H. & Liu, R. S. Recent Advancements in Li-Ion Conductors for All-Solid-State Li-Ion Batteries. *ACS Energy Letters* vol. 2 2734–2751 Preprint at https://doi.org/10.1021/acsenergylett.7b00849 (2017).

32. Wang, B., Kwak, B. S., Sales, B. C. & Bates, J. B. Ionic conductivities and structure of lithium phosphorus oxynitride glasses. *J Non Cryst Solids* **183**, 297–306 (1995).

33. Bates, J. B. *et al.* Fabrication and characterization of amorphous lithium electrolyte thin films and rechargeable thin-film batteries. *J Power Sources* **43**, 103–110 (1993).

34. Patil, A. *et al.* Issue and challenges facing rechargeable thin film lithium batteries. *Mater Res Bull* **43**, 1913–1942 (2008).

35. Lacivita, V. *et al.* Resolving the Amorphous Structure of Lithium Phosphorus Oxynitride (Lipon). *J Am Chem Soc* **140**, 11029–11038 (2018).

36. Lacivita, V., Artrith, N. & Ceder, G. Structural and Compositional Factors That Control the Li-Ion Conductivity in LiPON Electrolytes. *Chemistry of Materials* **30**, 7077–7090 (2018).

37. Kuwata, N. *et al.* Lithium diffusion coefficient in amorphous lithium phosphate thin films measured by secondary ion mass spectroscopy with isotope exchange methods. *Solid State Ion* **294**, 59–66 (2016).

38. Ivanov-Shitz, A. K., Kireev, V. v., Mel'nikov, O. K. & Demianets, L. N. Growth and ionic conductivity of γ-Li3PO4. *Crystallography Reports* **46**, 864–867 (2001).

39. Balaish, M. *et al.* Processing thin but robust electrolytes for solid-state batteries. *Nat Energy* **6**, 227–239 (2021).

40. Johnson, R. T. *et al.* A Stable Thin-Film Lithium Electrolyte: Lithium Phosphorus Oxynitride. *Solid State Ion* **1**, 173–178 (2018).

41. Su, Y. *et al.* LiPON thin films with high nitrogen content for application in lithium batteries and electrochromic devices prepared by RF magnetron sputtering. *Solid State Ion* **282**, 63–69 (2015).

42. Hamon, Y. *et al.* Influence of sputtering conditions on ionic conductivity of LiPON thin films. *Solid State Ion* **177**, 257–261 (2006).

43. Kozen, A. C., Pearse, A. J., Lin, C. F., Noked, M. & Rubloff, G. W. Atomic Layer Deposition of the Solid Electrolyte LiPON. *Chemistry of Materials* **27**, 5324–5331 (2015).

44. Ruzmetov, D. *et al.* Electrolyte stability determines scaling limits for solid-state 3D Li ion batteries. *Nano Lett* **12**, 505–511 (2012).

45. West, W. C. *et al.* Reduction of charge-transfer resistance at the solid electrolyte - Electrode interface by pulsed laser deposition of films from a crystalline Li2PO2N source. *J Power Sources* **312**, 116–122 (2016).

46. Kuwata, N., Iwagami, N., Matsuda, Y., Tanji, Y. & Kawamura, J. Thin Film Batteries with Li3PO4 Solid Electrolyte Fabricated by Pulsed Laser Deposition. *ECS Trans* **16**, 53 (2009).

47. Kuwata, N., Iwagami, N., Tanji, Y., Matsuda, Y. & Kawamura, J. Characterization of Thin-Film Lithium Batteries with Stable Thin-Film Li[sub 3]PO[sub 4] Solid Electrolytes Fabricated by ArF Excimer Laser Deposition. *J Electrochem Soc* **157**, A521 (2010).

48. Li, J., Ma, C., Chi, M., Liang, C. & Dudney, N. J. Solid electrolyte: The key for high-voltage lithium batteries. *Adv Energy Mater* **5**, 1401408 (2015).

49. Fuller, E. J. *et al.* Li-Ion Synaptic Transistor for Low Power Analog Computing. *Advanced Materials* **29**, 1604310 (2017).

50. Bachman, J. C. *et al.* Inorganic Solid-State Electrolytes for Lithium Batteries: Mechanisms and Properties Governing Ion Conduction. *Chem Rev* **116**, 140–162 (2016).

51. Knauth, P. Inorganic solid Li ion conductors: An overview. *Solid State Ion* **180**, 911–916 (2009).

52. Hong, H. Y. P. Crystal structures and crystal chemistry in the system Na1+xZr2SixP3-xO12. *Mater Res Bull* **11**, 173–182 (1976).

53. Goodenough, J. B., Hong, H. Y. P. & Kafalas, J. A. Fast Na+-ion transport in skeleton structures. *Mater Res Bull* **11**, 203–220 (1976).

54. Petit, D., Colomban, P., Collin, G. & Boilot, J. P. Fast ion transport in LiZr2(PO4)3: Structure and conductivity. *Mater Res Bull* **21**, 365–371 (1986).

55. Aono, H., Sugimoto, E., Sadaoka, Y., Imanaka, N. & Adachi, G. Ionic Conductivity of Solid Electrolytes Based on Lithium Titanium Phosphate. *J Electrochem Soc* **137**, 1023 (1990).

56. Arbi, K., Tabellout, M., Lazarraga, M. G., Rojo, J. M. & Sanz, J. Non-Arrhenius conductivity in the fast lithium conductor Li1.2Ti1.8Al0.2(PO4)3: A Li7 NMR and electric impedance study. *Phys Rev B Condens Matter Mater Phys* **72**, 094302 (2005).

57. Arbi, K., Hoelzel, M., Kuhn, A., García-Alvarado, F. & Sanz, J. Structural factors that enhance lithium mobility in fast-ion Li 1+xTi2-xAlx(PO4)3 ($0 \leq x \leq 0.4$) conductors investigated by neutron diffraction in the temperature range 100-500 K. *Inorg Chem* **52**, 9290–9296 (2013).

58. Cretin, M. & Fabry, P. Comparative study of lithium ion conductors in the system Li1+xAlxA2-xIV (PO4)3 with AIV=Ti or Ge and $0 \leq x \leq 0{\cdot}7$ for use as Li+ sensitive membranes. *J Eur Ceram Soc* **19**, 2931–2940 (1999).

59. Zhu, Y., He, X. & Mo, Y. First principles study on electrochemical and chemical stability of solid electrolyte-electrode interfaces in all-solid-state Li-ion batteries. *J Mater Chem A Mater* **4**, 3253–3266 (2016).

60. Hartmann, P. *et al.* Degradation of NASICON-type materials in contact with lithium metal: Formation of mixed conducting interphases (MCI) on solid electrolytes. *Journal of Physical Chemistry C* **117**, 21064–21074 (2013).

61. West, W. C., Whitacre, J. F. & Lim, J. R. Chemical stability enhancement of lithium conducting solid electrolyte plates using sputtered LiPON thin films. *J Power Sources* **126**, 134–138 (2004).

62. Jadhav, H. S., Kalubarme, R. S., Jadhav, A. H. & Seo, J. G. Highly stable bilayer of LiPON and B2O3 added Li1.5Al0.5Ge1.5(PO4) solid electrolytes for non-aqueous rechargeable Li-O2 batteries. *Electrochim Acta* **199**, 126–132 (2016).

63. Xiao, W., Wang, J., Fan, L., Zhang, J. & Li, X. Recent advances in Li1+xAlxTi2−x(PO4)3 solid-state electrolyte for safe lithium batteries. *Energy Storage Mater* **19**, 379–400 (2019).

64. Wu, X. M., Chen, S., Mai, F. R., Zhao, J. H. & He, Z. Q. Influence of the annealing technique on the properties of Li ion-conductive Li1.3Al0.3Ti1.7(PO4)(3) films. *Ionics (Kiel)* **19**, 589–593 (2013).

65. Popovici, D., Nagai, H., Fujishima, S. & Akedo, J. Preparation of Lithium Aluminum Titanium Phosphate Electrolytes Thick Films by Aerosol Deposition Method. *Journal of the American Ceramic Society* **94**, 3847–3850 (2011).

66. Ling, Q. *et al.* Preparation and electrical properties of amorphous Li-Al-Ti-P-O thin film electrolyte. *Mater Lett* **169**, 42–45 (2016).

67. Tan, G., Wu, F., Li, L., Liu, Y. & Chen, R. Magnetron sputtering preparation of nitrogen-incorporated lithium-aluminum-titanium phosphate based thin film electrolytes for all-solid-state lithium ion batteries. *Journal of Physical Chemistry C* **116**, 3817–3826 (2012).

68. Akedo, J. Room temperature impact consolidation (RTIC) of fine ceramic powder by aerosol deposition method and applications to microdevices. *Journal of Thermal Spray Technology* **17**, 181–198 (2008).

69. Akedo, J. & Lebedev, M. Piezoelectric properties and poling effect of Pb(Zr, Ti)O3 thick films prepared for microactuators by aerosol deposition. *Appl Phys Lett* **77**, 1710–1712 (2000).

70. Imanaka, Y., Takenouchi, M. & Akedo, J. Ceramic dielectric film for microwave filter deposited at room temperature. *J Cryst Growth* **275**, e1313–e1319 (2005).

71. Nakada, M., Ohashi, K. & Akedo, J. Electro-optic properties of Pb(Zr1-xTix)O 3 (X = 0, 0.3, 0.6) films prepared by aerosol deposition. *Japanese Journal of Applied Physics, Part 2: Letters* **44**, L1088 (2005).

72. Stramare, S., Thangadurai, V. & Weppner, W. Lithium Lanthanum Titanates: A Review. *Chemistry of Materials* **15**, 3974–3990 (2003).

73. Yashima, M., Itoh, M., Inaguma, Y. & Morii, Y. Crystal structure and diffusion path in the fast lithium-ion conductor La0.62Li0.16TiO3. *J Am Chem Soc* **127**, 3491–3495 (2005).

74. Kitaoka, K., Kozuka, H., Hashimoto, T. & Yoko, T. Preparation of La0.5Li0.5TiO3 perovskite thin films by the sol-gel method. *J Mater Sci* **32**, 2063–2070 (1997).

75. Inaguma, Y. *et al.* High ionic conductivity in lithium lanthanum titanate. *Solid State Commun* **86**, 689–693 (1993).

76. Takada, K. Progress and prospective of solid-state lithium batteries. *Acta Mater* **61**, 759–770 (2013).

77. García-Martín, S., Amador, U., Morata-Orrantia, A., Rodríguez-Carvajal, J. & Alario-Franco, M. Á. Structure, microstructure, composition and properties of lanthanum lithium titanates and some substituted analogues. *Z Anorg Allg Chem* **635**, 2363–2373 (2009).

78. Mei, A. *et al.* Role of amorphous boundary layer in enhancing ionic conductivity of lithium-lanthanum-titanate electrolyte. *Electrochim Acta* **55**, 2958–2963 (2010).

79. Bohnke, O., Emery, J. & Fourquet, J. L. Anomalies in Li+ ion dynamics observed by impedance spectroscopy and 7Li NMR in the perovskite fast ion conductor (Li3xLa2/3-x□1/3-2x)TiO3. *Solid State Ion* **158**, 119–132 (2003).

80. Aguesse, F., López Del Amo, J. M., Roddatis, V., Aguadero, A. & Kilner, J. A. Enhancement of the grain boundary conductivity in ceramic Li0.34La0.55TiO3 electrolytes in a moisture-free processing environment. *Adv Mater Interfaces* **1**, 1300143 (2014).

81. Ma, C. *et al.* Atomic-scale origin of the large grain-boundary resistance in perovskite Li-ion-conducting solid electrolytes. *Energy Environ Sci* **7**, 1638–1642 (2014).

82. Li, C. L., Zhang, B. & Fu, Z. W. Physical and electrochemical characterization of amorphous lithium lanthanum titanate solid electrolyte thin-film fabricated by e-beam evaporation. *Thin Solid Films* **515**, 1886–1892 (2006).

83. Kim, S. *et al.* Low temperature synthesis and ionic conductivity of the epitaxial Li 0.17La0.61TiO3 film electrolyte. *CrystEngComm* **16**, 1044–1049 (2014).

84. Aguesse, F. *et al.* Microstructure and ionic conductivity of LLTO thin films: Influence of different substrates and excess lithium in the target. *Solid State Ion* **272**, 1–8 (2015).

85. Ulusoy, S., Gulen, S., Aygun, G., Ozyuzer, L. & Ozdemir, M. Characterization of thin film Li0.5La0.5Ti1−xAlxO3 electrolyte for all-solid-state Li-ion batteries. *Solid State Ion* **324**, 226–232 (2018).

86. Xiong, Y., Tao, H., Zhao, J., Cheng, H. & Zhao, X. Effects of annealing temperature on structure and opt-electric properties of ion-conducting LLTO thin films prepared by RF magnetron sputtering. *J Alloys Compd* **509**, 1910–1914 (2011).

87. Zheng, Z. F., Song, S. D. & Wang, Y. Sol-gel-processed amorphous lithium ion electrolyte thin films: Structural evolution, theoretical considerations, and ion transport processes. *Solid State Ion* **287**, 60–70 (2016).

88. Teranishi, T., Ishii, Y., Hayashi, H. & Kishimoto, A. Lithium ion conductivity of oriented Li0.33La0.56TiO3 solid electrolyte films prepared by a sol-gel process. *Solid State Ion* **284**, 1–6 (2016).

89. Le, H. T. T., Ngo, D. T., Kim, Y. J., Park, C. N. & Park, C. J. A perovskite-structured aluminium-substituted lithium lanthanum titanate as a potential artificial solid-electrolyte interface for aqueous rechargeable lithium-metal-based batteries. *Electrochim Acta* **248**, 232–242 (2017).

90. Ahn, J. K. & Yoon, S. G. Characteristics of amorphous lithium lanthanum titanate electrolyte thin films grown by PLD for use in rechargeable lithium microbatteries. *Electrochemical and Solid-State Letters* **8**, A75 (2005).

91. Schmitt, R. *et al.* Accelerated Ionic Motion in Amorphous Memristor Oxides for Nonvolatile Memories and Neuromorphic Computing. *Adv Funct Mater* **29**, 1804782 (2019).

92. Thangadurai, V. & Weppner, W. Li6ALa2Ta2O12 (A=Sr, Ba): Novel garnet-like oxides for fast lithium ion conduction. *Adv Funct Mater* **15**, 107–112 (2005).

93. Thangadurai, V. & Weppner, W. Li6ALa2Nb2O12 (A = Ca, Sr, Ba): A new class of fast lithium ion conductors with garnet-like structure. *Journal of the American Ceramic Society* **88**, 411–418 (2005).

94. Bernuy-Lopez, C. *et al.* Atmosphere controlled processing of ga-substituted garnets for high li-ion conductivity ceramics. *Chemistry of Materials* **26**, 3610–3617 (2014).

95. Rangasamy, E., Wolfenstine, J. & Sakamoto, J. The role of Al and Li concentration on the formation of cubic garnet solid electrolyte of nominal composition Li 7La 3Zr 2O 12. *Solid State Ion* **206**, 28–32 (2012).

96. Wolfenstine, J., Ratchford, J., Rangasamy, E., Sakamoto, J. & Allen, J. L. Synthesis and high Li-ion conductivity of Ga-stabilized cubic Li7La3Zr2O12. *Mater Chem Phys* **134**, 571–575 (2012).

97. Shimonishi, Y. *et al.* Synthesis of garnet-type Li7 - XLa3Zr 2O12 - 1/2x and its stability in aqueous solutions. *Solid State Ion* **183**, 48–53 (2011).

98. Rawlence, M. *et al.* Effect of Gallium Substitution on Lithium-Ion Conductivity and Phase Evolution in Sputtered Li7-3 xGa x La3Zr2O12 Thin Films. *ACS Appl Mater Interfaces* **10**, 13720–13728 (2018).

99. Afyon, S., Krumeich, F. & Rupp, J. L. M. A shortcut to garnet-type fast Li-ion conductors for all-solid state batteries. *J Mater Chem A Mater* **3**, 18636–18648 (2015).

100. Rawlence, M., Garbayo, I., Buecheler, S. & Rupp, J. L. M. On the chemical stability of post-lithiated garnet Al-stabilized Li7La3Zr2O12 solid state electrolyte thin films. *Nanoscale* **8**, 14746–14753 (2016).

101. Miara, L. J. *et al.* Effect of Rb and Ta doping on the ionic conductivity and stability of the garnet Li7+2x-y(La3-xRbx)(Zr 2-yTay)O12 ($0 \leq x \leq 0.375$, $0 \leq y \leq 1$) Superionic conductor: A first principles investigation. *Chemistry of Materials* **25**, 3048–3055 (2013).

102. Ren, Y. *et al.* Effects of Li source on microstructure and ionic conductivity of Al-contained Li6.75La3Zr1.75Ta0.25O12 ceramics. *J Eur Ceram Soc* **35**, 561–572 (2015).

103. Thompson, T. *et al.* Tetragonal vs. cubic phase stability in Al-free Ta doped Li 7La3Zr2O12 (LLZO). *J Mater Chem A Mater* **2**, 13431–13436 (2014).

104. Awaka, J. *et al.* Crystal structure of fast lithium-ion-conducting cubic Li 7La3Zr2O12. *Chem Lett* **40**, 60–62 (2011).

105. Murugan, R., Thangadurai, V. & Weppner, W. Fast lithium ion conduction in garnet-type Li7La 3Zr2O12. *Angewandte Chemie - International Edition* **46**, 7778–7781 (2007).

106. Tenhaeff, W. E. *et al.* Resolving the Grain Boundary and Lattice Impedance of Hot-Pressed Li7La3Zr2O12 Garnet Electrolytes. *ChemElectroChem* **1**, 375–378 (2014).

107. Kalita, D. J., Lee, S. H., Lee, K. S., Ko, D. H. & Yoon, Y. S. Ionic conductivity properties of amorphous Li-La-Zr-O solid electrolyte for thin film batteries. *Solid State Ion* **229**, 14–19 (2012).

108. Nong, J., Xu, H., Yu, Z., Zhu, G. & Yu, A. Properties and preparation of Li-La-Ti-Zr-O thin film electrolyte. *Mater Lett* **154**, 167–169 (2015).

109. Tan, J. & Tiwari, A. Fabrication and characterization of Li7La3Zr 2O12 thin films for lithium ion battery. *ECS Solid State Letters* **1**, Q57 (2012).

110. Kim, S., Hirayama, M., Taminato, S. & Kanno, R. Epitaxial growth and lithium ion conductivity of lithium-oxide garnet for an all solid-state battery electrolyte. *Dalton Transactions* **42**, 13112–13117 (2013).

111. Garbayo, I. *et al.* Glass-Type Polyamorphism in Li-Garnet Thin Film Solid State Battery Conductors. *Adv Energy Mater* **8**, 1702265 (2018).

112. Park, J. S. *et al.* Effects of crystallinity and impurities on the electrical conductivity of Li-La-Zr-O thin films. *Thin Solid Films* **576**, 55–60 (2015).

113. Katsui, H. & Goto, T. Preparation of cubic and tetragonal Li7La3Zr2O12 film by metal organic chemical vapor deposition. *Thin Solid Films* **584**, 130–134 (2015).

114. Tadanaga, K. *et al.* Preparation of lithium ion conductive Al-doped Li7La3Zr2O12 thin films by a sol-gel process. *J Power Sources* **273**, 844–847 (2015).

115. Bitzer, M., van Gestel, T., Uhlenbruck, S. & Hans-Peter-Buchkremer. Sol-gel synthesis of thin solid Li7La3Zr2O12 electrolyte films for Li-ion batteries. *Thin Solid Films* **615**, 128–134 (2016).

116. Chen, R. J. *et al.* Sol-gel derived Li-La-Zr-O thin films as solid electrolytes for lithium-ion batteries. *J Mater Chem A Mater* **2**, 13277–13282 (2014).

117. Ehre, D., Cohen, H., Lyahovitskaya, V. & Lubomirsky, I. X-ray photoelectron spectroscopy of amorphous and quasiamorphous phases of BaTi O3 and SrTi O3. *Phys Rev B Condens Matter Mater Phys* **77**, 184106 (2008).

118. Wachtel, E. & Lubomirsky, I. Quasi-amorphous inorganic thin films: Non-crystalline polar phases. *Advanced Materials* **22**, 2485–2493 (2010).

119. Schmitt, R. *et al.* A review of defect structure and chemistry in ceria and its solid solutions. *Chem Soc Rev* **49**, 554–592 (2020).

120. Pfenninger, R., Struzik, M., Garbayo, I., Stilp, E. & Rupp, J. L. M. A low ride on processing temperature for fast lithium conduction in garnet solid-state battery films. *Nat Energy* **4**, 475–483 (2019).

121. Rettenwander, D. One Step Closer to Realizing Solid-State Batteries with Cubic Li7La3Zr2O12 Garnets. *Chem* **5**, 1695–1696 (2019).

122. Zhu, Y., Hood, Z. D., Miara, L. J. & Rupp, J. L. M. Solution-processed solid-state electrolyte and method of manufacture thereof. (2018).

123. Struzik, M., Garbayo, I., Pfenninger, R. & Rupp, J. L. M. A Simple and Fast Electrochemical CO2 Sensor Based on Li7La3Zr2O12 for Environmental Monitoring. *Advanced Materials* **30**, 1804098 (2018).

124. Horejs, C. M. Sense and sustainability. *Nat Rev Mater* **3**, 415 (2018).

125. Jones, S. D., Akridge, J. R. & Shokoohi, F. K. Thin film rechargeable Li batteries. *Solid State Ion* **69**, 357–368 (1994).

126. Bates, J. B., Dudney, N. J., Neudecker, B., Ueda, A. & Evans, C. D. Thin-film lithium and lithium-ion batteries. *Solid State Ion* **135**, 33–45 (2000).

127. Lee, J. Z., Wang, Z., Xin, H. L., Wynn, T. A. & Meng, Y. S. Amorphous Lithium Lanthanum Titanate for Solid-State Microbatteries. *J Electrochem Soc* **164**, A6268 (2016).

128. Rahaman, M. N. *Ceramic processing and sintering, second edition*. (CRC press, 2017).

129. Kim, K. J. & Rupp, J. L. M. All ceramic cathode composite design and manufacturing towards low interfacial resistance for garnet-based solid-state lithium batteries. *Energy Environ Sci* **13**, 4930–4945 (2020).

130. Geng, H., Lan, J., Mei, A., Lin, Y. & Nan, C. W. Effect of sintering temperature on microstructure and transport properties of Li3xLa2/3-xTiO3 with different lithium contents. *Electrochim Acta* **56**, 3406–3414 (2011).

131. Liu, Y. *et al.* Development of the cold sintering process and its application in solid-state lithium batteries. *J Power Sources* **393**, 193–203 (2018).

132. Berbano, S. S., Guo, J., Guo, H., Lanagan, M. T. & Randall, C. A. Cold sintering process of Li1.5Al0.5Ge1.5(PO4)3 solid electrolyte. *Journal of the American Ceramic Society* **100**, 2123–2135 (2017).

133. Maria, J. P. *et al.* Cold sintering: Current status and prospects. *Journal of Materials Research* vol. 32 3205–3218 Preprint at https://doi.org/10.1557/jmr.2017.262 (2017).

134. Fu, K. *et al.* Three-dimensional bilayer garnet solid electrolyte based high energy density lithium metal-sulfur batteries. *Energy Environ Sci* **10**, 1568–1575 (2017).

135. Hitz, G. T. *et al.* High-rate lithium cycling in a scalable trilayer Li-garnet-electrolyte architecture. *Materials Today* **22**, 50–57 (2019).

136. Hood, Z.D.; Zhu, Y.; Miara, L.J.; Chang, W.S.; Simons, P.; Rupp, J. L. M. A Sinter-Free Future for Solid-State Battery Designs. *Energy Environ Sci* **15**, 2927–2936 (2022).

137. Zhu, Y., Hood, Z. D., Rupp, J. L. M. & Miara, L. J. Solid-state electrolyte and method of manufacture thereof. (2022).

138. Zhu, Y. *et al.* High Entropy Amorphous Li-Battery Electrolytes. *Under review* (2022).

139. T. Schneller M. Kosec, D. Payne, R. W. *Chemical Solution Deposition of Functional Oxide Thin Films*. (Springer, 2013).

140. Han, F. *et al.* High electronic conductivity as the origin of lithium dendrite formation within solid electrolytes. *Nat Energy* **4**, 187–196 (2019).

141. Fu, L. J. *et al.* Electrode materials for lithium secondary batteries prepared by sol-gel methods. *Prog Mater Sci* **50**, 881–928 (2005).

142. Fragnaud, P., Nagarajan, R., Schleich, D. M. & Vujic, D. Thin-film cathodes for secondary lithium batteries. *J Power Sources* **54**, 362–366 (1995).

143. Kushida, K. & Kuriyama, K. Sol-gel growth of LiCoO2 films on Si substrates by a spin-coating method. *J Cryst Growth* **237–239**, 612–615 (2002).

144. Castro-García, S., Castro-Couceiro, A., Señarís-Rodríguez, M. A., Soulette, F. & Julien, C. Influence of aluminum doping on the properties of LiCoO2 and LiNi0.5Co0.5O2 oxides. *Solid State Ion* **156**, 15–26 (2003).

145. Hood, Z. D., Chang, W. S., Miara, L. J. & Rupp, J. L. M. Bilayer component for Li metal battery. (2020).

146. Zhu, Y., Hood, Z. D., Rupp, J. L. M. & Miara, L. J. Solid-state electrolyte and method of manufacture thereof. (2020).

147. Nicholas, J. D. & de Jonghe, L. C. Prediction and evaluation of sintering aids for Cerium Gadolinium Oxide. *Solid State Ion* **178**, 1187–1194 (2007).

148. Rho, Y. H. *et al.* Preparation of Li4Ti5O12 and LiCoO2 thin film electrodes from precursors obtained by sol-gel method. *Solid State Ion* **151**, 151–157 (2002).

149. Maranchi, J. P., Hepp, A. F. & Kumta, P. N. LiCoO2 and SnO2 thin film electrodes for lithium-ion battery applications. *Materials Science and Engineering: B* **116**, 327–340 (2005).

150. Hao, Y. J. *et al.* Synthesis and characterization of spinel Li4Ti5O12 anode material by oxalic acid-assisted sol-gel method. *J Power Sources* **158**, 1358–1364 (2006).

151. Haetge, J., Hartmann, P., Brezesinski, K., Janek, J. & Brezesinski, T. Ordered large-pore mesoporous Li4Ti5O12 spinel thin film electrodes with nanocrystalline framework for high rate rechargeable lithium batteries: Relationships among charge storage, electrical conductivity, and nanoscale structure. *Chemistry of Materials* **23**, 4384–4393 (2011).

152. Song, M. Y. & Lee, R. Synthesis by sol-gel method and electrochemical properties of LiNiO2 cathode material for lithium secondary battery. *J Power Sources* **111**, 97–103 (2002).

153. Rho, Y. H., Kanamura, K. & Umegaki, T. LiCoO2 and LiMn2O4 thin-film electrodes for rechargeable lithium batteries: Preparation using PVP sol-gel to produce excellent electrochemical properties. *J Electrochem Soc* **150**, A107 (2002).

154. Croce, F. *et al.* A novel concept for the synthesis of an improved LiFePO4 lithium battery cathode. *Electrochemical and Solid-State Letters* **5**, A47 (2002).

155. Chen, R. J. *et al.* Improvement of the conductivity of sol-gel derived Li-La-Zr-O thin films by the addition of surfactant. *Ceram Int* **43**, S603–S608 (2017).

156. Kim, H. J., Choi, J. W., do Kim, S. & Yoo, K. S. Thick-film CO2 sensors based on NASICON synthesized by a sol-gel process. in *Eco-Materials Processing and Design Viii* vols 544–545 925–928 (2007).

157. Takada, K. *et al.* Sol-gel preparation of Li+ ion conductive thin film. *Appl Surf Sci* **189**, 300–306 (2002).

158. Balaish, M. & Rupp, J. L. M. Widening the Range of Trackable Environmental and Health Pollutants for Li-Garnet-Based Sensors. *Advanced Materials* **33**, 2100314 (2021).

159. Han, F. D., Zhu, Y. Z., He, X. F., Mo, Y. F. & Wang, C. S. Electrochemical Stability of Li10GeP2S12 and Li7La3Zr2O12 Solid Electrolytes. *Adv Energy Mater* **6**, 1501590 (2016).

160. Balaish, M. *et al.* Processing thin but robust electrolytes for solid-state batteries. *Nat Energy* **6**, 227–239 (2021).

161. Zhu, Y. *et al.* Lithium-film ceramics for solid-state lithionic devices. *Nat Rev Mater* **6**, 313–331 (2021).

162. Kim, K. J., Hinricher, J. J. & Rupp, J. L. M. High energy and long cycles. *Nat Energy* **5**, 278–279 (2020).

163. Janek, J. & Zeier, W. G. A solid future for battery development. *Nat Energy* **1**, 16141 (2016).

164. Bauer, C. *et al.* Charging sustainable batteries. *Nat Sustain* **5**, 176–178 (2022).

165. Xu, W. *et al.* Lithium metal anodes for rechargeable batteries. *Energy Environ Sci* **7**, 513–537 (2014).

166. Albertus, P. Integration and Optimization of Novel Ion-Conducting Solids (IONICS) Funding Opportunity Announcement . https://arpa-e-foa.energy.gov/FileContent.aspx?FileID=cfac9ce8-5a19-4623-b942-c3e65f3ccf77 (2016).

167. Swamy, T. *et al.* Lithium Metal Penetration Induced by Electrodeposition through Solid Electrolytes: Example in Single-Crystal Li6La3ZrTaO12 Garnet. *J Electrochem Soc* **165**, A3648–A3655 (2018).

168. Buschmann, H. *et al.* Structure and dynamics of the fast lithium ion conductor 'li 7La3Zr2O12'. *Physical Chemistry Chemical Physics* **13**, 19378–19392 (2011).

169. Allen, J. L., Wolfenstine, J., Rangasamy, E. & Sakamoto, J. Effect of substitution (Ta, Al, Ga) on the conductivity of Li7La3Zr2O12. *J Power Sources* **206**, 315–319 (2012).

170. Liu, Q. *et al.* Challenges and perspectives of garnet solid electrolytes for all solid-state lithium batteries. *J Power Sources* **389**, 120–134 (2018).

171. Cheng, E. J., Sharafi, A. & Sakamoto, J. Intergranular Li metal propagation through polycrystalline Li6.25Al0.25La3Zr2O12 ceramic electrolyte. *Electrochim Acta* **223**, 85–91 (2017).

172. Liu, X. *et al.* Local electronic structure variation resulting in Li 'filament' formation within solid electrolytes. *Nat Mater* **20**, 1485–1490 (2021).

173. Cho, J. H. *et al.* An Investigation of Chemo-Mechanical Phenomena and Li Metal Penetration in All-Solid-State Lithium Metal Batteries Using In Situ Optical Curvature Measurements. *Adv Energy Mater* **12**, 2200369 (2022).

174. Dixit, M. B. *et al.* Polymorphism of garnet solid electrolytes and its implications for grain-level chemo-mechanics. *Nat Mater* **21**, 1298–1305 (2022).

175. Zhu, Y., Balaish, M. & Rupp, J. L. M. Uncovered Phase Polymorphism Steers Chemo-Mechanics of Garnet Electrolytes. *Joule* **6**, 2680–2682 (2022).

176. Schwobel, A., Hausbrand, R. & Jaegermann, W. Interface reactions between LiPON and lithium studied by in-situ X-ray photoemission. *Solid State Ion* **273**, 51–54 (2015).

177. Cheng, D. *et al.* Unveiling the Stable Nature of the Solid Electrolyte Interphase between Lithium Metal and LiPON via Cryogenic Electron Microscopy. *Joule* **4**, 2484–2500 (2020).

178. Hood, Z. D. *et al.* Elucidating Interfacial Stability between Lithium Metal Anode and Li Phosphorus Oxynitride via in Situ Electron Microscopy. *Nano Lett* **21**, 151–157 (2021).

179. Ehre, D., Cohen, H., Lyahovitskaya, V., Tagantsev, A. & Lubomirsky, I. Structural transformations during formation of quasi-amorphous BaTiO 3. *Adv Funct Mater* **17**, 1204–1208 (2007).

180. Lyahovitskaya, V. *et al.* Formation and thermal stability of quasi-amorphous thin films. *Phys Rev B Condens Matter Mater Phys* **71**, 094205 (2005).

181. Senevirathne, K., Day, C. S., Gross, M. D., Lachgar, A. & Holzwarth, N. A. W. A new crystalline LiPON electrolyte: Synthesis, properties, and electronic structure. *Solid State Ion* **233**, 95–101 (2013).

182. Belous, A. G., Novitskaya, G. N., Polyanetskaya, S. v & Gornikov, Y. I. Study of complex oxides with the composition La2/3-xLi3xTiO3. *Inorganic Materials* **23**, 412 (1987).

183. Sastre, J. *et al.* Blocking lithium dendrite growth in solid-state batteries with an ultrathin amorphous Li-La-Zr-O solid electrolyte. *Commun Mater* **2**, 1–10 (2021).

184. Shelby, J. E. *Introduction to Glass Science and Technology: Edition 2*. (Royal Society of Chemistry, 2005). doi:10.1039/9781847551160.

185. Chen, S. *et al.* Sulfide solid electrolytes for all-solid-state lithium batteries: Structure, conductivity, stability and application. *Energy Storage Mater* **14**, 58–74 (2018).

186. Saienga, J. & Martin, S. W. The comparative structure, properties, and ionic conductivity of LiI + Li2S + GeS2 glasses doped with Ga2S3 and La2S3. *J Non Cryst Solids* **354**, 1475–1486 (2008).

187. Kumar, G., Desai, A. & Schroers, J. Bulk metallic glass: The smaller the better. *Advanced Materials* **23**, 461–476 (2011).

188. Moskovskikh, D. *et al.* Extremely hard and tough high entropy nitride ceramics. *Sci Rep* **10**, 1–8 (2020).

189. Oses, C., Toher, C. & Curtarolo, S. High-entropy ceramics. *Nat Rev Mater* **5**, 295–309 (2020).

190. Calahoo, C. & Wondraczek, L. Ionic glasses: Structure, properties and classification. *Journal of Non-Crystalline Solids: X* **8**, 100054 (2020).

191. Mani, P. D. *et al.* Ionic conductivity of bias sputtered lithium phosphorus oxy-nitride thin films. *Solid State Ion* **287**, 48–59 (2016).

192. Mascaraque, N., Fierro, J. L. G., Durán, A. & Muñoz, F. An interpretation for the increase of ionic conductivity by nitrogen incorporation in LiPON oxynitride glasses. *Solid State Ion* **233**, 73–79 (2013).

193. López-Grande, A., Dagupati, R., Galán del Sastre, P. & Muñoz, F. Ionic conductivity of Li2O–P2O5 glasses from thermodynamic modeling of their chemical structure. *Journal of the American Ceramic Society* **104**, 5625–5635 (2021).

194. Hashimoto, T. & Moriwake, H. Structure of amorphous BaTiO3 by molecular dynamics simulations using a shell model. *Physica B Condens Matter* **579**, 411799 (2020).

195. Wu, J. F. & Guo, X. Origin of the low grain boundary conductivity in lithium ion conducting perovskites: Li3xLa0.67-xTiO3. *Physical Chemistry Chemical Physics* **19**, 5880–5887 (2017).

196. Sharafi, A., Haslam, C. G., Kerns, R. D., Wolfenstine, J. & Sakamoto, J. Controlling and correlating the effect of grain size with the mechanical and electrochemical properties of Li7La3Zr2O12 solid-state electrolyte. *J Mater Chem A Mater* **5**, 21491–21504 (2017).

197. Kim, K. J., Balaish, M., Wadaguchi, M., Kong, L. & Rupp, J. L. M. Solid State Batteries: Solid-State Li–Metal Batteries: Challenges and Horizons of Oxide and Sulfide Solid Electrolytes and Their Interfaces. *Adv Energy Mater* **11**, 2002689 (2021).

198. Tsai, C. L. *et al.* Li7La3Zr2O12 Interface Modification for Li Dendrite Prevention. *ACS Appl Mater Interfaces* **8**, 10617–10626 (2016).

199. Larraz, G., Orera, A. & Sanjuán, M. L. Cubic phases of garnet-type Li7La3Zr 2O12: The role of hydration. *J Mater Chem A Mater* **1**, 11419–11428 (2013).

200. Tietz, F., Wegener, T., Gerhards, M. T., Giarola, M. & Mariotto, G. Synthesis and Raman micro-spectroscopy investigation of Li7La3Zr2O12. *Solid State Ion* **230**, 77–82 (2013).

201. Mastelaro, V. R. & Zanotto, E. D. X-ray Absorption Fine Structure (XAFS) studies of oxide glasses-A 45-year overview. *Materials.* **11**, 204 (2018).

202. Stern, E.A.; Heald, S. M. Vol. 1. in *Handbook on Synchrotron Radiation* (ed. E.E. Koch North-Holland) (1983).

203. Dargaud, O. *et al.* In situ study of nucleation of zirconia in an MgO-Al2O 3-SiO2 glass. *Journal of the American Ceramic Society* **93**, 342–344 (2010).

204. Farges, F., Ponader, C. W. & Brown, G. E. Structural environments of incompatible elements in silicate glass/melt systems: I. Zirconium at trace levels. *Geochim Cosmochim Acta* **55**, 1563–1574 (1991).

205. Ferlat, G. *et al.* Evidence for symmetric cationic sites in zirconium-bearing oxide glasses. *Phys Rev B Condens Matter Mater Phys* **73**, 214207 (2006).

206. Grunes, L. A. Study of the K edges of the 3d transition metals in pure and oxide form by x-ray-absorption spectroscopy. *Phys Rev B* **27**, 2111 (1983).

207. Li, P., Chen, I. W. & Penner-Hahn, J. E. X-ray-absorption studies of zirconia polymorphs. I. Characteristic local structures. *Phys Rev B* **48**, 10063 (1993).

208. Brown, G. E., Calas, G., Waychunas, G. A. & Petiau, J. X-ray absorption spectroscopy and its applications in mineralogy and geochemistry. in *Spectroscopic Methods in Mineralogy and Geology* (De Gruyter, 2019).

209. Chen, Y. T. *et al.* Voltammetric Enhancement of Li-Ion Conduction in Al-Doped Li7-xLa3Zr2O12 Solid Electrolyte. *Journal of Physical Chemistry C* **121**, 15565–15573 (2017).

210. Chen, Y., Rangasamy, E., Liang, C. & An, K. Origin of High Li+ Conduction in Doped Li7La3Zr2O12 Garnets. *Chemistry of Materials* **27**, 5491–5494 (2015).

211. Alam, T. M., Conzone, S., Brow, R. K. & Boyle, T. J. 6Li, 7Li nuclear magnetic resonance investigation of lithium coordination in binary phosphate glasses. *J Non Cryst Solids* **258**, 140–154 (1999).

212. Xu, Z. & Stebbins, J. F. 6Li nuclear magnetic resonance chemical shifts, coordination number and relaxation in crystalline and glassy silicates. *Solid State Nucl Magn Reson* **5**, 103–112 (1995).

213. Posch, P. *et al.* Ion dynamics in Al-Stabilized Li7La3Zr2O12 single crystals – Macroscopic transport and the elementary steps of ion hopping. *Energy Storage Mater* **24**, 220–228 (2020).

214. Ravel, B. & Newville, M. ATHENA, ARTEMIS, HEPHAESTUS: Data analysis for X-ray absorption spectroscopy using IFEFFIT. in *Journal of Synchrotron Radiation* (2005). doi:10.1107/S0909049505012719.

215. Dunstan, M. T., Griffin, J. M., Blanc, F., Leskes, M. & Grey, C. P. Ion Dynamics in Li2CO3 Studied by Solid-State NMR and First-Principles Calculations. *Journal of Physical Chemistry C* **119**, 24255–24264 (2015).

216. Bielecki, A. & Burum, D. P. Temperature Dependence of207Pb MAS Spectra of Solid Lead Nitrate. An Accurate, Sensitive Thermometer for Variable-Temperature MAS. *J Magn Reson A* **116**, 215–220 (1995).

217. Bruker Biospin: Rheinstetten. Topspin v3.5, Software for NMR Spectral Analysis. Preprint at (2018).

218. Deiseroth, H. J. *et al.* Li6PS5X: A class of crystalline Li-rich solids with an unusually high Li+ mobility. *Angewandte Chemie - International Edition* **47**, 755–758 (2008).

219. Boulineau, S., Courty, M., Tarascon, J. M. & Viallet, V. Mechanochemical synthesis of Li-argyrodite Li 6PS 5X (X = Cl, Br, I) as sulfur-based solid electrolytes for all solid state batteries application. *Solid State Ion* **221**, 1–5 (2012).

220. Mizuno, F., Hayashi, A., Tadanaga, K. & Tatsumisago, M. New, highly ion-conductive crystals precipitated from Li 2S-P2S5 glasses. *Advanced Materials* **17**, 918–921 (2005).

221. Schweiger, L., Hogrefe, K., Gadermaier, B., Rupp, J. L. M. & Wilkening, H. M. R. Ionic Conductivity of Nanocrystalline and Amorphous Li10GeP2S12: The Detrimental Impact of Local Disorder on Ion Transport. *J Am Chem Soc* **144**, 9597–9609 (2022).

222. Xu, H., Yu, Y., Wang, Z. & Shao, G. First Principle Material Genome Approach for All Solid-State Batteries. *Energy and Environmental Materials* **2**, 234–250 (2019).

223. Muramatsu, H., Hayashi, A., Ohtomo, T., Hama, S. & Tatsumisago, M. Structural change of Li2S-P2S5 sulfide solid electrolytes in the atmosphere. *Solid State Ion* **182**, 116–119 (2011).

224. Miara, L. *et al.* About the Compatibility between High Voltage Spinel Cathode Materials and Solid Oxide Electrolytes as a Function of Temperature. *ACS Appl Mater Interfaces* **8**, 26842–26850 (2016).

225. Huang, Y. & Li, J. Key Challenges for Grid-Scale Lithium-Ion Battery Energy Storage. *Adv Energy Mater* **12**, 2202197 (2022).

226. Mandal, B. P., Krishna, P. S. R. & Tyagi, A. K. Order-disorder transition in the Nd2-yYyZr2O7 system: Probed by X-ray diffraction and Raman spectroscopy. *J Solid State Chem* **183**, 41–45 (2010).

227. Scheetz, B. E. & White, W. B. Characterization of Anion Disorder in Zirconate A2B2O7 Compounds by Raman Spectroscopy. *Journal of the American Ceramic Society* **62**, 468–470 (1979).

228. Gouteron, J., Michel, D., Lejus, A. M. & Zarembowitch, J. Raman spectra of lanthanide sesquioxide single crystals: Correlation between A and B-type structures. *J Solid State Chem* **38**, 288–296 (1981).

229. Orera, A., Larraz, G. & Sanjuán, M. L. Spectroscopic study of the competition between dehydration and carbonation effects in La2O3-based materials. *J Eur Ceram Soc* **33**, 2103–2110 (2013).

230. Rangasamy, E., Wolfenstine, J., Allen, J. & Sakamoto, J. The effect of 24c-site (A) cation substitution on the tetragonal-cubic phase transition in Li7-xLa3-xAxZr 2O12 garnet-based ceramic electrolyte. *J Power Sources* **230**, 261–266 (2013).

231. Rettenwander, D. *et al.* The solubility and site preference of Fe3+ in Li7-3xFexLa3Zr2O12 garnets. *J Solid State Chem* **230**, 266–271 (2015).

232. Brooker, M. H. & Wang, J. Raman and infrared studies of lithium and cesium carbonates. *Spectrochim Acta A* **48**, 999–1008 (1992).

233. Hase, Y. & Yoshida, I. V. P. Raman and infrared spectra of6Li2C2O4 and7Li2C2O4. *Monatsh Chem* **111**, 1265–1272 (1980).

234. Voyles, P. M. & Muller, D. A. Fluctuation microscopy in the STEM. *Ultramicroscopy* **93**, 147–159 (2002).

235. Yastrebtsev, A. A. *et al.* Comparative neutron and X-ray diffraction analysis of anionic and cationic ordering in rare-earth zirconates (Ln = La, Nd, Tb, Yb, Y). *J Alloys Compd* **832**, 154863 (2020).

236. Millikan, R. A. X-rays and Crystal Structure. *Science (1979)* **40**, 795–802 (1914).

237. Scherrer, P. Bestimmung der Gröss Kolloidteilchen Mittels Nachrichten von der Gesellschaft der Wissenschaften, Göttingen," Vol. 2, 1918, pp. 98-100. *Mathematisch-Physikalische Klasse* (1918).

238. Oey, T. *et al.* The role of the network-modifier's field-strength in the chemical durability of aluminoborate glasses. *J Non Cryst Solids* **505**, 279–285 (2019).

239. Slater, J. C. Atomic radii in crystals. *J Chem Phys* **41**, 3199–3204 (1964).

240. Anderson, O. L. & Stuart, D. A. Calculation of Activation Energy of Ionic Conductivity in Silica Glasses by Classical Methods. *Journal of the American Ceramic Society* **37**, 573–580 (1954).

241. Murawski, L. Electrical conductivity in iron-containing oxide glasses. *J Mater Sci* **17**, 2155–2163 (1982).

242. Kennedy, E. *et al.* Tilted fluctuation electron microscopy. *Appl Phys Lett* **117**, 091903 (2020).

243. Ding, Y., Cano, Z. P., Yu, A., Lu, J. & Chen, Z. Automotive Li-Ion Batteries: Current Status and Future Perspectives. *Electrochemical Energy Reviews* **2**, 1–28 (2019).

244. Schmuch, R., Wagner, R., Horpel, G., Placke, T. & Winter, M. Performance and cost of materials for lithium-based rechargeable automotive batteries. *Nat Energy* **3**, 267–278 (2018).

245. Yang, X. G., Liu, T. & Wang, C. Y. Thermally modulated lithium iron phosphate batteries for mass-market electric vehicles. *Nat Energy* **6**, 176–185 (2021).

246. Bhutada, G. Breaking Down the Cost of an EV Battery Cell. *Visual Capitalist* https://www.visualcapitalist.com/breaking-down-the-cost-of-an-ev-battery-cell/ (2022).

247. *National Blueprint for Lithium Batteries 2021-2030*. https://www.energy.gov/sites/default/files/2021-06/FCAB National Blueprint Lithium Batteries 0621_0.pdf (2021).

248. Kim, K. J., Balaish, M., Wadaguchi, M., Kong, L. & Rupp, J. L. M. Solid-State Li-Metal Batteries: Challenges and Horizons of Oxide and Sulfide Solid Electrolytes and Their Interfaces. *Adv Energy Mater* **11**, 2002689 (2021).

249. Kalnaus, S., Westover, A. S., Kornbluth, M., Herbert, E. & Dudney, N. J. Resistance to fracture in the glassy solid electrolyte Lipon. *J Mater Res* **36**, 787–796 (2021).

250. Yi, E. *et al.* All-Solid-State Batteries Using Rationally Designed Garnet Electrolyte Frameworks. *ACS Appl Energy Mater* **3**, (2020).

251. Cheng, E. J., Liu, M., Li, Y., Abe, T. & Kanamura, K. Effects of porosity and ionic liquid impregnation on ionic conductivity of garnet-based flexible sheet electrolytes. *J Power Sources* **517**, 230705 (2022).

252. Ohta, S., Kobayashi, T. & Asaoka, T. High lithium ionic conductivity in the garnet-type oxide Li7-X La3(Zr2-X, NbX)O12 (X = 0-2). *J Power Sources* **196**, 3342–3345 (2011).

253. Wang, C. *et al.* A general method to synthesize and sinter bulk ceramics in seconds. *Science (1979)* **368**, 521–526 (2020).

254. Clemenceau, T. *et al.* Flash sintering of Li-ion conducting ceramic in a few seconds at 850 °C. *Scr Mater* **172**, 1–5 (2019).

255. Li, Y. *et al.* Ionic distribution and conductivity in lithium garnet Li 7La 3Zr 2O 12. *J Power Sources* **209**, 278–281 (2012).

256. Sakamoto, J., Rangasamy, E., Kim, H., Kim, Y. & Wolfenstine, J. Synthesis of nano-scale fast ion conducting cubic Li7La 3Zr2O12. *Nanotechnology* **24**, 424005 (2013).

257. Mahbub, R. *et al.* Text mining for processing conditions of solid-state battery electrolyte. *Electrochem commun* **121**, 106860 (2020).

258. Carter, C. B. & Norton, M. G. Solid-State Phase Transformations and Reactions. in *Ceramic Materials* vol. 25 457–475 (2013).

259. Uhlmann, D. R. Nucleation, crystallization and glass formation. *J Non Cryst Solids* **38**, 693–698 (1980).

260. Weinberg, M. C., Birnie, D. P. & Shneidman, V. A. Crystallization kinetics and the JMAK equation. *J Non Cryst Solids* **219**, 89–99 (1997).

261. Rupp, J. L. M., Scherrer, B., Schauble, N. & Gauckler, L. J. Time-Temperature-Transformation (TTT) Diagrams for Crystallization of Metal Oxide Thin Films. *Adv Funct Mater* **20**, 2807–2814 (2010).

262. Kissinger, H. E. Reaction Kinetics in Differential Thermal Analysis. *Anal Chem* **29**, 1702–1706 (1957).

263. vander Voort, G. F. *Atlas of Time-Temperature Diagrams for Irons and Steels*. *ASM International* (1991).

264. Zhu, Y., Chang, W. S., Miara, L. & Rupp, J. L. M. Lithium Solid Electrolyte and Method of Manufacture Thereof. (2019).

265. Shi, Y. U., Bork, A. H., Schweiger, S. & Rupp, J. L. M. The effect of mechanical twisting on oxygen ionic transport in solid-state energy conversion membranes. *Nat Mater* **14**, 721–727 (2015).

266. Bernstein, N., Johannes, M. D. & Hoang, K. Origin of the structural phase transition in Li 7La 3Zr 2O 12. *Phys Rev Lett* **109**, 205702 (2012).

267. Zhao, M., Zou, L. & Wu, Y. Experimental analysis on crucible selection of thermal properties of nitrate salt. in *Energy Procedia* vol. 143 (2017).

268. Höhne, G. W. H. *et al.* Theoretical Fundamentals of Differential Scanning Calorimeters. in *Differential Scanning Calorimetry* vol. 3 31–63 (2003).

269. Chattopadhyay, C., Prasad, A. & Murty, B. S. Phase prediction in high entropy alloys – A kinetic approach. *Acta Mater* **153**, 214–225 (2018).

270. Zarabad, M. S. & Rezvani, M. Time-temperature-transformation diagrams for crystallization of the oxyfluoride glass system. *Results Phys* **10**, 356–359 (2018).

271. Geiger, C. A. *et al.* Crystal chemistry and stability of 'Li7La 3Zr2O12' garnet: A fast lithium-ion conductor. *Inorg Chem* **50**, 1089–1097 (2011).

272. Zio´lkowski, J. New relation between ionic radii, bond length, and bond strength. *J Solid State Chem* **57**, 269–290 (1985).

273. Brown, I. D. & Shannon, R. D. Empirical bond-strength–bond-length curves for oxides. *Acta Crystallographica Section A* **29**, 266–282 (1973).

274. Tarascon, J. M. & Armand, M. Issues and challenges facing rechargeable lithium batteries. *Nature* vol. 414 359–367 Preprint at https://doi.org/10.1038/35104644 (2001).

275. Quartarone, E. & Mustarelli, P. Electrolytes for solid-state lithium rechargeable batteries: Recent advances and perspectives. *Chem Soc Rev* **40**, 2525–2540 (2011).

276. Chu, S., Cui, Y. & Liu, N. The path towards sustainable energy. *Nature Materials* vol. 16 16–22 Preprint at https://doi.org/10.1038/nmat4834 (2016).

277. US Department of Energy. *Vehicle Technologies Office annual merit review Vehicle Technologies Office annual merit review 2017 report*. (2017).

278. Andre, D. *et al.* Future generations of cathode materials: An automotive industry perspective. *Journal of Materials Chemistry A* vol. 3 6709–6732 Preprint at https://doi.org/10.1039/c5ta00361j (2015).

279. Ohta, S., Kobayashi, T., Seki, J. & Asaoka, T. Electrochemical performance of an all-solid-state lithium ion battery with garnet-type oxide electrolyte. *J Power Sources* **202**, 332–335 (2012).

280. Wu, J. F., Pang, W. K., Peterson, V. K., Wei, L. & Guo, X. Garnet-Type Fast Li-Ion Conductors with High Ionic Conductivities for All-Solid-State Batteries. *ACS Appl Mater Interfaces* **9**, 12461–12468 (2017).

281. Ahn, B. Y. *et al.* Omnidirectional printing of flexible, stretchable, and spanning silver microelectrodes. *Science (1979)* **323**, 1590–1593 (2009).

282. Oudenhoven, J. F. M., Baggetto, L. & Notten, P. H. L. All-solid-state lithium-ion microbatteries: A review of various three-dimensional concepts. *Adv Energy Mater* **1**, 10–33 (2011).

283. Roberts, M. *et al.* 3D lithium ion batteries - From fundamentals to fabrication. *J Mater Chem* **21**, 9876–9890 (2011).

284. Taberna, P. L., Mitra, S., Poizot, P., Simon, P. & Tarascon, J. M. High rate capabilities Fe3O4-based Cu nano-architectured electrodes for lithium-ion battery applications. *Nat Mater* **5**, 567–573 (2006).

285. Mazor, H., Golodnitsky, D., Burstein, L. & Peled, E. High power copper sulfide cathodes for thin-film microbatteries. *Electrochemical and Solid-State Letters* **12**, A232 (2009).

286. Baggetto, L., Knoops, H. C. M., Niessen, R. A. H., Kessels, W. M. M. & Notten, P. H. L. 3D negative electrode stacks for integrated all-solid-state lithium-ion microbatteries. *J Mater Chem* **20**, 3703–3708 (2010).

287. Cheah, S. K. *et al.* Self-Supported three-dimensional nanoelectrodes for microbattery applications. *Nano Lett* **9**, 3230–3233 (2009).

288. Min, H. S. *et al.* Fabrication and properties of a carbon/polypyrrole three-dimensional microbattery. *J Power Sources* **178**, 795–800 (2008).

289. Nishizawa, M., Mukai, K., Kuwabata, S., Martin, C. R. & Yoneyama, H. Template Synthesis of Polypyrrole-Coated Spinel LiMn2 O 4 Nanotubules and Their Properties as Cathode Active Materials for Lithium Batteries. *J Electrochem Soc* **144**, 1923 (1997).

290. Kotobuki, M. *et al.* Electrochemical property of honeycomb type all-solid-state Li battery at high temperature. *Electrochemistry* **79**, 464–466 (2011).

291. Shaijumon, M. M. *et al.* Nanoarchitectured 3D cathodes for Li-ion microbatteries. *Advanced Materials* **22**, 4978–4981 (2010).

292. Mazor, H., Golodnitsky, D., Burstein, L., Gladkich, A. & Peled, E. Electrophoretic deposition of lithium iron phosphate cathode for thin-film 3D-microbatteries. *J Power Sources* **198**, 264–272 (2012).

293. Kim, H., Proell, J., Kohler, R., Pfleging, W. & Pique, A. Laser-printed and processed LiCoO2 cathodethick films for Li-Ion Microbatteries. *Journal of Laser Micro Nanoengineering* **7**, 320–325 (2012).

294. Gowda, S. R., Leela Mohana Reddy, A., Zhan, X., Jafry, H. R. & Ajayan, P. M. 3D nanoporous nanowire current collectors for thin film microbatteries. *Nano Lett* **12**, 1198–1202 (2012).

295. Lai, W. *et al.* Ultrahigh-energy-density microbatteries enabled by new electrode architecture and micropackaging design. *Advanced Materials* **22**, E139–E144 (2010).

296. Yoshima, K., Munakata, H. & Kanamura, K. Fabrication of micro lithium-ion battery with 3D anode and 3D cathode by using polymer wall. *J Power Sources* **208**, 404–408 (2012).

297. Pikul, J. H., Gang Zhang, H., Cho, J., Braun, P. v. & King, W. P. High-power lithium ion microbatteries from interdigitated three-dimensional bicontinuous nanoporous electrodes. *Nat Commun* **4**, 1732 (2013).

298. Gaikwad, A. M., Whiting, G. L., Steingart, D. A. & Arias, A. C. Highly flexible, printed alkaline batteries based on mesh-embedded electrodes. *Advanced Materials* **23**, 3251–3255 (2011).

299. Nathan, M. *et al.* Three-dimensional thin-film Li-ion microbatteries for autonomous MEMS. *Journal of Microelectromechanical Systems* **14**, 879–885 (2005).

300. Sun, K. *et al.* 3D printing of interdigitated Li-ion microbattery architectures. *Advanced Materials* **25**, 4539–4543 (2013).

301. Perre, E. *et al.* Direct electrodeposition of aluminium nano-rods. *Electrochem commun* **10**, 1467–1470 (2008).

302. Pearse, A. *et al.* Three-Dimensional Solid-State Lithium-Ion Batteries Fabricated by Conformal Vapor-Phase Chemistry. *ACS Nano* **12**, 4286–4294 (2018).

303. Yao, H. *et al.* Crab shells as sustainable templates from nature for nanostructured battery electrodes. *Nano Lett* **13**, 3385–3390 (2013).

304. Hyde, S. T. & Schröder-Turk, G. E. Geometry of interfaces: Topological complexity in biology and materials. *Interface Focus* **2**, 529–538 (2012).

305. Zhu, C. *et al.* Highly compressible 3D periodic graphene aerogel microlattices. *Nat Commun* **6**, 6962 (2015).

306. Kim, C. *et al.* High-Power Aqueous Zinc-Ion Batteries for Customized Electronic Devices. *ACS Nano* **12**, 11838–11846 (2018).

307. Porz, L. *et al.* Mechanism of Lithium Metal Penetration through Inorganic Solid Electrolytes. *Adv Energy Mater* **7**, 1701003 (2017).

308. Westover, A. S., Dudney, N. J., Sacci, R. L. & Kalnaus, S. Deposition and Confinement of Li Metal along an Artificial Lipon-Lipon Interface. *ACS Energy Lett* **4**, 651–655 (2019).

309. Dudney, N. J. Solid-state thin-film rechargeable batteries. *Materials Science and Engineering: B* **116**, 245–249 (2005).

310. Tan, D. H. S., Banerjee, A., Chen, Z. & Meng, Y. S. From nanoscale interface characterization to sustainable energy storage using all-solid-state batteries. *Nat Nanotechnol* **15**, 170–180 (2020).

311. Li, X. *et al.* LiNbO3-coated LiNi0.8Co0.1Mn0.1O2 cathode with high discharge capacity and rate performance for all-solid-state lithium battery. *Journal of Energy Chemistry* **40**, 39–45 (2020).

312. Gurney, K. R. *et al.* High resolution fossil fuel combustion CO2 emission fluxes for the United States. *Environ Sci Technol* **43**, 5535–5541 (2009).

313. Wang, C., Chen, J. & Zou, J. Decomposition of energy-related CO2 emission in China: 1957-2000. *Energy* **30**, 73–83 (2005).

314. Joughin, I., Smith, B. E. & Medley, B. Marine ice sheet collapse potentially under way for the thwaites glacier basin, West Antarctica. *Science (1979)* **344**, 735–738 (2014).

315. Feldmann, J. & Levermann, A. Collapse of the West Antarctic Ice Sheet after local destabilization of the Amundsen Basin. *Proceedings of the National Academy of Sciences* **112**, 14191–14196 (2015).

316. Obama, B. The irreversible momentum of clean energy. *Science (1979)* **355**, 126–129 (2017).

317. Aleixandre, M. & Gerboles, M. Review of small commercial sensors for indicative monitoring of ambient gas. in *Chemical Engineering Transactions* vol. 30 (2012).

318. Szulczyński, B. & Gębicki, J. Currently commercially available chemical sensors employed for detection of volatile organic compounds in outdoor and indoor air. *Environments - MDPI* **4**, 21 (2017).

319. Dinh, T. V., Choi, I. Y., Son, Y. S. & Kim, J. C. A review on non-dispersive infrared gas sensors: Improvement of sensor detection limit and interference correction. *Sens Actuators B Chem* **231**, 529–538 (2016).

320. Park, C. O. & Akbar, S. A. Ceramics for chemical sensing. *J Mater Sci* **38**, 4611–4637 (2003).

321. Liu, Y., Parisi, J., Sun, X. & Lei, Y. Solid-state gas sensors for high temperature applications-a review. *J Mater Chem A Mater* **2**, 9919–9943 (2014).

322. Yamazoe, N. & Miura, N. Environmental gas sensing. *Sens Actuators B Chem* **20**, 90–102 (1994).

323. Maskell, W. C. Inorganic solid state chemically sensitive devices: Electrochemical oxygen gas sensors. *J Phys E* **20**, 1156 (1987).

324. Ramamoorthy, R., Dutta, P. K. & Akbar, S. A. Oxygen sensors: Materials, methods, designs and applications. *J Mater Sci* **38**, 4271–4282 (2003).

325. Gauthier, M. & Chamberland, A. Solid-State Detectors for the Potentiometric Determination of Gaseous Oxides: I . Measurement in Air. *J Electrochem Soc* **124**, 1579 (1977).

326. Worrell, W. L. & Liu, Q. G. A new sulphur dioxide sensor using a novel two-phase solid-sulphate electrolyte. *Journal of Electroanalytical Chemistry* **168**, 355–362 (1984).

327. Akila, R. & Jacob, K. T. Use of the Nasicon/Na2SO4 couple in a solid state sensor for SOx (x=2,3). *J Appl Electrochem* **18**, 245–251 (1988).

328. Lee, C., Akbar, S. A. & Park, C. O. Potentiometric CO2 gas sensor with lithium phosphorous oxynitride electrolyte. *Sens Actuators B Chem* **80**, 234–242 (2001).

329. Wang, H., Chen, D., Zhang, M. & Wang, J. Influence of the sensing and reference electrodes relative size on the sensing properties of Li3PO4-based potentiometric CO2 sensors. *Surf Coat Technol* **320**, 542–547 (2017).

330. Alonso-Porta, M. & Kumar, R. v. Use of NASICON/Na2CO3 system for measuring CO2. *Sens Actuators B Chem* **71**, 173–178 (2000).

331. Sahner, K. *et al.* CO2 selective potentiometric sensor in thick-film technology. *Sensors* **8**, 4774–4785 (2008).

332. Obata, K., Kumazawa, S., Shimanoe, K., Miura, N. & Yamazoe, N. Potentiometric sensor based on NASICON and In2O3 for detection of CO2 at room temperature - Modification with foreign substances. *Sens Actuators B Chem* **76**, 639–643 (2001).

333. Dang, H. Y. & Guo, X. M. Characteristics of NASICON-based thick-film CO 2 sensor attached with integrated auxiliary electrode. *IEEE Sens J* **12**, 2430–2434 (2012).

334. Yao, S., Shimizu, Y., Miura, N. & Yamazoe, N. Solid electrolyte carbon dioxide sensor using sodium-ion conductor and Li2CO3–BaCO3 electrode. *Jpn J Appl Phys* **31**, L197 (1992).

335. Kida, T., Kishi, S., Yuasa, M., Shimanoe, K. & Yamazoe, N. Planar NASICON-Based CO[sub 2] Sensor Using BiCuVO[sub x]/Perovskite–Type Oxide as a Solid-Reference Electrode. *J Electrochem Soc* **155**, J177 (2008).

336. Aono, H., Sadaoka, Y., Montanaro, L., di Bartolomeo, E. & Traversa, E. Humidity influence on the CO2 response of potentiometric sensors based on NASICON pellets with new compositions, Na3Zr2-(x/4)Si2-xP1+xO12 (x = 1.333). *Journal of the American Ceramic Society* **85**, 585–589 (2002).

337. Ménil, F., Daddah, B. O., Tardy, P., Debéda, H. & Lucat, C. Planar LiSICON-based potentiometric CO2 sensors: Influence of the working and reference electrodes relative size on the sensing properties. *Sens Actuators B Chem* **107**, 695–707 (2005).

338. Obata, K., Motohi, S. & Matsushima, S. NO2 and CO2 Sensing properties of lisiconbased sensor operative at room temperature. *Sensors and Materials* **24**, 43–56 (2012).

339. Satyanarayana, L., Choi, G. P., Noh, W. S., Lee, W. Y. & Park, J. S. Characteristics and performance of binary carbonate auxiliary phase CO2 sensor based on Li3PO4 solid electrolyte. *Solid State Ion* **177**, 3485–3490 (2007).

340. Lee, H. K., Choi, N. J., Moon, S. E., Yang, W. S. & Kim, J. A solid electrolyte potentiometric CO 2 gas sensor composed of lithium phosphate as both the reference and the solid electrolyte materials. *Journal of the Korean Physical Society* **61**, 938–941 (2012).

341. Choi, N. J., Lee, H. K., Moon, S. E., Yang, W. S. & Kim, J. Stacked-type potentiometric solid-state CO2 gas sensor. *Sens Actuators B Chem* **187**, 340–346 (2013).

342. Sun, G., Wang, H., Li, P., Liu, Z. & Jiang, Z. Response characteristics of a potentiometric CO2 gas sensor based on Li3PO4 solid electrolyte using Au film as the electrodes. *J Appl Phys* **115**, 124505 (2014).

343. Noh, W. S., Satyanarayana, L. & Park, J. S. Potentiometric CO2 sensor using Li+ ion conducting Li3PO4 thin film electrolyte. *Sensors* **5**, 465–472 (2005).

344. Zhu, Y., Thangadurai, V. & Weppner, W. Garnet-like solid state electrolyte Li6BaLa2Ta 2O12 based potentiometric CO2 gas sensor. *Sens Actuators B Chem* **176**, 284–289 (2013).

345. Yoon, J., Hunter, G., Akbar, S. & Dutta, P. K. Interface reaction and its effect on the performance of a CO2 gas sensor based on Li0.35La0.55TiO3 electrolyte and Li2CO3 sensing electrode. *Sens Actuators B Chem* **182**, 95–103 (2013).

346. Yan, Y., Shimizu, Y., Miura, N. & Yamazoe, N. High-performance solid-electrolyte SOx sensor using MgO-stabilized zirconia tube and Li2SO4CaSO4SiO2 auxiliary phase. *Sens Actuators B Chem* **20**, 81–87 (1994).

347. Yan, Y., Shimizu, Y., Miura, N. & Yamazoe, N. Solid-State Sensor for Sulfur Oxides Based on Stabilized Zirconia and Metal Sulphate. *Chem Lett* **21**, 635–638 (1992).

348. Maruyama, T., Saito, Y., Matsumoto, Y. & Yano, Y. Potentiometric sensor for sulfur oxides using NASICON as a solid electrolyte. *Solid State Ion* **17**, 281–286 (1985).

349. Min, B. K. & Choi, S. D. SO2-sensing characteristics of Nasicon sensors with Na2SO4-BaSO4 auxiliary electrolytes. *Sens Actuators B Chem* **93**, 209–213 (2003).

350. Ma, C. *et al.* Sub-ppb SO2 gas sensor based on NASICON and LaxSm1-xFeO3 sensing electrode. *Sens Actuators B Chem* **256**, 648–655 (2018).

351. Izu, N., Hagen, G., Schönauer, D., Röder-Roith, U. & Moos, R. Planar potentiometric SO2 gas sensor for high temperatures using NASICON electrolyte combined with V2O5/WO 3/TiO2+ Au or Pt electrode. *Journal of the Ceramic Society of Japan* **119**, 687–691 (2011).

352. Wang, L. & Kumar, R. v. A SO2 gas sensor based upon composite Nasicon/Sr-β-Al 2O3 bielectrolyte. *Mater Res Bull* **40**, 1802–1815 (2005).

353. Rao, N., van den Bleek, C. M., Schoonman, J. & Sørensen, O. T. A novel temperature-gradient Na+-β″-alumina solid electrolyte based SOx gas sensor without gaseous reference electrode. *Solid State Ion* **53**, 30–38 (1992).

354. Itoh, M., Sugimoto, E. & Kozuka, Z. Solid reference electrode of SO2 sensor using β-alumina solid electrolyte. *Transactions of the Japan Institute of Metals* **25**, 504–510 (1984).

355. Jianhua, Y., Pinghua, Y. & Guangyao, M. A fully solid-state SOx (x = 2, 3) gas sensor utilizing Ag-β″-alumina as solid electrolyte. *Sens Actuators B Chem* **31**, 209–212 (1996).

356. Yang, P. H., Yang, J. H., Chen, C. S., Peng, D. K. & Meng, G. Y. Performance evaluation of SOx (x = 2,3) gas sensors using Ag-β″-alumina solid electrolyte. *Solid State Ion* **86**, 1095–1099 (1996).

357. Mari, C. M., Beghi, M., Pizzini, S. & Faltemier, J. Electrochemical solid-state sensor for SO2 determination in air. *Sens Actuators B Chem* **2**, 51–55 (1990).

358. Wang, L. & Kumar, R. v. Potentiometric SO2 gas sensor based on a thick film of Ca 2+ ion conducting solid electrolyte. *J Appl Electrochem* **36**, 173–178 (2006).

359. Wang, L. & Kumar, R. v. A new SO2 gas sensor based on an Mg2+ conducting solid electrolyte. *Journal of Electroanalytical Chemistry* **543**, 109–114 (2003).

360. Wang, H., Liu, Z., Chen, D. & Jiang, Z. A new potentiometric SO2 sensor based on Li3PO4 electrolyte film and its response characteristics. *Review of Scientific Instruments* **86**, 075007 (2015).

361. Zhuiykov, S., Ono, T., Yamazoe, N. & Miura, N. High-temperature NOx sensors using zirconia solid electrolyte and zinc-family oxide sensing electrode. *Solid State Ion* **152**, 801–807 (2002).

362. White, B., Chatterjee, S., MacAm, E. & Wachsman, E. Effect of electrode microstructure on the sensitivity and response time of potentiometric NOX sensors. *Journal of the American Ceramic Society* **91**, 2024–2031 (2008).

363. Zhuiykov, S., Nakano, T., Kunimoto, A., Yamazoe, N. & Miura, N. Potentiometric NOx sensor based on stabilized zirconia and NiCr2O4 sensing electrode operating at high temperatures. *Electrochem commun* **3**, 97–101 (2001).

364. Mondal, S. P. *et al.* Development of high sensitivity potentiometric NOx sensor and its application to breath analysis. *Sens Actuators B Chem* **158**, 292–298 (2011).

365. Miura, N., Lu, G. & Yamazoe, N. High-temperature potentiometric/amperometric NOx sensors combining stabilized zirconia with mixed-metal oxide electrode. *Sens Actuators B Chem* **52**, 169–178 (1998).

366. Romanytsia, I., Viricelle, J. P., Vernoux, P. & Pijolat, C. Application of advanced morphology Au-X (X = YSZ, ZrO2) composites as sensing electrode for solid state mixed-potential exhaust NOx sensor. *Sens Actuators B Chem* **207**, 391–397 (2015).

367. Yoo, J., Chatterjee, S. & Wachsman, E. D. Sensing properties and selectivities of a WO3/YSZ/Pt potentiometric NOx sensor. *Sens Actuators B Chem* **122**, 644–652 (2007).

368. Obata, K. & Matsushima, S. NASICON-based NO2 device attached with metal oxide and nitrite compound for the low temperature operation. *Sens Actuators B Chem* **130**, 269–276 (2008).

369. Shimizu, Y. & Maeda, K. Solid electrolyte NOx sensor using pyrochlore-type oxide electrode. *Sens Actuators B Chem* **52**, 84–89 (1998).

370. Yao, S., Shimizu, Y., Miura, N. & Yamazoe, N. Use of Sodium Nitrite Auxiliary Electrode for Solid Electrolyte Sensor to Detect Nitrogen Oxides. *Chem Lett* **21**, 587–590 (1992).

371. Thangadurai, V., Narayanan, S. & Pinzaru, D. Garnet-type solid-state fast Li ion conductors for Li batteries: Critical review. *Chem Soc Rev* **43**, 4714–4727 (2014).

372. Aono, H., Sadaoka, Y., Montanaro, L., di Bartolomeo, E. & Traversa, E. Humidity influence on the CO2 response of potentiometric sensors based on NASICON pellets with new compositions, Na3Zr2-(x/4)Si2-xP1+xO12 (x = 1.333). *Journal of the American Ceramic Society* **85**, 585–589 (2002).

373. Kida, T., Shimanoe, K., Miura, N. & Yamazoe, N. Stability of NASICON-based CO2 sensor under humid conditions at low temperature. *Sens Actuators B Chem* **75**, 179–187 (2001).

374. Kaneyasu, K. *et al.* Carbon dioxide gas sensor based on solid electrolyte for air quality control. *Sens Actuators B Chem* **66**, 56–58 (2000).

375. Izquierdo, R. *et al.* Pulsed Laser Deposition of NASICON Thin Films for the Fabrication of Ion Selective Membranes. *J Electrochem Soc* **144**, L323 (1997).

376. Wang, L. & Kumar, R. v. Cross-sensitivity effects on a new carbon dioxide gas sensor based on solid bielectrolyte. *Meas Sci Technol* **15**, 1005 (2004).

377. Hong, H. S., Kim, J. W., Jung, S. J. & Park, C. O. Suppression of NO and SO 2 cross-sensitivity in electrochemical CO 2 sensors with filter layers. *Sens Actuators B Chem* **113**, 71–79 (2006).

378. Salam, F., Bredikhin, S., Birke, P. & Weppner, W. Effect of the thickness of the gas-sensitive layer on the response of solid state electrochemical CO2 sensors. *Solid State Ion* **110**, 319–325 (1998).

379. Dutta, A. & Ishihara, T. Amperometric NOX sensor based on oxygen pumping current by using LaGaO3-based solid electrolyte for monitoring exhaust gas. *Sens Actuators B Chem* **108**, 309–313 (2005).

380. Miura, N., Nakatou, M. & Zhuiykov, S. Impedancemetric gas sensor based on zirconia solid electrolyte and oxide sensing electrode for detecting total NOx at high temperature. *Sens Actuators B Chem* **93**, 221–228 (2003).

381. Miura, N., Lu, G., Ono, M. & Yamazoe, N. Selective detection of NO by using an amperometric sensor based on stabilized zirconia and oxide electrode. *Solid State Ion* **117**, (1999).

382. Miura, N., Iio, M., Lu, G. & Yamazoe, N. Solid-state amperometric NO2 sensor using a sodium ion conductor. *Sens Actuators B Chem* **35**, (1996).

383. Thompson, T. *et al.* Electrochemical Window of the Li-Ion Solid Electrolyte Li7La3Zr2O12. *ACS Energy Lett* **2**, 462–468 (2017).

384. Hwang, J. & Voyles, P. M. Variable resolution fluctuation electron microscopy on cu-zr metallic glass using a wide range of coherent stem probe size. *Microscopy and Microanalysis* **17**, 67–74 (2011).

385. Daulton, T. L., Bondi, K. S. & Kelton, K. F. Nanobeam diffraction fluctuation electron microscopy technique for structural characterization of disordered materials-Application to Al88-xY7Fe5Tix metallic glasses. *Ultramicroscopy* **110**, 1279–1289 (2010).

386. Avrami, M. Kinetics of phase change. I: General theory. *J Chem Phys* **7**, 1103–1112 (1939).

387. Avrami, M. Granulation, phase change, and microstructure kinetics of phase change. III. *J Chem Phys* **9**, 177–184 (1941).

388. Han, J. K., Jung, W. C., Shin, D. K. & Kwang, S. Y. Thick-film CO2 sensors based on NASICON synthesized by a sol-gel process. in *Materials Science Forum* vol. 544 925–928 (2007).

389. Chen, K., Zhang, M., Wang, H. & Gu, H. A potentiometric SO2 gas sensor based on the Li3PO4-Li2SiO3 solid electrolyte thin film. *Review of Scientific Instruments* **90**, 065001 (2019).

390. Uneme, Y., Tamura, S. & Imanaka, N. Moderate-temperature operable SO2 gas sensor based on Zr4+ ion conducting solid electrolyte. *Journal of Sensors and Sensor Systems* **1**, 29–32 (2012).